Dissertation

SUBMITTED TO THE

Combined Faculties of the Natural Sciences and Mathematics
of the Ruperto-Carola-University of Heidelberg, Germany

FOR THE DEGREE OF

Doctor of Natural Sciences

Put forward by

Andreas Fischer
born in Kaiserslautern, Germany

Oral examination: January 13th, 2015

Dissociative Photoionization of Molecular Hydrogen

A Joint Experimental and Theoretical Study of the
Electron-Electron Correlations induced by XUV Photoionization
and
Nuclear Dynamics on IR-Laser Dressed Transition States

Referees:

Priv.-Doz. Dr. Robert Moshammer
Prof. Dr. Selim Jochim

Abstract – In this thesis, the dissociative single-ionization of molecular hydrogen is investigated in a kinematically complete experiment by employing extreme ultraviolet attosecond pulse trains and infrared femtosecond laser pulses. Induced by the absorption of a single XUV photon, a pronounced energy-dependent asymmetry of the relative emission direction of the photoelectron and the ion is observed. The asymmetry pattern is explained in terms of an interference of two ionization pathways involving a doubly-excited state. This interpretation is validated by a semi-classical model which only takes the nuclear motion into account. Using this model and the observed asymmetry, it is furthermore possible to disentangle the two dissociation pathways which allows for the determination of the autoionization lifetime of the contributing doubly-excited state as a function of the internuclear distance.

Moreover, using a pump–probe experiment the dissociation dynamics of molecular hydrogen is investigated. A time-delay dependent momentum distribution of the fragments is observed. With a combined quantum mechanical and semi-classical approach the mechanism giving rise to the observed time-dependence is identified in terms of an intuitive elevator mechanism.

* * *

Zusammenfassung – In dieser Arbeit wird die dissoziative Einfachionisation von molekularem Wasserstoff unter dem Einsatz von Attosekundenpulszügen und infrarot Laserpulsen in einem kinematisch vollständigen Experiment untersucht. Ausgelöst durch die Absorption eines einzelnen XUV Photons wird eine stark ausgeprägte, energieabhängige Asymmetrie in der relativen Propagationsrichtung der gemessenen Photoelektronen und der Ionen beobachtet. Das Verhalten der Asymmetrie kann durch die Interferenz zweier Ionisationskanäle, unter denen sich ein doppelt angeregter Zustand befindet, erklärt werden. Diese Interpretation wird durch ein semiklassisches Model, welches nur dir Kernbewegung berücksichtigt, verifiziert. Unter der Verwendung des Models und der gemessenen Asymmetrie, ist es möglich die zwei dissoziativen Ionisationskanäle zu trennen. Dies ermöglicht die Bestimmung der Autoionisationszeit des involvierten doppelt angeregten Zustands als Funktion des Kernabstands.

Des Weiteren wird die Dissoziationsdynamik von molekularem Wasserstoff in einem zeitauflösendem Pump–Probe Experiment untersucht. Eine zeitabhängige Impulsverteilung der Fragmente wird beobachtet. Durch die Kombination von quantenmechanischen Rechnungen und einem semi-klassischen Model kann ein intuitiver Fahrstuhlmechanismus identifiziert werden, welcher die Zeitabhängigkeit der Fragmentimpulse verursacht.

List of Publications

Electron Localization Involving Doubly Excited States in Broadband Extreme Ultraviolet Ionization of H_2
A. Fischer, A. Sperl, P. Cörlin, M. Schönwald, H. Rietz, A. Palacios, A. González-Castrillo, F. Martín, T. Pfeifer, J. Ullrich, A. Senftleben, and R. Moshammer
Phys. Rev. Lett. 110, 213002 (2013)

Measurement of the autoionization lifetime of the energetically lowest doubly excited $Q_1\,{}^1\Sigma_u^+$ state in H_2 using electron ejection asymmetry
A. Fischer, A. Sperl, P. Cörlin, M. Schönwald, S. Meuren, J. Ullrich, T. Pfeifer, R. Moshammer and A. Senftleben
J. Phys. B: At. Mol. Opt. Phys. 47, 021001 (2014)

Extracting Phase and Amplitude Modifications of Laser-Coupled Fano Resonances
A. Kaldun, C. Ott, A. Blättermann, M. Laux, K. Meyer, T. Ding, A. Fischer, and T. Pfeifer
Phys. Rev. Lett. 112, 103001 (2014)

Molecular wave-packet dynamics on laser-controlled transition states
A. Fischer, M. Gärttner, P. Cörlin, A. Sperl, M. Schönwald, T. Mizuno, G. Sansone, A. Senftleben, J. Ullrich, B. Feuerstein, T. Pfeifer, and R. Moshammer
Submitted
arXiv:1410.8032 [physics] (2014)

Contents

1 Introduction

With his pioneering work of observing molecular motion [1–6], Ahmed Zewail established femtochemistry as a new field of science. The focus of femtochemistry is to observe, understand and ultimately control the atomic motion in chemical reactions as the reagents pass through transition states. Considering the small length scale of chemical reactions (typically a few Ångström, i.e. 10^{-10} m) and the large velocity of the involved atoms leads to reaction times in the femtosecond regime. Since the particles move in the combined potential of electrons and nuclei, the electrons are far more than just spectators in chemical reactions. The dynamics of these processes is a consequence of the complex interplay between the electrons and the nuclei. Since molecules are inherently multi-particle systems, various phenomena such as electron-electron correlations (which can lead e.g. to the decay of transition states) and couplings between the electronic and nuclear dynamics form an essential aspect of femtochemistry.

In the interaction of ionizing radiation with matter, electron-electron correlation plays an important role as it allows, among other processes, the preparation of superexcited states. Superexcited states have an potential energy above the first ionization threshold and are therefore embedded in the single-ionization continuum. Acting as intermediate states they play an important role in single-photon and multiphoton absorption, electron impact ionization and diverse scattering processes. Already in 1962 Robert Platzman investigated and predicted the importance of superexcited states in the interaction of high-energetic, ionizing radiation with matter [7–9]. They tremendously enlarge photoionization cross-sections and are therefore an important aspect of dissociative photoionization.

Molecular hydrogen, with its apparent simplicity, has always been a popular target for the investigation of photochemical reactions. Having only two electrons, H_2 is the ideal candidate to study the effects of electron correlations which are, unlike in helium, influenced by the nuclear motion. Another advantage is that for some cases a theoretical description of hydrogen molecules is still possible by means of modern approaches, even fully quantum mechanically. This allows for precise tests of theoretical predictions by comparing with experimental results.

In early measurements on the photo-induced dissociative ionization of hydrogen molecules conducted by Browning and Fryar in 1973 [10], an increase of the production ratio of H^+/H_2^+ was observed at photon energies of 26 eV [11]. This increase was ascribed to the presence of doubly-excited states[1] [11]. Only three years later Strathdee and Browning [12] reported on signatures of doubly-excited states in the observed proton kinetic energy distribution. It comes as no surprise that later, by employing synchrotrons as a high-quality light source, great progress was made in the spectroscopy and in dynamical investigations of superexcited states [9]. Many investigations were conducted that shed light on the mechanisms involving doubly-exited states in the creation of H^+ and H_2^+ by the absorption of a single high-energetic photons, e.g. Refs. [13–18].

Doubly-excited states decay through two competing processes: (I) dissociation into neutral (atomic) states and (II) autoionization due to electron-electron interaction [19]. The autoionization of doubly-excited states in H_2 occurs very fast and is therefore on the order of the molecule's dissociation time (some femtoseconds). Since with the presence of autoionizing doubly-excited states, resonant and non-resonant dissociative ionization channels are available strong interference effects can occur. With the availability of detection systems which are capable of detecting photoelectrons and the dissociating protons in coincidence, vector correlation methods were introduced to the field. With these methods, it was possible to observe so-called molecular frame photoelectron angular distributions (MFPADs) where for each event the momentum vectors are rotated such that the proton momentum vectors point in the same direction. The results showed a strongly asymmetric distribution of the photoelectrons, which are a result of the above mentioned interference, see e.g. [20, 21]. So far the reported investigations on the asymmetric MFPADs did not discuss the full dependence of the asymmetry on the photoelectron momenta, the proton momenta and the photon energy.

For this reason, in this work a doubly-differential energy-correlated study of these processes has been performed by employing a reaction microscope which gives the complete kinematic information of the charged particles. Using the reaction microscope, we are able to determine the energy of the absorbed photons by measuring the energies of the reaction fragments and by exploiting energy conservation. Instead of a synchrotron, we use laser-driven high-order harmonic generation (see e.g. [22]) as a source for high-energy photons. The obtained results are interpreted in terms of an intuitive energetically fully differential semi-classical model (which was developed as part of this thesis) and are supported by fully quantum-mechanical calculations performed by the group of Fernando Martín (for methodology see e.g. [23]). Further, the measured asymmetry is used for the first time to disentangle the non-resonant dissociative ionization channel from the resonant channel. After having disentangled the reaction channels, it is possible to determine the lifetime of the energetically lowest doubly-excited state of Σ_u^+ symmetry[2] as a function of the internuclear sepa-

---

[1] The doubly-excited states in H_2 are all superexcited states, i.e. they all are embedded within the first ionization continuum.

[2] This state has a very high population cross-section is therefore of utmost importance in high-energetic photoionization.

ration. This novel approach makes the lifetime accessible over a very large range of internuclear separations, previously inaccessible by experiments. The result is in very good agreement with theoretical predictions as well as with previous experiments for the applicable internuclear distances.

The second part of this thesis focuses on the understanding and controlling aspect of femtochemistry. Control over the nuclear motion in chemical reactions is often exerted by lasers acting on the molecule's electrons by influencing the molecule's electronic states. It is therefore clear that the advent of laser systems delivering ultra-short pulses in the femtosecond regime and extreme peak intensities triggered enormous scientific advances by enabling pump–probe measurements.

The decrease in pulse durations of optical lasers to only a few optical cycles allowed to observe the vibrational motion and fragmentation dynamics of even molecular hydrogen (see e.g. [24–32]), the lightest and fastest molecule. The ultrafast dynamics for such light systems occurs on very short time scales (a few femtoseconds).

In many experiments infrared (IR) laser pulses were used in the pump and probe step. Recently the investigation scheme was extended by Kelkensberg et al. [31] when they used attosecond pulse trains (APTs) in an innovative experiment as a pump pulse and an IR pulse to subsequently probe in order to observe the molecular motion of vibrational wave packets in H_2. Since the APTs have photons with energies well within the extreme ultraviolet (XUV) regime, a single photon is sufficient to ionize molecular hydrogen and launch vibrational wave packets in the binding potential of H_2^+. In many cases this is an advantage, since the molecular potential is hardly distorted by the low intensities of today's attosecond pulse trains, which allows to launch molecular wave packets in the natural environment of the molecular hydrogen ion. Another advantage arises by the low intensity as it allows the XUV excitation to be described within perturbation theory.

In addition to the ability to observe the molecular motion of even the fastest system, modern experiments are able to influence photochemical reactions in a desired way. For instance, using advanced pulse shaping techniques, it has been demonstrated that light pulses can be used to steer photochemical reactions [33–36]. Having photon energies of $\approx 1\,\mathrm{eV}$ IR lasers are exceptionally well suited to couple and therefore modify different molecular potential energy surfaces. With this technique it is also possible to obtain control over reactions as it has been demonstrated in previous approaches (see e.g. [37–39]).

In this work, we combine the advantages of XUV wave packet preparation and the capabilities of the IR pulse to couple molecular states via an XUV-IR experiment. In contrast to previously conducted experiments concerning the nuclear wave-packet dynamics the focus of this work is put on the IR induced dissociation process. A time-delay dependent momentum of the fragments is observed which is analyzed using a Fourier technique. By employing quantum calculations (which have been conducted as an integral part of this work) as well as a semi-classical model (also developed as part of this work) – which treats the potential energy curves within the Floquet picture – a fundamental mechanism is identified which leads to the time dependence of the reaction fragments.

This thesis is organized as follows: Chapter 2 begins with the description of molecular hydrogen in laser fields. Tunnel ionization, multiphoton ionization and single-photon ionization are discussed as different single-ionization mechanisms. After that a short introduction to molecular symmetry is given and the dipole selection rules are introduced. Subsequently in Chapter 3, the experimental setup is presented. An overview is given by splitting the setup in three modules, (I) the laser system, (II) the high-order harmonic generation chamber and (III) the reaction microscope. Then, in Chapter 4 the experimental results of the single XUV photon induced electron localization are presented. It starts by conveying additional theoretical concepts essential for the interpretation of the measured results in terms of a semi-classical model. Thereafter, an overview over the for this thesis relevant ionization channels in molecular hydrogen is presented. Then, the chapter concludes by presenting the measured electron asymmetry and its interpretation as well as the derivation of the lifetime of the energetically lowest doubly-excited $Q_1\,{}^1\Sigma_u^+$ state. Chapter 5 presents the results of the XUV-pump IR-probe experiment. First, the necessary theoretical concepts for solving the time-dependent Schrödinger equation are given which are important for the understanding of quantum calculations conducted in this work. Then, the Floquet picture is introduced, which is an essential part of the semi-classical model used for the interpretation of the data. The chapter concludes by presenting the measured results in comparison to the performed simulations. Finally, Chapter 6 gives a summary of this thesis and an outlook on future investigations.

Note: Throughout this work atomic units are used if not stated otherwise.

2 Molecular Hydrogen in Laser Fields

Exposing molecular hydrogen to laser fields leads to a great number of effects, among them the ionization of the molecule. Therefore theoretical descriptions strongly rely on different approximations to describe the ionization process accurately. When the field strength of the laser's electromagnetic field is much weaker than the molecular[1] field it is possible to treat the influence of the laser within the framework of the time-dependent perturbation theory. The appearing perturbation series gives rise to the process interpretation in terms of (multi-) photon transitions, where integer multiples of the fundamental field energies (frequencies) $E = \omega$ are absorbed by the atomic or molecular system. This perturbation treatment is no longer possible if the laser field strength becomes of the order of the molecular electric field, where the potential is deformed by the laser so far that a tunneling of an electron out of the molecular potential becomes possible (tunnel ionization). An approach to the theoretical description of this case was presented by M. V. Ammosov, N. B. Delone and V. P. Krainov [40] by introducing their today well known ADK-theory (for reference see e.g. Ref. [41]). In 2002 a group around C. D. Lin [42] further extended the ADK-formalism to molecules (molecular ADK or MO-ADK). The range of applicability of these two theoretical approaches (multiphoton ionization and tunnel ionization) can be described using the Keldysh parameter [43] which depends on the laser intensity and the wavelength.

Therefore, for optical lasers which have photon energies ($\approx 1\,\mathrm{eV}$) much smaller than the ionization potential I_p, two possible ionization mechanisms exist: the multiphoton ionization and the tunnel ionization. An alternative approach to photoionization is the increasing of the photon energy to the order of the ionization potential, as it can be done in synchrotrons and free electron lasers (FEL) or by exploiting the high-order harmonic generation (as it is the case in this work). With these techniques, single-photon ionization becomes available which is possible for weak fields and can be described by first-order perturbation theory.

Since ionization is a fundamental aspect of this thesis Sec. 2.1, gives a brief summary of the different single-ionization processes applied to molecules: (I) tunnel ionization, (II) multiphoton ionization, and (III) single-photon ionization. Subsequently, Sec. 2.2 gives a short introduction to molecular symmetry and molecular selection rules which will play a key role in the determination of wave functions in Chap. 4.

---

[1] Most of the arguments presented in this chapter also apply to atoms.

2.1 Single-Ionization Processes

In the following we discuss laser induced processes leading to a singly ionized molecule or atom, i.e. a system from which one electron is removed. When single-photon ionization is forbidden due to low photon energies, essentially two induced ionization mechanisms exist: (I) tunnel ionization and (II) multiphoton ionization. In 1965 it was shown by L. V. Keldysh that these two ionization regimes can be separated by introducing the adiabaticity parameter

$$\gamma = \omega_0 \sqrt{\frac{2I_p}{I}}, \tag{2.1}$$

where I_p is the molecules ionization potential, $E_\gamma = \omega_0$ the photon energy and I the laser intensity. For $\gamma \ll 1$ the ionization has a character best described by tunneling whereas for $\gamma \gg 1$ a multiphoton perturbation approach is best suited [44].

The Keldysh parameter is often expressed in terms of the ponderomotive potential

$$U_p = {}^{I}\!/_{4\omega_0^2}, \tag{2.2}$$

which is the kinetic energy of an electron in a periodic laser field averaged over one cycle. With this definition Eq. (2.1) can be rewritten as

$$\boxed{\gamma = \sqrt{\frac{I_p}{2U_p}}} \tag{2.3}$$

In reality, however, laser parameters often have to be chosen such that $\gamma \approx 1$ for which a clear classification in terms of the Keldysh parameter is impossible [45]. Here, it has to be decided from case to case which approach seems to yield the most promising results.

In this work high-order harmonics in the XUV regime with low intensity and high photon energies are used and it turns out that in this case we have $\gamma \gg 1$, indicating that we are in the regime where we could use perturbation theory to describe the dipole transitions leading to ionization as multi-photon transitions. However, as a single photon suffices to ionize molecular hydrogen, another process becomes the predominant contributor to photo-ionization: (III) the single-photon ionization. All experimental results presented in Chap. 4 and Chap. 5 are obtained using single-photon ionization. Nevertheless, tunnel ionization and multi-photon ionization are treated in the following sections as well in order to give a complete overview and also because tunnel ionization plays an important role in the high-harmonics generation process used to generate XUV attosecond pulse trains.

2.1.1 Tunnel Ionization

The tunnel ionization regime ($\gamma \ll 1$) is reached when the laser intensity becomes very large and the photon energy very small where the light field is described as a classical field in the limit of infinitely many photons. The high field strength of the laser strongly distorts the molecular potential which is illustrated in Fig. 2.1. The field strength can become so strong that a bound electron can escape the binding potential of the molecule by (horizontally) tunneling through the potential barrier. In order to calculate the tunnel-ionization probability the MO-ADK theory [42, 46] is applied. For a diatomic molecule the probability reads (as a function of the laser field strength $\mathcal{E}$)

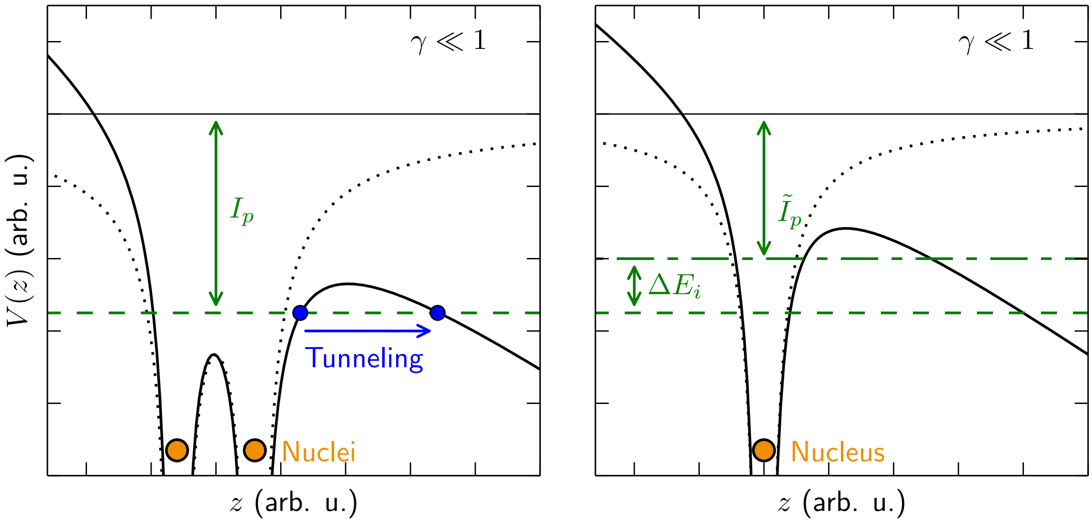

Figure 2.1: Illustration of the tunnel ionization for the molecular (left) and atomic (right) case. The strong laser field lowers the potential and an electron can tunnel out resulting in an ionization of the molecule. When a (linear) molecule is aligned with the laser polarization axis (z-direction), the larger extension of the electron orbitals results in a stronger lowering of the potential as compared to the atomic case. Therefore, for aligned molecules an enhancement of the tunnel-ionization rate is observed. Further, the tunnel ionization within an aligned molecule is equivalent to that within an atom with lowered ionization potential $\tilde{I}_p = I_p - \Delta E_i$ (see right figure).

$$\boxed{w(\mathcal{E}) = A(l,m)\,\kappa^{-\frac{2Z_{\mathrm{eff}}}{\kappa-1}} \left(\frac{2\kappa^3}{\mathcal{E}}\right)^{\frac{2Z_{\mathrm{eff}}}{\kappa-|m|-1}} e^{-\frac{2\kappa^3}{3\mathcal{E}}}} \qquad (2.4)$$

where $A(l, m)$ is the orbital structure factor as a function of the quantum numbers l and m, Z_{eff} is the molecule's effective nuclei charge[2] and $\kappa = \sqrt{2I_p}$.

Figure 2.1 further compares the tunnel process for the molecular case (left) to the atomic case (right) for equal ionization potentials I_p. We consider only the case where the molecule is aligned with the laser polarization axis (z-axis). Due to the larger extension of the electronic molecular orbitals, the laser induced distortion is stronger for the molecular case which, in contrast to the atomic case, further lowers the tunnel barrier resulting in a higher tunnel ionization rate for aligned molecules. The molecular tunnel rate is equivalent to the one observed for atoms with a reduced ionization potential $\tilde{I}_p = I_p - \Delta E_i$ [see Fig. 2.1 (right)]. It should for completeness be noted that if the electric field strength of the laser is further increased, the electron can overcome the barrier without tunneling (see Fig. 2.2). This process is referred to as over-the-barrier ionization [47].

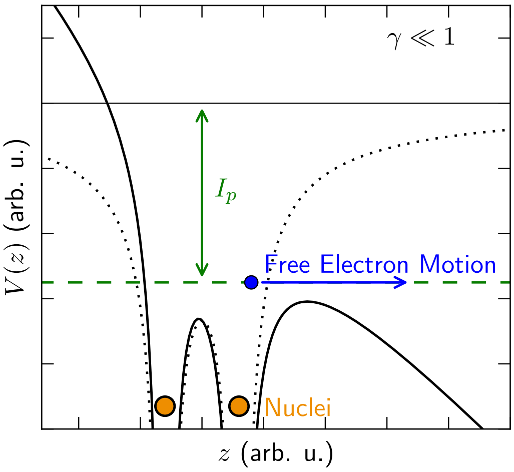

Figure 2.2: Over-the-barrier ionization. The electric field strength is so high that the electron can simply leave the molecular potential horizontally, which leads to the ionization.

High-Order Harmonic Generation: Three-Step Model

In this work the tunnel ionization is not used to investigate physical processes in molecular hydrogen. However, it is used in the creation of high-order harmonic generation (HHG) in argon gas. Even though we will not attempt to give a deep introduction to the topic at this point (for this please refer to Refs. [22, 47–56] and to the dissertations [57–59] with respect to our experiment) we will briefly discuss

---

[2] Even though in a molecule the attractive force is not a Coulomb potential, a very good approximation is achieved by modeling it as Z_{eff}/r as an effective Coulomb field.

the three-step model introduced by Corkum and Kulander [52, 60–62] which gives an intuitive understanding of the generation process.

In the three-step model, a strong laser pulse distorts the atomic potential such that an electron can tunnel out (see Fig. 2.3). The electron is accelerated away from the ion by the strong laser field. When the laser field changes the sign, the electron is decelerated and eventually driven back toward the ion. In the last step, the electron recombines with the ion emitting an XUV photon with the sum energy of the ionization potential and the gained kinetic energy.

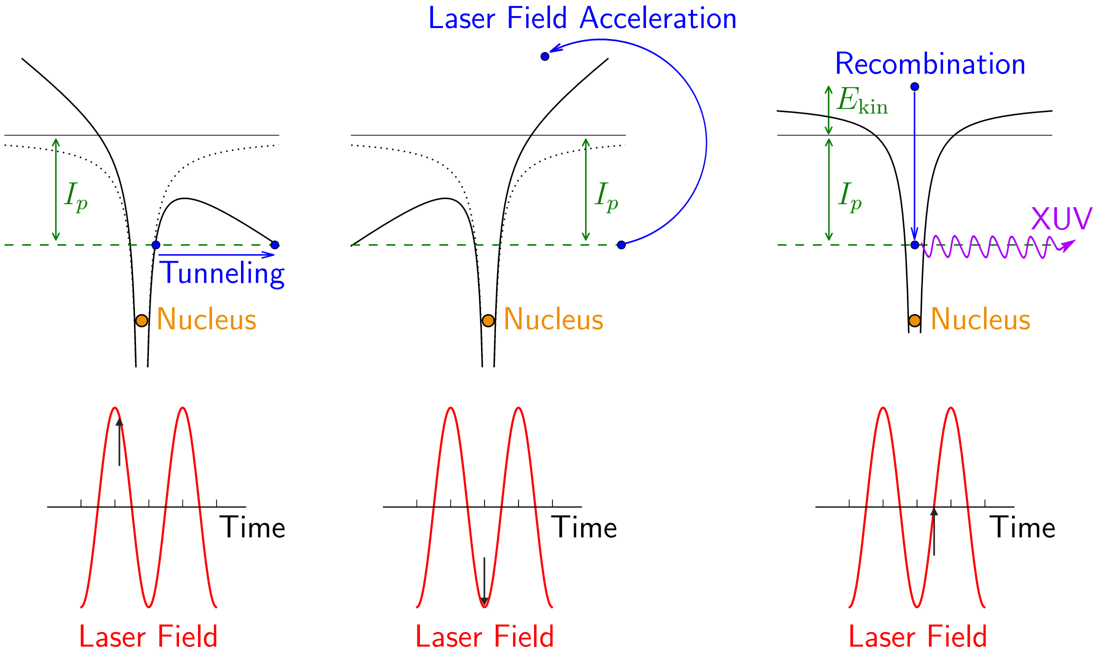

Figure 2.3: Three-step model. In the first step, an atom is ionized in a strong laser field (tunnel ionization). The freed electron is accelerated away from the atom by the laser field. Due to the oscillation of the electric field the electron is eventually driven back toward the ion. In the third step, the electron recombines with the ion. The kinetic energy gained in the laser field plus the ionization potential is emitted in the form of high-order harmonics which consist of photons with energies in the extreme ultraviolet range.

As this process occurs in every half-cycle of the laser pulse, the XUV photons are irradiated in so-called attosecond pulse trains (APTs). From Fourier theory it is clear that having a temporal spacing of $T/2$ (where T is the period of the intense driving laser pulse) leads to photon energies of the APTs with an even integer multiple of the fundamental photon energy ($\omega_{\mathrm{XUV}} = 2n\omega_0$ with $n \in \mathbb{N}$).

The semi-classical interpretation has of course limits, as it cannot correctly predict amplitudes and phases of the photons in the HHG [59]. A quantum mechanical treatment of the HHG overcoming these difficulties became available in 1994 when

Lewenstein et al. [63] presented an analytical solution using the strong field approximation.

To conclude the section we briefly characterize the spectrum of the high-order harmonics used for ionization and excitation. The photon energy extends over the large range from 16 eV to 55 eV making it difficult to measure the spectrum with a homogeneous approach with the available experimental means. To overcome this problem the spectrum is measured using two different techniques, (I) photoelectron spectra obtained using the reaction microscope with different noble gases as a target and (II) using grating spectrometer with CCD camera, which is sensitive at photon energy above ≈ 30 eV (because of the used transmission grating, photons of lower energy are absorbed and cannot enter the detection system).

Figure 2.4 shows four different spectra, three obtained as photo electron spectra using Argon, Neon, and Helium, and one spectrum using the grating spectrometer. Combing the four obtained spectra the energy range from 20 eV to 55 eV can be

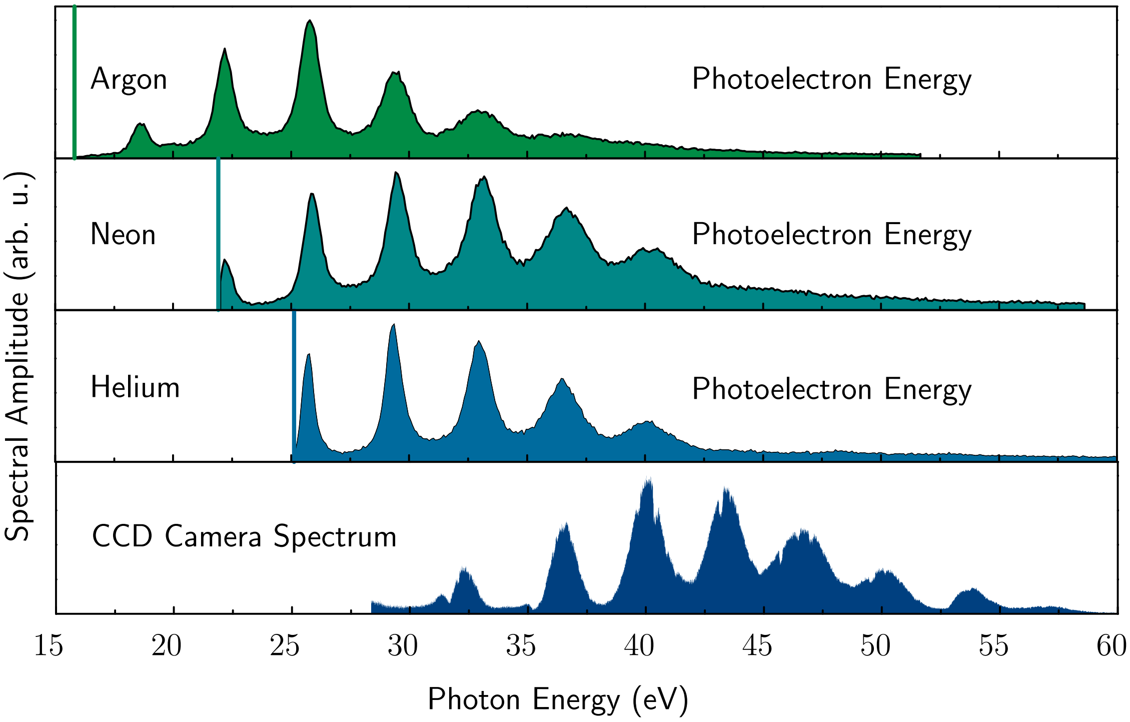

Figure 2.4: Spectral structure of the high-order harmonics (HH). Since the spectrometer used to measure the HH relies on a transmission grating, photons with energies below 30 eV are absorbed. In order to make the harmonic structure visible below this point, different gases have been ionized and the photoelectron kinetic energy was measured. Knowing the ionization potential and the fundamental photon energy the spectra are calibrated. However, the here shown amplitudes do not reflect the spectral amplitudes of the HH as the ionization cross-sections of the atoms are not considered. Figure taken from [59].

covered. It is, however, clear that the true amplitudes of the HH spectrum is not recovered by this method, because (a) the atom dependent and energy dependent photo-ionization cross sections of the three gases and (b) the sensitivity of the CCD camera as well as the absorption in the diffraction grating are not taken into account.

The essential information obtained from these spectra for our experiment is that we have a series of photon energies with approximately 3.4 eV spacing over the entire observed spectral range.

2.1.2 Multiphoton Ionization

The second process to be discussed is the multiphoton ionization. It occurs for (relatively) low field intensities[3] and small photon energies compared to the ionization potential I_p. Figure 2.5 shows an illustration of the multiphoton ionization. For this process many low energetic photons are absorbed to overcome the molecules ionization potential. The transition is said to occur vertically [64]. When more photons are absorbed than necessary to ionize the molecule, the access energy is transfered into kinetic energy of the photoelectron. This is called above-threshold-

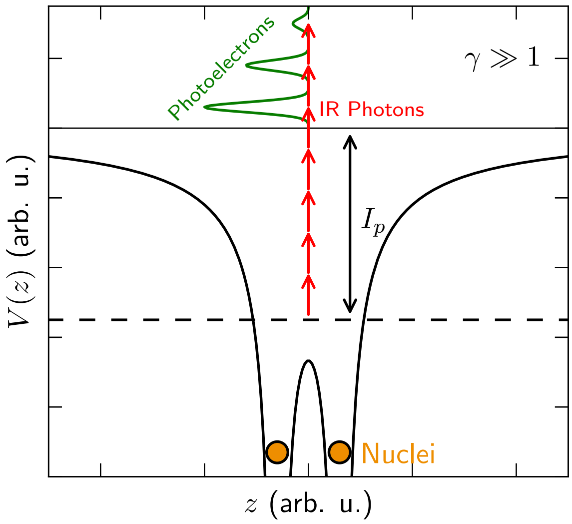

Figure 2.5: Illustration of the multiphoton ionization. In order to overcome the ionization potential many low energetic photons (red arrows) are absorbed. The ionization probability for this process scales with the laser intensity as I^n, where n is the number of absorbed photons. The photoelectron kinetic energy depends on the number of absorbed photons above the ionization potential I_p. The higher the photoelectron kinetic energy the more photons have to be absorbed, which explains the drop-off in yields for fast electrons.

---

[3] The intensity is low compared to the tunnel ionization case.

ionization (ATI). The higher the photoelectron energy the more photons are absorbed in the process which reduces the process probability.

Multiphoton processes can be understood in terms of time-dependent perturbation theory. For a perturbation Hamiltonian H^1 the Schrödinger equation reads

$$i\frac{d|\Psi,t\rangle}{dt} = (H + H^1)|\Psi,t\rangle, \tag{2.5}$$

in which we consider the unperturbed problem (involving H) to be solved. By introducing the time evolution operators T and U, corresponding to unperturbed system H and the perturbation H^1 respectively, the time-dependence of the states can be absorbed into the operators[4], which is achieved by identifying $|\Psi,t\rangle = TU|\Psi\rangle$ ($|\Psi\rangle$ is a time-independent ket now). Since Eq. (2.5 has to hold for all $|\Psi\rangle$, one can reformulate it as an operator equation

$$i\frac{dTU}{dt} = i\frac{dT}{dt}U + iT\frac{dU}{dt} = H\,TU + H^1\,TU, \tag{2.6}$$

in which

$$i\frac{dT}{dt}U = H\,TU \Leftrightarrow i\frac{dT}{dt} = H\,T \tag{2.7}$$

can be identified as the unperturbed Schrödinger equation which is considered to be known. Hence, with the unitarity of the time-evolution operators ($T^\dagger T = \mathbb{1} = U^\dagger U$) and after multiplication from the left with $T^\dagger$ Eq. (2.6) simplifies to

$$i\frac{dU}{dt} = T^\dagger H^1 T\,U = H_{\text{int}}U \quad \text{with} \quad H_{\text{int}} = T^\dagger H^1 T. \tag{2.8}$$

This equation has the (formal) solution in form of the Neumann series

$$U = \mathbb{1} - i\int\limits_{t_0}^{t} dt_1 H_{\text{int}}(t_1) - \int\limits_{t_0}^{t} dt_1 \int\limits_{t_0}^{t_1} dt_2 H_{\text{int}}(t_1) H_{\text{int}}(t_2) + \ldots \tag{2.9}$$

As the transitions from an initial state $|\Psi_i\rangle$ to a final state $|\Psi_f\rangle$ is described by the transition amplitude

$$\langle\Psi_f|U\Psi_i\rangle \tag{2.10}$$

---

[4] The time-evolution operator is thoroughly discussed in Sec. 5.1.2 as it will continue to play an important role throughout Chap. 5. Also the form of the operators will become important in Chap. 5 as it will be used to solve the time-dependent Schrödinger equation numerically. However, at this point it is only important to know that such operators exist.

we obtain by inserting (completeness relation)

$$\sum\!\!\!\!\!\!\!\int |\Psi_k\rangle\langle\Psi_k| = \mathbb{1} \tag{2.11}$$

in between adjacent interaction Hamiltonians in Eq. (2.9)

$$\langle\Psi_f|U\Psi_i\rangle = -i\int_{t_0}^{t} dt_1 \langle\Psi_f|H_{\text{int}}(t_1)|\Psi_i\rangle - \sum\!\!\!\!\!\!\!\int \int_{t_0}^{t} dt_1 \int_{t_0}^{t_1} dt_2 \langle\Psi_f|H_{\text{int}}(t_1)|\Psi_{\mathrm{k}}\rangle\langle\Psi_{\mathrm{k}}|H_{\text{int}}(t_2)|\Psi_i\rangle + \dots \tag{2.12}$$

In here, the first term is interpreted to be a one-photon process in which H_{int} induces a direct transition from the initial to the final state. The next term describes a two-photon process where the interaction Hamiltonian first drives a transition to an intermediate state $|\Psi_k\rangle$ and subsequently to the final state. As Eq. (2.12) is an infinite series, in principle it describes all orders of photon transitions.

In order to evaluate the laser intensity I dependence of the n-photon transition probability $w^{(n)}_{i\rightarrow f}(t)$, we insert the interaction Hamiltonian for a monochromatic linear polarized laser field in dipole approximation[5]

$$H_{\text{int}} = T^{\dagger} z\mathcal{E}e^{-i\omega t}T, \tag{2.13}$$

into Eq. (2.12) . In Eq. (2.13), $\mathcal{E} \propto \sqrt{I}$ is the electric field and ω the field's carrier frequency (classically equivalent to the photon energy). By separating the different

---

[5] Inserting $H_{\text{int}} = T^{\dagger} z\mathcal{E}e^{i\omega t}T$ would lead to the description of stimulated emission.

orders of the series we find[6]

$$\begin{aligned}
w^{(1)}_{i\to f}(t) &\propto \left| -i\int\limits_{t_0}^{t} dt_1 \langle\Psi_f|T^\dagger z\mathcal{E}e^{-i\omega t_1}T|\Psi_i\rangle \right|^2 \\
&= \mathcal{E}^2 \left| \int\limits_{t_0}^{t} dt_1 \langle\Psi_f|z|\Psi_i\rangle e^{-i(\omega+E_i-E_f)t} \right|^2 \\
w^{(2)}_{i\to f}(t) &\propto \left| -\sum\!\!\!\!\!\!\!\int \int\limits_{t_0}^{t} dt_1 \int\limits_{t_0}^{t_1} dt_2 \langle\Psi_f|T^\dagger z\mathcal{E}e^{-i\omega t_1}T|\Psi_\mathrm{k}\rangle\langle\Psi_\mathrm{k}|T^\dagger z\mathcal{E}e^{-i\omega t_2}T|\Psi_i\rangle \right|^2 \\
&= \mathcal{E}^4 \left| -\sum\!\!\!\!\!\!\!\int \int\limits_{t_0}^{t} dt_1 \int\limits_{t_0}^{t_1} dt_2 \langle\Psi_f|z|\Psi_\mathrm{k}\rangle\langle\Psi_\mathrm{k}|z|\Psi_i\rangle e^{-i(2\omega+E_i-E_f)} \right|^2 \\
&\vdots \\
w^{(n)}_{i\to f}(t) &\propto \mathcal{E}^{2n} \left| \sum\!\!\!\!\!\!\!\int \cdots \sum\!\!\!\!\!\!\!\int \int \cdots \int \langle\Psi_f|z|\Psi_\mathrm{l}\rangle \cdots \langle\Psi_\mathrm{k}|z|\Psi_i\rangle e^{-i(n\omega+E_i-E_f)} \right|^2
\end{aligned} \tag{2.14}$$

This result clearly shows the intensity dependence of the n-photon process, which can be written as

$$\begin{aligned}
w^{(1)}_{i\to f}(t) &\propto I^1 \\
w^{(2)}_{i\to f}(t) &\propto I^2 \\
&\vdots \\
&\boxed{w^{(n)}_{i\to f}(t) \propto I^n}
\end{aligned} \tag{2.15}$$

The here presented perturbation theory considers resonant transition to isolated states. Since for ionization the final states are embedded within a continuum, the derivation has to be slightly altered and the probability of ionization into states lying within an energy differential dE has to be obtained (see e.g. Ref. [65]).

2.1.3 Single-Photon Ionization

The laser pulses used in this thesis to ionize molecular hydrogen are created in the so-called high-order harmonic generation process. In our experiment this leads to

---

[6] We use the fact that applying the time-evolution operator to an time-independent eigenstate yields $T|\Psi_n\rangle = e^{iE_n t}|\Psi_n\rangle$, which is the trivial time-dependence of a stationary state.

extreme ultraviolet pulses with high energetic photons (compare the photoelectron spectrum shown in Fig. 2.4) and very low pulse intensities ($\approx 10^7\,\mathrm{W/cm^2}$). Hence, the above described ionization described by the perturbation approach is possible with only a single photon (see Fig. 2.6 for an illustration). The ionization amplitude

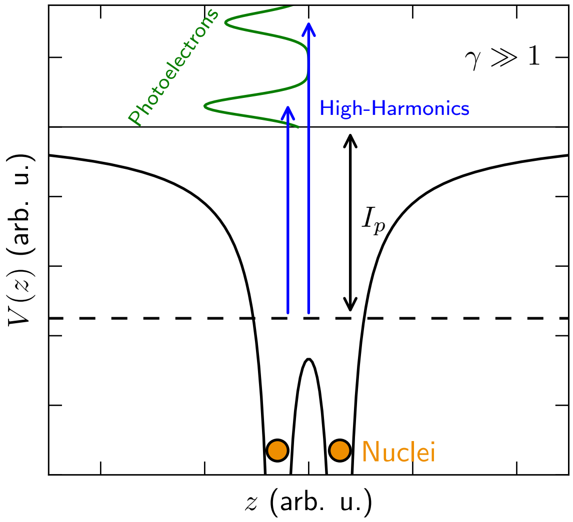

Figure 2.6: Illustration of single-photon ionization of molecular hydrogen. The kinetic energy of the photoelectron depends on the photon energy. The green line illustrates a distribution of the electron kinetic energies for the two lowest photon energies of the high-order harmonics.

is therefore very well described by the first order term in the perturbation series presented in Eq. (2.12). With this it is clear that the single-photon ionization is a special case of multiphoton ionization.

Ionizing with a very weak electric field strength and a single photon with high energy has additional advantages: (I) the laser field does not distort the molecular potential significantly, (II) different final states are always coherently populated, and (III) large photoelectron energies can be achieved with a high probability (this mainly due to the presence of photons with large energy). These features make single-photon ionization a very well suited tool for the investigation of atomic and molecular systems.

2.2 Molecular Symmetry: An Introduction to Molecular Selection Rules

Exploiting symmetries is an important concept and powerful tool of modern physics. The idea of symmetry is introduced to molecular physics by the theory of point groups. Since group theory is a large field, only a brief introduction can be given in this section (for a more complete presentation see e.g. Refs. [66–70]).

The most straight forward way is to classify the molecules by the symmetry operations that keep their geometry unchanged. To each symmetry operation a symmetry element can be assigned which is a point, line or plane that further defines the operation. A set of symmetry operations (identity, rotations, reflections, inversion and improper rotations) defines a point group[7] which in this context represents the symmetry properties of a given molecule. Since we are concerned with molecular hydrogen throughout this thesis it is instructive to use its respective point group $D_{\infty h}$ as a discussion example.

It is clear that the system energy is invariant under all symmetry operations, which means that molecular Hamiltonian remains unchanged. This is generalized by stating that all physical observables of the system also reflect this symmetry, among them the probability density $|\Psi|^2$.

In order to physically apply a symmetry operation a basis set has to be chosen, which can be a set of Cartesian vectors as well as e.g. atomic wave functions. With this basis set (as long it is not an uncountably infinite set) each symmetry operation can be written in terms of a matrix. The complete set of matrices in the chosen basis is called a representation of the point group. By applying similarity transformation to the matrices representing the symmetry operations it is possible to simultaneously bring them into block diagonal form in which no block is further reducible. Each irreducible block is called an irreducible representation matrix. Since a block diagonal matrix can always be expressed as the direct sum of lower dimensional matrices, each representation of the point group can be written as a direct sum of irreducible representations (which for the group $D_{\infty h}$ are called Σ_g^+, Σ_g^+, Σ_u^+, Σ_u^-, Π_g, Π_u, Δ_g, Δ_u, …). The number of irreducible representations of a point group is connected to the number of symmetry elements which are both infinite for the case of linear molecules. The irreducible representations are not unique, however as similarity transformations leave the character[8] of a matrix unchanged it can be used to classify the transformation of the irreducible representation under each symmetry. The characters for each symmetry operation belonging to the irreducible representations of the point group can be summarized in so-called character tables. A character table for the case of the $D_{\infty h}$ group is shown in Tab. 2.1, where each line describes one irreducible representation. In group theory it is shown that each group necessarily possesses a fully symmetric irreducible representation having a character of one for each symmetry operation. In the case of the group $D_{\infty h}$ it is denoted Σ_g^+. Finally, in a symmetric molecular system the wave functions (which can be rotational, vibrational or electronic wave functions) solving Schrödinger's equation have to transform

---

[7] The name point group is due to the fact that each symmetry operation of the point group has at least one fixed point which remains unchanged under the operation.

[8] In group theory the character of a matrix denotes its trace $\mathrm{char}(A) = Tr(A) = \sum_i a_{ii}$.

Table 2.1: Character table for the $D_{\infty h}$ point group. The symmetry operations are the identity E, the rotation around the molecular axis C_∞^φ, reflection at planes including the molecular axis σ_v, inversion i, improper rotations around the molecular axis S_∞^φ and the 2-fold rotations C_2. The last column indicates some possible different basis sets spanning the corresponding irreducible representations.

	E	$2C_\infty^\varphi$	$\infty\sigma_v$	i	$2S_\infty^\varphi$	∞C_2	
Σ_g^+	1	1	1	1	1	1	z^2, x^2+y^2
Σ_g^-	1	1	-1	1	1	-1	z
Σ_u^+	1	1	1	-1	-1	-1	R_z
Σ_u^-	1	1	-1	-1	-1	1	
Π_g	2	$2\cos(\varphi)$	0	2	$-2\cos(\varphi)$	0	(xz, yz), (R_x, R_y)
Π_u	2	$2\cos(\varphi)$	0	-2	$2\cos(\varphi)$	0	(x, y)
Δ_g	2	$2\cos(2\varphi)$	0	2	$2\cos(\varphi)$	0	(xy, x^2-y^2)
Δ_u	2	$2\cos(2\varphi)$	0	-2	$-2\cos(\varphi)$	0	

under the symmetry transformations of the corresponding point group like one of its irreducible representations and are thus labeled accordingly (in the case of $D_{\infty h}$ with the symbols $\Sigma_{g,u}^\pm$, $\Pi_{g,u}$ and so on).

2.2.1 Vanishing Integrals: A One-Dimensional Exercise

Group theory is a powerful tool in determining whether an integral is necessarily vanishing or not. One can show that an integral is necessarily vanishing, if the integrand does not contain a part that is invariant under all symmetry operations of the system's point group. In other words, this part has to transform under symmetry like the fully symmetric irreducible representation. Vanishing integrals impose discrete selection rules on quantized physical properties, which are among the key concepts of quantum mechanics. These selection rules are nothing more than deciding whether or not an integral of the form

$$T_{fi} = \langle \Psi_f | O | \Psi_i \rangle \tag{2.16}$$

vanishes due to symmetry. Here the Ψ_i and Ψ_f are, respectively, an arbitrarily chosen initial and final state and O a quantum mechanical operator. As the integrand is a product of three terms $\Psi_f^* \, O \, \Psi_i$, the above said is applied by requiring that the amplitude T_{fi} is non-zero only if the tensor product of the irreducible representations, corresponding to Ψ_f, Ψ_i and O, contains the fully symmetric representation.

The decision process, based on group theoretical arguments, can be explained intuitively for a one dimensional example (here we follow the argument given in Ref. [69]). From Fig. 2.7 we see that an antisymmetric function [i.e. $f(-x) = -f(x)$] integrated over a symmetric range ($-a$ to a) must vanish. For symmetric integrands

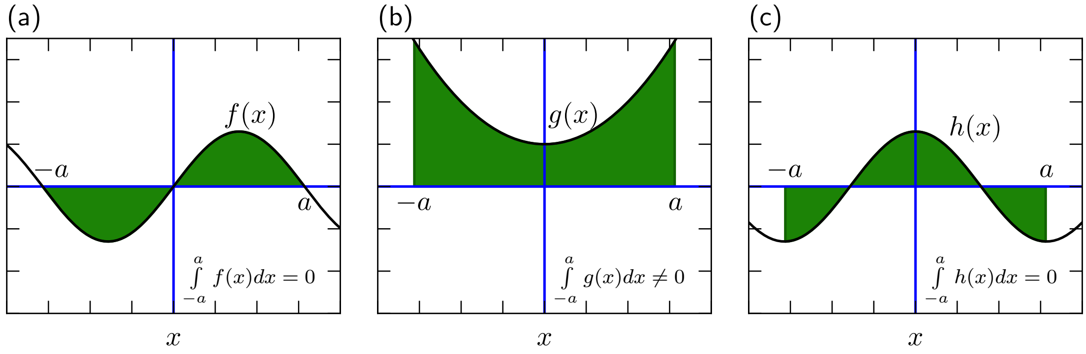

Figure 2.7: (a) Illustration of an integral over a symmetric range with an antisymmetric integrand. The integral necessarily vanishes. (b) Non-vanishing integral with symmetric integrand. (c) Vanishing integral with symmetric integrand.

this is not the case as is illustrated in Fig. 2.7 (b) with $[g(-x) = g(x)]$. However, it cannot in general be said that an integral over a symmetric range ($-a$ to a) with a symmetric integrand yields non-zero values [compare Fig. 2.7 (b) and (c)]. In other words, the integral shown in Fig. 2.7 (a) is necessarily zero, whereas the integral shown in (c) only accidentally vanishes.

To translate this into the language of group theory we need to identify the point group for this one-dimensional problem. Since the only possible symmetry operations are obviously the identity E and mirroring the x-axis using the operation σ_h, we find right away that the point group has to be C_s. The character table for this group is given in Tab 2.2. Since $Ef = f$ and $\sigma_h f = -f$ we find that f transforms like the irreducible representation A'', whereas g (and h similarly) fulfills $Eg = g$ and $\sigma_h g = g$ and hence belongs to A' (same holds for h). This makes clear that if the integrand does not behave like the group's totally symmetric representation A' the integral necessarily vanishes.

Table 2.2: Character table for the point group C_s.

	E	$2\sigma_h$
A'	1	1
A''	1	−1

This still has to be extended to products in the integrand. For this we take a look at Fig. 2.8 where two cases of function products are considered. In the first the product of a symmetric and an antisymmetric function are shown, which is obviously an antisymmetric function. The integral has to vanish. In the second, the result of two antisymmetric functions is a symmetric function. The integral over a symmetric range therefore yields in general only non-zero values.

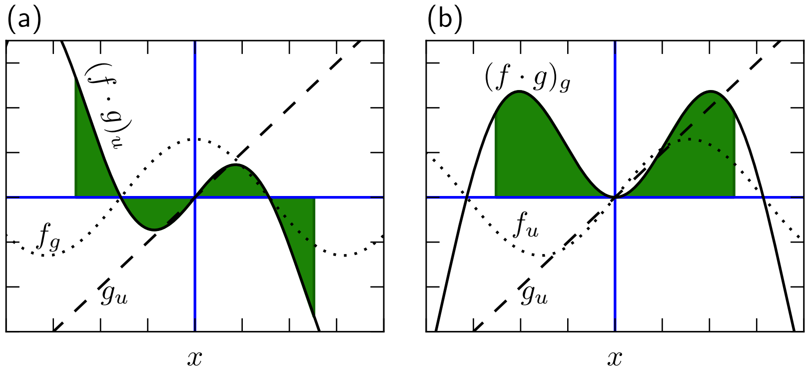

Figure 2.8: (a) The product of a symmetric and an antisymmetric function yields an anti symmetric function. Hence the integral over a symmetric range necessarily vanishes. (b) The product of two antisymmetric functions yields a symmetric function. The integral over a symmetric range only accidentally yields zero.

Table 2.3: Determination of the irreducible representation of the product shown in Fig. 2.8 (a).

	E	$2\sigma_h$
A'	1	1
A''	1	-1
$A' \otimes A'' = A''$	$1\times 1 = 1$	$1\times -1 = -1$

This is formalized by considering the statement above that the tensor product of the irreducible representations – corresponding to the product – needs to include the fully symmetric representation. For the case shown in Fig. 2.8 (a) the representation of the symmetric function is written as $R(f_g) = A'$ whereas for the antisymmetric function this is expressed as $R(g_u) = A''$. To see which irreducible representation is contained in the product of the two functions we have to determine the characters of the symmetry operations of the C_s groups for this product. This is achieved by column-wise multiplying the characters of Tab. 2.2 and subsequently expressing the result as a "linear combination" of the irreducible representations A' and A''. The result is shown in Tab. 2.3. In this case it is not necessary to rewrite the result as a direct sum of irreducible representations as it directly yields $A' \otimes A'' = A''$ from which we directly know that an integral over a symmetric interval has to vanish.

Let us do the same for the case shown in Fig. 2.8 (b) where the integral is carried out over the product of two antisymmetric functions. The product is written as shown in Tab. 2.4, from which we find $A'' \otimes A'' = A'$. Since the representation of the integrand $[(f \cdot g)_g]$ is the fully symmetric representation, an integral over a symmetric range does not necessarily vanish.

Table 2.4: Illustration of how to determine the irreducible representation of the product shown in Fig. 2.8 (b).

	E	$2\sigma_h$
A''	1	-1
A''	1	-1
$A'' \otimes A'' = A'$	$1 \times 1 = 1$	$-1 \times -1 = 1$

2.2.2 Excitation and Ionization: Molecular Selection Rules

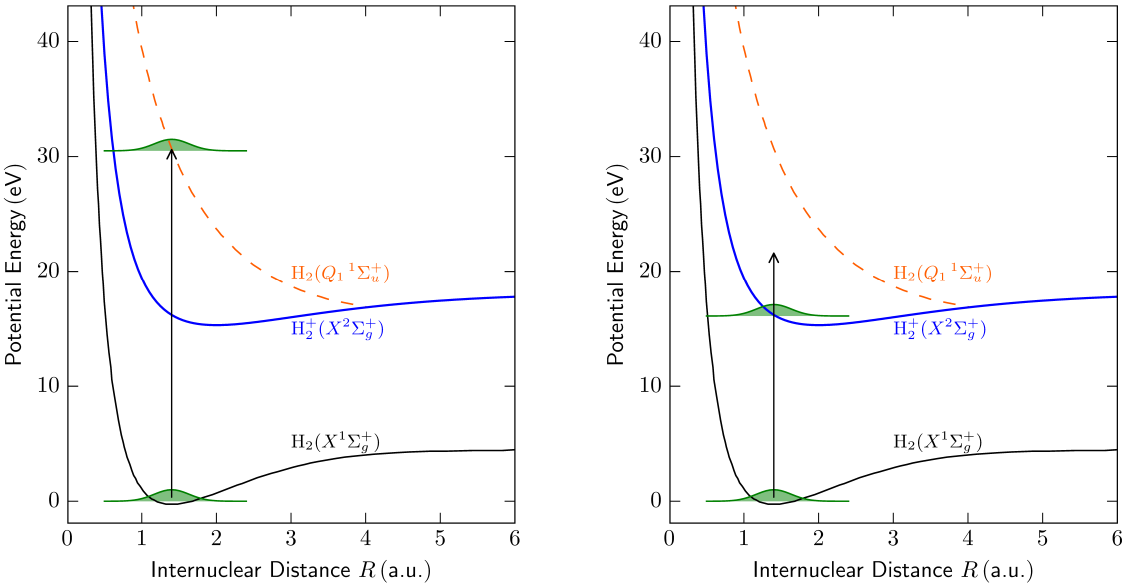

(a) Resonant excitation channel to the lowest-lying optically active doubly-excited state of the neutral hydrogen molecule.

(b) Ionization channel to the ground state of the molecular hydrogen ion.

Figure 2.9: Two different dipole allowed transitions. One is resonant and the other ionizes the molecule by transferring one electron to the continuum.

After having discussed that integrals necessarily vanish if the integrand (which can be a product) does not include the fully symmetric representation of the point group under consideration, we now discuss molecular selection rules for the case of the group $D_{\infty h}$ to which all homonuclear diatomic molecules belong. For this Fig. 2.9 shows two different dipole transition scenarios: (I) resonant transition to the lowest-lying optically active doubly-excited state and (II) ionization to the ground state of the molecular hydrogen ion.

In the following we discuss under which conditions the transitions shown in Fig. 2.9 are dipole allowed. For this we only consider parallel transitions (i.e. the electric field polarization is along the z-axis). We start with the resonant transition shown in (a) for which the dipole transition reads

$$T_{fi} = -\mathcal{E}\langle Q_1\,{}^1\Sigma_u^+|z|X\,{}^1\Sigma_g^+\rangle, \tag{2.17}$$

where $\mathcal{E}$ is the electric field amplitude. From the nomenclature of the states we can directly take the irreducible representation which transforms like the states, namely Σ_g^+ and Σ_u^+, whereas the irreducible representation corresponding to the dipole operator (which is linear in z) is taken from Tab. 2.1, where we find it to be Σ_u^+. Therefore the tensor product of the irreducible representations reads $\Sigma_u^+ \otimes \Sigma_u^+ \otimes \Sigma_g^+$. Like in the one-dimensional case we now have to multiply the characters of the three representations for each symmetry operation. This is shown in Tab. 2.5 where the result shows that the tensor product is the fully symmetric irreducible representation. Therefore the dipole transition is symmetry allowed.

For the second case, the ionization shown in Fig. 2.9 (b), this is a little more complicated, as the final state wave function consists of a part describing the bound electron as well as a part describing the photoelectron. If we assume the total wave function to be described by a product of the bound electron and the photoelectron, we can write the dipole transition as

$$T_{fi} = -\mathcal{E}\langle X\,{}^2\Sigma_g^+;\Psi_{e^-}|z|X\,{}^1\Sigma_g^+\rangle, \tag{2.18}$$

where the bra $\langle X\,{}^2\Sigma_g^+;\Psi_{e^-}| = \langle X\,{}^2\Sigma_g^+| \otimes \langle\Psi_{e^-}|$ describes the product state. As we initially do not know the irreducible representation corresponding to the photoelectron state, we have to start by computing the irreducible representation of the tensor product of the remaining known states. The result is shown in Tab. 2.6. The result of this tensor product has now to be multiplied with the (yet unknown) photoelectron representation. Since the tensor product is not the fully symmetric irreducible representation of $D_{\infty h}$, the photoelectron cannot transform like the fully symmet-

Table 2.5: Calculation of the irreducible representation of the tensor product $\Sigma_u^+ \otimes \Sigma_u^+ \otimes \Sigma_g^+$.

	E	$2C_\infty^\varphi$	$\infty\sigma_v$	i	$2S_\infty^\varphi$	∞C_2
Σ_u^+	1	1	1	-1	-1	-1
Σ_u^+	1	1	1	-1	-1	-1
Σ_g^+	1	1	1	1	1	1
$\Sigma_u^+ \otimes \Sigma_u^+ \otimes \Sigma_g^+$	1^3	1^3	1^3	$(-1)^2 \times 1$	$(-1)^2 \times 1$	$(-1)^2 \times 1$
$= \Sigma_g^+$	$= 1$	$= 1$	$= 1$	$= 1$	$= 1$	$= 1$

Table 2.6: Calculation of the irreducible representation of the tensor product $\Sigma_g^+ \otimes \Sigma_u^+ \otimes \Sigma_g^+$.

	E	$2C_\infty^\varphi$	$\infty\sigma_v$	i	$2S_\infty^\varphi$	∞C_2
Σ_g^+	1	1	1	1	1	1
Σ_u^+	1	1	1	-1	-1	-1
Σ_g^+	1	1	1	1	1	1
$\Sigma_g^+ \otimes \Sigma_u^+ \otimes \Sigma_g^+$	1^3	1^3	1^3	$-1 \times (1)^2$	$-1 \times (1)^2$	$-1 \times (1)^2$
$= \Sigma_u^+$	$= 1$	$= 1$	$= 1$	$= -1$	$= -1$	$= -1$

ric representation either. Considering the previously learned we take an educated guess and test if the photoelectron wave function transforms like the irreducible representation Σ_u^+. We therefore have to evaluate the tensor product $\Sigma_u^+ \otimes \Sigma_u^+$ which indeed yields the totally symmetric representation Σ_g^+ as shown in Tab 2.7. With this we know that the transition is dipole allowed only if the photoelectron state transforms like the irreducible representation Σ_u^+. The symmetry of the photoelectron wave function manifests in the photoelectron angular distribution observed in an ionization experiment. We later find that if the symmetry of the ionic molecular hydrogen state changes, the photoelectron symmetry changes as well. This is a direct consequence of the symmetry rules discussed above.

Table 2.7: Calculation of the irreducible representation of the tensor product $\Sigma_u^+ \otimes \Sigma_u^+$.

	E	$2C_\infty^\varphi$	$\infty\sigma_v$	i	$2S_\infty^\varphi$	∞C_2
Σ_u^+	1	1	1	-1	-1	-1
Σ_u^+	1	1	1	-1	-1	-1
$\Sigma_u^+ \otimes \Sigma_u^+$	1×1	1×1	$1 \times 1 = 1$	-1×-1	-1×-1	-1×-1
$= \Sigma_g^+$	$= 1$	$= 1$	$= 1$	$= 1$	$= 1$	$= 1$

3 Experimental Setup

In this thesis, light induced dissociative ionization of the hydrogen molecule is investigated. For this purpose we ionize H_2 with extreme ultraviolet (XUV) attosecond laser pulses with photon energies ranging from 16 eV to 40 eV. In addition, the experimental setup allows a second ultra-short infrared (IR) laser pulse, with a sub-10 fs pulse duration, to be used as probe pulse with a controllable time-delay τ. Therefore, experiments using one and two-color laser fields can be conducted. The charged final products of the H_2-light interaction are detected by a reaction microscope [71, 72]. In a reaction microscope, the charged particles emerging from an ionizing reaction are guided onto time- and position-sensitive detectors by means of weak homogeneous electric and magnetic fields. In this manner the detection of charged particles within a solid angle close to 4π is possible.

The purpose of this chapter is the introduction of the used experimental setup allowing a more fundamental understanding of the experimental results presented later. Figure 3.1 shows an overview of the complete experimental setup which consists of five modular parts: (1) the femtosecond laser oscillator (yellow boxes in Fig. 3.1), (2) the amplifier (green), (3) the hollow-core fiber system (orange), (4) the high-order harmonics generation unit (blue), and (5) the reaction microscope (red).

To briefly describe the experimental setup, IR laser pulses are created in a Ti:sapphire oscillator. These pulses are subsequently amplified using a chirped-pulse ring amplifier and are guided into a hollow-core fiber to broaden the spectral profile of the pulse in order to allow further temporal compression. This temporal compression is achieved using specially designed multilayer mirrors, so-called chirped-mirrors. The laser system is described in Sec 3.1. Within the high-order harmonics generation (HHG) chamber the laser beam is split into two parts, one carrying 70% of the IR-laser intensity which is used for the generation of the attosecond pulse trains (APTs) (via the process of HHG[1]) and another with 30% intensity to be used as a probe pulse (see Sec. 3.2). The APTs and (optionally) the probe pulse are then collinearly focused into a cold supersonic gas jet of H_2 molecules in the center of the reaction microscope, where the desired reactions with single molecules occur (see Sec. 3.3).

---

[1] In the following, the APT will also be referred to as high harmonics to accommodate for their spectral profile.

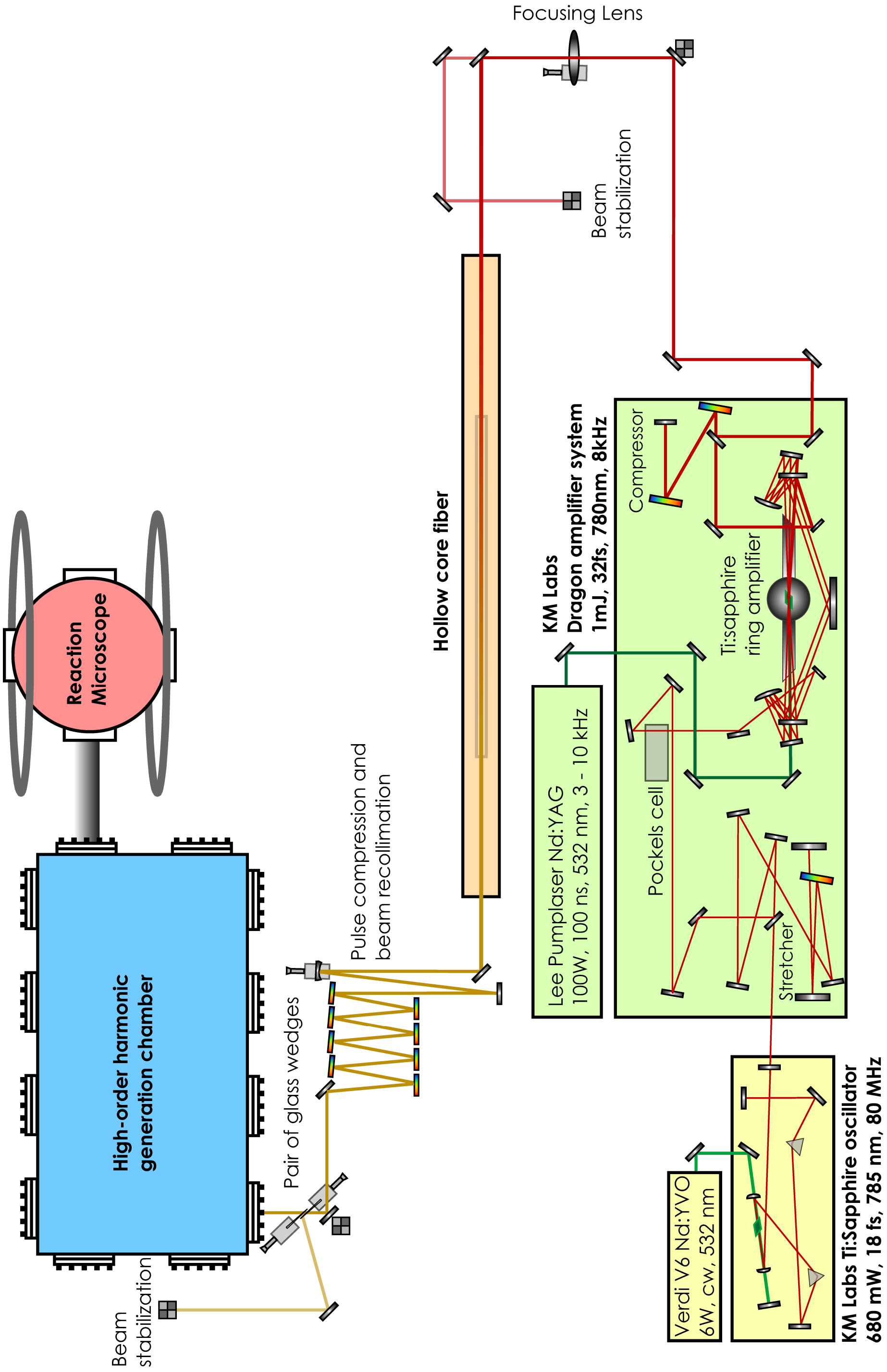

Figure 3.1: Schematic of the experimental setup. The different stages of the experiment are indicated by differently colored background. The first stage, the creation of pulses in the femtosecond oscillator is indicated in yellow. The pulse then enters the KM Labs *Dragon* ring amplifier (green). After that the amplified pulse is focused into a hollow-core fiber (orange), where it is spectrally broadened and subsequently temporally recompressed to approximately 10 fs, before entering the higher-order harmonic generation chamber (blue). There, a large part of the pulse is used to create attosecond pulse trains (APT) via HHG. The created pulses are focused into the reaction microscope (red) to perform experiments. Adapted from [59].

3.1 The Laser System

Femtosecond Laser Oscillator

The Kerr-lens mode-locked Ti:sapphire oscillator *MTS-I* build by KMLabs provides ultrashort laser pulses with a temporal duration of 18 fs and a repetition rate of 80 MHz. It is capable of operating with a central wavelength of 785 nm, a spectral bandwidth (FWHM) of $\approx$ 60 nm, and an average output power of 650 mW corresponding to a single-pulse energy of approximately 8 nJ. In order to provide energy to the oscillator system, a *Verdi* V6 (Coherent Inc.) $Nd:YVO_4$ (neodymium-doped yttrium orthovanadate) frequency-doubled continuous-wave laser, emitting at a wavelength of 532 nm, is used as a pump laser. Dispersion compensating prisms keep the laser pulses temporally compressed in every round-trip in the cavity, which allows high pulse intensities enabling the Kerr-lens mode-locking scheme, see e.g. [73–75].

Amplifier System

The pulse energy provided by the femtosecond oscillator is too small to drive the HHG process efficiently. In order to increase the pulse intensity, a commercially available *Dragon* ring-amplifier build by KMLabs is employed (see Fig. 3.2). The *Dragon* is based on the chirped-pulse amplification (CPA) scheme[2] [77] and leads to a gain of pulse energy of 5–6 orders of magnitude, which results in a pulse energy of approximately 1 mJ. It is pumped by a frequency-doubled Q-switched Nd:YAG laser (wavelength of 532 nm) provided by Lee Lasers Inc. with an average optical output power of up to 120 W and a pulse duration of 100 ns, which delivers the required energy for the amplification process[3]. The amplifier consists of four stages which are

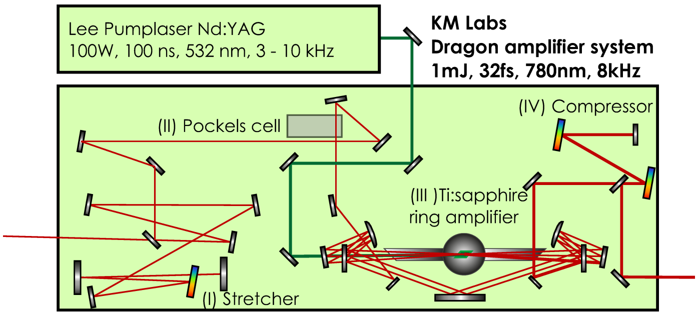

Figure 3.2: Illustration of the *Dragon* (KM Labs) chirped-pulse multi-pass ring amplifier together with the employed pump laser. The four different stages (see main text) of a CPA amplifier are presented. Figure adapted from Ref. [59]

---

[2] Chirped-pulse amplification was used in radar technology long before emerging in laser systems [76].

[3] In our laboratory the pump laser is usually operated at an average power of approximately 70 W and 8 kHz repetition rate.

in Fig. 3.2 labeled as follows: (I) stretcher, (II) pockels cell, (III) Ti:sapphire ring amplifier, and (IV) compressor.

In stage (I), by using a grating the oscillator pulse is temporally stretched by nearly 5 orders of magnitude [58], which allows an amplification of the pulse without exceeding the damage threshold of the amplifier's optical components (i.e. in particular the Ti:sapphire crystal). However, the repetition rate of the oscillator is with 80 MHz far too high to be efficiently amplified. For this reason, the repetition rate is reduced in stage (II) (by a factor 10^4) to 8 kHz. This is achieved by employing a pockels cell which turns the polarization for every 10 000th laser pulse such that this particular pulse can pass a subsequent polarization filter. Then, the pulse enters the multi-pass ring-amplifier [stage (III)] where it is focused together with the synchronized Q-switched pump-laser pulse into the helium cooled Ti:sapphire crystal (exploiting the Joule-Thomson expansion a temperature of approximately $-200\,^\circ$C is reached). In the current mode of operation each laser pulse passes the amplification crystal thirteen times. The number of amplification round-trips is chosen such that a maximal amplification is achieved. Before leaving the amplifier, the previously stretched pulse is recompressed by a pair of gratings in stage (IV).

The resulting laser pulses have a pulse energy of approximately 1 mJ and a pulse duration of 32 fs.[4] After having drastically amplified the pulse energy, in order to improve the efficiency of the HHG process as well as to increase the temporal resolution in pump–probe experiments a further reduction of the pulse duration is achieved through the use of a hollow-core fiber setup.

Hollow-Core Fiber

The setup of the hollow-core fiber is shown in Fig. 3.3. In order to achieve temporally shorter laser pulses the spectral bandwidth of the laser pulses has to be increased. This is necessary as the bandwidth is connected to the duration of the laser pulse via Fourier transform[5] (where the spectral phase has to be considered). For this, a hollow-core fiber system is employed in this work. The laser pulse is focused[6] into a glass-capillary[7] with a hole diameter of 250 μm filled with neon gas at a pressure of 3.5 bar. Acting as a wave-guide the intensity within the hollow-fiber is very high throughout the entire propagation length of approximately 1 m. The intensity dependence of the index of refraction $n(I)$ of the neon gas leads to self-phase modulation [78], which is the most important bandwidth broadening effect acting in the hollow-core fiber[8].

---

[4] In comparison to the duration of the oscillator pulses it comes to attention that the amplified pulses are longer. This is to the so-called gain-narrowing effect in the amplifier.

[5] The broader the spectral profile of a pulse the shorter it is under optimal conditions.

[6] An anti-reflection coated plano-convex lens with a focal length of $f = 1500$ mm is used for focusing.

[7] The glass-capillary is often referred to as hollow-core fiber.

[8] Other non-linear processes such as self-steepening also occur within the fiber. A detailed discussion, however, is beyond the scope of this work. For further information see e.g. Ref. [56].

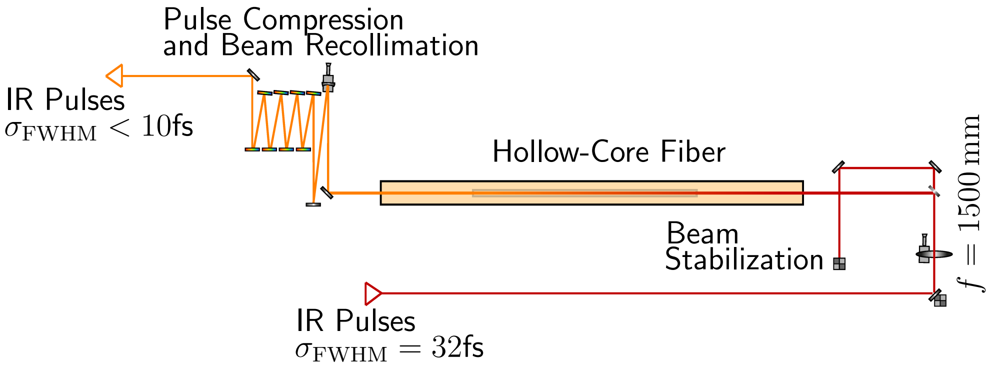

Figure 3.3: Illustration of the hollow-core fiber setup. The initial temporally long laser pulse (32 fs) is focused with a plano-convex lens into the Neon filled glass-capillary in which by self-phase modulation the spectral profile of the pulse is broadened. In order to guarantee the pointing stability of the initial laser and thus optimal focusing conditions into the fiber core a feedback beam stabilizer is employed. After the hollow-core fiber the pulse is recompressed using a set of chirped mirrors. Figure adapted from Ref. [59].

The results of this spectral broadening are shown in Fig. 3.4, where the spectral profile of the laser pulses is shown for 0 bar of neon pressure in the hollow-fiber (blue line) in comparison to the case where 3.6 bar were used (red line). The process of self-phase modulation preserves the temporal envelope of the pulse, however, it introduces new frequency components such that the carrier frequency temporally changes within the envelope (chirp). With $n(\omega, I) = n_0(\omega) + n_2(I)$ being the medium's intensity dependent index of refraction, this change of frequency as a function of time is given

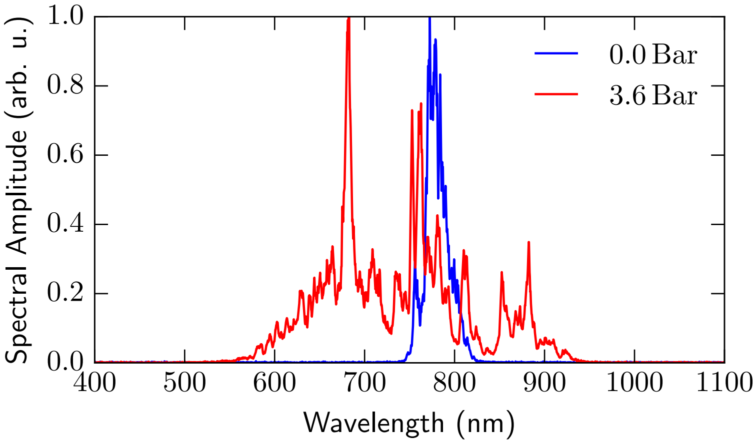

Figure 3.4: Pulse spectral profile after the hollow-core fiber for the case of 0 bar neon in the capillary (blue line) as well as for 3.6 bar of neon. A tremendous broadening for increasing neon pressure is observed.

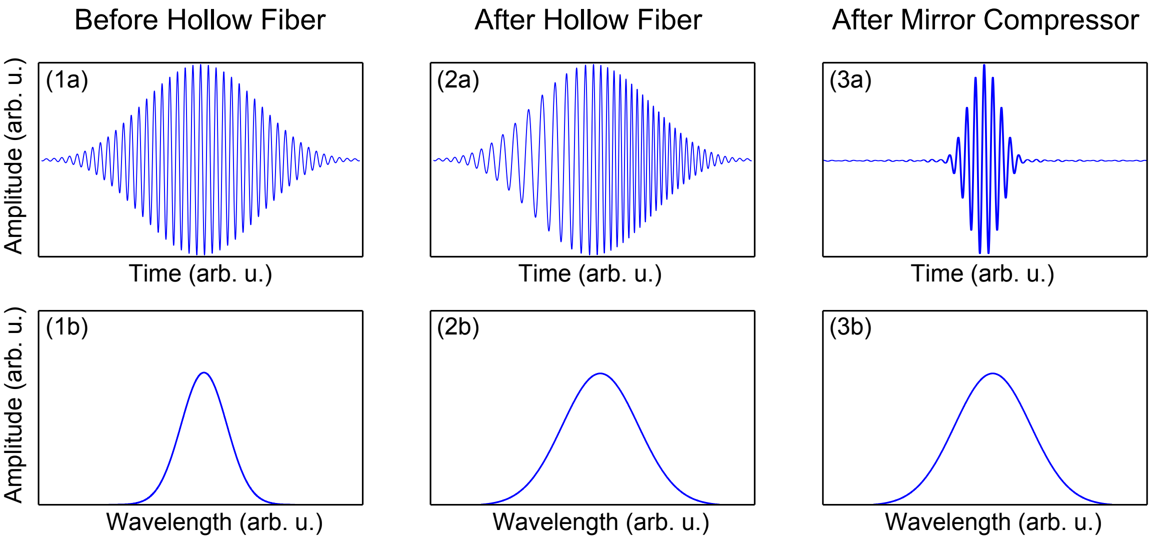

Figure 3.5: Illustration of the spectral broadening by self-phase modulation in the hollow-core fiber. Subsequently, the pulse is recompressed by chirped mirrors.

by (see e.g. [78])

$$\omega(t) = \frac{d\phi(t)}{dt} = \omega_0 - \frac{n_2 \omega L}{c} \frac{dI(t)}{dt}. \tag{3.1}$$

where L is the propagation length, ω_0 the carrier frequency, and $I(t)$ the temporal profile of the laser pulse intensity. This means that after the self-phase modulation the pulse is no longer temporally compressed. The pulses are recompressed by six pairs of chirped mirrors [79], which feature multilayer reflective coatings specifically designed such that the pulse is temporally recompressed to its minimal time duration. With this approach it is possible to reduce the pulse durations from 32 fs to sub-10 fs. Thus, the pulses consist only of a few cycles of the electric field [80, 81]. The above described is illustrated in Fig. 3.5. The first column shows the pulse (1a) and its corresponding spectral profile (1b) before entering the hollow-core fiber where it is spectrally broadened (2b) but exhibits a strong change of the carrier frequency as a function of the time (2a). In the last step the chirped mirror recompresses the pulse and a pulse duration of much less than the initial length is achievable (3a). This recompression leaves the spectral profile of the pulse unchanged. For more details to the here used hollow-core fiber setup please refer to Ref. [59].

3.2 High-Order Harmonics Generation Chamber

In this section the high-order harmonics generation chamber [shown in Fig. 3.6 (a)] is presented. The purpose of the high-order harmonics unit is the generation of XUV pulses from the input IR pulses and the controlled overlay of the IR beam with the

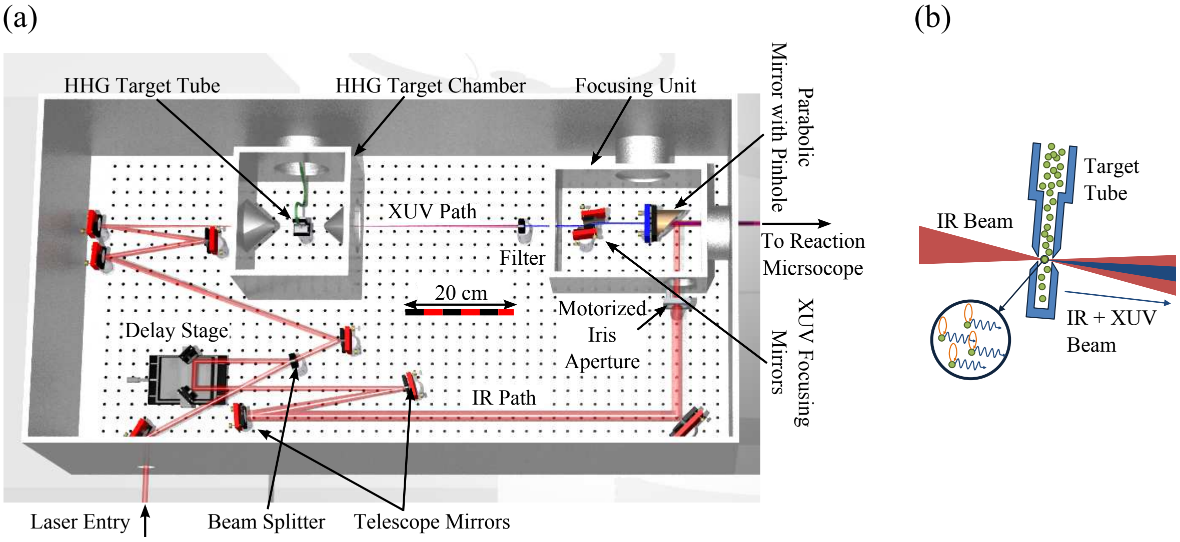

Figure 3.6: (a) High-order harmonics generation chamber. High-order harmonics are generated in one arm of a large interferometer, which is used to combine the generated high harmonics (XUV) with the fundamental IR beam at the output with a controllable delay between XUV and IR pulses. One arm (IR path) can be shortened or elongated using a delay stage in order to impose a variable time-delay onto the IR pulse propagating through it. In the other arm (XUV path) of the interferometer the high-order harmonics are generated by focusing 70% of the fundamental IR-pulse into an Argon filled tube (HHG target). Finally, the two arms are collinearly overlaid and focused into the reaction microscope. The figure of the HHG chamber is a courtesy of Philipp Cörlin. (b) Magnification of the target tube containing argon gas in which the laser is focused in order to create high-order harmonics. Figure adapted from [59].

XUV beam with an adjustable delay between the XUV and the IR pulse. In order to allow the overlay of the generated XUV beam with the initial IR beam, the high harmonics unit is integrated into a Mach-Zehnder type interferometer.

A beam splitter at the input side of the interferometer splits the incoming IR beam into two paths, which we denote the XUV path and the IR path in the following. 70% of the incoming IR laser intensity is directed toward the XUV path, 30% to the IR path. To explain the function of the HHG chamber we describe the two interferometer paths separately.

On the IR path the laser beam is first guided onto a retro-reflector which is mounted on a motorized translation stage with a maximum range of motion of 1 500 μm. The translation stage is hence able to introduce a variable time delay of up to 10 000 fs. Since the delay is controllable this arrangement allows pump–probe experiments with a variable delay between the pump and probe pulse. After passing the delay stage the IR beam diameter is increased from approximately 10 mm to 20 mm [see Fig. 3.6 (a)] using a two-mirror telescope. A motorized iris aperture placed in the expanded beam is used to control the IR pulse energy before it enters the focusing unit. The focusing unit is integrated in a differentially pumped vacuum stage within the HHG unit, kept at a pressure of 10^{-6} mbar in normal operation. The purpose of the focusing unit is overlaying the IR and the XUV beam and focusing both beams onto the molecular target within the adjacent reaction microscope. In case of the IR path, focusing is accomplished by an off-axis parabolic mirror with a focal length of about 600 mm (for infrared light) leading to a focal diameter in the reaction zone of about 30 μm (FWHM). Together with the pulse-energy controlling iris aperture, IR-pulse intensities of $(0 - 10^{15})$ W/cm^2 can be set. A 3 mm hole in the off-axis parabolic mirror allows the XUV beam to enter from the rear side to overlay the pulses from XUV and the IR paths[9], as is illustrated in Fig. 3.6 (a).

After describing the IR path, we now address the XUV path. In this interferometer arm the fundamental IR pulse[10] is focused using a spherical mirror with a focal length of 500 mm into the argon-filled HHG tube located within the HHG target chamber [see Fig. 3.6 (a)]. The HHG target chamber is, like the focusing unit, a differentially pumped stage exhibiting a pressure of 10^{-2} mbar under full target-gas load. Isolating the gas target in its own differential pump-stage has the advantage that the argon gas is efficiently pumped without contaminating the vacuum in the main chamber. The HHG tube has a 200 μm entry hole for the IR beam and a 150 μm exit hole for the generated high-harmonic XUV light and the fundamental IR light [see Fig. 3.6 (b)]. The high-field strength within the tube leads to the HHG process (see e.g. [47–52, 54–56]). The high-order harmonics are emitted in the form of attosecond pulse trains (APTs) with photon energies in the range $3.4 - 40$ eV (XUV photon energies). Subsequently, the XUV pulse and the IR pulse propagate collinearly. In order to separate the XUV pulse from the fundamental light a thin aluminum filter (thickness between 200 μm and 400 μm) is used which is opaque for photon energies below 16 eV. IR light is completely absorbed and XUV light above 16 eV is only attenuated. Therefore we obtain a pure (no IR contamination) XUV pulse.

Finally, we combine a concave mirror (5 000 mm curvature) and a cylindrical mirror (60 mm curvature), which are reflecting the XUV pulse with an angle of incidence of only 6° (gracing incidence) towards the hole in the XUV/IR beam combination mirror [see Fig. 3.6 (a)]. This modified Kirkpatrick-Baez configuration [82] has a focal length of 750 mm. The focused XUV pulse, containing $10^6 - 10^7$ photons, propagates through the hole of the off-axis parabolic beam combination mirror and is spatially overlapped with the IR pulse from the IR path [see Fig. 3.6 (a)]. A detailed description of the HHG setup used here is found in the diploma and PhD theses of Helga Rietz [57, 83] who has mainly constructed and built the chamber during her PhD work. Further descriptions can be found in Refs. [58, 59, 84].

---

[9] It is not possible to use a second optical beam splitter to overlay the XUV and the IR beam as the generated high-order harmonics would be absorbed by it.

[10] 70% of the fundamental IR pulse is propagating in the XUV path of the interferometer and is used to generate the high-order harmonics (XUV pulse).

3.3 Reaction Microscope

A key element of the experiment is the reaction microscope (see Fig. 3.7) [71, 72] which allows the detection of ions and electrons emitted by dissociative ionization processes into a solid angle of 4π. Ions and electrons are detected in temporal coincidence to establish their origin from the same ionization process. From the measured data it is possible to obtain the complete three dimensional momenta of each observed particle. This allows in many cases to separate different reaction channels which is exploited in this work to isolate and investigate specific quantum dynamical mechanisms. This technique has impressively demonstrated its capabilities in many experiments resulting in numerous publications (for a review see [71]).

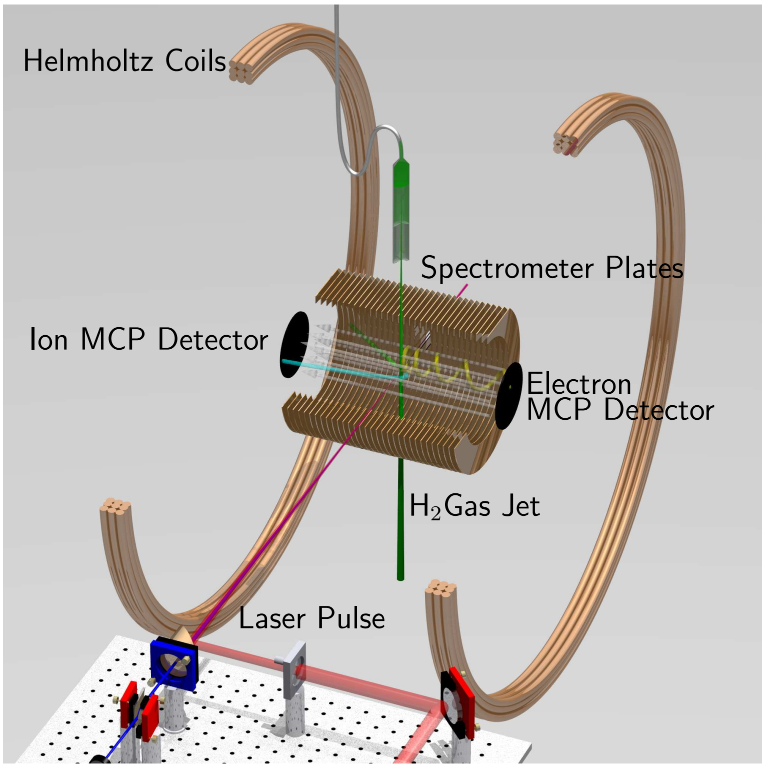

Figure 3.7: Illustration of the reaction microscope. A supersonic gas-jet is intersected in the center of the spectrometer by a laser beam resulting in the ionization of preferably a single gas particle per pulse. The created charged particles (ions and electrons) are guided onto position sensitive detectors by homogeneous electric and magnetic fields (together indicated by gray arrows). Using the time of flight and the detection position the full three dimensional momentum vectors of the particles are calculated yielding highly differential observations of the ionization process. Figure is a courtesy of Philipp Cörlin.

3.3.1 Operation Principle

In the center of the reaction microscope a supersonic gas jet (see also Fig. 3.8) is intersected at a right angle by the laser beam[11]. Within the intersection region atoms or molecules are ionized. The reaction microscope has two detectors, one dedicated to the detection of ions and the other to the detection of electrons. A homogeneous electric field[12] (indicated by gray arrows in Fig. 3.7) caused by the 32 equidistantly spaced (7 mm) spectrometer plates (electrodes) is used to guide the ions and electrons to their respective detectors. Due to the electron's small mass, typical ionization reactions yield high electron energies, which leads in the presence of only an electric field to a small detection acceptance, as most electrons would escape the spectrometer undetected. To circumvent this problem, Helmholtz coils are implemented providing a homogeneous magnetic field of strength[13] $B = 7.88\,\mathrm{G}$ [59] (also indicated by the gray arrows in Fig. 3.7) within the spectrometer plates. This field forces the electrons on spiral trajectories leading to their confinement within the spectrometer.

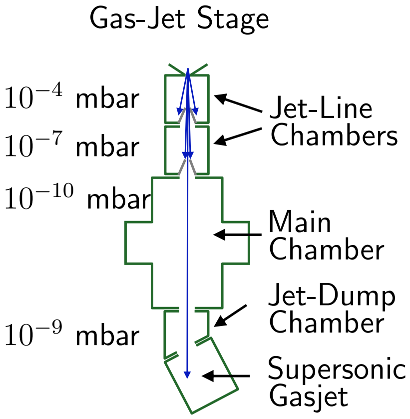

Figure 3.8: Jet stage in which the supersonic expansion takes place. With this setup jet temperatures on the order of 1 K are reached. Further, the typical pressures in our setup are indicated. Figure adapted from [59].

Therefore, the combination of an electric and a magnetic field guides the charged fragments onto their respective detector. Shortly before the particles impinge on the detectors, the homogeneous electric field of the spectrometer is terminated by a grid. Since a high voltage is applied to the front of the detector, the charged particles are strongly accelerated toward the detector. The detection is realized by employing (for each detector) two charge-multiplying microchannel plates (MCP)[14] [89] followed by

---

[11] Due to the supersonic expansion of the gas, very low temperatures are reached [85]. For further details on supersonic gas expansion the interested reader is referred to Refs. [86–88].

[12] A study using *TRICOMP* to verify the homogeneity of the electric field was conducted in Ref. [58].

[13] The unit Gauss can be expressed in Tesla as follows: $1\,\mathrm{G} = 10^{-4}\,\mathrm{T}$.

[14] More precisely, a stack of MCPs in chevron configuration is employed.

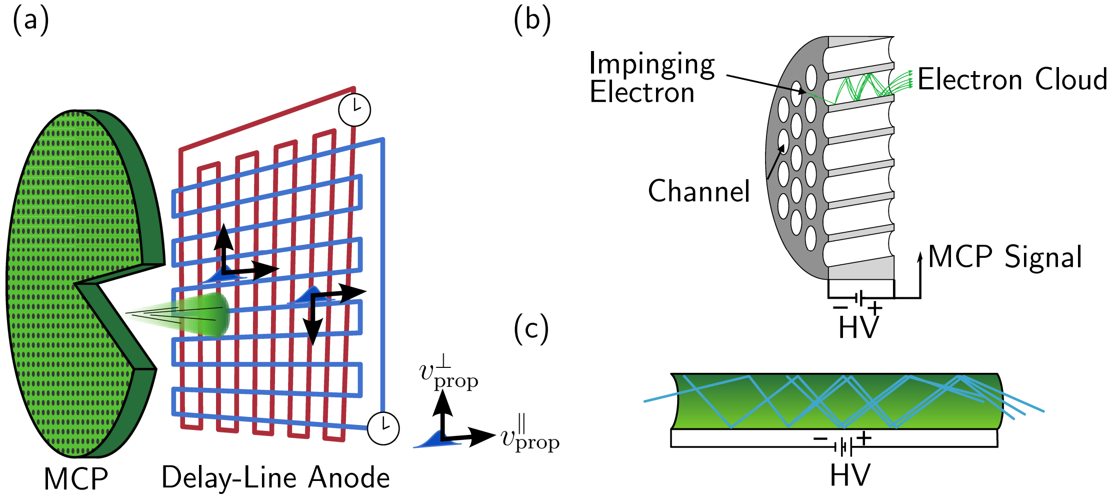

Figure 3.9: (a) MCP with subsequent pair of delay-line anode. From the two measured times per anode the position on the detector can be deduced. Also the two propagation velocities of the electron signal are indicated, one parallel to delay-line wire and one perpendicular to it. (b) Illustration of the channels belonging to an MCP. (c) Illustration of how a charged fragment triggers the electron multiplication in the MCP channel. In order to make these illustrations, figures from Refs. [57, 91] were used and adapted.

a pair of delay-line anodes[15] [90] [see Fig. 3.9 (a)]. When a charged particle hits the MCP front secondary electrons are freed within the corresponding MCP channels. Due to the potential difference of the MCP between the front and the back, the MCP channels act like electron-multipliers and the secondary electrons are accelerated as well and contribute to freeing electrons within the channels [see Fig. 3.9 (b) and (c)]. This leads to an electron avalanche (approximately $10^7 - 10^8$ electrons for 2 kV [92]), which manifests as an electron cloud at the back of the MCP that impinges on the delay-line anodes [see Fig. 3.9 (a)] where a signal is induced in the copper delay lines. Since the two delay-line anodes are crossed, it is possible to determine the position on the detector where the electron cloud impinged on the MCP by measuring the time the signal needs to reach the ends of the individual delay-lines (t_1^x, t_2^x, t_1^y and t_2^y) [91]

$$x = v_{\text{prop},x}^{\perp}(t_1^x - t_2^x) \quad \text{and} \quad y = v_{\text{prop},y}^{\perp}(t_1^y - t_2^y), \tag{3.2}$$

where $v_{\text{prop},i}^{\perp}$ are the signal velocities perpendicular to the delay-line wires in x and y direction ($v_{\text{prop},i}^{\perp}$ are functions of the signal velocity in a copper wire $v_{\text{prop},i}^{\parallel}$ and the

---

[15] In reality each delay-line anode consists of two wires (a signal wire and a reference wire). By applying a positive voltage to the signal wire and a negative to the reference wire, the electron cloud induces a signal mainly in the signal wire. The difference signal of both signals (signal and reference) is much less noisy, as electronic interferences induced in both wires cancel each other out. For simplicity, in the main text only one wire per anode is considered.

delay-line wire winding), see Fig. 3.9 (a). Further, events have to fulfill

$$t^x_{\text{sum}} = (t^x_1 + t_0) + (t^x_2 + t_0) = t^x_1 + t^x_2 + 2t_0$$

and

$$t^y_{\text{sum}} = (t^y_1 + t_0) + (t^y_2 + t_0) = t^y_1 + t^y_2 + 2t_0 \tag{3.3}$$

where t_0 is the time of arrival of the charged particle on the MCP. As a signal to determine t_0 the voltage break-in between the electrodes of the microchannel plate is used [labeled MCP signal in Fig. 3.9 (b)]. In Eq. (3.3) t^x_{sum} and t^y_{sum} are constants, which can be used to determine whether or not an event is genuine or to reconstruct a missing delay-wire signal. Further details on detection, signal acquisition and processing can be found in Refs. [58, 92].

Having established the fundamental operating principle of the reaction microscope, in the next section the calculation of the particles momenta from the measured time of flight and the hit position on the detectors is presented.

3.3.2 Calculation of the Particle Momenta

Note: Throughout this section SI units are used to make the appearance of the elementary charge in equations more clear.

As mentioned above, the particle momenta are calculated using the measured time of flight (TOF) as well as the detection position on the MCP which are exemplarily shown for measured ions in Fig. 3.10. Since the electric and magnetic field is directed along the spectrometer (pointing longitudinal toward the ion MCP which we define as the positive z direction) it only has a field component parallel to z (see Fig. 3.8). Therefore the problem exhibits a cylindrical symmetry which we exploit by using cylindrical coordinates for the momentum calculation.

Therefore, the task of finding the initial momentum for the particles is split in two parts[16]: (I) the calculation of the longitudinal momentum and (II) the calculation of the transversal momentum. For a given spectrometer geometry and a given charge-to-mass ration, the longitudinal momentum is only a function of the TOF, whereas the transversal momentum also depends on the hit-position (x, y) of the charged particle on the detector.

---

[16] In principle it is possible to distinguish between electrons and ions in the calculation of the momenta. The reason for this is that, due to the ions large masses, approximations can be made that simplify the momentum calculation in transversal direction. However, here we will treat both species on equal footing.

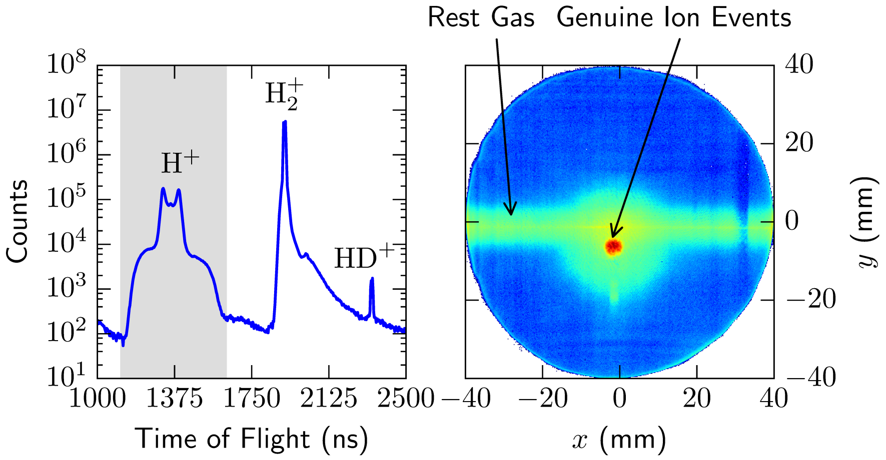

Figure 3.10: Left: Measured time-of-flight spectrum. Due to the mass differences the singly charged ions H^+, H_2^+ and HD^+ arrive at different times which makes it possible to sort the events and even impose conditions for further processing. The broad distribution of the H^+ peak is due to high initial velocities gained when H_2 is ionized and subsequently dissociates. Right: Impact position of the ions on the MCP as a function of the x and the y coordinate. The pronounced peak slightly below the center of the detector corresponds to events stemming from low energetic H_2^+ ions out of the supersonic jet. Due to their initial velocity along the negative y axis the ions impinge on the detector below the center. The horizontal line is caused by ionized rest gas in the chamber. These events are produced along the propagation (negative x) direction of the laser pulse.

Longitudinal Momentum

After ionization in the reaction volume, the charged particles (ions and electrons) are uniformly accelerated toward the respective detector (longitudinal acceleration). Therefore, obtaining the longitudinal momentum is a one-dimensional problem for which we have to solve the equation

$$s = v_\parallel \,\mathrm{TOF} + \frac{1}{2} a \,\mathrm{TOF}^2 = \frac{p_\parallel}{m} \,\mathrm{TOF} + \frac{1}{2} a \,\mathrm{TOF}^2 \tag{3.4}$$

with a being the acceleration and s being the acceleration length. Since the acceleration in an electric field can be written by using the particle charge q and the particle mass m as

$$a = \frac{q}{m}\frac{U}{s} \tag{3.5}$$

Eq. (3.4), after rearrangement, yields

$$\boxed{p_\parallel = m\frac{s}{\mathrm{TOF}} - \frac{1}{2} q U \frac{\mathrm{TOF}}{s}} \tag{3.6}$$

In combination Eq. (3.4) and Eq. (3.5) further make clear that the ratio $^m/_q$ is proportional to the square of the TOF when zero initial momentum is assumed. This allows an identification of an ionic species if the charge to mass ratio is unique in a given experiment as it is the case in this work [see Fig. 3.10 (left)]. The gray shaded area in Fig. 3.10 (left) is the time-of-flight condition to select genuine events, i.e. in the scope of this thesis H^+.

Transversal Momentum

Due to the magnetic field applied to confine the electron's motion to the spectrometer, all charged particles are forced onto spiral trajectories to the detectors. Figure 3.11 depicts the trajectories of the charged particles. Since even H^+ being the lightest ion species has a mass of about 1836 times more than the electron mass, the spiral motion (which is exaggerated for the ions in the illustration) can be neglected for any ionic species. To make the effects of the magnetic field more obvious, we will derive the transversal momentum reconstruction exemplary for the case of the electrons. However, the obtained equations are applicable to ions as well.

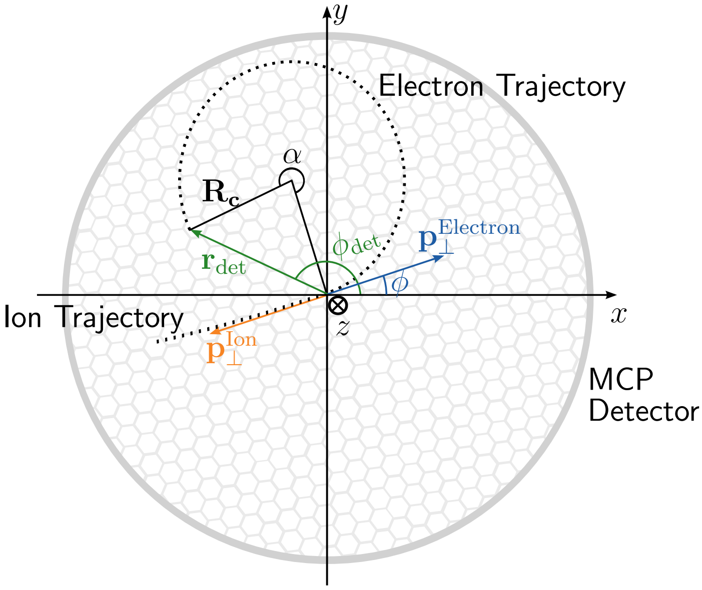

Figure 3.11: Illustration of the ion and electron trajectory in the spectrometer shown in the x-z-plane. As the ion trajectory is hardly influenced by the magnetic field the derivation of the momentum reconstruction is done for the electron (as it makes the effects more obvious) which can readily be applied later on to the ions as well. The vector $p_\perp$ indicates the initial momentum of the charged particle after the ionization reaction, whereas $r_{\text{det}} = (x, y)^T$ indicates the position vector observed on the MCP detector.

After the ionization, the electron is emitted with a momentum $|p_\perp|$ under an angle ϕ to the x-axis (blue arrow) and after spiraling toward the detector it is observed at the position $r_{\text{det}} = (x,y)^T = (|r_{\text{det}}|, \phi_{\text{det}})$. Neglecting the propagation along the z-direction transforms the spiral into a circle, where the time for the electron to complete a full revolution is given by the cyclotron time T_c. The connection of the cyclotron time to the magnetic field is described by

$$\omega_c = \frac{2\pi}{T_c} = \frac{qB_z}{m}, \tag{3.7}$$

where ω_c is the cyclotron angular velocity. A value for T_c can be determined from Fig. 3.12 – showing a plot of electron events as a function of the time-of-flight and the radial position $|r_{\text{det}}|$ – by looking at the spacing between radial position nodes ($|r_{\text{det}}| = 0$). After each cyclotron time T_c the electron completes a revolution and arrives at $r_{\text{det}} = 0$ which makes it possible to determine T_c from the plot shown in Fig. 3.12. For the magnetic field used here (and the electrons charge-to-mass ratio) $T_c \approx 45\,\text{ns}$ is found.

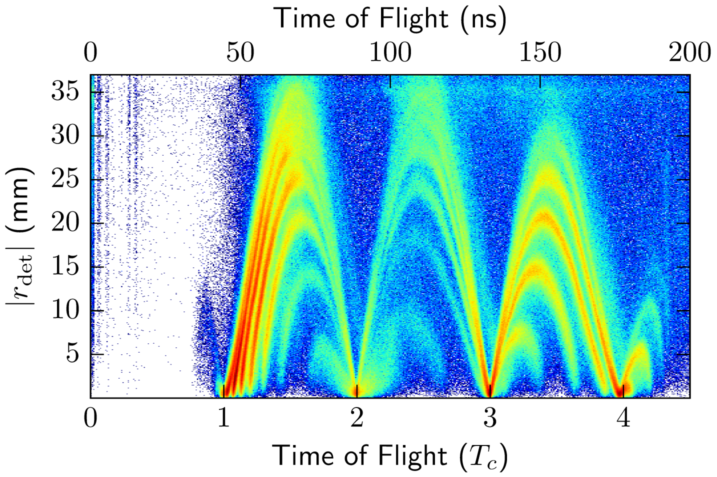

Figure 3.12: Electron events as a function of the time-of-flight and the radial detector position. After each cyclotron period the electron arrives at the initial radial position $|r_{\text{det}}| = 0$. Therefore from the time spacings of the observed nodes the cyclotron time $T_c \approx 45\,\text{ns}$ can be deduced.

By exploiting the fact that the electron's spiral trajectory is determined by the equilibrating of the magnetic and the centrifugal force we find

$$\frac{mv_\perp^2}{R_c} = qv_\perp B_z \quad \Leftrightarrow \quad p_\perp = qR_cB_z. \tag{3.8}$$

Solving Eq. (3.7) for B_z and inserting the result in Eq. (3.8) yields

$$p_\perp = R_c\omega_c m \tag{3.9}$$

As R_c is not directly observable Eq. (3.9) is merely a formal solution. From Fig. 3.12

it is clear that the angle α can be expressed as $\alpha = \omega_c\,\mathrm{TOF}$. With this, $|R_c|$ can be written as follows

$$|R_c| = \frac{|r_{\mathrm{det}}|}{2|\sin(\alpha/2)|}. \tag{3.10}$$

Hence, this result together with Eq. (3.9) yields the absolute value of $p_\perp$

$$|p_\perp| = \frac{\omega_c m|r_{\mathrm{det}}|}{2|\sin(\alpha/2)|}. \tag{3.11}$$

It only remains to find the azimuthal angle ϕ of the momentum vector $p_\perp = (|p_\perp|, \phi)^T$ which can be expressed by (see Fig. 3.11)

$$\phi = \phi_{\mathrm{det}} \pm \frac{\omega_c\,\mathrm{TOF}}{2} \mod 2\pi \tag{3.12}$$

where the negative sign holds for the electrons and the positive sign for the ions. Combining Eq. (3.11) and Eq. (3.12) yields the final result for the transversal momentum vector in polar representation

$$\boxed{p_\perp = \begin{pmatrix} \frac{\omega_c m|r_{\mathrm{det}}|}{2|\sin(\alpha/2)|} \\ \phi_{\mathrm{det}} \pm \frac{\omega_c\,\mathrm{TOF}}{2} \mod 2\pi \end{pmatrix}} \tag{3.13}$$

4 Single XUV-Photon Induced Electron Localization Involving the Autoionization of Doubly Excited States in H_2

Some of the aspects discussed in this chapter have been published in the following papers:

Electron Localization Involving Doubly Excited States in Broadband Extreme Ultraviolet Ionization of H_2
A. Fischer, A. Sperl, P. Cörlin, M. Schönwald, H. Rietz, A. Palacios, A. González-Castrillo, F. Martín, T. Pfeifer, J. Ullrich, A. Senftleben, and R. Moshammer
Phys. Rev. Lett. 110, 213002 (2013)

Measurement of the autoionization lifetime of the energetically lowest doubly excited $Q_1\,{}^1\Sigma_u^+$ state in H_2 using electron ejection asymmetry
A. Fischer, A. Sperl, P. Cörlin, M. Schönwald, S. Meuren, J. Ullrich, T. Pfeifer, R. Moshammer and A. Senftleben
J. Phys. B: At. Mol. Opt. Phys. 47, 021001 (2014)

Possessing only two electrons, molecular hydrogen is the simplest molecule exhibiting electron correlation. It therefore serves as a valuable system to explore fundamental physical mechanisms, including the autoionization of doubly-excited states (DES). These DES are energetically located well within the single-ionization continuum and ionize due to electron-electron interaction. The interplay of the nuclear and the electronic motion gives rise to ultra-fast phenomena, which are subject to recent experimental and theoretical research, e.g. [21, 93, 94]. Several experiments on dissociative photoionization demonstrated that the interference of molecular states with different parities results in a localization of the remaining bound electron, for multi-photon processes [95–100] as well as for single-photon transitions [20, 21, 101, 102].

In order to investigate the localization presented in this work we consider correlations between the photoelectron and proton momentum vector[1] in the dissociative ionization of H_2. For this we determine the angle between the proton momentum

---

[1] In a reference frame that is later specified, the proton momentum vector points along the molecular axis.

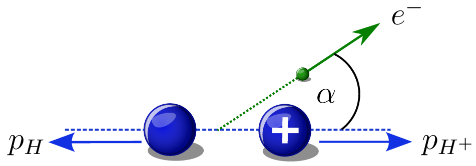

Figure 4.1: Illustration of dissociative photoionization of molecular hydrogen. When the angle $\alpha < 90°$ the electron and proton are going into the same hemisphere, whereas $\alpha > 90°$ refers to the opposite case. With this a molecular frame asymmetry can be defined.

vector p_{H^+} and the electron ejection direction, as is illustrated in Fig. 4.1. With this we (qualitatively) define an asymmetry[2] of the dissociative ionization as a normalized difference of the events where the electron and the proton are emitted in the same hemisphere and the events where they go in opposite hemispheres. This asymmetry is equivalent to a localization of the bound electron with regard to the ejected photoelectron. Therefore, the words asymmetry and localization are often used interchangeably throughout this chapter. A thorough discussion of the observed asymmetry in dissociative single-photon ionization of H_2 is presented in Sec. 4.3.

Further, in atoms the above discussed interference of two ionization processes manifests in Fano line shapes [103]. These line shapes have been used to determine various characteristics of the involved states, among them the autoionization lifetime of doubly-excited states. Despite being a straight-forward method in atoms this is not easily applicable to molecules, as the spectroscopic line-shapes disappear [104] due to the nuclear motion on the potential energy surfaces. The situation becomes particularly interesting when the dissociation of the molecule is on the same timescale as the autoionization lifetime as it is the case for molecular hydrogen. This leads to a coupling of the nuclear and the electronic motion and manifests in a nuclear velocity dependence of the (DES) autoionization amplitudes and lifetimes. Autoionization, being a prototype phenomenon of electron correlation correlating the nuclear motion to the electronic quantum dynamics, has been subject to numerous investigations, e.g. [14, 105–111]. In Sec. 4.4, having established the source of the asymmetry in Sec. 4.3, we then use the observed interference to disentangle the two reaction pathways contributing to the measured data. From this we are then able to derive the internuclear distance dependent lifetime of the energetically lowest doubly excited $H_2(^1\Sigma_u^+)$ state, which is on the time-scale of only 1 fs.

Chapter Outline

In order to present the obtained data comprehensibly, this chapter is split in three main sections. First (Sec. 4.1), theoretical concepts in form of the introduction of the Wentzel-Kramers-Brillouin (WKB) approximation are conveyed. This approximation will play an important role in the here performed simulation of the experimental data

---

[2] The asymmetry is be defined more precisely in Sec. 4.3.

In Sec. 4.2 the different dissociative ionization channels of H_2 are then presented and discussed in detail. After that, in the third section (Sec. 4.3), an electron localization stemming from the interference of two dissociative ionization pathways is described. The origin of the asymmetry is explained in terms of an intuitive semi-classical model accounting completely for the phases of the observed asymmetry oscillations. To conclude, the observed asymmetry as well as the semi-classical model is used in Sec. 4.4 to determine the lifetime of the energetically lowest doubly-excited Σ_u^+ state in molecular hydrogen.

4.1 Theoretical Concepts: The Wentzel-Kramers-Brillouin Approximation

Note: In this section SI units are used. In contrast to atomic units, this avoids that $\hbar$ disappears from the equations, which is helpful to illustrate classical limits.

The WKB approximation, named after the physicists Gregor Wentzel, Hendrik Anthony Kramers and Léon Brillouin who independently found and applied this approximation to quantum mechanics in 1926, is used to obtain analytical solutions of Schrödinger's equation[3].

The approximation method can only be readily applied to the one-dimensional case [113] where the time-dependent Schrödinger equation (TDSE) reads

$$\boxed{i\hbar\frac{\partial\Psi(x,t)}{\partial t} = \left[-\frac{\hbar^2}{2m}p^2 + V(x)\right]\Psi(x,t).} \tag{4.1}$$

We later find that the solution given by the WKB approximation is only valid if the potential $V(x)$ is a slowly varying function of x. The exact meaning of "slowly" is defined more accurately later on.

In the derivation of the WKB approximation presented in this section we follow Ref. [114]. In order to solve Eq. (4.1) for the case of a spatially slowly varying potential, (having the plane waves as a result of a constant potential in mind) it is intuitive to make the ansatz

$$\Psi(x,t) = \sqrt{\rho(x,t)}e^{\frac{i}{\hbar}S(x,t)}, \tag{4.2}$$

with $\rho(x,t) = |\Psi(x,t)|^2$ being the probability density and $S(x,t)$ a real phase function[4]. Inserting this ansatz into the TDSE [Eq. (4.1)] yields after dividing by $e^{iS/\hbar}$

---

[3] Starting with the Italian astronomer Francesco Carlini as early as 1817, many physicist and mathematicians used the same or very similar approaches to solve various problems, among them George Green (1837), Joseph Liouville (1837), John William Strutt 3rd Baron Rayleigh (1912), Richard Gans (1915), and Harold Jeffreys. Due to Jeffreys' contributions, the WKB approximation is sometimes also referred to as the Wentzel-Kramers-Brillouin-Jeffreys (WKBJ) Approximation [112].

[4] This is only true for the classical allowed region, where $E - V(x) > 0$. However, it is not a fundamental problem and is discussed in many textbooks covering the WKB approximation, e.g. [114, 115].

and omitting the space and time dependencies of all functions

$$i\hbar\left[\underbrace{\frac{1}{2\sqrt{\rho}}\frac{\partial\rho}{\partial t}}_{(c)}+\frac{i}{\hbar}\sqrt{\rho}\frac{\partial S}{\partial t}\right]=-\frac{\hbar^2}{2m}\left[\frac{1}{2\sqrt{\rho}}\frac{\partial^2\rho}{\partial x^2}-\frac{1}{4\sqrt{\rho^3}}\left(\frac{\partial\rho}{\partial x}\right)^2+\underbrace{\frac{i}{\hbar\sqrt{\rho}}\frac{\partial\rho}{\partial x}\frac{\partial S}{\partial x}}_{(a)}-\frac{\sqrt{\rho}}{\hbar^2}\left(\frac{\partial S}{\partial x}\right)^2+\underbrace{\frac{i}{\hbar}\sqrt{\rho}\frac{\partial^2 S}{\partial x^2}}_{(b)}\right]$$
$$+V(x)\sqrt{\rho} \qquad (4.3)$$

Using the one-dimensional continuity equation (describing the conservation of probability and therefore the conservation of the wave functions norm)

$$\boxed{\frac{\partial j}{\partial x}+\frac{\partial\rho}{\partial t}=0} \qquad (4.4)$$

where

$$j=-\frac{i\hbar}{2m}\left(\Psi^*\frac{\partial\Psi}{\partial x}-\Psi\frac{\partial\Psi^*}{\partial x}\right)=\frac{\rho}{m}\frac{\partial S}{\partial x} \qquad (4.5)$$

is the probability current, we rearrange two of the appearing terms [(a) and (b) on the right-hand-side of Eq. (4.3)]

$$-\frac{i\hbar}{2m\sqrt{\rho}}\frac{\partial\rho}{\partial x}\frac{\partial S}{\partial x}-\frac{i\hbar}{2m}\sqrt{\rho}\frac{\partial^2 S}{\partial x^2}=-\frac{i\hbar}{2\sqrt{\rho}}\frac{\partial j}{\partial x}=\frac{i\hbar}{2\sqrt{\rho}}\frac{\partial\rho}{\partial t} \qquad (4.6)$$

which then cancel with the term (c) on the left-hand-side. Dividing Eq. (4.3) by the term $\sqrt{\rho}$ and using Eq. (4.6) we obtain the partial differential equation determining the phase function $S(x,t)$

$$\boxed{-\frac{\partial S}{\partial t}=V(x)-\frac{\hbar^2}{4m\rho}\frac{\partial^2\rho}{\partial x^2}+\frac{\hbar^2}{8m\rho^2}\left(\frac{\partial\rho}{\partial x}\right)^2+\frac{1}{2m}\left(\frac{\partial S}{\partial x}\right)^2} \qquad (4.7)$$

Together with the continuity equation [Eq. (4.4)] this result [Eq. (4.7)] is equivalent to the time-dependent Schrödinger equation, as no approximation was applied so far. By defining the *"Quantum Potential"* [116–120]

$$V_Q(x)=V(x)-\frac{\hbar^2}{4m\rho}\frac{\partial^2\rho}{\partial x^2}+\frac{\hbar^2}{8m\rho^2}\left(\frac{\partial\rho}{\partial x}\right)^2 \qquad (4.8)$$

Eq. (4.7) further simplifies to

$$-\frac{\partial S}{\partial t} = V_Q(x) - \frac{1}{2m}\left(\frac{\partial S}{\partial x}\right)^2 . \tag{4.9}$$

By formally taking the limit $\hbar \to 0$, which performs the transition from quantum mechanics to the classical equations of motion, the terms including $\hbar$ in Eq. (4.7) vanish. By further using (see Ref. [121] for definition of classical momentum within Hamilton-Jakobi theory) $p = \partial S/\partial x$ we obtain the Hamilton-Jakobi equation, governing the classical motion[5]

$$H\left(x, \frac{\partial S}{\partial x}, t\right) + \frac{\partial S}{\partial t} = 0, \tag{4.10}$$

with S being Hamilton's principle function.

The idea of the WKB approximation is to neglect the terms including $\hbar$ of the quantum potential, which is equivalent to reducing it to the classical potential. For this reason, the solutions obtained using the WKB approximation are often referred to as being semi-classical.

To obtain the WKB-solutions by solving

$$-\frac{\partial S}{\partial t} = V(x) - \frac{1}{2m}\left(\frac{\partial S}{\partial x}\right)^2 \tag{4.11}$$

we use the fact that stationary states of Schrödinger's equation have the general form

$$\Psi(x,t) = \phi(x) e^{-iEt/\hbar}. \tag{4.12}$$

Comparing this to the wave equation used in our ansatz [Eq. (4.2)] the conditions

$$\rho = \rho(x) \quad \text{and} \quad S(x,t) = W(x) - Et, \tag{4.13}$$

directly follow, where $W(x)$ is the time independent part of $S(x,t)$. Note that the functions $\rho(x)$ and $W(x)$ are time independent. Inserting this into Eq. (4.11) we obtain

$$E = -\frac{1}{2m}\left(\frac{\partial W}{\partial x}\right)^2 + V(x) \tag{4.14}$$

and solving for $W(x)$ we get the WKB-solution for the time-independent phase (where

---

[5] The theorem of Jakobi states that whenever Hamilton's principle function is known, a complete solution of the canonical equations of motion can be given.

we restrict the values of x to the classical accessible region)

$$W(x) = \pm \int^{x} \sqrt{2m[E - V(x')]}dx' = \pm \int^{x} p(x')dx' \tag{4.15}$$

with $p = \sqrt{2m[E - V(x')]}$ being the particle's momentum[6].

It only remains to derive an expression for $\rho(x)$ to quantify the WKB states, for which we use the continuity equation again. Knowing that the probability density is time independent [Eq. (4.13)] and, in accordance with the Hamilton-Jakobi formalism, using $p = {}^{\partial S}\!/_{\partial x} = \sqrt{2m[E - V(x')]}$ we write

$$\frac{\partial \rho}{\partial t} + \frac{\partial j}{\partial x} \xrightarrow{\frac{\partial \rho}{\partial t}=0} \frac{\partial j}{\partial x} = 0 \xrightarrow[\text{Eq. (4.15)}]{\text{Eq. (4.5)}} j = \frac{\rho}{m} p(x, E) = const. \text{ (in } x) \tag{4.16}$$

Therefore, the probability density is written as $\rho = {}^{const}\!/_{p(x,E)}$, which accounts for the fact, that classically the probability of finding a particle in a volume dx is inversely proportional to the particle's velocity. The WKB-states therefore read

$$\boxed{\Psi(x,t) = \frac{const}{\sqrt{2m[E - V(x)]}} e^{\pm \frac{i}{\hbar} \int^{x} \sqrt{2m[E - V(x')]}dx'} e^{-iEt/\hbar}} \tag{4.17}$$

Having established all this, we quantify the conditions on which the WKB approximation yields accurate results. From Eq. (4.17) it is clear that the solution becomes invalid for $V(x)$ approaching E (the classical turning points), as the norm of the states diverges. Further, we have only derived the result for the classically accessible region where $E - V(x) > 0$ is fulfilled. However, for the classically forbidden region solutions very similar to the one given in Eq. (4.17) can be derived. It is far more challenging to give solutions at the turning points and their vicinity, connecting the classically allowed and the forbidden regions. This is achieved by linearizing the potential around the turning points and solving the Schrödinger equation exactly (connection formula, see e.g. [114,115]). Then, when all three solutions for the different regions are known, the coefficients of the three solutions have to be chosen such that the solutions continuously connect to each other, which is a lengthy derivation. As in the framework of this thesis only the solutions in the classically allowed region are of interest, we do not derive the full solution, but proceed with the one found in Eq. (4.17).

Finalizing this section we quantify under what conditions the approximation of

---

[6] This is merely a definition, but the similarity of this expression to the classical momentum reflects the connection to semi-classics. It also gives rise to the interpretation that a classical particle is propagating in a potential.

reducing the quantum potential to the classical one is valid. As the probability

$$\rho(x) = const/p(x,E) = const/\sqrt{2m(E-V)} \tag{4.18}$$

is inversely proportional to the momentum of the particle we use this to rearrange the two quantum terms of Eq. (4.7)

$$\frac{\hbar^2}{4m\rho}\frac{\partial^2\rho}{\partial x^2} \propto \frac{\hbar^2 p}{4m}\frac{\partial^2}{\partial x^2}\frac{1}{p} = \frac{\hbar^2 V''(x)}{8p^2} + \frac{3\hbar^2 m V'^2}{16p^4} \tag{4.19}$$

and

$$\frac{\hbar^2}{8m\rho^2}\left(\frac{\partial\rho}{\partial x}\right)^2 \propto \frac{\hbar^2 p^2}{8m}\left(\frac{\partial}{\partial x}\frac{1}{p}\right)^2 = \frac{\hbar^2 m V'^2}{8p^4} \tag{4.20}$$

We therefore find that the WKB approximation holds well if the terms ${}^{\hbar\sqrt{m}V'}/_{p^2}$ and ${}^{\hbar^2V''}/_{p^2}$ become small. This is formally equivalent to taking the classical limit $\hbar \to 0$ of the quantum potential.

4.2 Identification of Reaction Channels

After having discussed the WKB approximation, the next three sections (including this one) present the experimental results obtained by irradiating molecular hydrogen with extreme ultraviolet (XUV) laser pulses. Because of the large variety of the obtained results, this section focuses only on the identification of different reaction channels. The knowledge of the different reaction channels is used in the next section (Sec. 4.3), where an electron localization effect is observed and analyzed. In the third section (Sec. 4.4), this electron localization is used in order to extract the lifetime of the energetically lowest doubly-excited state of H_2 with Σ_u^+ symmetry.

Throughout the chapter (not only this section) we consider the process of dissociative photoionization

$$\mathrm{H_2} \xrightarrow{\mathrm{XUV}} \mathrm{H_2^+} + e^- \xrightarrow{\mathrm{Dissociation}} \mathrm{H} + \mathrm{H^+} + e^- \tag{4.21}$$

which we isolate using conditions on the proton's time-of-flight, see Fig. 3.10 (left). In this an attosecond pulse train[7] with energies of approximately 18 eV to 40 eV ionizes the molecular hydrogen, which subsequently dissociates. Using a reaction microscope only the charged fragments are detected, namely the proton and the electron. Due to conservation of momentum it is possible to reconstruct the momentum and with

---

[7] The pulse duration of the attosecond pulse trains does not play a role for the single pulse experiments presented here, as we consider only one-photon processes, which lead to the same result no matter at what absolute time (within the pulse) they were started. Using reference measurements, however, we have estimated the pulse train used throughout this chapter to feature a pulse duration of $\tau \approx 6\,\mathrm{fs}$. The pulse length plays a role in the next chapter.

this the kinetic energy of the undetected hydrogen atom. If the measured events are plotted as a function of the kinetic energy release (KER) and the electron energy, we obtain Fig. 4.2. In this, the KER

$$\mathrm{KER} = E_{\mathrm{kin}}(\mathrm{H}^+) + E_{\mathrm{kin}}(\mathrm{H}), \tag{4.22}$$

is the sum kinetic energy of the measured proton and the undetected neutral hydrogen atom. Exploiting the full capabilities of the reaction microscope (especially the accessibility of the full three-dimensional momenta of all fragments), we are further able to select events, in which the molecular axis was oriented parallel to the laser polarization axis[8]. With this, the irreducible representation of the dipole operator, responsible for electronic transitions[9], becomes solely Σ_u^+ (eliminating the operator's Π_u component). Imposing this condition and re-plotting Fig. 4.2 we obtain Fig. 4.3. In addition, we have illustrated three areas (indicated by red, green and black dashes) which correspond to overlapping regions in which a particular reaction channel is contributing to the count distribution. We present the evidence and thorough description of these channels in the following sections, but immediately name them:

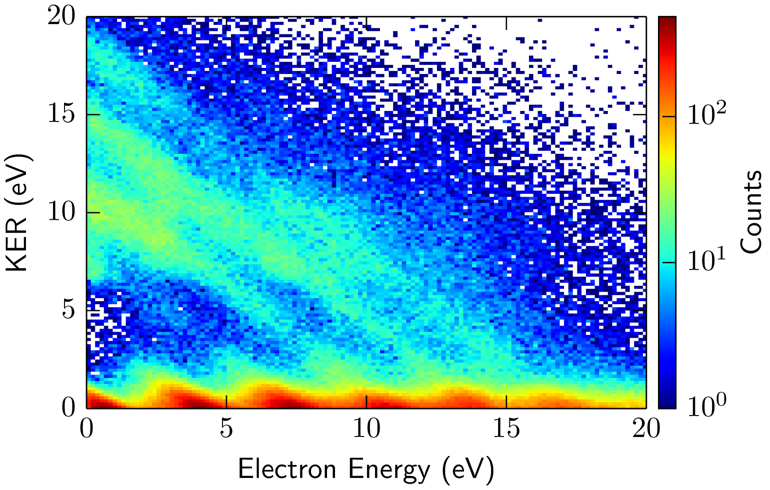

Figure 4.2: Energy correlation diagram of the fragments of the reaction described by Eq. (4.21). The count distribution is shown as a function of the kinetic energy release (KER) [the sum of the measured proton and the hydrogen atom] and the electron energy.

---

[8] In this section we refer to parallel orientation, if the angle θ between the molecular axis and the polarization vector of the field is less than $\theta < \arccos(0.8) \approx 35°$, as the solid angle needs to cover a finite range.

[9] Throughout this work the multipole expansion of the transition operator is truncated after the dipole term, which is why these transitions are commonly referred to as dipole transitions.

1. The ground-state dissociation (below the black dashes).
2. The dissociation via the $H_2^+(A\,^2\Sigma_u^+)$ (first excited) electronic state (within green dashed zone). This channel is in the following often referred to as direct ionization.
3. Dissociation via a doubly-excited state with subsequent decay to the $H_2^+(X\,^2\Sigma_g^+)$ ground state. This is referred to as the autoionization channel (see Fig. 4.8).

Especially the latter two play an important role in the interpretation of the measured data, with regard to the observed electron localization.

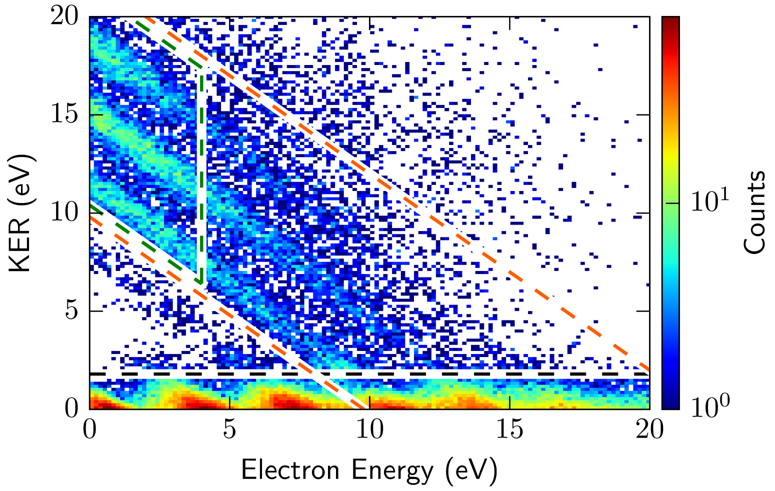

Figure 4.3: Energy correlation diagram for parallel transitions. The dashed lines indicate regions where different mechanisms predominantly contribute to the observed count distribution. At low KER (below the dashed black line) the ground-state dissociation is the dominant channel. Within the green dashed lines the direct dissociation via the first excited ionic state $[H_2(A\,^2\Sigma_u^+)]$ is the main contributing channel. Between the red lines the dissociation occurs via a doubly-excited state of the neutral H_2 before it decays to the ionic $H_2(X\,^2\Sigma_g^+)$, on which the dissociation is completed (see Fig. 4.8).

However, before proceeding with the explanation of these reaction channels, we first interpret the meaning of the (diagonal) line-like structures shown in Fig. 4.3. With the assumption of single-photon transitions, events with the same photon energy E_γ have to appear on diagonal lines. The lines are described by the relation

$$E_\gamma = \mathrm{KER} + E_e + E_{\mathrm{limit}}, \tag{4.23}$$

where E_e is the electron energy and E_{limit} the dissociation limit, which is the potential energy of the final system for an infinite internuclear distance (see Fig. 4.4). With E_{limit} in Eq. (4.23) being a constant for a given reaction channel, the energy conservation leads to the diagonal lines in Fig. 4.3.

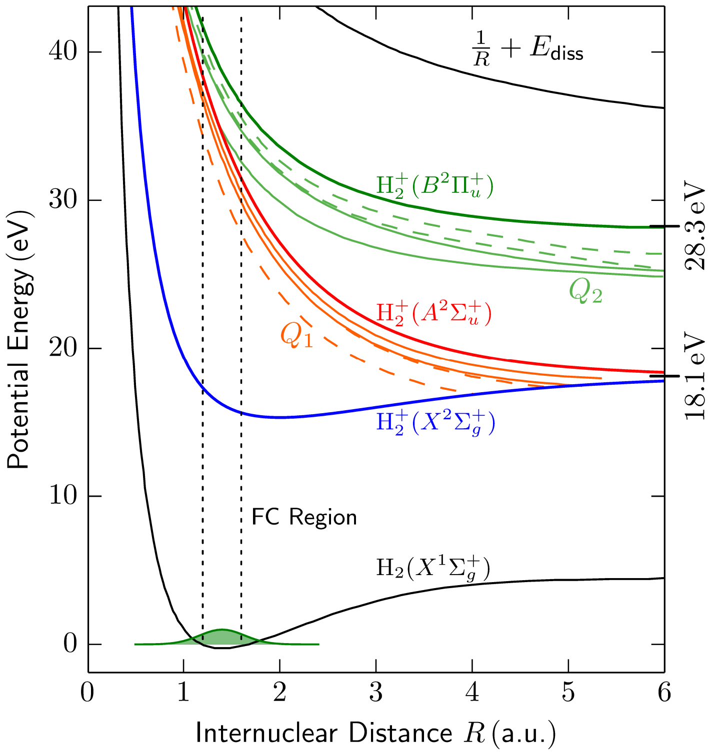

Figure 4.4: Potential energy curves corresponding to a selection of electronic states of the H_2 and H_2^+ molecules. The energetically lowest black line represents the potential of the $H_2(X\,^2\Sigma_g^+)$ ground state. The bold colored lines correspond to the ionic states (H_2^+). Doubly-excited states are indicated by thin lines labeled Q_1 and Q_2. They always come in "band-like" groups having their energy limit at an ionic state of the H_2^+ molecule. The dashed Q_1 and Q_2 states represent states of Σ_u symmetry, while the solid ones represent Π_u symmetry. Only the doubly-excited states which can be dipole coupled to the H_2 ground state are drawn. Further, the two lowest dissociation limits E_{limit} are indicated at 18.1 eV and 28.3 eV.

Figure 4.4 shows that for H_2^+ the two lowest values for E_{limit}, with regard to the neutral H_2 ground state, are $E_{\text{limit}}^{(1)} = 18.1\,\text{eV}$ and $E_{\text{limit}}^{(2)} = 28.3\,\text{eV}$. The value 18.1 eV represents the dissociation limit for the two ionic states $H_2^+(X\,^2\Sigma_g^+)$ and $H_2^+(A\,^2\Sigma_u^+)$, which are the only two states that contribute significantly to our data. This is verified by the fact that dissociating to a different dissociation limit would lead to additional diagonal lines in the energy correlation map at $E_{\text{limit}}^{(2)} - E_{\text{limit}}^{(1)} = 10.2\,\text{eV}$ less kinetic energy. These additional lines are not observed in the measured data. Knowing that the high-order harmonics have an energy spacing of approximately 3.4 eV (the fundamental IR photon energy is 1.7 eV) and by setting $E_{\text{limit}} = 18.1\,\text{eV}$, the diagonals lines at KER+$E_e \approx 10.8\,\text{eV}$, 14.2 eV and 17.6 eV can be assigned to the high-order harmonics HH17, HH19 and HH21, respectively.

Keeping in mind the above listed overview of possible reaction channels, we proceed to identify and explain these three reaction channels. In the following we investigate the different processes in the order listed above by commencing with the ground-state dissociation.

4.2.1 Ground-State Dissociation

The XUV pulses used to ionize the molecular hydrogen exhibit photon energies between $E_\gamma = 16\,\mathrm{eV}$ and $40\,\mathrm{eV}$. This is enough to ionize the H_2 by promoting the system from the neutral $H_2(X\,^1\Sigma_g^+)$ electronic ground state to the binding ionic $H_2^+(X\,^2\Sigma_g^+)$ state[10]. When an electronic transition is driven, the nuclear wave function, which throughout this work is assumed to be vertically promoted to the final potential[11], has to be expanded in the basis of vibrational eigenstates of the new electronic potential (e.g. compare Franck-Condon principle in Refs. [122–125]). In general this expansion not only consists of bound vibrational modes, but also of continuum states. In the case of a dipole transition from the binding $H_2(X\,^1\Sigma_g^+)$ state, where only the vibrational ground-state is populated, to the potential of the ionic $H_2^+(X\,^2\Sigma_g^+)$ state, the 20 bound vibrational states of the ionic potential are populated as well as the continuum states. Figure 4.5 shows the calculated[12] Franck-Condon factors for the bound states as well as for the continuum states below $3\,\mathrm{eV}$. We further find that the continuum states are only significantly populated up to approximately $2\,\mathrm{eV}$ above dissociation threshold. Therefore, the dissociation of these states leads to the observation of protons with a KER of less than $2\,\mathrm{eV}$. This is consistent with the experimentally obtained data presented in Fig. 4.3 (compare events below black dashed line).

Previously conducted experiments, e.g. [10, 15], suggested that only 2% of the molecules ionized to the $H_2^+(X\,^2\Sigma_g^+)$ state dissociate. This finding is not only in agreement with our experimental results, but also the calculated Franck-Condon factors shown in Fig. 4.5 yield a value of slightly below 2%.

Considering Fig. 4.4, it is clear that the low KER region of Fig. 4.3 can only result from processes involving the bound $H_2^+(X\,^2\Sigma_g^+)$ state, as all other potential energy curves only allow for a Franck-Condon overlap with vibrational states much higher in the continuum, which would result in typical KERs greater than $\approx 5\,\mathrm{eV}$.

It is in principle not possible to experimentally distinguish a direct ionization to the $H_2^+(X\,^2\Sigma_g^+)$ state from an excitation to a doubly-excited state (DES) which very

---

[10] The state symbols (for example: $X\,^1\Sigma_g^+$) belonging to the neural molecule can easily be distinguished from those belonging to the ion, by comparing the multiplicity of the states. A multiplicity of two is only possible for the ion, whereas the neutral molecule can only feature multiplicities of one or three. Throughout this work, the spin of the electron is never changed and the ground state of the hydrogen molecule has a multiplicity of one, the neutral states must reflect this.

[11] This is of course an assumption, but for the conditions considered in this work justified.

[12] The vibrational states, required to compute the Franck-Condon factors, were calculated using a method described in [126].

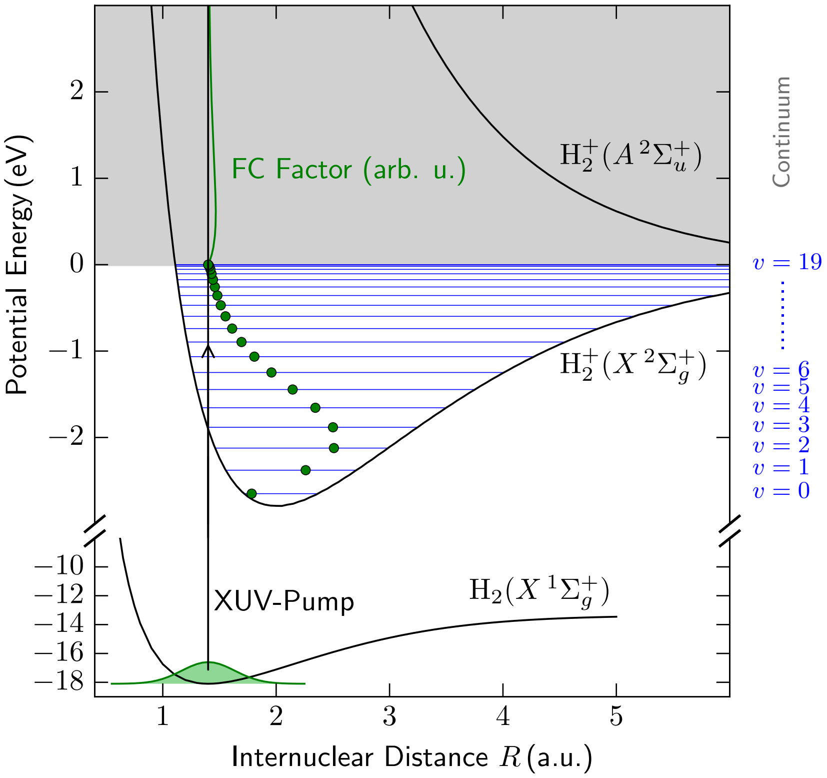

Figure 4.5: H_2 ground state together with the two energetically lowest ionic states. The blue lines indicate the total energy of the 20 bound vibrational states of the $H_2^+(X\,^2\Sigma_g^+)$ potential. Above them, marked in gray, are the (discrete) continuum states. The Franck-Condon factors are plotted in green and labeled "FC". The green dots indicate the Franck-Condon factors of the bound states while the thin green line represents the probability density for the continuum states. Here, positive potential energies translate directly to the resulting KER, as the corresponding states are all continuum states. The state density is energy dependent and given by $\rho = (m_p/2\pi^2\hbar^2)\sqrt{E}$ (m_p is the proton mass). The algorithm described in Ref. [126] was used to compute the eigenstates and their corresponding eigenenergies.

quickly (before the nuclei gain much kinetic energy) autoionizes to the same final state [$H_2^+(X\,^2\Sigma_g^+)$]. All observables for these two processes are equal. This is, however, only the case for sufficiently high photon energies above 26 eV, which allow to reach the energetically lowest DES. At this point, the ionization cross-section increases drastically due to the opening of a new ionization channel, see e.g. [19,127–129]. With increasing photon energy more DES belonging to the Q_1 band become accessible, further increasing the cross section of the ionization process.

4.2.2 Dissociation via the First Excited Ionic $H_2^+(A\,^2\Sigma_u^+)$ State

After having identified and explained the ionic ground-state dissociation we continue with the second process, namely the ionization via the first excited ionic state. At equilibrium internuclear distance, the minimal photon energy required to ionize molecular hydrogen from the equilibrium internuclear distance of the neutral ground state to the $\mathrm{H}_2^+(A\,^2\Sigma_u^+)$ state is $E_\gamma \approx 33\,\mathrm{eV}$. This equivalently means that at this photon energy the dipole transition becomes possible from the center of the Franck-Condon region (see Fig. 4.4). Knowing that the observed events dissociate to the first ionic dissociation limit at $E_\mathrm{limit} = 18.1\,\mathrm{eV}$, we expect the dissociation to be observed on diagonals in the energy correlation plot fulfilling $E_\gamma = \mathrm{KER} + E_e + E_\mathrm{limit} \approx 33\,\mathrm{eV}$. Taking a look at Fig. 4.3 reveals that within the red dashed lines this condition is met for all events.

It is unlikely to obtain high photoelectron energies E_e through this channel. This is best understood if one considers a fixed photon energy E_γ (for which we choose 35 eV as a discussion example) and with this a unique diagonal line[13] in the energy correlation map (Fig. 4.3). With Fig. 4.6 we find that the larger the observed photoelectron energy is the further to the right the ionization process has to occur. However, moving the transition to the right means that the transition quickly becomes unlikely, as the ground state wave function (Fig. 4.6 green curve and filling) drastically falls off in amplitude (Gaussian shape). Therefore, the observation of the dissociation via the $\mathrm{H}_2^+(A\,^2\Sigma_u^+)$ state occurs predominantly together with small photoelectron energies E_e. We further note that, in contrast to the ground-state dissociation, this channel results in high kinetic energy release and, therefore, yields fast nuclear fragments. With this knowledge, we assign the dissociative ionization via the $\mathrm{H}_2^+(A\,^2\Sigma_u^+)$ state in Fig. 4.3 state to the region confined by the green dashed line, leaving only the region within the red dashed line to be identified.

Before doing so, it is important to take a look at the photoelectron angular distribution that is connected to the dissociative ionization of molecular hydrogen via the above discussed channel. The reason for this is that the asymmetry defined in the introduction of this chapter includes the photoelectron as well as the bound electron.

With this in mind, we proceed by investigating the photoelectron distribution for this channel. Knowing that for photon energies $E_\gamma = 35\,\mathrm{eV}$ the transition to the $\mathrm{H}_2^+(A\,^2\Sigma_u^+)$ state is energetically allowed from the center of the Franck-Condon region (where the probability amplitude of the channel to occur is thus maximal), producing events $E_e \approx 0$ and $\mathrm{KER} = E_\gamma - E_\mathrm{limit} - E_e = 16.9\,\mathrm{eV}$, we minimize the influence of other channels by selecting events simultaneously fulfilling the conditions

$$E_e < 1\,\mathrm{eV} \quad \text{and} \quad \mathrm{KER} = E_\gamma - E_\mathrm{limit} - E_e = (16.9 \pm 1)\,\mathrm{eV}. \tag{4.24}$$

---

[13] The line is unique only if one ionic dissociation limit is contributing to the dissociation, as it is the case here.

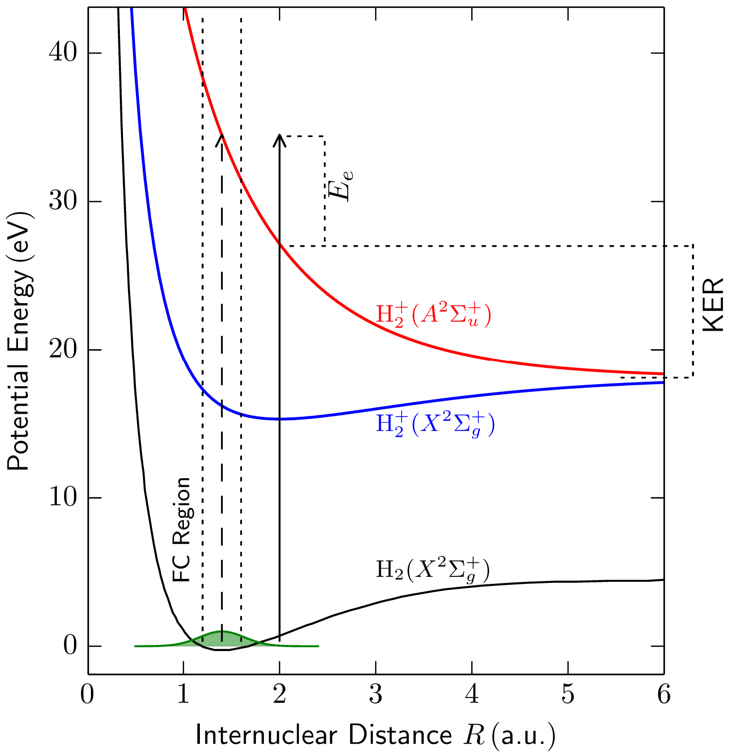

Figure 4.6: H_2 ground state (black line) together with the nuclear ground-state wave function. The two energetically lowest ionic states are depicted by the colored lines. The Franck-Condon region (region of non-vanishing ground-state wave function) is marked with by vertical dotted lines. The two arrows indicate photons with energy $E_e = 35\,\text{eV}$. This figure illustrates that in order to obtain high photoelectron energies the transition has to be driven far to the right of the Franck-Condon region, which strongly suppresses the likelihood of such an event. Further, the resulting photoelectron energy E_e and KER for the reaction are indicated.

By plotting the angle θ between the electron momentum vector and the laser polarization axis for the chosen events, Fig. 4.7 is obtained. This distribution has strong contributions from partial waves of gerade symmetry[14], especially the first σ_g^+ partial wave (s-wave). Deviations from a perfectly symmetric (spherical) distribution are mainly caused by detection inefficiencies (electrons emitted initially away from the electron detector are less likely to be detected) and contributions from competing channels with different parity, such as the dissociation via the doubly-excited states (subject of the next sub-subsection).

To conclude the discussion of this channel, we use group theoretical arguments to deduce the symmetry representation of the photoelectron partial wave (which is connected to the photoelectron angular distribution), which allows us to write

---

[14] For the case of a distribution governed by ungerade partial waves, one would expect to observe at least one node of the distribution.

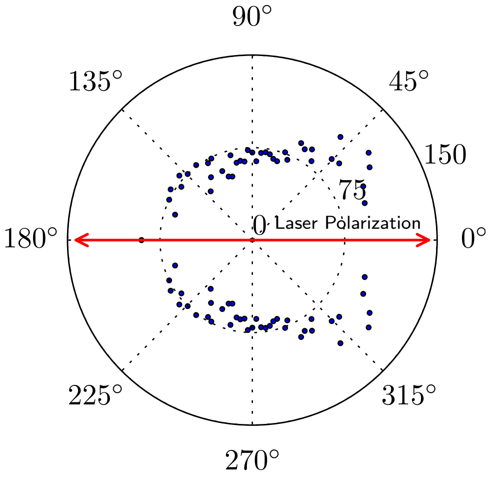

Figure 4.7: Photoelectron angular distribution for the dissociation via the $H_2^+(A\,^2\Sigma_u^+)$ channel. The distance from the center is proportional to the count number. Note, near the poles (0° and 180°) the bins are larger to account for a reduced solid angle in this region. A distribution with strong contribution from gerade partial waves is observed. Also compare to Fig. 4.9 which shows a distribution governed by an ungerade wave function, which (in contrast) clearly features a node. Note: In a three dimensional space the angle between two vectors is uniquely defined only within 0 and π, therefore the distribution is mirrored at the polarization axis for illustrative reasons.

down a product wave function of the bound electron and the photoelectron[15]. The point group of linear homonuclear molecules is $D_{\infty h}$. We have to consider the dipole transition amplitude

$$\begin{aligned} c_I &= -\mathcal{E}\langle A\,^2\Sigma_u^+;\, \psi_{e^-}|z|X\,^1\Sigma_g^+\rangle \\ \text{with} \quad \langle A\,^2\Sigma_u^+;\, \psi_{e^-}| &= \langle A\,^2\Sigma_u^+| \otimes \langle \psi_{e^-}| \end{aligned} \tag{4.25}$$

where $|\psi_{e^-}\rangle$ is the photoelectron wave function, $|A\,^2\Sigma_u^+\rangle$ the wave function corresponding to the bound electron of the H_2^+ molecule, $|X\,^1\Sigma_g^+\rangle$ the wave function of the neutral H_2 and $-\mathcal{E}z$ the dipole operator. For this we assumed that the final wave function of the ionized system is described by a product wave function of the bound electron and the photoelectron. We further know that in the point group $D_{\infty h}$ for parallel transitions the dipole operator's irreducible representation is Σ_u^+ and the representations of the initial and final state of the bound electron(s) are Σ_g^+ and Σ_u^+, respectively. The only unknown representation is the one corresponding to the photoelectron, which we denote $R(e^-)$. If put together, we are able to identify the symmetry representation of the photoelectron by evaluating the product of irreducible representations (for which we demand that the totally symmetry

---

[15] Sec. 2.2 gives a short introduction to group theory and molecular symmetry. A more thorough description of group theory is e.g. found in Refs [66–69].

representation is included in order to be dipole allowed)

$$\underbrace{\Sigma_u^+ \otimes R(e^-)}_{\langle A\,^2\Sigma_u^+;\psi_{e^-}|} \otimes \underbrace{\Sigma_u^+}_{z} \otimes \underbrace{\Sigma_g^+}_{|X\,^1\Sigma_g^+\rangle} \overset{!}{=} \Sigma_g^+ \oplus \ldots, \tag{4.26}$$

where the labels below the braces indicate the basis which spans the above representation. The transition is symmetry forbidden if the product of irreducible representations cannot be written as a sum of irreducible representations including the totally symmetric Σ_g^+ one (see e.g. [66, 69]). Using a multiplication table (to the group $D_{\infty h}$) we find that the sum includes Σ_g^+ only if $R(e^-)$ is identified as the Σ_g^+ irreducible representation. To make it clear whether we are talking about a bound- or a photoelectron, we use in the following upper-case Greek letters to name states of the bound electron(s) and lower-case letters for the photoelectron states[16].

With this we conclude that the wave function of the final system (after ionization) via the $H_2^+(A\,^2\Sigma_u^+)$ state can be written as the product

$$\boxed{|\Psi_I\rangle = |A\,^2\Sigma_u^+\rangle|\sigma_g^+\rangle = |A\,^2\Sigma_u^+;\,\sigma_g^+\rangle} \tag{4.27}$$

This is an important result, which is later extensively needed in the derivation of the observed asymmetry.

4.2.3 Dissociation Including Doubly-Excited States

The last of the previously mentioned processes (region between the red dashed lines in Fig. 4.3) is the dissociation including doubly-excited states (DES), which are states where both electrons are no longer in the energetically lowest molecular orbital. The DES considered throughout this work are solely the ones labeled Q_1 in Fig. 4.4. For parallel dipole transitions only the DES with Σ_u^+ symmetry can be excited (selection rules) while the Π_u states are only accessible through perpendicular transitions (where the molecular axis is oriented perpendicularly to the polarization axis). Because of the very large cross-section at the photon energies considered in this work, the energetically lowest doubly-excited $H_2(Q_1\,^1\Sigma_u^+(1))$ state is the predominantly populated DES [130], to which we also refer to as $Q_1\ \Sigma_u^+(1)$ in the following.

Due to the electron correlation, the DES, which are embedded in the single-ionization continuum, of the hydrogen molecule are not stable and autoionize. The timescale of the autoionization is comparable to the dissociation time, which plays an important role in the later reported electron localization. A detailed investigation of the lifetime τ of the $Q_1\ \Sigma_u^+(1)$ state is the subject of Sec. 4.4, where we find τ to be between 0.4 fs and 1 fs depending on the internuclear separation R. Figure 4.8

---

[16] Note that the states e.g. $|\sigma_g^+\rangle$ and $|\Sigma_g^+\rangle$ belong to the same irreducible representation Σ_g^+.

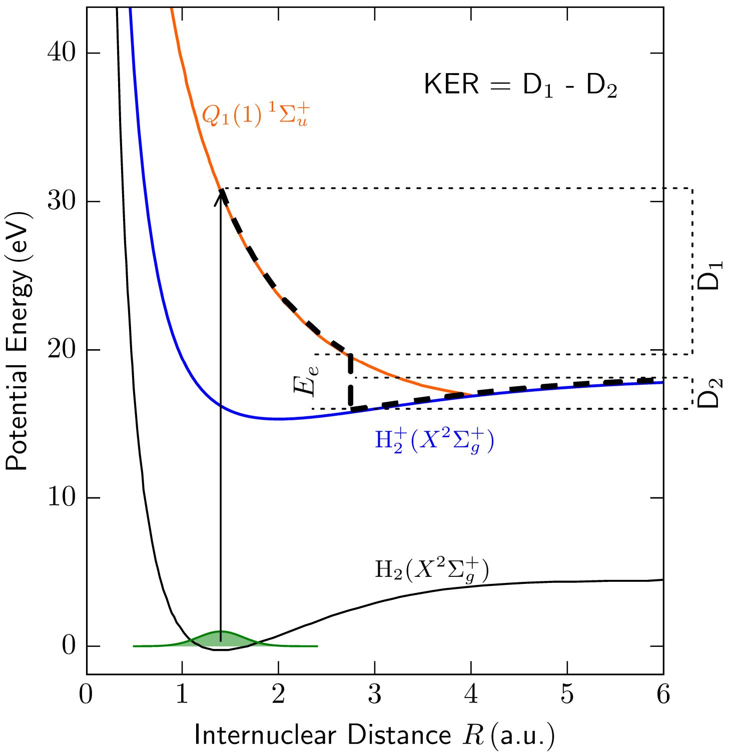

Figure 4.8: Illustration of the autoionization process. First, the doubly-excited (dissociative) state is resonantly populated by a single-photon transition. As a consequence the molecule starts to dissociate and decays at some internuclear distance by ejecting an electron. The previously gained kinetic energy is conserved in the transition, therefore when enough kinetic energy has been gained, the molecule continues to dissociate along the ionic ground state ($X\,^2\Sigma_g^+$) accumulating a total kinetic energy release of $\mathrm{KER} = \mathrm{D}_1 - \mathrm{D}_2$.

illustrates the process behind the here investigated dissociative ionization channel. After being excited, the molecule starts to dissociate along the potential energy curve given by the state $Q_1\ \Sigma_u^+(1)$. When it decays at the internuclear separation R_{decay}, an electron with the difference energy $E_e = V_{Q_1}(R_{\mathrm{decay}}) - V_{X\,^2\Sigma_g^+}(R_{\mathrm{decay}})$ is emitted. The nuclei, which have at this point gained enough kinetic energy, continue to dissociate along the potential of the ionic ground state.

The decay of the DES can happen at all internuclear separations, which means that this channel produces all possible combinations of KER and E_e that fulfill conservation of energy

$$E_\gamma = \mathrm{KER} + E_e + E_{\mathrm{limit}}. \tag{4.28}$$

The reason why this channel manifests in the appearance of the pronounced diagonal lines in Fig. 4.3 is that the photon energy supplied by the attosecond pulse trains is

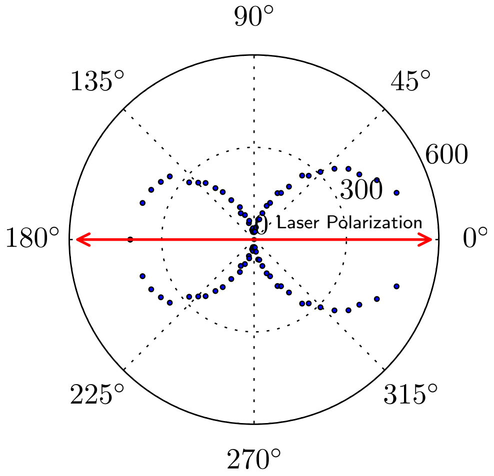

Figure 4.9: Photoelectron angular distribution for the channel of dissociation including doubly-excited states. A strong contribution from ungerade partial waves is observed, especially the lowest order (p-wave). Again, the differences in detection efficiency of the electrons initially going toward or away from the electron detector cause a slight left-right asymmetry. Also compare to Fig. 4.7 that shows a distribution governed by a gerade wave function. Again, the counts are mirrored at the polarization axis.

shared between the nuclei and the photoelectrons.

The regions of the here and the above discussed processes overlap (see Fig. 4.3 red dashed region and green dashed region), which means that the observables of the processes in the overlap region do not permit an identification of the two channels, allowing for an interference of the two reaction pathways.

However, before we continue to present the results of the measured asymmetry in the next section, it remains to show that the electron wave function corresponding to the observed electron events stemming from the here discussed channel is of opposite parity as the one presented above. In contrast to the above shown photoelectron distribution, we can choose a region in Fig. 4.3 where only this one pathway contributes. Therefore, a much cleaner and more symmetric distribution is expected for this channel. The result of the photoelectron distribution for events simultaneously fulfilling the conditions

$$E_e > 3\,\mathrm{eV} \quad \text{and} \quad 4\,\mathrm{eV} < \mathrm{KER} < 12\,\mathrm{eV} \tag{4.29}$$

is shown in Fig. 4.9. The remaining photoelectron-distribution asymmetry (left to right) observed here is caused by the detection efficiency of the reaction microscope for electrons initially going toward or away from the electron detector (as previously explained). It appears that the leading order of the electrons partial wave is a p-wave and therefore of ungerade parity[17].

---

[17] Recall that the parity of a spherical harmonic is $(-1)^l$.

Again, we conclude this section by applying group theory to find the final wave function of the dissociation products. For this, we write the transition amplitude for the here discussed channel, with $|X\,{}^2\Sigma_g^+\rangle$ being the electronic ground state of the H_2^+ molecule, $Q_1\,{}^1\Sigma_u^+(1)$ the DES, and $|X\,{}^1\Sigma_g^+\rangle$ the ground state of the neutral hydrogen molecule,

$$\begin{aligned} c_A = -\,\big\langle X\,{}^2\Sigma_g^+;\,\psi_{e^-}\big|\,{}^1\!/\!_{|r_1-r_2|}|Q_1\,{}^1\Sigma_u^+(1)\rangle\langle Q_1\,{}^1\Sigma_u^+|\mathcal{E}z|X\,{}^1\Sigma_g^+\rangle \\ \text{with}\quad \langle X\,{}^2\Sigma_g^+;\,\psi_{e^-}| = \langle X\,{}^2\Sigma_g^+|\otimes\langle\psi_{e^-}| \end{aligned} \tag{4.30}$$

which consists of a product of two quantum mechanical amplitudes, one dipole transition to the DES and one electron-correlation induced autoionization [induced by the operator $(|r_1-r_2|)^{-1}$] to the ionic state. Let us again translate this into a product of irreducible representations

$$\underbrace{\Sigma_g^+\otimes R(e^-)}_{\langle X\,{}^2\Sigma_g^+;\psi_{e^-}|}\otimes\underbrace{\Sigma_g^+}_{1/|r_1-r_2|}\otimes\underbrace{\Sigma_u^+}_{|Q_1\,{}^1\Sigma_u^+\rangle}\otimes\underbrace{\Sigma_u^+}_{\langle Q_1\,{}^1\Sigma_u^+(1)|}\otimes\underbrace{\Sigma_u^+}_{\mathcal{E}z}\otimes\underbrace{\Sigma_g^+}_{|X\,{}^1\Sigma_g^+\rangle}\overset{!}{=}\Sigma_g^+\oplus\cdots \tag{4.31}$$

which has to be equivalent to a sum of irreducible representations including the totally symmetry representation Σ_g^+ in order to be symmetry allowed. Again, by using the group's character table (or alternatively its multiplication table) we find that the amplitudes are only non-vanishing if $R(e^-)$ is identified as the Σ_u^+ irreducible representation. The wave function of the photoelectron is therefore, in accordance with the previously introduced nomenclature, written as $|\sigma_u^+\rangle$. Using this result, we write the total wave function of the final state of this dissociative ionization channel as the product

$$\boxed{|\Psi_A\rangle = |X\,{}^2\Sigma_g^+\rangle|\sigma_u^+\rangle = |X\,{}^2\Sigma_g^+;\,\sigma_u^+\rangle} \tag{4.32}$$

Comparing this result to Eq. (4.27) it is verified that the bound and the photoelectron states of both reactions are of opposite parity, respectively.

4.2.4 Brief Section Summary

To give a brief summary of the section the important findings shall be reviewed. The different dissociation channels contributing to the count distribution presented in Fig. 4.3 have been identified and explained. Further a region where two different channels, namely the dissociative ionization via the $H_2^+(A\,{}^2\Sigma_u^+)$ state and the other involving the doubly-excited Q_1 state, leading to the same observables has been identified (overlap of green and red dashed area). By using group theoretical arguments, the wave functions for the final states of these two pathways have been deduced. Combining these results gives a total wave function that is valid within the region of overlap[18]

$$|\Psi_{\text{fin}}\rangle = c_I|A\,^2\Sigma_u^+\rangle|\sigma_g^+\rangle + c_A|X\,^2\Sigma_g^+\rangle|\sigma_u^+\rangle, \tag{4.33}$$

where other channels can be neglected. In the following we simplify this expression by writing

$$\boxed{|\Psi_{\text{fin}}\rangle = c_I|\Sigma_u\rangle|\sigma_g\rangle + c_A|\Sigma_g\rangle|\sigma_u\rangle} \tag{4.34}$$

Since the total wave function cannot be written as factors of the bound electron and the photoelectron, it describes the entanglement of the two electrons. It further plays an important role when we project it onto a basis set describing electron localization. This allows the derivation of an expression which subsequently permits the application of a semi-classical model in order to calculate the observed localization effect.

4.3 Electron Localization Involving Doubly-Excited States

After having established the dissociative ionization channels contributing to the measured count distribution shown in Fig. 4.3, we proceed by investigating vector correlations between the observed fragments. We find, by comparing the electron momentum vector to the proton momentum vector, that depending on E_γ, E_e and KER the photoelectron and the proton are (after the dissociation) co- or counterpropagating.

It is important to note that the electron emission exerts a recoil onto the remaining H_2^+ ion. Therefore, depending on the relative emission direction, the nuclei have different momentum in the laboratory frame, see Fig. 4.10. For the analysis, we

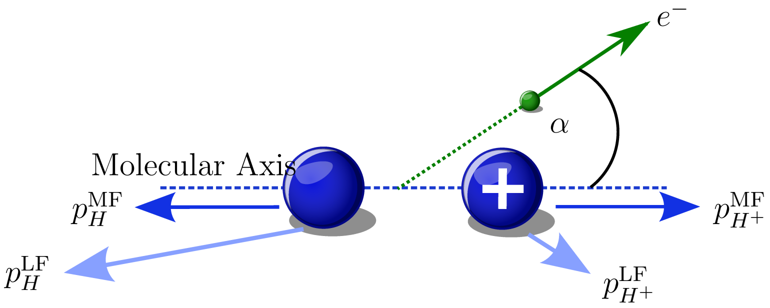

Figure 4.10: Illustration of the angle used to define the asymmetry. The asymmetry parameter A is defined as the angle between the proton momentum vector in the molecular frame (denoted MF) and the electron momentum vector. The momentum vectors of the nuclei as observed the laboratory frame (p_i^{LF}) are drawn in light blue. The vectors are not to scale as this is simply an illustration.

---

[18] It should ne noted that the wave function has to be antisymmetrized. However, as this leads to the same results it is not written out in order to simplify the notation.

therefore transform the nuclei momenta into a frame of reference where both nuclei have the same absolute momentum, but in opposite directions. This molecular frame of reference is in the following be the standard frame of reference, which is always used if not stated otherwise[19]. Further, we define α to be the angle between the electron momentum vector and the proton momentum vector in the molecular frame $p_{H^+}^{\mathrm{MF}}$. With this, in order to quantitatively investigate the localization effect, the asymmetry parameter A is defined in the molecular frame as follows (see e.g. [95–97, 131])

$$\boxed{A = \frac{N_{\alpha<90^\circ} - N_{\alpha>90^\circ}}{N_{\alpha<90^\circ} + N_{\alpha>90^\circ}}} \tag{4.35}$$

where $N_{\alpha<90^\circ}$ and $N_{\alpha>90^\circ}$ denote the number of electron/proton pairs with an angle $\alpha < 90^\circ$ and $\alpha > 90^\circ$, respectively. This means that in the molecular frame the electron is either co- or counterpropagating with the proton. Figure 4.10 illustrates the definition given by Eq. (4.35). It should be noted that the asymmetry parameter effectively describes a localization of the bound electron with regard to the emission direction of the photoelectron (the proton is always on the opposite side of the bound electron which is the reason why in this work the words localization and asymmetry are often used interchangeably).

With this definition of the asymmetry parameter A at hand, the next section presents the experimentally obtained results of the asymmetry.

4.3.1 Experimentally Observed Electron Localization

For the visualization of the measured data we make use of the energy correlation diagrams [see Figure 4.11 (top)]. Again, we observe the diagonal lines as a consequence of the photon spectrum of the high-order harmonics. To be able to plot the data on a linear color scale (instead of a logarithmic scale as in Fig. 4.3) the low KER region of the plot is omitted. This leaves out the process of ground-state dissociation, which is by far the dominant channel. Further, due to the low photon flux above $E_\gamma = 37\,\mathrm{eV}$ the plot is truncated at a total kinetic energy ($\mathrm{KER} + E_e$) of the fragments of $19\,\mathrm{eV}$ (recall that $E_\gamma = \mathrm{KER} + E_e + 18.1\,\mathrm{eV}$).

Plotting the asymmetry parameter A [Eq. (4.35)] into the energy correlation diagram instead of the counts results in Fig. 4.11 (bottom). Because the asymmetry parameter is defined by a ratio of the count difference to the total counts [see

---

[19] Be aware that the transformation is not applied to the electron momentum vector. The physical reason for this is that we are interested in the angle of the electron momentum vector to a vector along the molecular axis. The direction of the proton is important, as we later construct an oriented molecular frame for which an axis alone does not suffice. This is due to the fact that an angle would only be well defined for values between zero and $\pi/2$ and not for values between zero and π as needed to describe co- and counterpropagation.

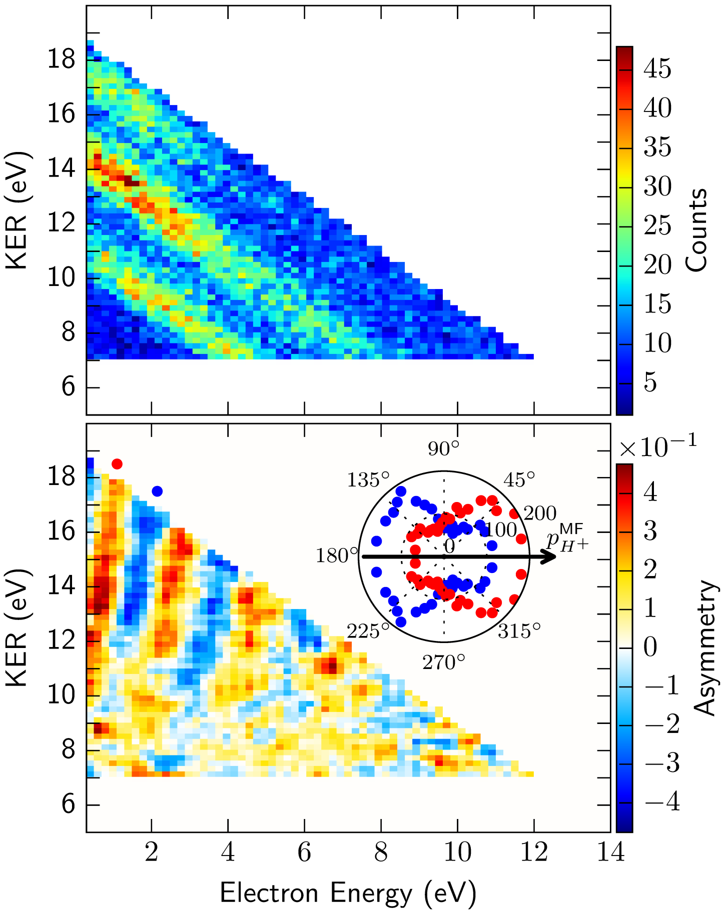

Figure 4.11: Top: Energy correlation diagram for KER > 7 eV and KER + E_e < 19 eV. Bottom: Measured asymmetry A for the same region as shown in the top figure. A pronounced oscillation (mainly as a function of the electron energy) is visible. In the inset the electron angular distribution with regard to the proton momentum vector p_{H+}^{MF} is shown for two cases: (i) red dots copropagation and (ii) blue dots for counterpropagation. The corresponding regions of the selected events are the two asymmetry stripes marked by a red and blue dot, respectively.

Eq. (4.35)], the diagonal lines as shown in Fig. 4.11 (top) are not visible. With the above chosen definition of the asymmetry parameter A, we know that a positive value (red) corresponds to the case where the electron and the proton are emitted in the same direction and negative values describe counterpropagation. Prominent oscillations between co- and counterpropagation are observed mainly as function of the electron energy. The dependence on the KER is much weaker, though not completely absent.

The inset in Fig. 4.11 (bottom) shows the angular distribution of the observed photoelectrons for two individual (almost vertical) asymmetry stripes. The angular distribution of the photoelectrons primarily emitted in the same direction as the proton momentum vector are plotted in red and the opposite case in blue. The observed photoelectron angular distributions (inset Fig. 4.11) strongly suggest a superposition of the two photoelectron wave functions discussed earlier for the individual channels (see Fig. 4.7 and Fig. 4.9). Depending on the relative phase of the s- and the p-wave of the photoelectrons, a localized photoelectron wave function is formed. Remember, that this localization is only observed in the molecular frame (i.e. it is defined by an angle to the proton momentum vector).

The explanation for this surprising observation is the subject of the next section (Sec. 4.3.2), in which a basis set of localized states is introduced. With this, it becomes possible to derive an expression for the asymmetry which in turn is used to perform simulations.

4.3.2 Origin of the Asymmetry

Before going into the thorough analysis of the origin of the asymmetry, a brief reminder of the previously presented is given. In Sec. 4.2 the different channels of the reaction

$$\mathrm{H}_2 \xrightarrow{\mathrm{XUV}} \mathrm{H}_2^+ + e^- \xrightarrow{\mathrm{Dissociation}} \mathrm{H} + \mathrm{H}^+ + e^-, \tag{4.36}$$

were discussed. To illustrate the experimental results, the energy correlation diagram was introduced (Fig. 4.3). It was further shown that three different channels significantly contribute to the measured data. The asymmetry is observed only for kinetic energy releases KER $> 7\,\mathrm{eV}$, which rules out the ground-state dissociation to be contributing to the asymmetry signal. This leaves only the direct ionization channel going to the $\mathrm{H}_2^+(A\,^2\Sigma_u^+)$ state and the channel involving the doubly-excited states. By using arguments from group theory, the final wave functions of the two dissociation pathways could be identified as

$$\begin{aligned} |\Psi_I\rangle &= c_I|A\,^2\Sigma_u^+\rangle|\sigma_g^+\rangle = c_A|\Sigma_u\rangle|\sigma_g\rangle \\ |\Psi_A\rangle &= c_A|X\,^2\Sigma_g^+\rangle|\sigma_u^+\rangle = c_I|\Sigma_g\rangle|\sigma_u\rangle, \end{aligned} \tag{4.37}$$

with $|\Psi_A\rangle$ corresponding to the channel involving the doubly-excited states which subsequently autoionize (hence the subscript A) and $|\Psi_I\rangle$ to the channel of direct ionization (subscript I), respectively. The knowledge that these two channels mainly[20] contribute to the measured data shown in Fig. 4.11 further allows us to write the final state wave function, which is also illustrated in Fig. 4.12, describing the observation as

$$|\Psi_{\mathrm{fin}}\rangle = c_I|\Sigma_u\rangle|\sigma_g\rangle + c_A|\Sigma_g\rangle|\sigma_u\rangle. \tag{4.38}$$

As the wave function cannot be separated in a product of bound electron and

---

[20] This is of course an approximation which, however, holds very well for the photon energies considered in this work.

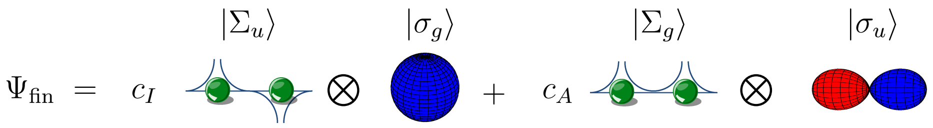

Figure 4.12: Illustration of the final state wave function. It is a superposition of product wave functions corresponding to the bound electron and the photoelectron. The total parity as well as the parity of each channel contribution is ungerade.

photoelectron wave functions Eq. (4.12) describes an entangled state. With this wave function and by exploiting the *law of large numbers* the count distribution $C(\text{KER}, E_e)$ shown in the energy correlation diagram gives an approximation of the probability distribution[21]

$$\lim_{N\to\infty} \frac{C(\text{KER}, E_e)}{N} = |\langle\Psi_{\text{fin}}(\text{KER}, E_e)|\Psi_{\text{fin}}(\text{KER}, E_e)\rangle|^2 = |c_I(\text{KER}, E_e)|^2 + |c_A(\text{KER}, E_e)|^2, \tag{4.39}$$

where the orthogonality of the bound electron wave functions $\langle\Sigma_u|\Sigma_g\rangle = 0$ and the partial waves of opposite parity $\langle\sigma_u|\sigma_g\rangle = 0$ was used. The sum $|c_I|^2 + |c_A|^2$ is not equal to one as Ψ_{fin} does not represent the probability for the complete state but only for a specific pair of photoelectron energy E_e and KER[22]. For the normalization condition Eq. (4.39) an integration over the possible photoelectron energies and KERs has to be carried out

$$\int_0^\infty \int_0^\infty |\langle\Psi_{\text{fin}}|\Psi_{\text{fin}}\rangle|^2 dE_e d\text{KER} = 1. \tag{4.40}$$

Analogously, the measured asymmetry A (see Fig. 4.11) is connected to the final state wave function [Eq. (4.38)]. To see the analogy, the asymmetry parameter [Eq. (4.35)] is best written in terms of probabilities[23]

$$\lim_{N\to\infty} A = a = \frac{n_{\alpha<90^\circ} - n_{\alpha>90^\circ}}{n_{\alpha<90^\circ} + n_{\alpha>90^\circ}}, \tag{4.41}$$

with $N = N_{\alpha<90^\circ} + N_{\alpha>90^\circ}$. In order to access these probabilities in the next section we construct two operators (projectors) describing the measurement

$$P_{<90^\circ} \quad \text{and} \quad P_{>90^\circ}. \tag{4.42}$$

---

[21] Recall that $c_I(\text{KER}, E_e)$ and $c_A(\text{KER}, E_e)$ can be interpreted as functions of the KER and the electron energy E_e.

[22] Note that our main observable, the asymmetry parameter, as defined below, does not require the wave function to be normalized.

[23] The probabilities are connected to the measured data by the law of large numbers.

With these operators Eq. (4.41) becomes

$$\boxed{a = \frac{\langle \Psi_{\text{fin}} | P_{<90^\circ} | \Psi_{\text{fin}} \rangle - \langle \Psi_{\text{fin}} | P_{>90^\circ} | \Psi_{\text{fin}} \rangle}{\langle \Psi_{\text{fin}} | P_{<90^\circ} | \Psi_{\text{fin}} \rangle + \langle \Psi_{\text{fin}} | P_{>90^\circ} | \Psi_{\text{fin}} \rangle}} \tag{4.43}$$

This is still a formal solution, as we need further knowledge of the operators. To achieve this, we have to construct a basis set in which we can represent the operators to actually perform a computation. The next section "Basis Set of Localized States" derives such an explicit form of the basis.

Basis Set of Localized States

The purpose of this section is to derive an explicit form of the operators

$$P_{<90^\circ} \quad \text{and} \quad P_{>90^\circ}. \tag{4.44}$$

such that the formal solution of the asymmetry given by Eq. (4.43) can be evaluated. As explained in the previous section, the asymmetry parameter "a" [Eq. (4.41)] essentially compares the number of events where the proton and electron are emitted in the same direction to the number of events in the counterpropagating case, which corresponds to $P_{<90^\circ}$ and $P_{>90^\circ}$, respectively.

Therefore we construct the projectors to describe the measurement as follows

$$\begin{aligned} P_{<90^\circ} &= |n_{\rightrightarrows}\rangle\langle n_{\rightrightarrows}| + |n_{\leftleftarrows}\rangle\langle n_{\leftleftarrows}| \\ P_{>90^\circ} &= |n_{\rightleftarrows}\rangle\langle n_{\rightleftarrows}| + |n_{\leftrightarrows}\rangle\langle n_{\leftrightarrows}|. \end{aligned} \tag{4.45}$$

In Eq. (4.45) the upper arrow indicates the propagation direction of the proton, whereas the lower arrow corresponds to the propagation direction of the photoelectron. Thus, we write

$$\begin{aligned} |n_{\rightrightarrows}\rangle &= |p_{\rightarrow}\rangle|e_{\rightarrow}\rangle, \qquad & |n_{\leftleftarrows}\rangle &= |p_{\leftarrow}\rangle|e_{\leftarrow}\rangle, \\ |n_{\rightleftarrows}\rangle &= |p_{\rightarrow}\rangle|e_{\leftarrow}\rangle, \qquad & |n_{\leftrightarrows}\rangle &= |p_{\leftarrow}\rangle|e_{\rightarrow}\rangle, \end{aligned} \tag{4.46}$$

where the $|p\rangle$ and $|e\rangle$ describe the proton and electron propagation along the laser polarization, respectively. With this we are now able to make the final step by expanding $|p_{\rightarrow}\rangle$, $|p_{\leftarrow}\rangle$, $|e_{\rightarrow}\rangle$, and $|e_{\leftarrow}\rangle$ in terms of molecular orbitals (Σ_g and Σ_u describing the bound electron) and free waves (σ_g and σ_u describing the photoelectron,

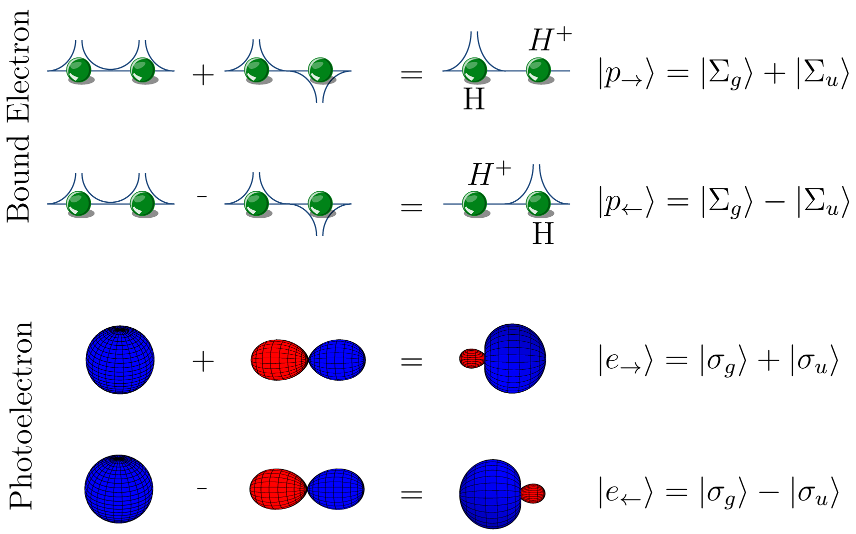

Figure 4.13: Visualization of the basis set of localized bound-electron and photoelectron states. The top panel shows the superposition for the bound electron. The localization of the proton is indirectly described by the wave function of the bound electron, because the proton is always on the opposite side of the localized electron. The bottom panel features the localization states of the photoelectron. For this only the lowest partial waves $l = 0$ and $l = 1$ were considered, which is a reasonable approximation for the photon energy range considered in this work.

for which we choose a basis of spherical harmonics[24]), respectively.

Using the molecular orbitals of the H_2^+ molecule and the spherical harmonics, we superimpose these wave functions such that a localization of the electron wave functions occurs as is illustrated in Fig. 4.13. For the desired superpositions we find

$$\begin{aligned} |p_{\rightarrow}\rangle &= |\Sigma_g\rangle + |\Sigma_u\rangle, \qquad & |p_{\leftarrow}\rangle &= |\Sigma_g\rangle - |\Sigma_u\rangle, \\ |e_{\rightarrow}\rangle &= |\sigma_g\rangle + |\sigma_u\rangle, \qquad & |e_{\leftarrow}\rangle &= |\sigma_g\rangle - |\sigma_u\rangle. \end{aligned} \tag{4.47}$$

Inserting these definitions into Eq. (4.46) yields the final result for the basis set of localized states which is used to diagonalize the operators given in Eq. (4.45)

$$\begin{aligned} |n_{\rightrightarrows}\rangle &= \big(\,|\Sigma_g\rangle + |\Sigma_u\rangle\,\big)\big(\,|\sigma_g\rangle + |\sigma_u\rangle\,\big), \qquad & |n_{\leftleftarrows}\rangle &= \big(\,|\Sigma_g\rangle - |\Sigma_u\rangle\,\big)\big(\,|\sigma_g\rangle - |\sigma_u\rangle\,\big), \\ |n_{\rightleftarrows}\rangle &= \big(\,|\Sigma_g\rangle + |\Sigma_u\rangle\,\big)\big(\,|\sigma_g\rangle - |\sigma_u\rangle\,\big), \qquad & |n_{\leftrightarrows}\rangle &= \big(\,|\Sigma_g\rangle - |\Sigma_u\rangle\,\big)\big(\,|\sigma_g\rangle + |\sigma_u\rangle\,\big). \end{aligned} \tag{4.48}$$

---

[24] Throughout this work, the question of which partial waves build up the wave functions is not important. It is only important that $|\sigma_g\rangle$ consists only of gerade and $|\sigma_u\rangle$ of ungerade partial waves. The parity of the spherical harmonics are given by $(-1)^l$. Therefore g corresponds to even l's and u to odd ones. However, the amplitude of the observed asymmetry is dependent on the contributing partial waves.

The complete set of basis states used to construct the diagonal projection operators [Eq. (4.45)] applied to the entangled wave function [Eq. (4.38)] are illustrated in Fig. 4.14.

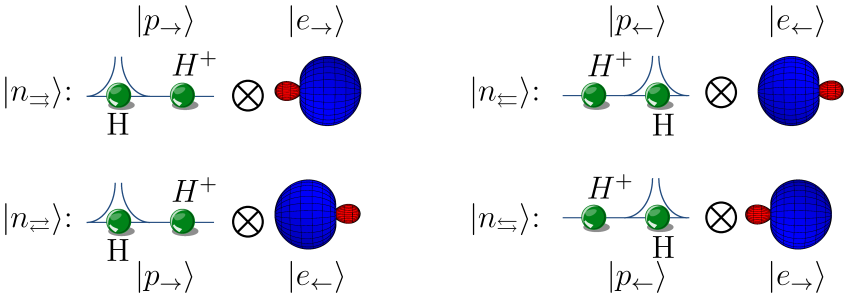

Figure 4.14: Illustration of the basis set of localized states which are used to describe the projection operators needed to compute the asymmetry [Eq. (4.43)].

Having established an appropriate basis set to derive an expression for the asymmetry parameter, by inserting Eq. (4.38), Eq. (4.46) and Eq. (4.48) into Eq. (4.43), we are in the position to derive a final expression for the asymmetry parameter. A straight forward, but tedious calculation exploiting

$$\langle \Sigma_{n_1} | \Sigma_{n_2} \rangle = \delta_{n_1,n_2}$$

and

$$\langle \sigma_{n_1} | \sigma_{n_2} \rangle = \delta_{n_1,n_2} \quad \text{with} \quad n_i \in \{g, u\} \tag{4.49}$$

directly leads to the asymmetry parameter as a function of c_I and c_A

$$\boxed{a = -\frac{2\,\mathrm{Re}[c_I c_A^*]}{|c_I|^2 + |c_A|^2}} \tag{4.50}$$

where c_I and c_A are the developing coefficients of the final-state wave-function derived above [see Eq. (4.38)].

This simple expression for the asymmetry is used in the following section for the simulation of the asymmetry using an intuitive semi-classical model, based on the WKB approximation. The WKB approximation allows to obtain numerical solutions of Schrödinger's equation which in turn allows to reproduce the observed asymmetry oscillations to a high degree of accuracy. It turns out that the nuclear motion, which is inherently determined by the shape of the different potential energy curves on which the dissociative-ionization process occurs, causes the observed oscillatory behavior of the electron localization.

Be aware that the dependence on the motion is the classical interpretation to the fact that in the WKB approximation the phases of the stationary states are given by

$$\varphi = \int^{x} \sqrt{2m[E - V(x')]}dx'. \tag{4.51}$$

In this equation the term $p = \sqrt{2m[E - V]}$ is interpreted as the classical momentum of a particle, which then connects quantum mechanics to the classical picture. It should further be noted that even though one can interpret this in terms of classical mechanics the description remains to be quantum mechanical in which p is merely a definition. Throughout this work we therefore refer to the description using the WKB approximation as being semi-classical and ascribe the phase change of the quantum mechanical states to the nuclear motion.

4.3.3 Semi-Classical Description

With the derivation of Eq. (4.50) an expression was obtained to describe the observed asymmetry by means of only two complex amplitudes, namely the expansion coefficients of the final state wave function Ψ_{fin} [Eq. (4.38)]. It is an involved calculation to theoretically obtain quantitative values for c_I and c_A, as it would have to include the ionization, excitation and the autoionization (due to electron correlation) of hydrogen molecules. Therefore, in this work approximations are made which still allow to investigate the oscillatory behavior of the observed asymmetry, but with which a quantitative analysis of the oscillation's amplitude is not possible.

In order to simulate the asymmetry, the complex amplitudes c_I and c_A are first written in polar form as a modulus and a phase factor

$$c_I = r_I e^{i\chi_I} \quad \text{and} \quad c_A = r_A e^{i\chi_A} \tag{4.52}$$

The moduli r_I and r_A, which are only accessible through a fully quantum mechanical calculation, stand responsible for the amplitude of the asymmetry, which is not under investigation at this point. For this reason, they are in the following be set to unity, which simplifies Eq. (4.52) to

$$c_I = e^{i\chi_I} \quad \text{and} \quad c_A = e^{i\chi_A} \tag{4.53}$$

The phases χ_k are split into two contributions $\chi_k = \varphi_k + \xi_k$, where the ξ_k describe the phases acquired in the electronic transitions between electronic states and in the autoionization and the φ_k are the nuclear phases. This is illustrated in Fig. 4.15 where the electronic transitions are labeled by Ⓐ, Ⓑ and Ⓒ, while the phases caused by to the nuclear motion are indicated by encircled numbers and the colored dashed and dotted lines.

The ξ_k are obtainable through fully quantum mechanical computations as well as

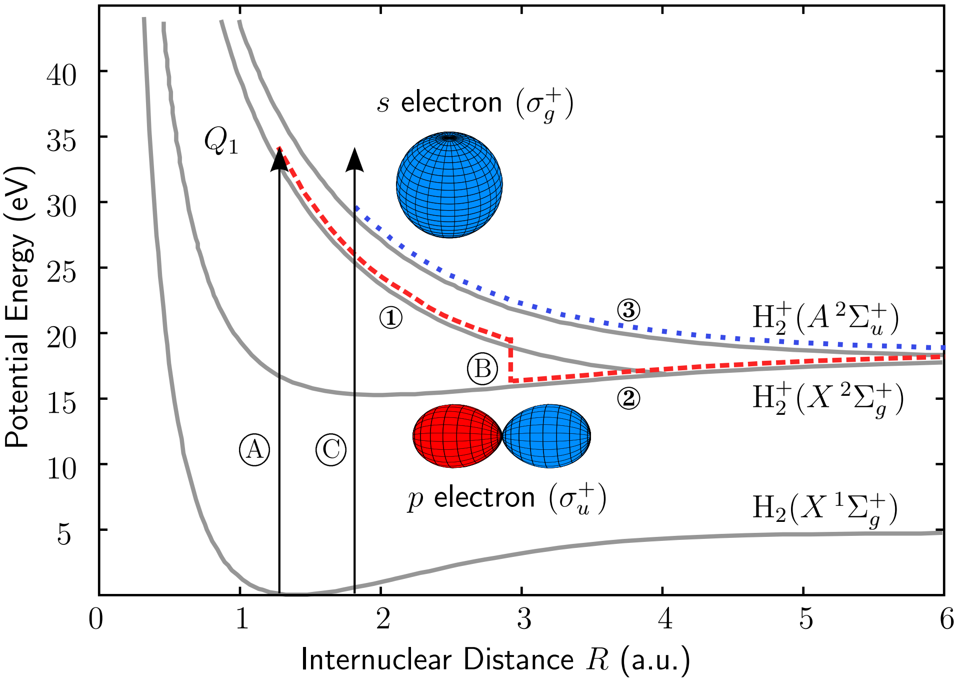

Figure 4.15: Relevant potential energy curves for the H_2 and H_2^+ states. The electronic transitions involved in the dissociative ionization process are indicated by encircled letters, while the nuclear dynamics, leading to the nuclear phases, is labeled by encircled numbers. The two dissociation pathways, namely the autoionization and the direct ionization channel, are indicated by a red dashed and a blue dotted line, respectively. Figure adapted from Ref. [132] using the potential energy curves given by Ref. [21].

by comparing the behavior of different isotopes [104]. However, for the purpose of this work it is sufficient that they are functions of the photon energy and kinetic energy of the electron, which vary only slightly within the parameters used throughout this work. This has been verified by fully quantum mechanical calculations carried out by Alicia Palacios, Alberto González-Castrillo and Fernando Martín (using a method described in Ref. [23]) and later prove to be consistent with the experimental observations. Therefore, throughout the semi-classical approach they are approximated by constants, which remain unspecified at this point.

Inserting Eq. (4.53) into Eq.(4.50) yields the following relation for the asymmetry parameter

$$a = \cos(\Delta\varphi_N + \Delta\xi_E), \tag{4.54}$$

where $\Delta\varphi_N = \varphi_I - \varphi_A$ describes the difference of phase of the nuclear wave functions and $\Delta\xi_E = \xi_I - \xi_A$ the difference in the electronic transition phases. As the electronic transition phases are here considered constant, the asymmetry oscillation is fully ascribed (with the exception of a constant phase offset) to the phase corresponding to the nuclear motion.

In order to obtain the phases corresponding to the nuclear motion, we make use of the WKB approximation described in Sec. 4.1. Further, as we are only interested in the phases of the stationary vibrational states, Eq. (4.17) simplifies to[25]

$$\Psi(x,t) = e^{i\int^{x}\sqrt{2m[E-V(x')]}dx'} = e^{i\varphi} \tag{4.55}$$

With this, the following correspondence between the desired phase and the WKB-solution is readily established

$$\varphi = \int^{x} \sqrt{2m[E-V(x')]}dx'. \tag{4.56}$$

Again, the fact that $\sqrt{2m[E-V(x')]}$ can be identified with a classical particle's momentum p is the reason why the approach presented is labeled as to be semi-classical. To use Eq. (4.56) for the numerical computation of the phases we have to find the dissociation pathways for each set of photon energy, KER and electron energy E_e yielding the same observables (KER and E_e)[26]. One such pair of dissociation pathways is depicted in Fig. 4.15 by the red dashed and the blue dotted line. Once knowing the pairs of pathways we can calculate their corresponding phases by evaluating the integral

$$\varphi_{I,A} = \int_{R^t_{I,A}}^{\infty} p_{I,A}(R)dR, \tag{4.57}$$

where $R^t_{I,A}$ are the internuclear distances at which the XUV transition occurs and $p_{I,A}$ the nuclear momenta along the different dissociation pathways. The initial momentum after the XUV transition is assumed to be zero. Note that the pathway corresponding to the autoionization channel includes a transition from one potential energy curve to another, which means that two integrals along two different potential energy curves have to be evaluated. The phases of the two pathways are then used together with Eq. (4.54) to compute the asymmetry.

The results of the simulation shown in Fig. 4.16, where we have set the electronic phase difference to $\Delta\xi_E = \pi$, are in very good agreement with the experimental observations (compare Fig. 4.16 middle and bottom). The value $\Delta\xi_E = \pi$, as it is not accessible through a simple model as presented here and therefore being left as fit-parameter, is close to that obtained by averaging the phase difference resulting

---

[25] In this section, in contrast to the section in which the WKB approximation was derived, atomic units are used again leading to the omission of $\hbar$.

[26] Finding unique dissociation pathways considering only the photon energy and the observed electron energy is only possible when the potential energy curve V_{Σ_u} and the difference $V_{Q_1}(R) - V_{\Sigma_g}(R)$ – respectively corresponding to the electronic states $\mathrm{H}_2^+(A\,^2\Sigma_u^+)$, $\mathrm{H}_2(Q_1\,^1\Sigma_u^+(1))$, and $\mathrm{H}_2^+(X\,^2\Sigma_g^+)$ – are both strictly monotone functions.

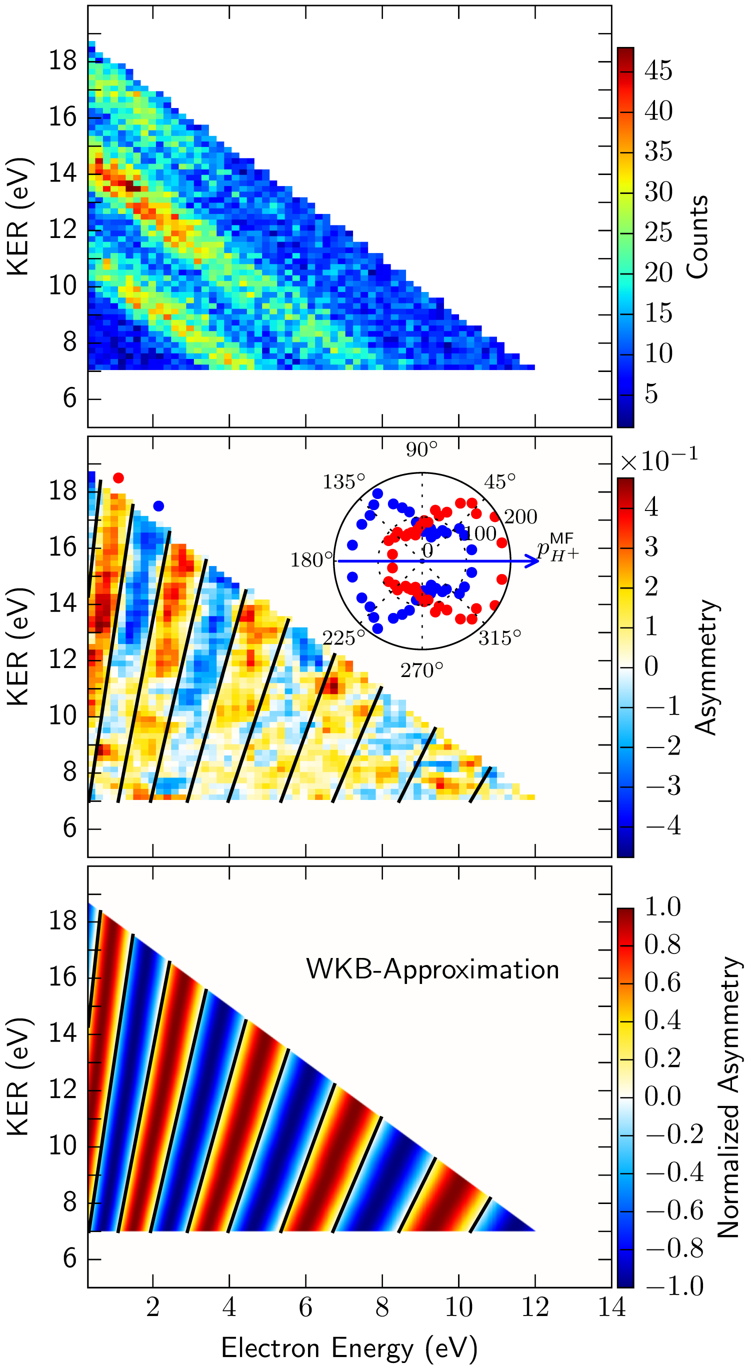

Figure 4.16: Top: measured count distribution as a function of KER and electron energy. Middle and bottom: comparison of the experimental obtained asymmetry to the one computed using the semi-classical approach described in this section. Black contour lines of symmetric ejection ($a = 0$) are overlaid onto the experimental data as well as on the theoretical results to enhance comparability.

from the *ab initio* calculation in the Franck-Condon region and in the photon energy range considered in this work.

For better comparability of the experimental data to the semi-classical calculation, Fig. 4.16 features black-contour lines of calculated symmetric ejection ($a = 0$), which are overlaid on the experimental asymmetry as well as on the theoretical results. Except for the fading contrast of the asymmetry visible in the experimental data, which is encoded on the moduli of the expansion coefficients of the final state wave function (not being investigated here), the semi-classical approach using the WKB approximation yields excellent agreement with the experimental observations.

4.3.4 Brief Section Summary

An electron localization effect in the single-photon induced dissociative ionization of molecular hydrogen has been observed and explained in terms of two interfering dissociation pathways which entangles the bound electron and the photoelectron. Using a semi-classical model it has been possible to simulate the oscillation structure with a high degree of accuracy yielding insight in the mechanism leading to the molecular frame electron ejection asymmetry. This asymmetry can be interpreted as a localization of the bound electron with respect the the ejected electron. Though not presented in detail here, a fully quantum mechanical study has been carried out by A. Palacios, A. González-Castrillo and F. Martín (see Fig. 4.17), which confirms

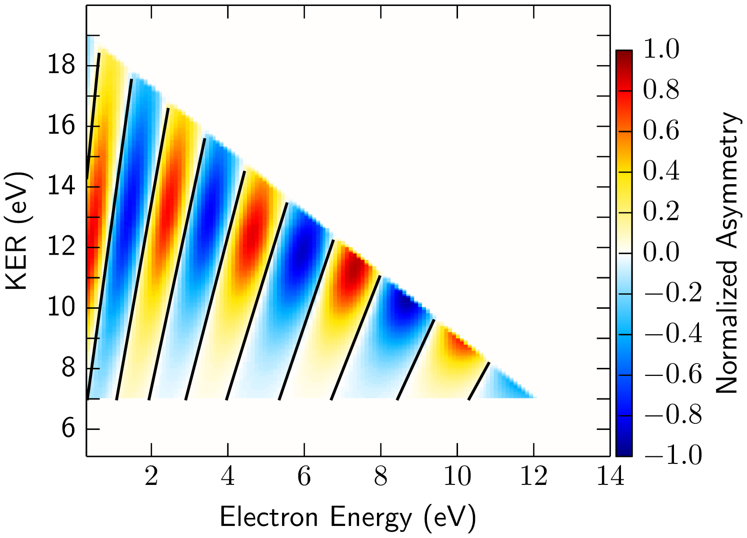

Figure 4.17: Fully quantum mechanical model. The result is in excellent agreement with the experimental data, even featuring the fading contrast of the osculation's amplitude. The black lines show regions of symmetric electron-proton ejection obtained by the semi-classical simulation.

the analysis presented above. The methodology of the full quantum calculation is, among others, found in Ref. [23]. In addition to reproducing the period of the oscillation, the fully quantum mechanical simulation has access to the moduli of the expansion coefficients of the final state wave function, which enables the simulation to compute the amplitudes of the asymmetry. The theoretical calculation features a similar fading contrast of the asymmetry amplitude as observed in the experiment.

4.4 Measurement of the Lifetime of the Energetically Lowest Doubly-Excited $Q_1\ \Sigma_u^+$ State in the Hydrogen Molecule

In this section a method is introduced to retrieve the autoionization lifetime of the energetically lowest doubly-excited state (DES) with Σ_u^+ symmetry in dependence of the internuclear distance R. For this purpose, we device the measured asymmetry presented above in combination with a semi-classical model. It is shown that the two contributions, autoionization and direct ionization, to the measured total counts can be separated, by exploiting the KER and electron-energy dependent asymmetry signal. Based on a mapping of the electron kinetic energy to the corresponding internuclear separation R these separated signals are in turn used to derive the autoionization lifetime of the DES that ranges from $400\,\mathrm{as} = 400 \cdot 10^{-18}\,\mathrm{s}$ to $1\,\mathrm{fs}$ depending on the internuclear separation.

4.4.1 Experimental Data

The experimental data analyzed in this section is the same as presented in the previous section, where the interference of two dissociation pathways lead to a localization effect of the electrons. However, due to reasons that become obvious later on in the discussion, it is helpful to change the representation of the data set. Instead of the energy correlation diagram presented above featuring the total counts as a function of the KER and the electron energy, this section makes use of a diagram correlating the electron energy to the XUV-photon energy, see Fig. 4.18 (a). In contrast to the previously shown diagonal lines, the photon energy signature of the attosecond pulse trains are now vertical lines.

As in the previous section we plot the asymmetry parameter instead of the counts into the energy correlation diagram. Figure 4.18 shows an overview of the measured data: (a) features the count distribution, (b) the asymmetry parameter, (c) shows a section through the count distribution for a photon energy of $E_\gamma = 35.7\,\mathrm{eV}$ and (d) shows the corresponding asymmetry section for a photon energy of $E_\gamma = 35.7\,\mathrm{eV}$.

In the previous section it was demonstrated that the final state wave function,

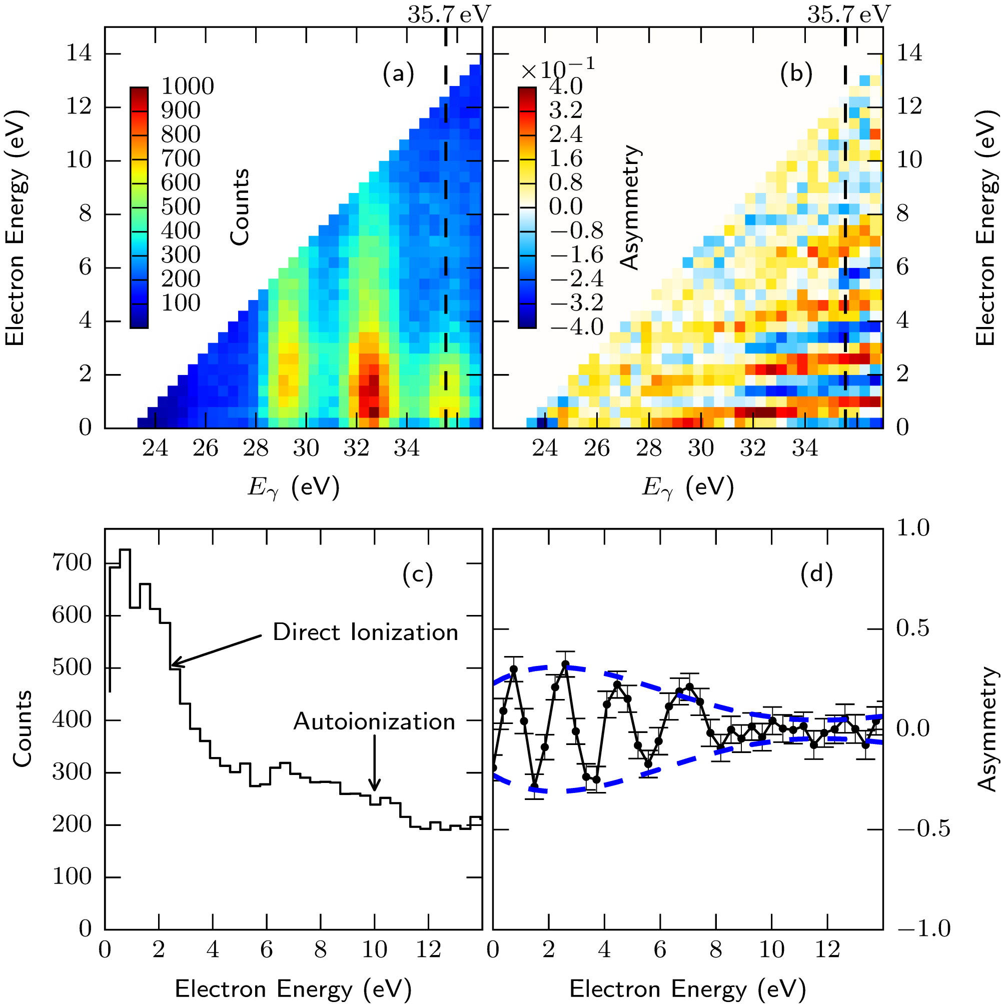

Figure 4.18: (a) Count distribution as a function of the photon energy E_γ and the photoelectron energy E_e. (b) Electron ejection asymmetry as a function of E_γ and E_e. (c) Section through the count distribution shown in (a) at a photon energy of $E_\gamma = (35.7 \pm 0.6)\,\mathrm{eV}$. (d) Corresponding section through of the measured asymmetry data. The blue dashed line is the envelope of the asymmetry amplitude obtained by Fourier analysis.

leading to the count distribution shown in Fig. 4.18 (a), can be written as

$$|\Psi_{\text{fin}}\rangle = c_I|A\,^2\Sigma_u^+\rangle|\sigma_g^+\rangle + c_A|X\,^2\Sigma_g^+\rangle|\sigma_u^+\rangle, \tag{4.58}$$

where the coefficients c_I and c_A stand for the two contributing dissociative ionization channels: (I) the direct ionization to the $H_2^+(A\,^2\Sigma_u^+)$ state and (II) the dissociating and autoionizing pathway involving the energetically lowest doubly-excited $H_2(Q_1\,^1\Sigma_u^+(1))$ state, respectively (see Fig. 4.15). The latter is an approximation, as the doubly-excited Q_1 states with Σ_u^+ symmetry exist as a series of many states [11, 109]. However, for the energy range considered in this thesis, the energetically lowest dipole-allowed[27] DES is predominantly populated [19]. Aiding the argument is the fact that the energetically higher DES decay more slowly [11], further decreasing their importance in the contribution to the ionization process as they mainly dissociate neutrally (and cannot be detected). For this reason, the above made assumption that the energetically lowest DES of Σ_u^+ symmetry contributes most significantly to the observed data is well justified.

4.4.2 Lifetime Extraction

In order to extract the lifetime of the energetically lowest doubly-excited $Q_1\,^1\Sigma_u^+(1)$ state we first have to separate the measured count distribution into the two contributing channels. It is of course not possible to assign each observed event to a channel, as both lead to the same final momenta and are thus individually indistinguishable. However, it is possible to give a statistical distribution corresponding to the two dissociative ionization channels. Once the count distribution N_A stemming from the autoionization is known (as a function of the photoelectron energy), a semi-classical mapping of the photoelectron energy to an internuclear separation R is performed. With the distribution given as a function of R it is then possible to extract the autoionization width $\Gamma(R) = {}^1/_{\tau(R)}$ from it, which is inversely proportional to the autoionization lifetime τ.

The following derivation is split into four sections. (I) The mathematical framework to separate the count rates of the individual dissociation channels. (II) The application to the experimental data and presentation of the resulting count distributions connected with each channel. (III) The mathematical framework to use the separated count distribution in order to obtain the autoionization lifetime. (IV) Finally, we show the experimental results for the R-dependent autoionization lifetime.

(I) Mathematical Framework to Separate the Interfering Dissociation Channels

Giving a brief overview, we first derive the relative probability ${}^{|c_A|^2}/_{|c_I|^2}$ of dissociating along the two pathways (I) and (II) defined in the sub-section above. With this and

---

[27] Dipole selection rules dictate a resonant transition to a Σ_u^+ state for the case of parallel transitions.

with the relation

$$N(E_\gamma, E_e) = |c_A(E_\gamma, E_e)|^2 + |c_I(E_\gamma, E_e)|^2 = N_A + N_I \tag{4.59}$$

we are able to solve the equations for the two count distributions N_A and N_I

$$\begin{aligned} N_A(E_\gamma, E_e) &= |c_A(E_\gamma, E_e)|^2 \\ N_I(E_\gamma, E_e) &= |c_I(E_\gamma, E_e)|^2. \end{aligned} \tag{4.60}$$

$N_A(E_\gamma, E_e)$ is very closely connected to the decay width $\Gamma(R)$, because when the doubly-excited state autoionizes an electron with an internuclear distance R dependent energy is emitted. Here, this emission is used to map $N(E_\gamma, E_e)$ onto $N_A(E_\gamma, R)$, which is the autoionization rate as a function of the internuclear distance. In decay processes the rate is always a measure of the decay probability, which we are therefore able to determine.

We start from the asymmetry parameter A derived in Sec. 4.3

$$A = -\frac{2\Re[c_I c_A^*]}{|c_I|^2 + |c_A|^2}, \tag{4.61}$$

which is used to first derive an expression for the relative population probability of the two channels $|c_A|^2/|c_I|^2$. For this it is essential to further decompose the expansion coefficients of the final state wave function (c_I and c_A). Recalling the KER and E_e dependent transition amplitudes

$$c_I = \underbrace{-\langle ^2\Sigma_u^+|\langle \psi_{e^-}|\mathcal{E}z|^1\Sigma_g^+\rangle}_{Ie^{i\phi_I}} \tag{4.62}$$

and

$$c_A = \underbrace{\langle X\,^2\Sigma_g^+|\,\langle \psi_{e^-}|^1/|r_1-r_2||Q_1\,^1\Sigma_u^+\rangle}_{De^{i\phi_1}}\underbrace{\langle Q_1\,^1\Sigma_u^+| - \mathcal{E}z|X\,^1\Sigma_g^+\rangle}_{Ee^{i\phi_2}}, \tag{4.63}$$

in which c_A is written as a product of two transition amplitudes, we write the decompositions of the amplitudes c_I and c_A, with $\phi_1 + \phi_2 = \phi_A$, as

$$\begin{aligned} c_I &= I(E_\gamma, E_e)e^{i\phi_I} \\ c_A &= E(E_\gamma)D(E_\gamma, E_e)e^{i\phi_A}, \end{aligned} \tag{4.64}$$

where I, E and D are the moduli of the transition amplitudes for the excitation to $H_2(Q_1\,^1\Sigma_u^+(1))$ Ⓐ, the subsequent autoionization Ⓑ, and the direct ionization Ⓒ (illustrated in Fig. 4.19). The phases ϕ_I and ϕ_A, as in the previous section, consist of a part corresponding to the nuclear motion (labeled ① + ② for ϕ_A and ③ for ϕ_I) as well as another part acquired during the electronic transitions. The magnitudes

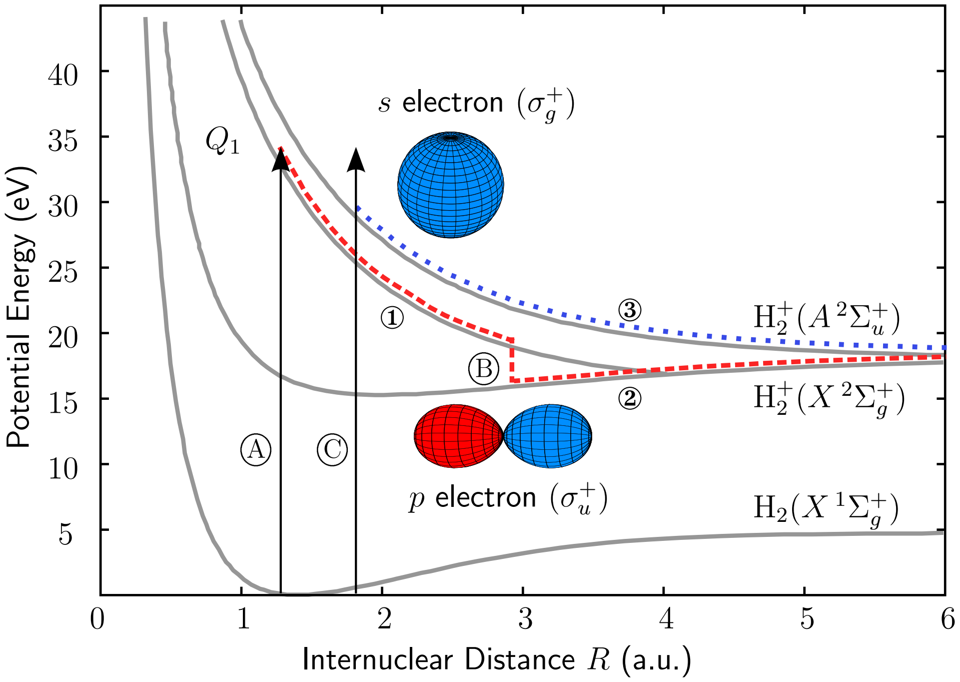

Figure 4.19: Relevant potential energy curves for the H_2 and H_2^+ states. The electronic transitions involved in the dissociative ionization process are indicated by encircled letters, while the nuclear dynamics, leading to the nuclear phases, is labeled by encircled numbers. The two dissociation pathways, namely the autoionization and the direct ionization channel, are indicated by a red dashed and a blue dotted line, respectively. Figure adapted from Ref. [132] using the data for the potential energy curves given by Ref. [21].

I, E and D can therefore be connected to the individual transitions involved in the processes

$$\begin{aligned} I &= \left| -\langle A\,^2\Sigma_u^+ | \langle \psi_{e^-} | \mathcal{E} z | X\,^1\Sigma_g^+ \rangle \right| \\ E &= \left| -\langle Q_1\,^1\Sigma_u^+ | \mathcal{E} z | X\,^1\Sigma_g^+ \rangle \right| \\ D &= \left| \left\langle X\,^2\Sigma_g^+ \right| \langle \psi_{e^-} | {}^{1}\!/\!_{|r_1 - r_2|} | Q_1\,^1\Sigma_u^+ \rangle \right| . \end{aligned} \tag{4.65}$$

Inserting Eq. (4.64) into Eq. (4.61) yields for the asymmetry

$$A = -\frac{2\,EDI}{(ED)^2 + I^2} \Re \left[e^{i\Delta\varphi_N + i\Delta\xi_E} \right] , \tag{4.66}$$

where $\Delta\varphi_N = \varphi_I - \varphi_A$ is the nuclear phase difference and $\Delta\xi_E = \xi_I - \xi_A$ the electronic phase difference (this is the same definition as in Sec. 4.3). It was shown that the best agreement to the experimental data was obtained, if the electronic transition phases were set to $\Delta\xi_E = \pi$ with which we simplify Eq. (4.66) to

$$A = \tilde{A}\cos(\Delta\varphi_N), \tag{4.67}$$

with

$$\tilde{A} = \frac{2\,EDI}{(ED)^2 + I^2}. \tag{4.68}$$

In this equation, $\tilde{A}$ represents the modulation amplitude of the asymmetry oscillation and, hence, the oscillation envelope [see Fig. 4.18 (c) dashed blue line]. Rearrangement of Eq. (4.68) leads to

$$\frac{(ED)^2}{I^2}\tilde{A} + \tilde{A} - 2\frac{ED}{I} = 0 \tag{4.69}$$

which is a quadratic equation in $^{ED}/_{I} =: \alpha(E_e)$. Therefore, the solutions to it are given by

$$\boxed{\alpha(E_e) = \frac{1}{\tilde{A}} \pm \sqrt{\frac{1}{\tilde{A}^2} - 1}} \tag{4.70}$$

which, after being squared, describe the relative probability of dissociating via the direct ionization channel and the autoionizing channel.

The second step in this derivation is to use this result together with Eq. (4.59) to obtain separated count distributions for the two interfering reaction pathways. For this we rewrite Eq. (4.59) using the definitions of c_I and c_A as

$$N(E_\gamma, E_e) = |c_A(E_\gamma, E_e)|^2 + |c_I(E_\gamma, E_e)|^2 = ED^2 + I^2 = N_A + N_I \tag{4.71}$$

From the definition of $\alpha^2 = {}^{(ED)^2}/_{I^2} = {}^{N_A}/_{N_I}$ and Eq. (4.70) together with Eq. (4.71) relations for the count distributions of the two channels directly follow

$$\begin{aligned} \alpha^2 N_I + N_I &= N \Longrightarrow \boxed{N_I(E_\gamma, E_e) = \frac{N(E_\gamma, E_e)}{1 + \alpha^2(E_\gamma, E_e)}} \\ \alpha^{-2} N_A + N_A &= N \Longrightarrow \boxed{N_A(E_\gamma, E_e) = \frac{N(E_\gamma, E_e)}{1 + \alpha^{-2}(E_\gamma, E_e)}} \end{aligned} \tag{4.72}$$

These describe the separated count rates N_I and N_A corresponding to the two dissociative ionization channels. Because the total count rate N is known from experiment [see Fig. 4.18 (a)] and α can be obtained by evaluation of the measured asymmetry amplitude $\tilde{A}$ [Eq. (4.70)], the two separated count distributions become directly accessible.

(II) Experimental Separation of Dissociation Channels

Before continuing in the derivation of an expression for the lifetime of the DES, it is instructive to apply the results presented above to the experimental data. By this it is possible to plot the count distribution of the two separated channels individually. However, before doing so, some physical interpretations of the experimental data are necessary.

We shall attempt to separate the count distributions N_I and N_A at a photon energy of $E_\gamma = 35.7\,\mathrm{eV}$. The advantages arising from this choice are discussed in the following. First, at this high photon-energy we obtain good count statistics over a large range of photoelectron energies E_e. Choosing a fixed photon energy simplifies the transition amplitude of the autoionizing channel to

$$c_A = E(E_\gamma = const)D(E_\gamma = const, E_e)e^{i\phi_A} = const' \cdot D(E_e), \tag{4.73}$$

as E becomes a constant. This has the direct consequence that N_A becomes solely dependent on the decay amplitude D which is intimately connected to the decay width Γ of the DES. In addition, we know that at this energy both dissociative ionization channels (as a reminder see Fig. 4.19) significantly contribute to the total count rate, which causes a large asymmetry signal. However, as discussed above the direct ionization channel predominantly produces low-energetic photoelectrons (caused by the vanishing Franck-Condon overlap for transitions yielding high photoelectron energies; review Fig. 4.6 and enclosing paragraphs for details), whereas the autoionization channel in principle results in all photoelectron energies compatible with energy conservation, see Eq. (4.28) and enclosing paragraph. With this, we are able to assign the dominant peak shown in Fig. 4.18 (c) at low photoelectron energies to the direct ionization channel and the flat shoulder in Fig. 4.18 (c) to the autoionization channel. Knowing that due to the Gaussian shape of the ground state vibrational wave function, the direct ionization channel needs to fall off very quickly (vanishing Franck-Condon overlap) as a function of photoelectron energy, it is clear that for some photoelectron energy the two continuous distributions have to intersect with each other (it later turns out to be $E_e \approx 2\,\mathrm{eV}$). The exact photoelectron energy where both channels contribute equally (point of intersection) is not important for the following discussion. Only the fact that such a photoelectron energy exists, which is supported by literature [15, 19, 133]. Mathematically, this means that there exists a E_e for which the following relation holds

$$N_I = N_A \Leftrightarrow (ED)^2 = I^2. \tag{4.74}$$

Inserting Eq. (4.74) into Eq. (4.68), which describes the asymmetry envelope we find for equal amplitudes $\tilde{A} = 1$ which means that the measured asymmetry amplitude should oscillate in the region of $E_e \approx 2\,\mathrm{eV}$ between -1 and 1. Experimentally, however, we find a much smaller amplitude [see Fig. 4.18 (d)] which we mainly ascribe

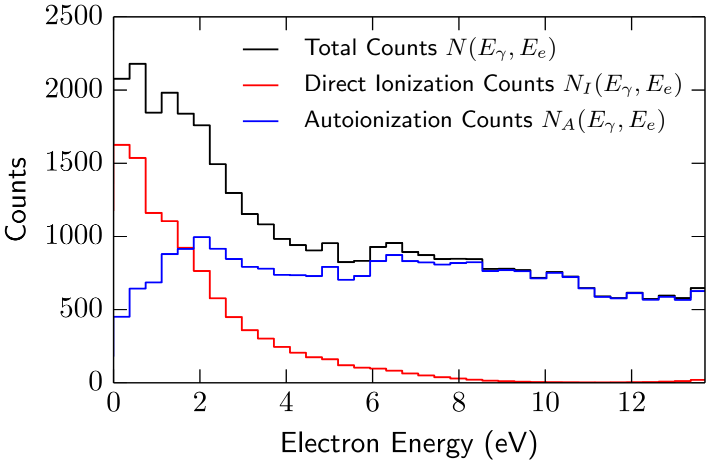

Figure 4.20: Separation of the measured total count rate (black). The count rate corresponding to the direct ionization channel (red) is rapidly decreasing with increasing photoelectron energy. The autoionization pathway yields a rather flat distribution (blue) for all photoelectron energies. The assumption that the two channels contribute equally at a photoelectron energy of approximately 2 eV is confirmed.

to false coincidences caused by the detection of uncorrelated electrons stemming mainly from the non-dissociative ionization of H$_2$.

Therefore, in order to use the above derived formalism, which led to Eqs. (4.72), the obtained asymmetry signal has to be rescaled such that the measured value of $\tilde{A}$ equals one. Using the rescaled asymmetry signal and Eqs. (4.72), we show the separated count distribution of the two dissociative ionization channels in Fig. 4.20. As predicted, we find that the direct ionization quickly decreases for increasing photoelectron energy, whereas the autoionization channel remains fairly constant over the entire range of photoelectron energies.

As mentioned above, the shape of the count distribution N_A is given by the decay amplitude D. Thus, N_A is intimately connected to the decay width $\Gamma = {}^1\!/\!_\tau$ which we intent to obtain in the following. It is common to seek an internuclear distance R dependent lifetime of the DES, which means that we have to perform a mapping from photoelectron E_e energy to R. In order to achieve this, we exploit the fact that E_e is classically given by the separation of the potential energy curves of the DES and the ionic ground state, given at the R_A at which the autoionization occurs. Therefore, for the mapping we use the relation

$$E_e(R_A) = V_{Q_1}(R_A) - V_{\Sigma_g^+}(R_A), \tag{4.75}$$

which is a strictly decreasing monotone function. In this, $V_{Q_1}(R)$ describes the potential energy curve of the DES and $V_{\Sigma_g^+}(R)$ the potential energy curve of the ionic ground state. Therefore, this allows to assign an unique R to each measured photoelectron energy E_e.

(III) Derivation of Lifetime of the Doubly-Excited State

Discussing points (I) and (II) it was found that the count distribution N_A corresponding to the autoionization channel is closely connected to the decay amplitude D [see Eq. (4.64)] and with this to the decay width $\Gamma = {}^1\!/\!_\tau$. In (III) we intend to derive the autoionization lifetime from $N_A(R)$. Unlike in atoms where a decay width of an electronic state is a constant in time, in molecules the autoionization rate, and hence the decay width Γ, strongly depends on the internuclear separation. As a consequence of the dissociation, the time the system stays in each volume element dR is a function of the nuclear velocity $dt = dR/v$, which further complicates the extraction of the lifetime and even makes models to describe the velocity necessary. It has been shown and intensively used in previous works, (e.g. [9, 134, 135]) that the autoionization probability in molecular systems can be described by

$$\frac{N_A(R)}{N_0} = H(R)\exp\left[-\int\limits_{R_0}^{R} H(R')dR'\right], \tag{4.76}$$

with N_0 being the total number of molecules being populated in the energetically lowest doubly-excited $H_2(Q_1\,{}^2\Sigma_u^+(1))$ state. In this equation, the decay width is contained in the variable H which is defined by

$$H(R) = \frac{\Gamma(R)}{v(R)} \tag{4.77}$$

where $R_0 = R(E_e^{\max})$ in which $E_e^{\max}$ is the maximum measured photoelectron energy. Further, v describes the semi-classical velocity of the nuclei given by

$$v(R) = \sqrt{\frac{2[E_\gamma - V_{Q_1}(R)]}{\mu}}, \tag{4.78}$$

where $\mu = m_p/2$ is the reduced mass of the system (half the proton mass). Equation (4.76) is to be solved for H, essentially yielding the decay width. The result reads[28]

$$H(R) = \frac{\Gamma(R)}{v(R)} = \frac{N_A(R)}{N_0 - \int_{R_0}^{R} N_A(R')dR'}, \tag{4.79}$$

---

[28] Solving Eq. (4.76) for H is tedious and lengthy, yielding little physical insight. For this reason, only the result is given here.

which after rearranging yields the final result

$$\boxed{\Gamma(R) = \frac{N_A(R)v(R)}{N_0 - \int_{R_0}^{R} N_A(R')dR'}} \tag{4.80}$$

The decay width derived here is dominated by the autoionization, as competing processes, such as fluorescent de-excitation, occur on much slower timescales for which they do not significantly contribute [9]. In addition, because the doubly-exited $H_2(Q_1\,^2\Sigma_u^+(1))$ state is so short-lived that almost all molecules autoionize before they reach the point of neutral dissociation at $R_d = 4.0\,\text{a.u.}$. Reference [128] recommends for the percentage of neutrally dissociating molecules the value $\chi_d = 4\%$. With this information, the up-to-this-point unknown value of N_0 is readily calculated by evaluating the integral

$$\boxed{N_0 = \frac{\int_{R_0}^{R_d} N_A(R')dR'}{1 - \chi_d}} \tag{4.81}$$

This result concludes the framework needed to evaluate the experimentally obtained data in order to determine the lifetime of the doubly-excited $H_2(Q_1\,^2\Sigma_u^+(1))$ state as shown in (IV).

(IV) Experimental Results for the Lifetime of the Doubly-Excited $H_2(Q_1\,^2\Sigma_u^+(1))$ State

The equations derived in (III) are now used to compute the lifetime of the doubly-excited $H_2(Q_1\,^2\Sigma_u^+(1))$ state. We have previously established the count distribution N_A (see Fig. 4.20) and have shown that this and the classical velocity are the only input needed to compute the decay width by using Eq. (4.80). With this, the lifetime is known via the relation $\tau(R) = {}^1\!/\!{}_{\Gamma(R)}$. Plotting the experimental result we obtain Fig. 4.21 where the measured data is indicated by black dots. The determined decay width ranges from $\approx 0.4\,\text{eV}$ to $\approx 1.5\,\text{eV}$ which corresponds to a lifetimes of only 400 as to 1 fs. Thus, the autoionization takes place on a very fast timescale.

In order to provide an estimation for the error to the measurement it should be noted that the obtained lifetime depends critically on the fraction of neutrally dissociating molecules χ_d. As in literature these values vary drastically (up to $\chi_d = 8\%$) we have chosen the values $\chi = 0\%$ and $\chi = 8\%$ to obtain the edges of the gray shaded area in Fig. 4.21. This area is then identified as the error to the measurement. Apparently, for large internuclear distances the error becomes very large. The reason for this is easily explained by considering Eq. (4.80). With increasing R the number of autoionized molecules $\int N_A dR'$ grows and rapidly approaches N_0. Because the difference appears as the denominator in Eq. (4.80), the denominator becomes very

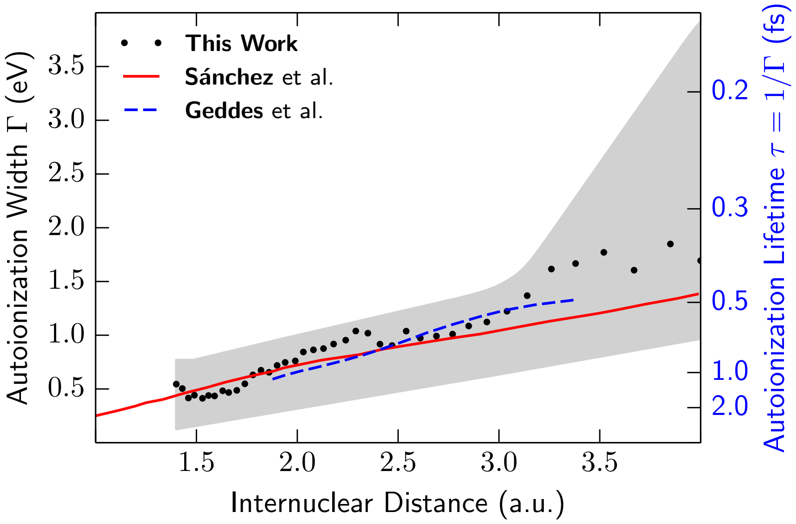

Figure 4.21: Lifetime of the doubly-excited $H_2(Q_1\,{}^2\Sigma_u^+(1))$ state. The black dots represent the here measured data, where the gray shaded area indicates the estimated error of the measurement. It is in very good agreement with quantum mechanical calculations performed by I. Sánchez and F. Martín [11] (red line). It also compares very well with experiments previously conducted by J. Geddes et al. [108] (blue dashes). In contrast to these experiments, here the lifetime for a much larger range of internuclear distances could be obtained. Due to the mixing of the two dissociation channels, it was prior to this measurement where the interference is considered, even in principle, impossible to determine the lifetime of the DES for small R.

small. Therefore, relative errors tend to become large and the result less accurate.

In comparison, a very good agreement to the quantum mechanical calculation performed by I. Sánchez and F. Martín [11] (red line) is obtained. The agreement is for small internuclear separations R better than for large R. This is likely due to the larger error in this region as explained above.

Also, a very good agreement to the experiment previously conducted by J. Geddes, F. K. Dunn, N. Kouchi, A. M. McDonald, and V. Srigengan [108] is achieved (blue dashes). In this experiment, however, it was not possible for small R to obtain data for the lifetime. This is due to the state mixing at low photoelectron energies which cannot, without using the interference signal of the two states, be separated. For this reason, the previously conducted experiments were restricted to photon energies that cannot ionize directly via the $H_2^+(A\,{}^2\Sigma_u^+)$ state. This means that photon energies well below 33 eV had to be employed. This in turn further imposes limits onto the experiment, because the excitation to the $H_2(Q_1\,{}^2\Sigma_u^+(1))$ state can no longer be driven for small R, where the energy separation of the neutral ground state and the DES is larger than the photon energy supplied. This experiment allows for the first time to access the regions of small and large R and, therefore, extract the lifetime of the $H_2^+(A\,{}^2\Sigma_u^+)$ state for a very large range of internuclear distances.

Further, in previously conducted experimental evaluations [14, 108] it was necessary to compare isotopes of the species in order to retrieve the autoionization time. In contrast, this section presented a method where only one species is needed to accomplish the same task.

4.4.3 Brief Section Summary

In this section it was shown that using the measured count distribution together with the corresponding asymmetry it is possible to isolate the count distribution for different dissociative ionization channels. The distribution connected to the autoionizing pathway is closely related to the autoionization width Γ which is proportional to the inverse of the autoionization lifetime. In order to retrieve the lifetime a semi-classical model was employed to describe the nuclear velocity which is essentially needed.

The results of the measurement were compared to a previously conducted experiment [108] and a very good agreement was found. Further, this experiment overcomes fundamental limitations of previously conducted experiments, as e.g. photon energies greater than $\approx 28\,\mathrm{eV}$ can be used in which in addition to the autoionizing channel the direct ionization to the $H_2^+(A\,^2\Sigma_u^+)$ state is populated. This was formerly impossible as the direct ionization could not be separated from the autoionization (no asymmetry signal measured[29]). With higher photon-energies it is possible to observe the autoionization lifetime for a larger range of internuclear distances.

In order to compare the results at internuclear distances previously inaccessible by experiment, we related the observation to a theoretical study [11], for which very good agreement was obtained.

---

[29] In oder to measure the asymmetry a kinematically complete experiment is required, as the molecular frame has to be created for each individual event.

5 XUV-Pump IR-Probe Investigation of Molecular Wave-Packet Dynamics on Laser-Induced Transition States of H_2^+

Some of the aspects discussed in this chapter will be published in the following paper:

Molecular wave-packet dynamics on laser-controlled transition states
A. Fischer, M. Gärttner, P. Cörlin, A. Sperl, M. Schönwald, T. Mizuno, G. Sansone, A. Senftleben, J. Ullrich, B. Feuerstein, T. Pfeifer, and R. Moshammer
Submitted
arXiv:1410.8032 [physics] (2014)

With the advances of femtosecond laser technology in the optical domain, allowing the creation of ultra-short pulses, pump–probe experiments have become a widespread scheme for imaging the ultra-fast quantum dynamics [5] of atomic (e.g. [136]) and molecular systems (e.g [137]). The idea behind this kind of experiments is to observe the ultra-fast dynamics of nuclear(e.g. [25, 29, 31, 138]) and/or electronic (e.g. [139–141]) systems, by launching the motion with a pump-pulse and after a time delay τ use a probe-pulse to query the systems current time-dependent state. Fig. 5.1 shows an illustration of a possible pump–probe[1] scheme for the case of molecular hydrogen[2]. Focusing on the nuclear dynamics of molecules, a common scheme is to launch a vibrational wave packet by photoionizing the molecule with a short laser pulse and to probe the vibrational dynamics by applying a second, time-delayed pulse leading to dissociation [142–147].

However, the long sought ultimate goal is not only to observe and image system dynamics, but to control and manipulate chemical reactions by intense laser fields which alter the process such that a specific final state is reached [148]. Among those reactions, the photodissociation as an important representative is investigated here, for which it is essential to understand the dissociation dynamics in detail. This understanding can consequently be used to tailor laser pulses to favor a specific outcome of the chemical reaction.

---

[1] In this work, the probe pulse is also referred to as coupling pulse as it couples two electronic states of the molecular ion.

[2] It should be emphasized that alternative schemes exist, where the molecule is not dissociated via a dissociative state. In example, it could instead further be ionized inducing a Coulomb-explosion.

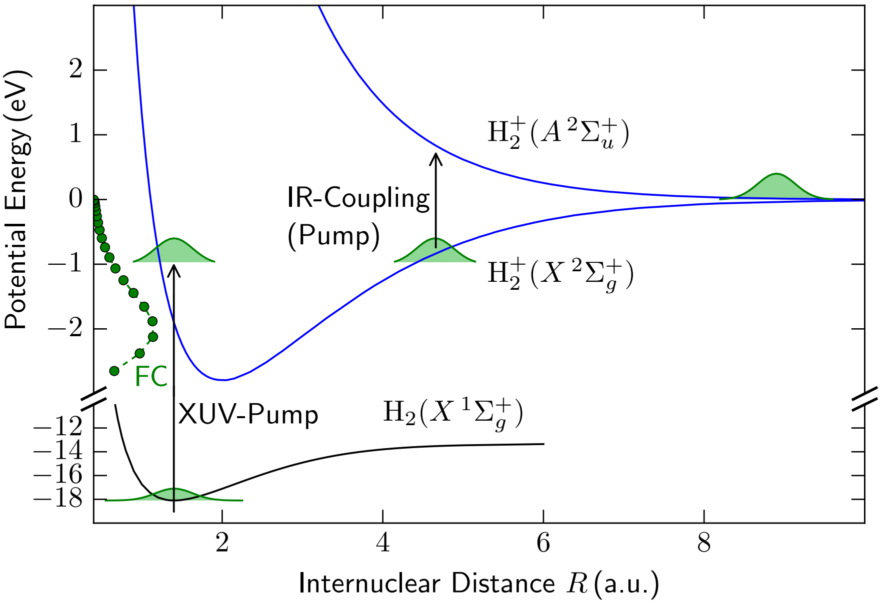

Figure 5.1: Illustration of the pump–probe principle for the case of molecular hydrogen. In a first step, the pump-pulse (here an XUV pulse) vertically promotes the nuclear wave function to the bound $H_2^+(X\,^2\Sigma_g^+)$ electronic state. The wave packet propagates to larger internuclear distances R, where it is transfered by a second laser pulse (here an IR-pulse) to the dissociating $H_2^+(A\,^2\Sigma_u^+)$ state. The dissociation of the molecule allows the detection of protons. The green distribution on the left side of the picture (labeled FC) depicts the Franck-Condon population of the 19 bound vibrational states of the molecular hydrogen ion.

However, it remains challenging to use intramolecular state coupling for a targeted manipulation of photochemical reactions. The challenge is mostly caused by the complexity of molecular systems, arising due to the fact that in quantum-control schemes not only many vibrational (and possibly rotational) states, but also electronic transitions are involved. To understand the fundamental mechanisms used to control quantum mechanical systems, it is therefore important to simplify either the entire system or the description of it.

To this end, we employ an analysis method to the case of H_2^+ with which we can reduce the number of contributing vibrational states to only two, which is the smallest number of states that still exhibit a quantum-mechanical time-dependency (motion). By employing laser-intensities chosen such that only two electronic states are coupled, the system investigated here represents the simplest case imaginable in the field of quantum-control. By comparing the obtained experimental data to quantum-dynamical simulations (based on the time-dependent Schrödinger equation) and to semi-classical simulations, we are able to identify one of the fundamental mechanisms allowing the control of photochemical reactions on laser induced transition states.

Outline

Throughout this chapter, the following process is considered:

$$\mathrm{H}_2(X\,{}^1\Sigma_g^+) \xrightarrow{\mathrm{XUV}} \mathrm{H}_2^+(X\,{}^2\Sigma_g^+) + e^- \xrightarrow{\mathrm{IR}(\tau)} \mathrm{H} + \mathrm{H}^+ + e^-. \tag{5.1}$$

For this, an attosecond pulse train ionizes a hydrogen molecule. This ionization triggers the nuclear dynamics in the H_2^+ molecule, which is then dissociated using an infrared pulse, coupling the wave function to a dissociative electronic state. For high coupling laser intensities a regime is entered in which the action of the coupling laser pulse can no longer be treated with a perturbation approach. For classical pump–probe experiments this is unwanted, as the dynamics of the unperturbed system is at the focus of the investigation. In contrast, laser-control schemes exploit this feature and use the time-dependency of the PES to control the dynamics and kinematics of photochemical processes. Even though the latter is of main interest for this work, the words probe- and control-pulse are used synonymously, as they both essentially describe the second laser pulse used for different purposes.

For the interpretation of the measured data extensive quantum mechanical computations to solve the time-dependent Schrödinger equation (TDSE) were carried out as a part of this work. In addition, using a picture of laser-field dressed states (Floquet picture) it is possible to describe the observations in a semi-classical model. In this the field dressing of the electronic states is treated quantum mechanically, while the nuclear motion is described by a classical motion in a time-dependent potential. The underlying theory to perform such calculations is discussed in Sec. 5.1. Following this the experimental results and their interpretation are presented in Sec. 5.2.

5.1 Theoretical Concepts

This section conveys the physical concepts needed to properly describe the process involved in this two-pulse experiment. First, the origin of the time-dependent dynamics of the nuclei, caused by the superposition of multiple nuclear eigenstates, is explained in Sec. 5.1.1. Thereafter, in Sec. 5.1.2, concepts for solving the time-dependent Schrödinger equation (TDSE) are presented. We intend to rewrite the Schrödinger equation in terms of the time-evolution operator which can be efficiently solved with numerical tools. Subsequently, such a numerical method, the well-known split step algorithm, for solving the TDSE is presented. Then, the introduction of field-dressed potential energy surfaces (Floquet states) in Sec. 5.1.4 paves the way for investigating the nuclear dissociation dynamics in a semi-classical way, which then enables the interpretation of the measurement (as presented in Sec. 5.2) in a very intuitive way.

5.1.1 Time Evolution of Nuclear Wave Packets in the Anharmonic $H_2^+(X\,^2\Sigma_g^+)$ Potential

The ionization of molecular hydrogen by an XUV pulse is described via a dipole transition to the $\mathrm{H}_2^+(X\,^2\Sigma_g^+)$ electronic ground state. The ionization leads to the occupation of many vibrational states of the H_2^+ molecule according to the Franck-Condon overlap [122–125] of each of the nuclear eigenstates. The resulting wave function can be written as the direct product (connecting the Hilbert spaces of the nuclear part and the electronic part)

$$\Psi^{\mathrm{tot}}_{\mathrm{H}_2^+}(x,R,t)=\sum_n \phi^n(R,t)\otimes\psi^n_R(r,t), \tag{5.2}$$

where $\psi^n_R(r,t)$ describes the n-th electronic wave function[3] and $\phi^n(R,t)$ the nuclear wave packet in the respective electronic state. In this, the nuclear wave function after ionization has to be written as a superposition of the vibrational eigenstates $|v,t\rangle$ of the PES

$$\phi^n(R,t)=\langle R|\sum_{v=0}^{\infty} a_v^n|v^n,t\rangle=\langle R|\sum_{v=0}^{\infty} a_v^n|v^n\rangle e^{-iE_v^n t}, \tag{5.3}$$

where the coefficient a_v^n is the population amplitude and $\exp(-iE_v^n t)$ the time-dependence.

Due to the anharmonicity of the PES corresponding to the $\mathrm{H}_2^+(X\,^2\Sigma_g^+)$ state, the nuclear wave packet starts to spatially disperse. As the time progresses the different phase accumulation leads to a dephasing of the spatial nuclear wave function. At a later time the wave function rephases again. This process, often called wave packet revival, is shown in Fig. 5.2.

In order to understand the revival structure, it is instructive to expand the eigenenergy distribution of the wave packet in a Taylor series, as shown in e.g. [24,150]. For this, it is assumed that many vibrational states centered around an expansion point v_e contribute and that the energy spacing of these eigenstates is small

$$\frac{|E(v_e)-E(v_e\pm 1)|}{E(v_e)}\ll 1, \tag{5.4}$$

which holds for high quantum numbers v. Therefore the eigenenergies of the states $|v_i\rangle$ can be treated as a continuum and

$$E(v)\approx E(v_\mathrm{e})+\left.\frac{dE(v)}{dv}\right|_{v_e}(v-v_\mathrm{e})+\frac{1}{2}\left.\frac{d^2E(v)}{dv^2}\right|_{v_e}(v-v_\mathrm{e})^2+\mathcal{O}(v^3) \tag{5.5}$$

---

[3] Having applied the Born-Oppenheimer approximation [69,123,124,149], which allows the separation of the electronic problem from the nuclear motion, R becomes parameter for the electronic wave function.

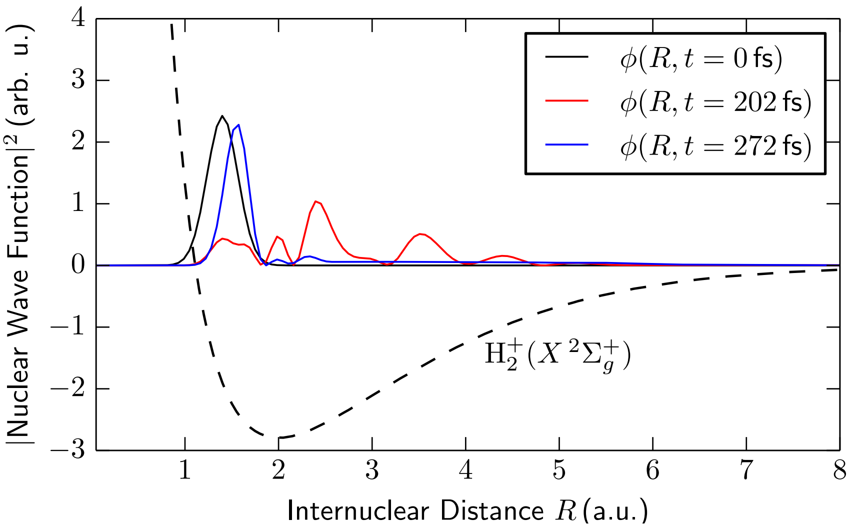

Figure 5.2: Numerical solution of the TDSE describing the nuclear dynamics (for details see Subsec. 5.1.2). The nuclear wave function is shown for thee different times. It is visible that initially the wave packet is well localized in an almost Gaussian distribution. This is due to the fact that the initial wave function is the vertically promoted ground state wave function of the neutral H_2 molecule. At a later time (here 202 fs) the wave packet is dephased. After some more time a half-revival (explanation below) occurs and the wave function is again well localized. The difference in shape from the initial wave function ($t = 0\,\mathrm{fs}$) to the one at $t = 272\,\mathrm{fs}$ appears partly because the initial wave function includes contributions from continuum eigenstates which cause a dissociation and, hence, a decrease of the bound wave function's amplitude and also a shift of the center position in R.

is obtained[4]. Using Eq. (5.5), the time development of each individual eigenstate is written as

$$\begin{aligned} |v,t\rangle &= |v\rangle \cdot \exp\left\{-i\left[E(v_\mathrm{e}) + \left.\frac{dE(v)}{dv}\right|_{v_e}(v - v_\mathrm{e}) + \frac{1}{2}\left.\frac{d^2E(v)}{dv^2}\right|_{v_e}(v - v_\mathrm{e})^2 + \cdots\right]t\right\} \\ &= |v\rangle \cdot \exp\left\{-i\left[E(v_\mathrm{e}) + E'(v_\mathrm{e})(v - v_\mathrm{e}) + \frac{1}{2}E''(v_\mathrm{e})(v - v_\mathrm{e})^2 + \cdots\right]t\right\} \qquad (5.6) \end{aligned}$$

By introducing the relations[5]

$$T_\mathrm{cl} = \frac{2\pi}{|E'(v_\mathrm{e})|} \quad \text{and} \quad T_\mathrm{rev} = \frac{2\pi}{|E''(v_\mathrm{e})|\,/2}, \qquad (5.7)$$

---

[4] Even though the "Big O notation" is used here, the equation only holds approximately since the Taylor series, given the derivatives involved, is only applicable for continuous variables.

[5] For higher derivatives one can define more revival times such as the super-revival time T_super, which is proportional to the inverse of the third derivative of the eigenenergy distribution.

which describe the classical and the revival oscillation times (see e.g. [151–153]) respectively, Eq. (5.6) simplifies to

$$|v,t\rangle = |v\rangle \cdot \exp\left\{-i\left[E(v_\mathrm{e}) + 2\pi(v-v_\mathrm{e})/T_\mathrm{cl} + 2\pi(v-v_\mathrm{e})^2/T_\mathrm{rev} + \cdots\right]t\right\}. \tag{5.8}$$

From Eq. (5.8), knowing that v and v_e are integer, it is clear that a localization of the wave packet appears at times t_i where many summands of the Taylor series become a multiple of 2π (see Fig. 5.2). In other words, the more summands are phase matched, the more localized the wave packet is.

The analytic Morse potential [154], which is used in the following, approximating the bound potential energy curve of the molecular hydrogen ion is given by

$$V_\mathrm{Morse}(R) = D_e\left[\exp(-2a(R-R_e)) - 2\exp(-a(R-R_e))\right], \tag{5.9}$$

with R_e being the equilibrium internuclear distance, a being a parameter that controls the width of the potential and D_e being the depth of the potential. D_e is connected to the dissociation energy D_0 by

$$D_0 = D_e - \frac{\omega_0}{2}, \tag{5.10}$$

where $\omega_0 = E(v=0)$ is the vibrational ground state energy. It can be shown that the exact energy eigenvalues are given by [124, 154]

$$E_\mathrm{Morse}(v) = \omega_0 \cdot \left[\left(v+\frac{1}{2}\right) - \frac{\omega_0}{4D_e}\left(v+\frac{1}{2}\right)^2\right], \tag{5.11}$$

where $\omega_0 = a\sqrt{2D_e/\mu}$ (and μ is the reduced mass).

Inserting Eq. (5.11) into Eq. (5.7) yields for the classical oscillation time T_cl and the revival time T_rev

$$\boxed{T_\mathrm{cl} = \frac{2\pi}{\left|\omega_0\left[1 - 2\frac{\omega_0}{4D_e}\left(v+\frac{1}{2}\right)\right]\right|}} \quad \text{and} \quad \boxed{T_\mathrm{rev} = \frac{2\pi}{\left|-\frac{\omega_0^2}{4D_e}\right|}} \tag{5.12}$$

Higher order revivals cannot appear in the Morse potential, as higher order derivatives vanish. It should further be noted (a proof is given in e.g. Ref. [24]), that for $t = \frac{1}{2}T_\mathrm{rev}$

Table 5.1: Molecular constants for H_2^+.

D_e (a.u.)	D_0 (a.u.)	ω_0 (a.u.)	a (a.u.)	R_e (a.u.)	μ (a.u.)
$1.0240 \cdot 10^{-1}$	$9.7424 \cdot 10^{-2}$	$9.9739 \cdot 10^{-3}$	$6.5222 \cdot 10^{-1}$	1.9880	918.5762

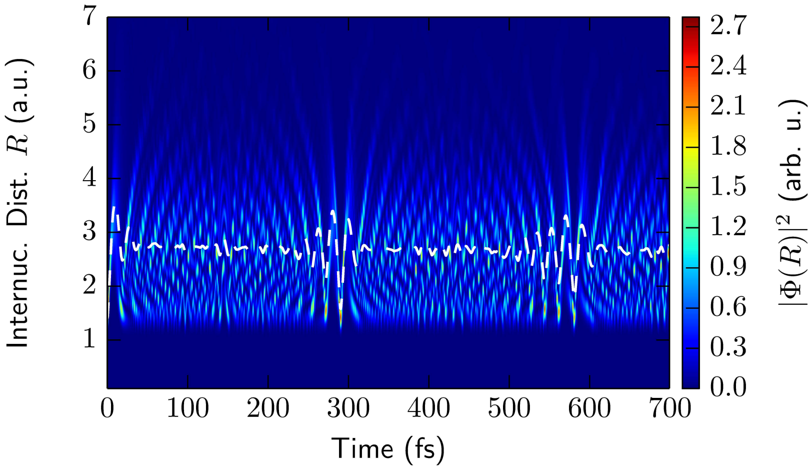

Figure 5.3: Quantum Simulation of the wave packet motion in the bound $H_2^+(X\,^2\Sigma_g^+)$ state. The probability density as a function of the internuclear distance R and the time is shown. The white line shows the expectation value of R as a function of time. The quantum mechanical calculated revivals, where the wave packet is well localized, compares fairly well to the ones obtained by using Morse's potential together with the here presented approximation.

a half-revival occurs, in which the even eigenfunctions $|2v\rangle$ are π out of phase with the odd ones $|2v+1\rangle$. For the half-revival the wave packet is again well localized, but is approximately $\omega_0 T_{\text{cl}}/2$ out of phase[6]. From Ref. [125] the following molecular constants in atomic units can be derived (shown in Tab. 5.1).

To give a physical meaning to the above derived equations for the revival time Trev we compare the results to a later explained quantum calculation. When inserting the variables given in Tab. 5.1 into Eq. 5.12 we obtain $T_{\text{rev}}/2 = 312\,\text{fs}$. This result is fairly close to the one obtained by the quantum simulation (see Fig. 5.3). In next section (Sec. 5.1.2) the fundamentals needed to perform such a quantum calculation are conveyed.

5.1.2 Solving the Time-Dependent Schrödinger Equation

The time-dependent Schrödinger equation (TDSE) [155–158] is a partial (parabolic) differential equation, which governs the non-relativistic quantum world. Even though it is of strikingly simple form

$$\boxed{i\frac{\mathrm{d}\Psi(r,t)}{\mathrm{d}t} = H(r,t)\Psi(r,t)} \tag{5.13}$$

---

[6] In reality this only holds if the ratio of $T_{\text{rev}}/T_{\text{cl}}$ is an integer. If this is not fulfilled it is still a good approximation as long $T_{\text{cl}} \ll T_{\text{rev}}$.

solving this equation analytically is only possible for very few problems, e.g. the hydrogen atom and the molecular hydrogen ion (but only if using the Born-Oppenheimer approximation). Therefore, approximations and numerical methods are often employed when confronted with Eq. (5.13).

The Schrödinger equation imposes a Cauchy type initial value problem, where a wave function is known for a time t_0 and the interest lies on its time-evolution, i.e.

$$|a, t_0\rangle \xrightarrow{\text{Time Evolution}} |a, t_0 \to t\rangle, \tag{5.14}$$

with a being a set of quantum numbers describing the system and $|a, t_0 \to t\rangle$ indicating the state $|a, t_0\rangle$ after a time propagation to the time t, which is in the following written in the simplified way $|a, t\rangle$. Solving this problem is formally achieved by introducing the time-evolution operator $U(t, t_0)$, which later yields an outstanding starting point for numerical approaches. With this, the time-evolution described by Eq. (5.14) is written as

$$|a, t\rangle = U(t, t_0)|a, t_0\rangle. \tag{5.15}$$

Following the derivation given in Ref. [159], we start by presenting the fundamental properties of this operator. First, since in non-relativistic quantum mechanics particles cannot be created nor be destroyed, it follows that the particle number must be conserved and, hence, the probability density is conserved as well. Therefore, an initially normalized state remains normalized at all times

$$\langle a, t_0|a, t_0\rangle = 1 = \langle a, t|a, t\rangle. \tag{5.16}$$

This has important implications for the properties of $U(t, t_0)$, because by inserting Eq. (5.15) into Eq. (5.16)

$$\langle a, t_0|U^\dagger(t, t_0)U(t, t_0)|a, t_0\rangle \overset{!}{=} 1 \Rightarrow U^\dagger(t, t_0)U(t, t_0) = \mathbb{1} \tag{5.17}$$

the unitarity of $U(t, t_0)$ follows. In order to be a physically reasonable operator for time-evolution, the composition property

$$U(t_2, t_0) = U(t_2, t_1)U(t_1, t_0) \tag{5.18}$$

has to be fulfilled, as we expect

$$|a, t_2\rangle = U(t_2, t_1)|a, t_1\rangle = U(t_2, t_1)U(t_1, t_0)|a, t_0\rangle \tag{5.19}$$

to be correct. Of course, the time-evolution operator is linear, as it needs to act on a superposition of states in the following manner

$$U(t, t_0)(|a, t_0\rangle + |b, t_0\rangle) = U(t, t_0)|a, t_0\rangle + U(t, t_0)|b, t_0\rangle = |a, t\rangle + |b, t\rangle. \tag{5.20}$$

Lastly, as the time is a continuous parameter, we demand

$$\lim_{t\to t_0}|a,t\rangle = \lim_{t\to t_0} U(t,t_0)|a,t_0\rangle = |a,t_0\rangle \Rightarrow \lim_{t\to t_0} U(t,t_0) = \mathbb{1}. \tag{5.21}$$

Keeping these demands in mind, we now construct U as an infinitesimal operator

$$U(t_0+dt,t_0) = 1 - iOdt, \tag{5.22}$$

where O is an hermitian operator ($O = O^\dagger$) to ensure the unitarity of U. It is easily shown that this definition of U fulfills the above imposed requirements. In order to obtain an equation to determine O, we exploit the composition property together with the infinitesimal form of U [Eq. (5.22)] [159]

$$U(t+dt,t_0) = U(t+dt,t)U(t,t_0) = (1-iOdt)U(t,t_0) \tag{5.23}$$

and rearrange the resulting equation to

$$U(t+dt,t) - U(t,t_0) = -iOdtU(t,t_0) \Rightarrow i\frac{U(t+dt,t)-U(t,t_0)}{dt} = OU(t,t_0). \tag{5.24}$$

We find that the left-hand side is equal to a time derivative. Therefore, by comparing Eq. (5.24) to the Schrödinger equation

$$\begin{aligned} &i\frac{dU(t+dt,t)}{dt}|a,t_0\rangle = HU(t+dt,t)|a,t_0\rangle \Rightarrow i\frac{dU(t+dt,t)}{dt} = HU(t+dt,t) \\ &\xRightarrow{\text{Eq. (5.24)}} i\frac{dU(t+dt,t)}{dt} = HU(t+dt,t) \overset{!}{\Leftrightarrow} i\frac{dU(t+dt,t)}{dt} = OU(t+dt,t) \end{aligned} \tag{5.25}$$

we see that we have constructed a time-evolution operator which obeys the Schrödinger equation, if we identify O with the Hamilton operator H. Therefore, the time-evolution operator (in infinitesimal form) is written as

$$\boxed{U(t+dt,t) = 1 - iH(t)dt} \tag{5.26}$$

Using Eq. (5.26), we are now in the position to generate a finite time translation of the state ket $|a,t_0\rangle$ via the application of infinitely many infinitesimal time-translation operators

$$U(t,t_0)|a,t_0\rangle = \lim_{N\to\infty} U(t,t_0+\tfrac{N-1}{N}\Delta t)U(t_0+\tfrac{N-1}{N}\Delta t,t_0+\tfrac{N-2}{N}\Delta t)\cdots U(t_0+\tfrac{1}{N}\Delta t,t_0)|a,t_0\rangle \tag{5.27}$$

with Δt being $t - t_0$. This equation can be simplified by constructing an analytic finite time-evolution operator. However, two different cases have to be considered[7]:

- The Hamiltonian H is time independent $\frac{\partial H}{\partial t} = 0$
- The Hamiltonian H is time-dependent $\frac{\partial H}{\partial t} \neq 0$

In the first case, it is evident that for all time steps in Eq. (5.27) the Hamiltonian is unchanged. This allows, using Eq. (5.26), to rearrange the equation to form an exponential function

$$U(t,t_0) = \lim_{N\to\infty}(1 - iH\tfrac{\Delta t}{N})^N = e^{-iH\Delta t} = e^{-iH(t-t_0)}. \tag{5.28}$$

In the second case of a time-dependent Hamiltonian, this Ansatz obviously does not work. The solution to this problem is usually given using the Neumann series which is a perturbation expansion [160]. As the Neumann series is not needed in the scope of this work, only the result is given for completeness

$$U(t,t_0) = 1 + \sum_{n=1}^{\infty}(-i)^n \int\limits_{t_0}^{t} dt_1 \int\limits_{t_0}^{t_1} dt_2 \cdots \int\limits_{t_0}^{t_{n-1}} dt_n H(t_1)H(t_2)\cdots H(t_n). \tag{5.29}$$

Instead of using the Neumann series, we introduce an approximation, which allows to write the time evolution in a way that is numerically very convenient to solve. For this, Δt is chosen very small which makes it evident that the Hamiltonian does not change significantly in this time span. In this time interval the time-evolution operator is (approximately) described by

$$\begin{aligned} U(t_0+\Delta t, t_0) &= \lim_{N\to\infty} U(t_0+\Delta t, t_0 + \tfrac{N-1}{N}\Delta t)\cdots U(t_0+\tfrac{1}{N}\Delta t, t) \\ &= \lim_{N\to\infty}(1 - iH\tfrac{\Delta t}{N})^N = e^{-iH(t_0)\Delta t} = e^{-iH(t_0)(t-t_0)}, \end{aligned} \tag{5.30}$$

with $H(t) = H(t_0)\ \ \forall t \in (t_0, t_0+\Delta t)$. If we construct the time evolution piece-wise on small intervals on which the Hamiltonian is constant, we obtain a full solution for the time-evolution over a finite time interval

$$U(t,t_0) = \lim_{\Delta t\to 0} U(t, t-\Delta t)U(t-\Delta t, t-2\Delta t)\cdots U(t_0+\Delta t, t_0). \tag{5.31}$$

---

[7] Actually three different cases have to be considered, because if the Hamiltonian is time-dependent, then it becomes important whether H fulfills the commutator relation $[H(t_1), H(t_0)] = 0$ or $[H(t_1), H(t_0)] \neq 0$. In the context of this work, however, $[H(t_1), H(t_0)] \neq 0$ holds, and the solution given in Eq. (5.28) cannot be generalized. The case $[H(t_1), H(t_0)] = 0$, where a generalization becomes possible, is discussed for example in Ref. [159].

Using Eq. (5.30) we can rewrite this to obtain the final result in operator form

$$\boxed{U(t,t_0) = \lim_{\Delta t \to 0} e^{-iH(t-\Delta t)\Delta t} \cdot e^{-iH(t-2\Delta t)\Delta t} \cdots e^{-iH(t_0)\Delta t}} \tag{5.32}$$

or with application to an inital ket state $|a, t_0\rangle$

$$\boxed{|a,t\rangle = U(t,t_0)|a,t_0\rangle = \lim_{\Delta t \to 0} e^{-iH(t-\Delta t)\Delta t} \cdot e^{-iH(t-2\Delta t)\Delta t} \cdots e^{-iH(t_0)\Delta t}|a,t_0\rangle} \tag{5.33}$$

This equation lays the starting point for the numerical calculations on the time-propagation of nuclear wave packets in H_2^+ which have been performed as a part of this thesis.

5.1.3 Numerical TDSE Solution: Split-Step Algorithm

In this work, a Split-Operator method [161, 162] is employed to solve Eq. (5.33). The split-step algorithms appear in many different forms and orders of accuracy, see e.g. [161–169]. The operation principle of the split-step algorithms is to decompose Eq. (5.32) into a product of operators which are diagonal in coordinate (real) space or in momentum space. Considering the time-dependent Hamiltonian in the length-gauge[8]

$$H(x,t) = \frac{p^2}{2m} + V(x,t) = T + V \tag{5.34}$$

it is evident that the operator $V(x)$ is diagonal in real space and p^2 is diagonal in momentum space. Here, T describes the kinetic energy- and V the potential energy-operator. Now, taking only one time step Δt in Eq. (5.32) and inserting Eq. (5.34), we obtain

$$U(t+\Delta t, t) = e^{-i[T+V(x,t)]\Delta t}. \tag{5.35}$$

The approximation of the split-step algorithm is to decompose this expression into a product of exponentials (the number of factors varies with different implementations of the algorithm), where each of the exponential operators is written in diagonal form in either real- or momentum space. Here we choose the splitting as follows

$$\boxed{U_{\mathrm{ap}}(t+\Delta t, t) = e^{-iT\Delta t/2} \cdot e^{-iV(x,t)\Delta t} \cdot e^{-iT\Delta t/2}} \tag{5.36}$$

---

[8] In this work, only the length-gauge is considered. The reason for this is that we later introduce a coupled channel calculation, in which two molecular electronic potentials are coupled via a laser-induced dipole coupling which is very intuitively described in the length-gauge.

This equation is of course an approximation (indicated by U_{ap}), because the exponentiated operators are only defined by their expansion series and by splitting the operators in factors, which is why non-vanishing commutators appear in the expansion series. To see that the approximation is correct to order $\mathcal{O}(\Delta t^2)$, we compare the corresponding expansion series of Eq. (5.35)

$$\begin{aligned} U(t+\Delta t, t) &= 1 - i(T+V)\Delta t - (T+V)^2\Delta t^2/2 + \mathcal{O}(\Delta t^3) \\ &= 1 - i(T+V)\Delta t - (T^2 + TV + VT + V^2)\Delta t^2/2 + \mathcal{O}(\Delta t^3) \end{aligned} \tag{5.37}$$

to the one of Eq. (5.36)

$$\begin{aligned} U_{\mathrm{ap}}(t+\Delta t, t) &= \left(1 - iT\Delta t/2 - T^2\Delta t^2/8\right)\left(1 - iV\Delta t - iV^2\Delta t/2\right)\left(1 - iT\Delta t/2 - T^2\Delta t^2/8\right) + \mathcal{O}(\Delta t^3) \\ &= 1 - i(T+V)\Delta t - (T^2 + TV + VT + V^2)\Delta t^2/2 + \mathcal{O}(\Delta t^3) \end{aligned} \tag{5.38}$$

and find them to be equal.

With Eq. (5.36) we now have a good starting point for applying numerics. Again, we want to propagate an initial state $|a, t\rangle$ in time to $|a, t+\Delta t\rangle$

$$\phi(p''', t+\Delta t) = \sum_{p,p',p'',x,x'} \langle p'''|e^{-iT\Delta t/2} \cdot |p''\rangle\langle p''|x'\rangle\langle x'|e^{-iV(x,t)\Delta t} \cdot |x\rangle\langle x|p'\rangle\langle p'|e^{-iT\Delta t/2}|p\rangle\langle p|a, t+\Delta t\rangle \tag{5.39}$$

for which we included basis transformations such that the operators are all in diagonal form[9]. Identifying the projectors $\sum_p |p\rangle\langle x| =: \mathrm{FT}$ and $\sum_x |x\rangle\langle p| =: \mathrm{FT}^{-1}$ as the Fourier- and inverse Fourier-transform, connecting real and momentum space and further indicating the basis of the potential energy and momentum operator by an index (T_p and V_x), Eq. (5.39) simplifies to

$$\phi(p, t+\Delta t) = e^{-iT_p\Delta t/2}\,\mathrm{FT}\left\{e^{-iV_x\Delta t}\,\mathrm{FT}^{-1}\left[e^{-iT_p\Delta t/2}\phi(p,t)\right]\right\}. \tag{5.40}$$

From this we derive the recipe of the split-step algorithm to evolve a momentum-space wave function by one time-step Δt:

1. take input wave function $\tilde{\phi}(p,t)$ and perform p half-step: $\tilde{\phi}(p) \leftarrow \tilde{\phi}(p,t)e^{-i\frac{p^2}{2m}\frac{\Delta t}{2}}$
2. perform inverse Fourier transform of result to real space $\phi_1(x) \leftarrow \mathrm{FT}^{-1}\left[\tilde{\phi}(p)\right]$
3. perform full-step in x: $\phi(x) \leftarrow \phi(x)e^{-iV\Delta t}$
4. perform Fourier transform back to momentum space: $\tilde{\phi}(p) \leftarrow \mathrm{FT}\left[\phi(x)\right]$
5. perform final p half-step: $\tilde{\phi}(p, t+\Delta t) \leftarrow \tilde{\phi}(p)e^{-i\frac{p^2}{2m}\frac{\Delta t}{2}}$

A flowchart of the program that uses the above described algorithm is shown in Fig. 5.4.

---

[9] Note: Here sums are rather than integrals, because in numerics the x and p spaces are discretized.

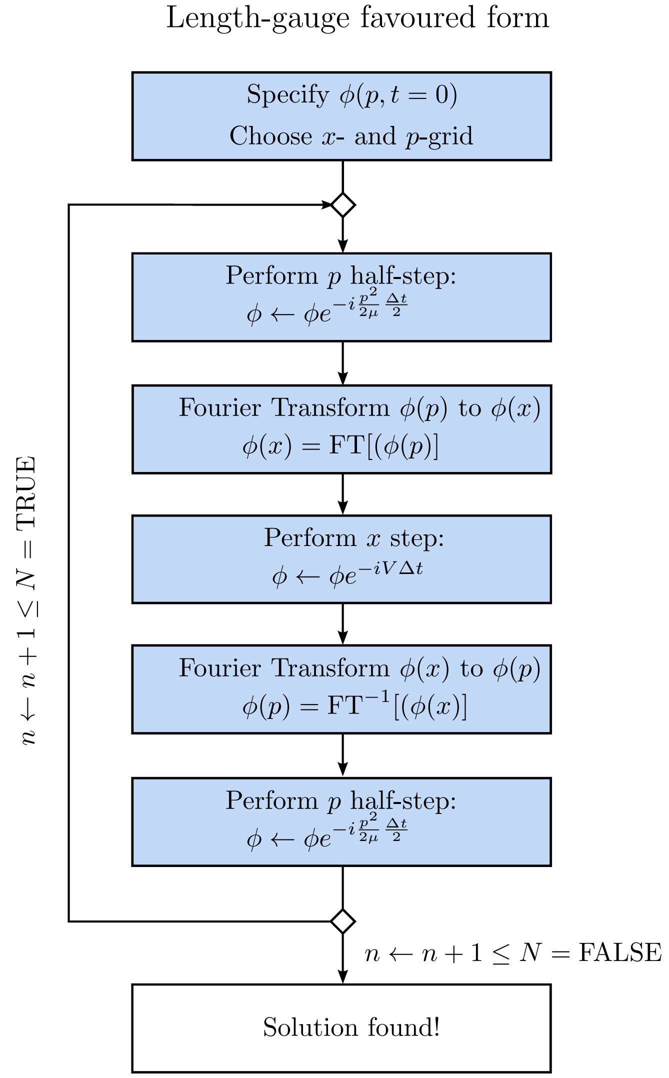

Figure 5.4: Flowchart of a program using the Split-Step algorithm. Here N propagation steps with step size Δt are carried out. First an initial wave function $\phi(p,t=0)$ (in momentum space) is specified on a user defined real space- and momentum-grid. After that the program enters a loop. This loop consists of a half-step ${}^{\Delta t}/_{2}$ in momentum space, an inverse Fast-Fourier-Transform $\mathrm{FT}^{-1}[p \to x]$, a full-time propagation step in x-space, a $\mathrm{FT}[x \to p]$ and finally a half-propagation step in momentum space.

Coupled Channels

We want to apply the above described numerical formalism to the case of many electronic states in the presence of a laser field. For this, we recall the general quantum mechanical wave function described in Eq. (5.2). Due to the fact that the electronic wave functions are eigenfunctions of the field free Hamiltonian it is clear that, without coupling among them, the summands are independently propagating in time. For this reason the Schrödinger equation describing the nuclei for such a sum can be written in the form

$$i\frac{d}{dt}\begin{pmatrix}\phi^1(R,t)\\ \vdots\\ \phi^n(R,t)\\ \vdots\end{pmatrix}=\begin{pmatrix}-\frac{p^2}{2\mu}+V_1 & 0 & \dots & 0\\ 0 & \ddots & 0 & \vdots\\ \vdots & 0 & -\frac{p^2}{2\mu}+V_n & 0\\ 0 & \dots & 0 & \ddots\end{pmatrix}\begin{pmatrix}\phi^1(R,t)\\ \vdots\\ \phi^n(R,t)\\ \vdots\end{pmatrix} \tag{5.41}$$

Without coupling induced by an external field, it is therefore possible to propagate the $\phi^n(R,t)$ independently [these $\phi^n(R,t)$ are the same as in Eq. (5.2)].

The situation gets more involved when a laser field is present, as transitions between former eigenstates can now be driven. Allowing only dipole transitions, we modify Eq. (5.41) with coupling elements (in length gauge) and obtain

$$i\frac{d}{dt}\begin{pmatrix}\phi^1(R,t)\\ \phi^2(R,t)\\ \phi^3(R,t)\\ \vdots\end{pmatrix}=\begin{pmatrix}-\frac{p^2}{2\mu}+V_1 & -\langle\psi_1|r\cdot\mathcal{E}|\psi_2\rangle & -\langle\psi_1|r\cdot\mathcal{E}|\psi_3\rangle & \dots\\ -\langle\psi_2|r\cdot\mathcal{E}|\psi_1\rangle & -\frac{p^2}{2\mu}+V_2 & -\langle\psi_2|r\cdot\mathcal{E}|\psi_3\rangle & \vdots\\ -\langle\psi_3|r\cdot\mathcal{E}|\psi_1\rangle & -\langle\psi_3|r\cdot\mathcal{E}|\psi_2\rangle & -\frac{p^2}{2\mu}+V_3 & \dots\\ \vdots & \dots & \dots & \ddots\end{pmatrix}\begin{pmatrix}\phi^1(R,t)\\ \phi^2(R,t)\\ \phi^3(R,t)\\ \vdots\end{pmatrix} \tag{5.42}$$

where the $D_{kl} =: -\langle\psi_k(R)|r\cdot\mathcal{E}|\psi_l(R)\rangle$ are the dipole transition amplitudes. This implies that the nuclear wave packets on different PES, each corresponding to respective electronic states, start to mix according to their respective dipole transition amplitude. In a more general form this can be written as

$$i\frac{d\Phi}{dt}=(\underbrace{T+V+H_{\mathrm{Int}}}_{H})\Phi \tag{5.43}$$

where T corresponds to the kinetic energy matrix, V to a matrix containing the potential energy surfaces of the molecule, and H_{Int} the (non-diagonal) interaction Hamiltonian.

Equation (5.42) governs the nuclear motion in the presence of a laser-field (in dipole approximation). However, the above described split-step algorithm relies on the possibility to split the Hamiltonian H into operators that are diagonal in the electronic part (for which the basis functions are the electronic wave functions) as well as in either real- or momentum space (where the basis is $|x\rangle$ and $|p\rangle$). This is no longer true for the dipole-coupled H of Eq. (5.43) and we have to modify the split-step algorithm one last time by introducing a digitalization step[10]

$$(T + V + H_{\mathrm{WW}})\Phi = T\Phi + M^\dagger \underbrace{M(V + H_{\mathrm{Int}})M^\dagger}_{V_{\mathrm{Int}}} M\Phi \tag{5.44}$$

where V_{Int} is the diagonalized interaction potential

$$V_{\mathrm{Int}} = \begin{pmatrix} V_{\mathrm{Int}}^1 & 0 & \dots & \dots \\ 0 & V_{\mathrm{Int}}^2 & \dots & \vdots \\ \dots & 0 & V_{\mathrm{Int}}^3 & \dots \\ \vdots & \dots & \dots & \ddots \end{pmatrix}. \tag{5.45}$$

With Eq. (5.44) we conclude that a basis transformation of Φ has to be performed (by applying M) before it can be applied to V_{Int}. Subsequently, the result has to be transformed back by applying $M^\dagger$. Therefore, the split-step algorithm scheme for the coupled channels becomes:

1. take multicomponent input wave function $\tilde{\phi}^n(p,t)$ and perform p half-step: $\tilde{\phi}^n(p) \leftarrow \tilde{\phi}^n(p,t)e^{-i\frac{p^2}{2m}\frac{\Delta t}{2}}$
2. perform inverse Fourier transform of result to real space $\phi^n(x) \leftarrow \mathrm{FT}^{-1}\left[\tilde{\phi}^n(p)\right]$
3. diagonalize real space operator V_{Int} and find the change of basis matrices M and $M^\dagger$
4. apply the first change of basis matrix M to the nuclear wave function vector
5. perform full-step in x: $\phi^n(x) \leftarrow \phi^n(x)e^{-iV^n\Delta t}$, where the V^n is the n-th eigenvalue of the matrix V_{Int}
6. apply the second (inverse) change of basis matrix $M^\dagger$ to the nuclear wave function vector
7. perform Fourier transform back to momentum space: $\tilde{\phi}^n(p) \leftarrow \mathrm{FT}\left[\phi^n(x)\right]$
8. perform final p half-step: $\tilde{\phi}^n(p,t+\Delta t) \leftarrow \tilde{\phi}^n(p)e^{-i\frac{p^2}{2m}\frac{\Delta t}{2}}$

This algorithm is capable of propagating Eq. (5.42) in time for a system of electronic states (channels) with and without coupling. We later use this scheme to calculate the nuclear dynamics for a system of coupled channels in order to describe laser-induced bond-softening in H_2^+.

For the experimental parameters used in this chapter, the IR-laser pulse couples the electronic states $\mathrm{H}_2^+(X\,^2\Sigma_g^+)$ and $\mathrm{H}_2^+(A\,^2\Sigma_u^+)$. The TDSE can therefore be written

---

[10] Commonly U and $U^\dagger$ are used to denote the transformation matrices, which could be confused with the time-evolution operator. We therefore use M and $M^\dagger$.

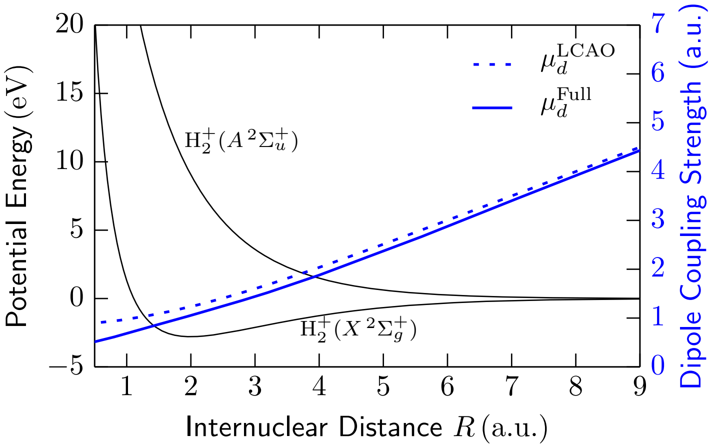

Figure 5.5: Comparison of R-dependent dipole coupling strength μ_d obtained by using *ab initio* molecular orbitals to one where the orbitals have been determined exploiting the LCAO approximation considering only s-orbitals of atomic hydrogen.

$$i\frac{d}{dt}\begin{pmatrix}\phi^1(R,t)\\ \phi^2(R,t)\end{pmatrix} = \begin{pmatrix} -\frac{p^2}{2\mu}+V_{\Sigma_g} & -\langle X\,^2\Sigma_g^+|r\cdot\mathcal{E}|A\,^2\Sigma_u^+\rangle \\ -\langle A\,^2\Sigma_u^+|r\cdot\mathcal{E}|X\,^2\Sigma_g^+\rangle & -\frac{p^2}{2\mu}+V_{\Sigma_u}\end{pmatrix}\begin{pmatrix}\phi^1(R,t)\\ \phi^2(R,t)\end{pmatrix} \tag{5.46}$$

where $\phi^1(R)$ and $\phi^2(R)$ are the nuclear wave functions corresponding to the states $H_2^+(X\,^2\Sigma_g^+)$ and $H_2^+(A\,^2\Sigma_u^+)$, respectively. Applying the above described split-step approach, this system of coupled-channels can be solved numerically. However, for this the integral

$$-\langle A\,^2\Sigma_u^+(R)|r\cdot\mathcal{E}|X\,^2\Sigma_g^+(R)\rangle \tag{5.47}$$

has to be evaluated. As we only consider molecules oriented parallel to the polarization axis, this can be written as

$$-\mathcal{E}\langle A\,^2\Sigma_u^+(R)|z|X\,^2\Sigma_g^+(R)\rangle = -\mathcal{E}\mu_d(R) \tag{5.48}$$

where μ_d is the R-dependent dipole coupling strength. For the parameters considered in this work, a linear combination of atomic s-orbitals (LCAO) to approximate the $H_2^+(X\,^2\Sigma_g^+)$ and $H_2^+(A\,^2\Sigma_u^+)$ state already yields very good results. Figure 5.5 compares the dipole coupling obtained by using LCAO (Linear Combination of Atomic Orbitals [123, 124]) molecular orbitals to one where *ab initio* molecular orbitals were used.

5.1.4 Field-Dressed Floquet-States

In order to interpret and simulate the later presented results, we use the so-called Floquet picture. In this presentation, the PES are dressed by a time-periodic electric-field oscillating with period T, modifying their potential energies [170, 171] and allowing for the dissociation of molecules in such fields.

The Schrödinger equation for this situation reads

$$\boxed{i\frac{d\Psi(x,t)}{dt} = H(x,t)\Psi(x,t) \text{ with } H(x,t+T) = H(x,t)} \tag{5.49}$$

Again, we seek numerical solutions for the field-dressed states [172–174] and, hence, want to derive an equation suitable to perform efficient computations. Due to the time-periodicity of the Hamiltonian, many results are similar to the ones found in textbooks about solid state physics [175,176], where Bloch functions are the solutions of the Schrödinger equation for space-periodic crystal structures. Here, we follow a derivation (e.g. presented in [177, 178]) again making use of the time-evolution operator developed in Sec. 5.1.2.

For a time periodic Hamiltonian, the time-evolution operator U gains another property, which can be written

$$U(t+T, t_0+T) = U(t, t_0). \tag{5.50}$$

We further define an extended Hamilton operator

$$\mathcal{H}(t) := H(t) - i\partial_t \tag{5.51}$$

and prove that simultaneous eigenfunctions $|\Psi(t)\rangle$ of this extended Hamiltonian and time-evolution operator $U(t+T, t)$ exist. For this it is necessary that the commutator $[\mathcal{H}(t), U(t+T, t)] = 0$ vanishes.

$$\begin{aligned}
U(t+T,t)\mathcal{H}(t)|\Psi(t)\rangle &= U(t+T,t)\mathcal{H}(t)\mathbb{1}|\Psi(t)\rangle \\
&= U(t+T,t)\mathcal{H}(t)U^\dagger(t+T,t)U(t+T,t)|\Psi(t)\rangle \\
&= \mathcal{H}(t+T)U(t+T,t)|\Psi(t)\rangle = \mathcal{H}(t)U(t+T,t)|\Psi(t)\rangle \\
&\Rightarrow [\mathcal{H}(t), U(t+T,t)] = 0 \qquad (5.52)
\end{aligned}$$

To solve Eq. (5.49) we first recall that due to the unitarity of U the eigenvalue equation

$$U(t+T,t)|\Psi(t)\rangle = e^{i\zeta(T)}|\Psi(t)\rangle \tag{5.53}$$

has to hold, where $\zeta(T)$ is a real valued (yet to be determined) function of T. Using the composition property introduced earlier, Eq. (5.50) and Eq. (5.53)

$$\begin{aligned} e^{i\zeta(2T)}|\Psi(t)\rangle &= U(t+2T,t)|\Psi(t)\rangle \\ &= U(t+2T,t+T)U(t+T,t)|\Psi(t)\rangle \\ &= U^2(t+T,t)|\Psi(t)\rangle \\ &= \left[e^{i\zeta(T)}\right]^2|\Psi(t)\rangle \end{aligned} \tag{5.54}$$

is derived. With this, we conclude that $\zeta(T) \propto T$ is proportional to T and we set $\zeta(T) = -ET$, where E is the Floquet exponent which is often called the quasi-energy [170, 179, 180]. Therefore, the eigenstates of $\mathcal{H}$ and U obey the relation

$$U(t+T,t)|\Psi(t)\rangle = e^{iET}|\Psi(t)\rangle \tag{5.55}$$

By splitting off the time dependent part from the simultaneous eigenstates, we write (this is merely an ansatz)

$$|\Psi(t)\rangle = e^{-iEt}|\phi(t)\rangle \tag{5.56}$$

where $|\phi(t)\rangle$ is periodic in time, which we verify in the following.

$$\begin{aligned} U(t+T,t)|\phi(t)\rangle &= |\phi(t+T)\rangle = e^{iE(t+T)}|\Psi(t+T)\rangle \\ &= e^{iE(t+T)}U(t+T,t)|\Psi(t)\rangle \\ &= e^{iE(t+T)}e^{-iET}|\Psi(t)\rangle = |\phi(t)\rangle \end{aligned} \tag{5.57}$$

Application of the extended Hamiltonian $\mathcal{H}$ on Eq. (5.56) yields (starting with Schrödinger's equation $\mathcal{H}|\Psi\rangle = 0$)

$$\begin{aligned} 0 &= \mathcal{H}(t)|\Psi(t)\rangle = (H - i\partial_t)|\Psi(t)\rangle = (H - i\partial_t)e^{-iEt}|\phi(t)\rangle \\ &= He^{-iEt}|\phi(t)\rangle - Ee^{-iEt}|\phi(t)\rangle - e^{-iEt}i\partial_t|\phi(t)\rangle \\ &= e^{-iEt}(H - i\partial_t)|\phi(t)\rangle - Ee^{-iEt}|\phi(t)\rangle \\ &\Leftrightarrow \mathcal{H}|\phi(t)\rangle = E|\phi(t)\rangle \end{aligned} \tag{5.58}$$

which is the Floquet-type Schrödinger equation that must be fulfilled in order to be compliant with the Schrödinger equation. The above obtained results are summarized by Floquet's theorem

Theorem 5.1.1 (Floquet's Theorem: applied to Schrödinger's equation) *The solutions to the time-dependent Schrödinger equation with time-periodic Hamiltonian $H(t+T) = H(t)$ are given by*

$$\boxed{|\Psi(t)\rangle = e^{-iE(t-t_0)}|\phi(t)\rangle \quad \textit{with} \quad |\phi(t+T)\rangle = |\phi(t)\rangle} \tag{5.59}$$

where E is the (time-independent) Floquet exponent (or quasi-energy) and $|\phi(t)\rangle$ the time-periodic Floquet states. The Floquet states are solutions to the Floquet-type Schrödinger *equation*

$$\boxed{\mathcal{H}|\phi(t)\rangle = E|\phi(t)\rangle} \tag{5.60}$$

where $\mathcal{H} = (H - i\partial_t)$ *is the extended Hamiltonian.*

It can easily be verified that multiplying a Floquet solution by $e^{ik\omega t}$, with $k \in \mathbb{N}_0$ and $\omega = {}^{2\pi}/_{T}$, generates a new solution

$$\boxed{\begin{array}{c} |\Psi'(t)\rangle = e^{ik\omega t}|\Psi\rangle \\ E' = E + k\omega \end{array}} \tag{5.61}$$

belonging to the same infinite set of equivalent states, though with shifted quasi-energies. It should be noted, that the different quasi-energies are unlike normal energies, for which the absolute magnitude of the energy carries physical significance. In contrast to that, the quasi-energies carry only a physical meaning in a range modulo 2π. This is analogous to the reduction of quasi-energies to a Brillouin zone in solid states physics.

Numerical Solution of the Floquet-states: The Floquet Matrix

We are now in the position to approach a numerical solution to the problem. For this we derive the well-known Floquet matrix, which is then used to compute the PES of Floquet states. Having established the periodicity of $|\phi(t)\rangle$ [see Eq. (5.59)] we Fourier expand it

$$|\phi(t)\rangle = \sum_{n=-\infty}^{\infty} e^{-in\omega t}|F_n\rangle \tag{5.62}$$

with $|F_n\rangle$ being the Fourier coefficients[11]. Then the Fourier coefficients are expanded in complete basis set $\{|k\rangle\}$[12]

$$|F_n\rangle = \sum_k c_k^n |k\rangle. \tag{5.63}$$

Inserting this equation and Eq. (5.62) together with Eq. (5.56) into the Floquet-type Schrödinger equation [Eq. (5.58)] yields

$$\sum_{n,k} \mathcal{H}(t) e^{-in\omega t} c_k^n |k\rangle = \sum_{n,k} E c_k^n |k\rangle e^{-in\omega t}. \tag{5.64}$$

---

[11] For simplicity, the summation ranges are dropped whenever it is clear from the context.

[12] Later this basis is chosen to be a small subset of the electronic wave functions of the molecular hydrogen ion.

Multiplying $\langle lm| := \langle l|e^{im\omega t}$ from the left and time-averaging yields

$$\begin{aligned}
\sum_{n,k} \frac{1}{T}\int_0^T dt \langle lm|\mathcal{H}(t)|nk\rangle &= \sum_{n,k} \frac{1}{T}\int_0^T dt \langle lm|Ec_k^n|nk\rangle \\
\sum_{n,k} \frac{1}{T}\int_0^T dt \langle lm|H_0 + V(t) - i\partial_t|nk\rangle &= \sum_{n,k} Ec_k^n \delta_{mn}\delta_{kl} \\
\sum_{n,k} \left\{ \langle l|H_0 c_k^n|k\rangle \delta_{nm} + \frac{1}{T}\int_0^T dt \langle lm|V(t)|nk\rangle + \langle l|n\omega\delta_{m,n}|k\rangle \right\} &= Ec_l^m \qquad (5.65)
\end{aligned}$$

If a monochromatic dressing-field $V(t) = \frac{-\mathcal{E}_0 r}{2}\left[e^{i\omega t} + e^{-i\omega t}\right]$ is assumed, this equation can further be simplified to

$$\boxed{\sum_{n,k} \left\{ \langle l|H_0 c_k^n|k\rangle \delta_{nm} + \langle l|\frac{-\mathcal{E}_0 r}{2}\left[\delta_{m,n+1} + \delta_{m,n-1}\right]|k\rangle + \langle l|n\omega\delta_{m,n}|k\rangle \right\} = Ec_l^m} \tag{5.66}$$

where, as mentioned earlier, the basis $\{|k\rangle\}$ is identified with the eigenfunctions of the field-free Hamiltonian H_0. In the case of the molecular hydrogen ion and for the approximation of fixed nuclei the field-free Hamiltonian simplifies to the electronic Hamiltonian of the system. Therefore the $|k\rangle$ are the electronic eigenstates of the molecular ion. Truncating the basis to the two energetically lowest states, namely the $\mathrm{H}_2^+(X\,^2\Sigma_g^+)$ and the $\mathrm{H}_2^+(A\,^2\Sigma_u^+)$ we can write the left-hand-side of Eq. (5.66) in form of an infinite matrix, the Floquet matrix

$$\boxed{\begin{pmatrix}
 & \vdots & \vdots & \vdots & \vdots & \\
\dots & V_{gu}(R) & 0 & 0 & 0 & \dots \\
\dots & V_u(R) + (n-1)\omega & V_{gu}(R) & 0 & 0 & \dots \\
\dots & V_{gu}(R) & V_g(R) + n\omega & V_{gu}(R) & 0 & \dots \\
\dots & 0 & V_{gu}(R) & V_u(R) + (n+1)\omega & V_{gu}(R) & \dots \\
\dots & 0 & 0 & V_{gu}(R) & V_g(R) + (n+2)\omega & \dots \\
\dots & 0 & 0 & 0 & V_{gu}(R) & \dots \\
 & \vdots & \vdots & \vdots & \vdots &
\end{pmatrix}} \tag{5.67}$$

where $V_{gu} = \langle {}^2\Sigma_g^+| -\frac{E_0 r}{2}|{}^2\Sigma_u^+\rangle$, $V_g(R) = \langle {}^2\Sigma_g^+|H_0|{}^2\Sigma_g^+\rangle$ and $V_u(R) = \langle {}^2\Sigma_g^+|H_0|{}^2\Sigma_u^+\rangle$. To obtain the field-dressed PES numerically, the matrix has to be truncated at a finite size and be diagonalized.

Intensity and Angular Dependence of the Field-Dressed Floquet States

The above described Floquet matrix [Eq. (5.67)] can be interpreted as a set of infinitely many PES which are dressed by laser-photons. The field-dressing leads to a shift in their quasi-energy by n photon energies ω, as shown in Fig. 5.6 (left). In the case of Floquet states, zero intensity forces a formal periodicity upon the problem, which is exploited in the Floquet formalism[13]. However, it is evident that the solutions are only formal, since the individual curves belong to the same irreducible representations (Σ_g^+), but do not repel each other as is expected for curves of the same symmetry (this is known as the formation of avoided crossings). As soon as the intensity of the dressing-laser no longer vanishes, the curves start to repel each other and form the predicted avoided crossings (see Fig. 5.7 right). This repulsion is a function of the laser intensity. The stronger the coupling field the further the curves separate in their quasi-energy. It should be noted that for higher intensities more

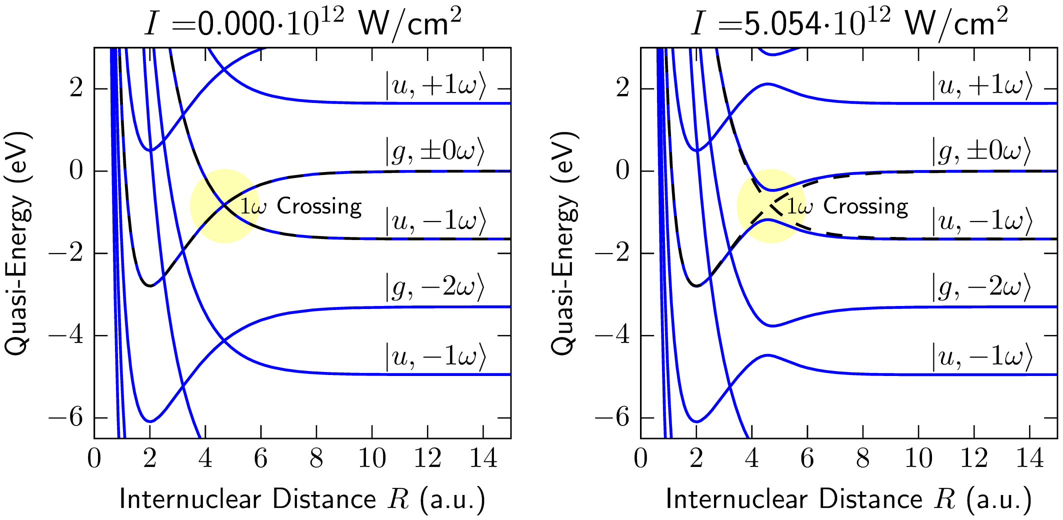

Figure 5.6: Floquet PES for two dipole coupled electronic states of the H_2^+ ion, namely the states $H_2^+(X\,{}^2\Sigma_g^+)$ and $H_2^+(A\,{}^2\Sigma_u^+)$ [compare Eq. (5.67)]. Left: Electric field intensity of 0 W/cm^2 (vanishing field). Right: Electric field intensity of $5.1\cdot10^{12}$ W/cm^2. For larger intensities corresponding to a stronger coupling of the $H_2^+(X\,{}^2\Sigma_g^+)$ and $H_2^+(A\,{}^2\Sigma_u^+)$ states, an avoided crossing is formed. At the energy considered in this work only the 1ω avoided crossing opens (see e.g. [181,182] for higher order avoided crossings).

---

[13] The case of zero intensity is comparable to the well-known case of an empty crystal in solid state physics, which results in Bloch function solutions of the formally periodic Hamiltonian.

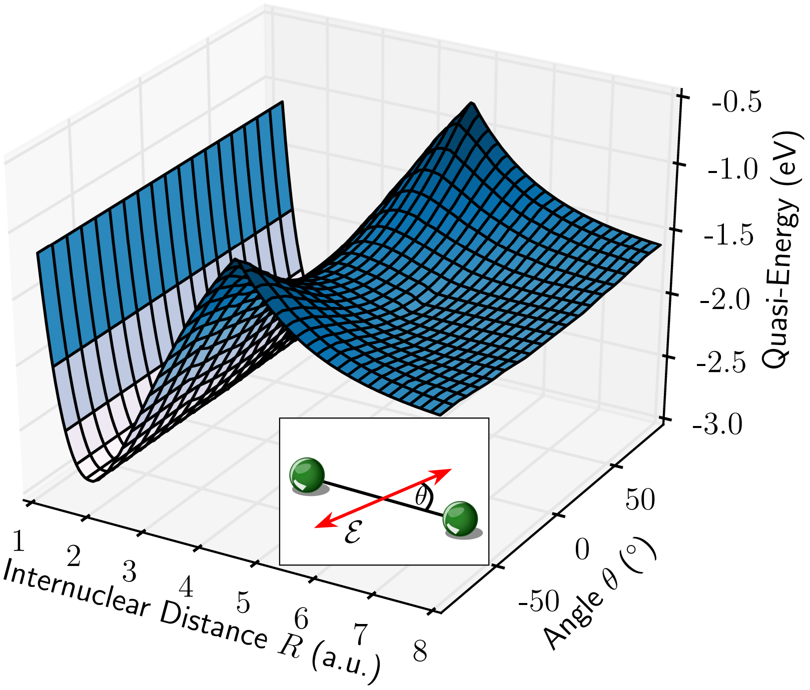

Figure 5.7: Angular dependence of the field-dressed 1ω PES of the H_2^+ molecule, where θ is the angle between the molecular axis and the polarization vector (see inset) of the electric field. The maximum intensity, corresponding to an angle of $\theta = 0$, is $5.1 \cdot 10^{12}\,\mathrm{W/cm^2}$. For each intensity (corresponding to an angle θ), the curves were obtained by diagonalization of a 100×100 Floquet matrix for all R.

and more crossings open (compare e.g. [181, 182]). For example, at approximately $5 \cdot 10^{13}\,\mathrm{W/cm^2}$ the 3ω crossing starts to open up. However, as $5.1 \cdot 10^{12}\,\mathrm{W/cm^2}$ is the highest intensity used in this work, only the 1ω avoided crossing presented (Fig. 5.6 right) is considered.

In the case, where the different PES are coupled via a laser-induced dipole coupling, the separation further depends on the orientation of the molecule with regard to the polarization axis of the laser field (see inset of Fig. 5.7). This is caused by the dipole selection-rules imposed on the transition, which only allows for parallel transitions between the $H_2^+(X\,{}^2\Sigma_g^+)$ and the $H_2^+(A\,{}^2\Sigma_u^+)$ electronic state. Therefore, the dipole transition amplitude can be written as

$$\begin{aligned} -\langle A\,^2\Sigma_u^+|r\cdot(\mathcal{E}_\parallel+\mathcal{E}_\perp)|X\,^2\Sigma_g^+\rangle &= -\langle A\,^2\Sigma_u^+|r\cdot\mathcal{E}_\parallel|X\,^2\Sigma_g^+\rangle - \langle A\,^2\Sigma_u^+|r\cdot\mathcal{E}_\perp|X\,^2\Sigma_g^+\rangle \\ &= -\langle A\,^2\Sigma_u^+|r\cdot\mathcal{E}_\parallel|X\,^2\Sigma_g^+\rangle = -\langle A\,^2\Sigma_u^+||r||\mathcal{E}|\cos(\theta)|X\,^2\Sigma_g^+\rangle \end{aligned} \tag{5.68}$$

Figure 5.7 shows the dependency of the quasi-energy of a field-dressed PES as a function of the angle θ between molecular axis and laser field.

Bond-Softening

In the unperturbed $H_2^+(X\,^2\Sigma_g^+)$ molecular potential 19 bound vibrational states exist. Using the above discussed Floquet mechanism, we find that in the presence of a laser field the binding electronic potential becomes distorted (compare solid and dotted line in Fig. 5.8). Formerly bound vibrational states now lie in the dissociation continuum and start to dissociate. For the case depicted in Fig. 5.8, this is the case for the vibrational states with quantum numbers larger then $v = 4$. However, the states with $v > 7$ are favored, as they may directly pass the potential barrier and do not have to tunnel through it. The energy of the fragments after dissociation (in a cw-laser field) is given by[14]

$$E_{\text{kin}} = E_v + \omega. \tag{5.69}$$

It is evident that the formerly bound vibrational states with $E_{\text{diss}} > 0$ are now dissociating, giving the reason to name this process bond-softening.

5.2 Nuclear wave-packet dynamics on laser induced transition states

After presenting the theoretical background, the experimental data and its interpretation is subject to this section. We find that in the laser induced dissociation of molecular hydrogen ions, it is possible to manipulate the final momentum of the proton by variation of the time-delay between the pump and the coupling laser. This observation is investigated an is explained in terms of an intuitive semi-classical mechanism. It is shown that the time dependence of the control-laser pulse leads to an up/down motion of the field-dressed potential energy curves on which the nuclear wave-packet propagates. With this it is possible to elevate the total energy of a state, which in the final analysis leads to a change of the observed proton momentum.

---

[14] Recall that the energy of a bound vibrational state is negative by the here applied definition.

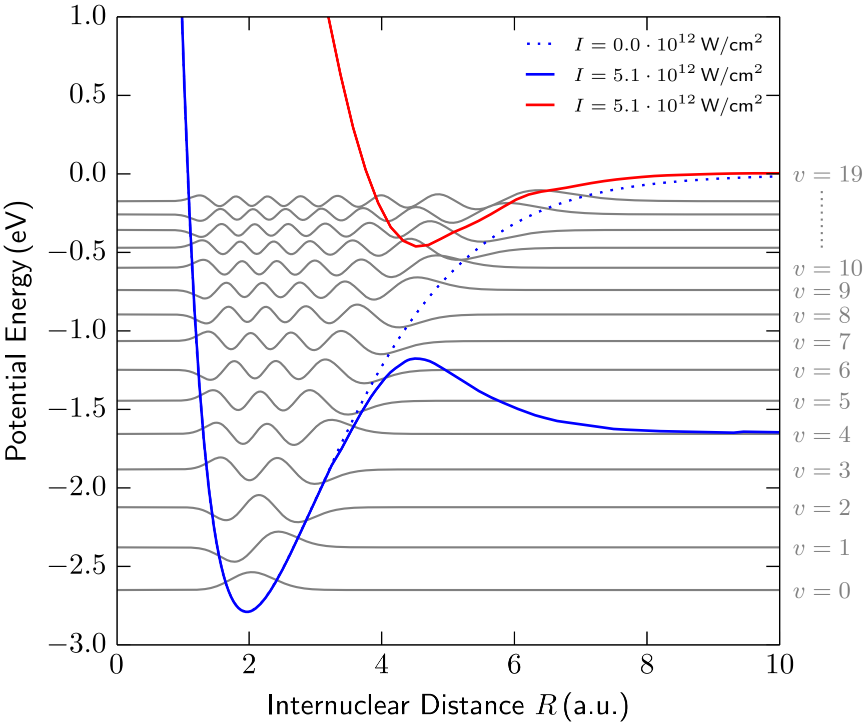

Figure 5.8: First 15 vibrational states of the undisturbed $H_2^+(X\,^2\Sigma_g^+)$ molecular potential. In the presence of a laser-field the PES gets distorted and the upper vibrational states are above the potential barrier (blue solid line), causing the molecule to dissociate. The vibrational states with energies lying in the range of the gap between the solid red- and solid blue curve are most efficiently dissociated (as shown by quantum simulations presented later). The vibrational states and eigenenergies where computed using an algorithm described in [126].

5.2.1 Experimental Conditions

In this section, we shall briefly review the experimental conditions and physical reactions used to obtain the data presented below. The key idea is that by irradiating a gas jet consisting of molecular hydrogen with an attosecond pulse train ($\sigma_{\mathrm{FWHM}}^{\mathrm{XUV}} \approx 6\,\mathrm{fs}$) followed by a time-delayed IR laser pulse with $\sigma_{\mathrm{FWHM}}^{\mathrm{IR}} = 8.6\,\mathrm{fs}$. Like in the previous chapter we are only interested in channels where a proton is created. If we plot the so obtained data into an energy correlation diagram as done in the previous chapter, we obtain Fig. 5.9. The reaction can be written as

$$H_2(X\,^1\Sigma_g^+) \xrightarrow{\mathrm{XUV}} H_2^+(X\,^2\Sigma_g^+) + e^- \xrightarrow{\mathrm{IR}(\tau)} H + H^+ + e^-. \tag{5.70}$$

By comparing Fig. 5.9 to Fig. 4.3 we find that at low KER an additional band of counts is observed. At the photon energies considered in this work, when the

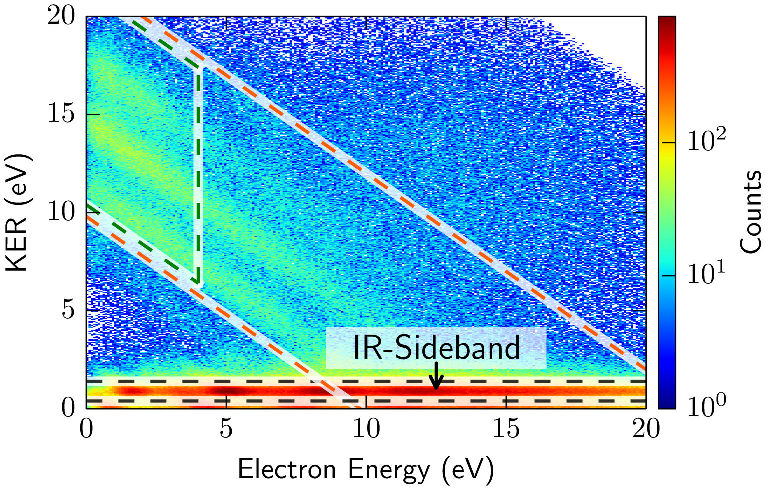

Figure 5.9: Energy correlation diagram. The observed H^+ counts are plotted as a function of the observed photoelectron energy and kinetic energy release of the nuclei (sum kinetic energy of proton and neutral hydrogen atom). The same structures as in the previous chapter are observed with the addition of a "band" (labeled IR-Sideband) appearing for low KER. It is precisely this region that we are interested in throughout this chapter.

XUV pulse ionizes the molecular hydrogen the ion is formed in the two ionic states $H_2^+(X\,^2\Sigma_g^+)$ and $H_2^+(A\,^2\Sigma_u^+)$. Only the first one is stable and when the delayed IR pulse arrives it can couple the binding $X\,^2\Sigma_g^+$ to the $H_2^+(A\,^2\Sigma_u^+)$ state (see Fig. 5.1). In this process an additional IR photon with an energy of approximately 1.7 eV is absorbed, which causes the appearance of events with a kinetic energy release $\text{KER} \approx 0.8\,\text{eV}$, which manifest as an IR-sideband in the energy correlation diagram (see region labeled "IR-Sideband" in Fig. 5.9). The time-delay resolved investigation of this energy band is subject to the following investigation.

5.2.2 Experimental Data

As mentioned in the chapter's introduction, we use attosecond pulse trains to ionize molecular hydrogen. With photon energies between 16 eV and 40 eV we are well able to populate the binding $H_2^+(X\,^2\Sigma_g^+)$ electronic state (see Fig. 5.10 left). Because the ionization of the molecule by XUV photons occurs very quickly (on time-scales of the nuclei: almost instantaneous) the nuclear wave function (describing the two protons) is vertically promoted to the ionic potential while maintaining its spatial shape [see Fig. 5.10 (left)]. As the molecular hydrogen in the target gas jet is vibrationally cold, the initial wave function is the vibrational ground state wave function of the neutral molecular hydrogen molecule. In the following we refer to the vertically promoted wave packet as the "*Franck-Condon wave packet*". According to the Franck-Condon

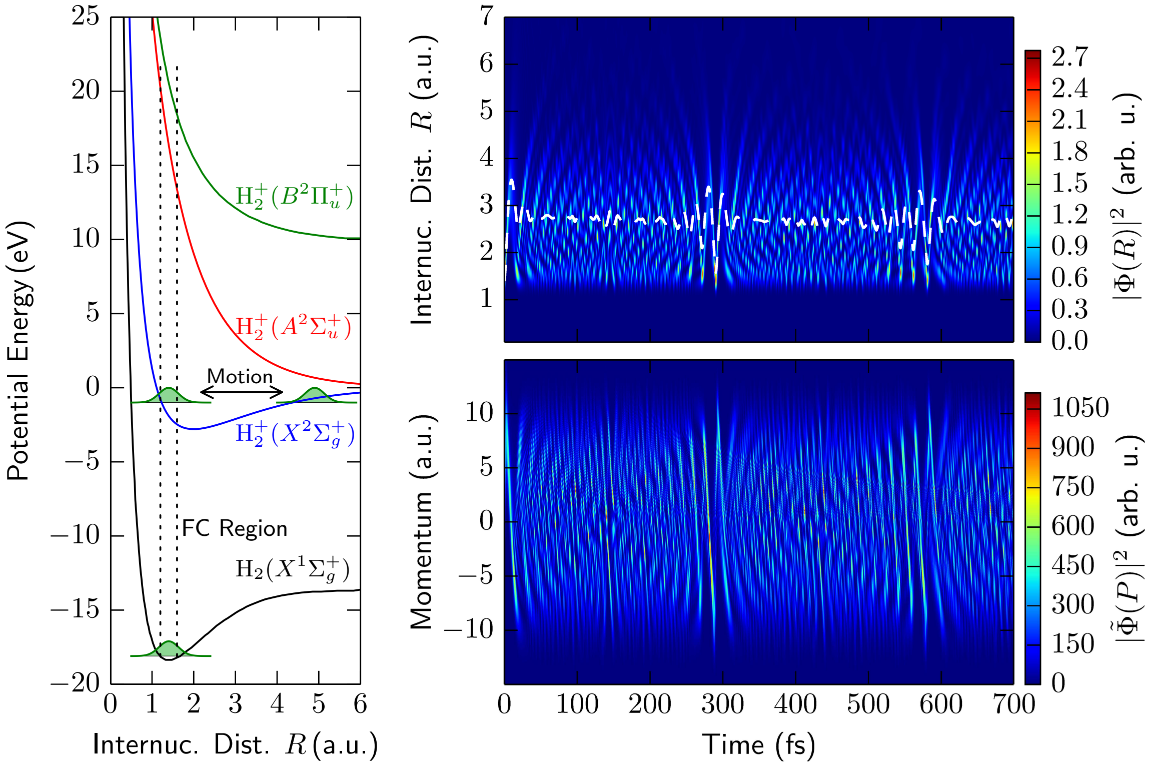

Figure 5.10: Left: Potential energy curves for the neutral H_2 ground state and the three energetically lowest H_2^+ ionic states. The region of significant Franck-Condon overlap is indicated by the dotted lines. Curves are adapted from [183]. Right: Simulated time-dependency of the wave function density for the coordinate space (top) and for the momentum space (bottom). Because the ionization by an XUV photon vertically promotes the ground state wave function to the ionic potential, the initial wave packet in the simulation is the ground state function of the neutral H_2 molecule. The fine dashed line is the expectation value of the internuclear Distance $\langle R\rangle = |\langle\Phi(R)|R|\Phi(R)\rangle|^2$, where $\Phi(R)$ is the nuclear wave function on the $H_2^+(X\,^2\Sigma_g^+)$ potential. At times when the wave packet is well localized, the time-dependence of $\langle R\rangle$ corresponds to the classical motion.

principle the nuclear wave function is projected onto the set of vibrational states belonging to the potential of the binding electronic state (compare Franck-Condon principle [122–125]). As the nuclear wave function is no longer a single eigenstate of the potential but rather a superposition of many states, it becomes time-dependent. A simulation, depicted in Fig. 5.10 (right), using the previously presented split-step algorithm visualizes this time-dependency of the wave function density for the coordinate space (top right) and for the momentum space[15] (bottom right). It is evident that the classical picture conveyed in Fig. 5.10 (left), where a localized wave

---

[15] Be aware that only the coordinate space wave function is normalized, as the momentum space wave function is computed by an unnormalizing FFT algorithm.

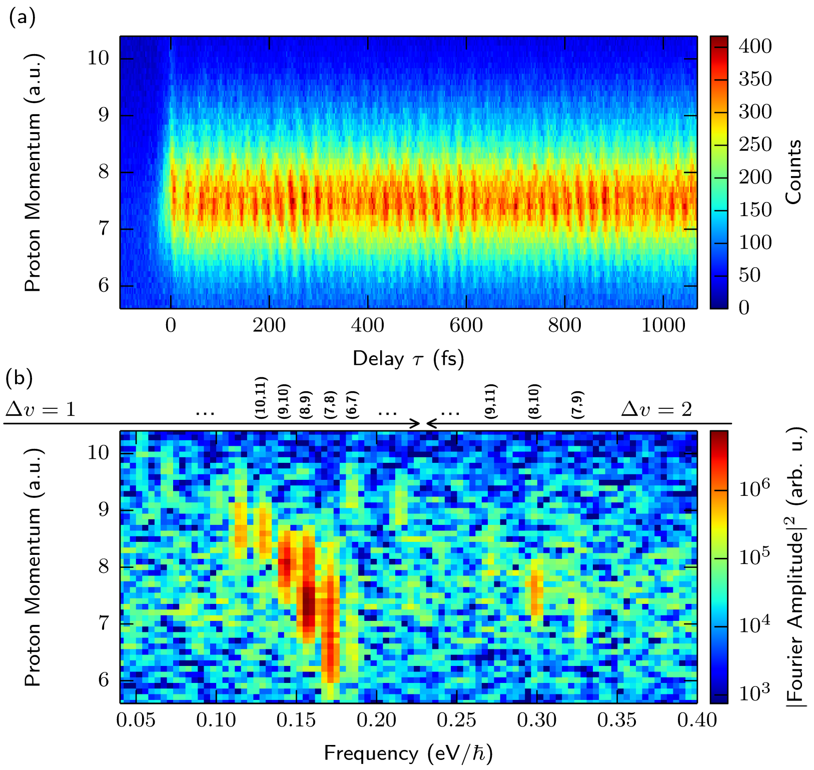

Figure 5.11: (a) Measured proton distribution $C(p,\tau)$ integrated over all detection angles θ as a function of the pulse delay τ and the proton momentum. Clearly visible is the rapid beating with a period of approximately 26 fs. The revivals of the wave packet discussed above are also clearly visible (half-revival period $T_{\text{rev}}/2 \approx 300\,\text{fs}$) (b) Fourier transform along the time delay direction of the count distribution $C(p,\tau)$. The distinct beating of neighboring vibrational states leads to the observed line structure. On the low frequency side, the vibrations induced by direct neighbors $\Delta v = 1$ show the highest amplitude. Further right, at higher frequencies the beating induced by $\Delta v = 2$ states is observed.

packet is moving in the potential is a over-simplified picture. The dephasing due to the anharmonicity of the $H_2^+(X\,^2\Sigma_g^+)$ described above leads to a smearing-out of the wave-packet's density[16] $\rho(R) = |\Phi(R)|^2$, where $\Phi(R)$ denotes the nuclear wave function in the potential of the binding $H_2^+(X\,^2\Sigma_g^+)$ electronic state. Only close to the revival times where the wave packet is well-localized it behaves like a classical oscillator.

The above presented time-dependent wave function [see Fig. 5.10 (right)] is, however, only accessible if the molecule is at certain time "probed". This means that the H_2^+ has to be dissociated by a second time-delayed laser pulse. This dissociation is achieved either by further ionizing the H_2^+ and, with this, inducing a Coulomb explo-

---

[16] The same argument holds for the wave function in momentum space.

sion[17] or by using the second laser pulse to resonantly couple the electronic ground state to a dissociative state leading to bond-softening (see Sec. 5.1.4). This intensity dependent bond-softening leads to a dissociation of the higher lying vibrational states. Figure 5.11 (a) shows the result for such a measurement, where the detected proton distribution $C(p,\tau)$ integrated over all detection angles θ as a function of time-delay τ and proton momentum is depicted. Clearly visible is a fast oscillation with a period of approximately 26 fs corresponding to the beating of directly neighboring vibrational states ($\Delta v = 1$). The previously discussed de- and rephasing manifests as a loss and regain of contrast in the measured proton yield. Applying a Fourier analysis, it is possible to determine the frequency contributions to the observed signal. To this end, we carry out a Fourier transform along the time-delay axis and obtain the result presented in Fig. 5.11 (b). At the low frequency side of the spectrum with highest amplitude, we observe contributions from directly neighboring states ($\Delta v = 1$). With increasing frequency, additional contributions from states with $\Delta v = 2$ begin to appear. Since the beating frequencies correspond to the energy separations of two vibrational states, we are able to identify each line and ascribe a pair of vibrational states to it [see labels above Fig. 5.11 (b)]. We find that the states $v = 7$ to $v = 10$ contribute the most to the observed signal. By comparing this finding to Fig. 5.8, where the Floquet curves for a laser intensity of $I = 5.1 \cdot 10^{12}\,\mathrm{W/cm^2}$ are shown, we see that the observed states are the ones energetically located in the formed gap between the upper and lower Floquet state (in the next section *Intensity Dependence and Intensity Calibration*, we learn that the peak intensity in the presented measurement is indeed $I = 5.1 \cdot 10^{12}\,\mathrm{W/cm^2}$).

Intensity Dependence and Intensity Calibration

In Sec. 5.1.4 we showed that the field-dressed Floquet states depend on the coupling laser intensity. Hence, the observed nuclear wave-packet dynamics must also be intensity dependent. The coupling is a function of the electric field component parallel to the molecular axis [compare Eq. (5.68)], and we can exploit this feature by selecting events where the molecular axis was oriented under an angle θ with regard to the electric field polarization axis. With this, we are experimentally able to post-select the effective field strength as a function of θ

$$\mathcal{E}_{\parallel}^{\mathrm{eff}} = \mathcal{E}_{\mathrm{peak}} \cdot \cos(\theta). \tag{5.71}$$

The experimental peak intensity is a priori unknown and is determined by comparing the experimentally obtained data, for parallel oriented molecules, to quantum simulations using the split-step algorithm described in Sec. 5.1.3. The best results are obtained for $I_{\mathrm{peak}} = 5.1 \cdot 10^{12}\,\mathrm{W/cm^2}$, $\sigma_{\mathrm{FWHM}}^{IR} = 8.6\,\mathrm{fs}$ and $\lambda_0 = 752\,\mathrm{nm}$, which

---

[17] In the absence of electrons the two protons strongly repel one another and the former molecule explodes.

are the peak intensity, the pulse duration T_{FWHM}, and the central wave length λ_0 of the coupling laser, respectively. Having fixed these parameters, we compare the experimental data for different effective field strengths to the corresponding quantum calculations. Figure 5.12 shows the results of the comparison in the frequency domain, which has the advantage of less time-independent background influencing it over the time-domain. It should be noted that the parameters were fixed for the highest intensity. The lower intensities were calculated from the maximal intensity by using Eq. (5.71).

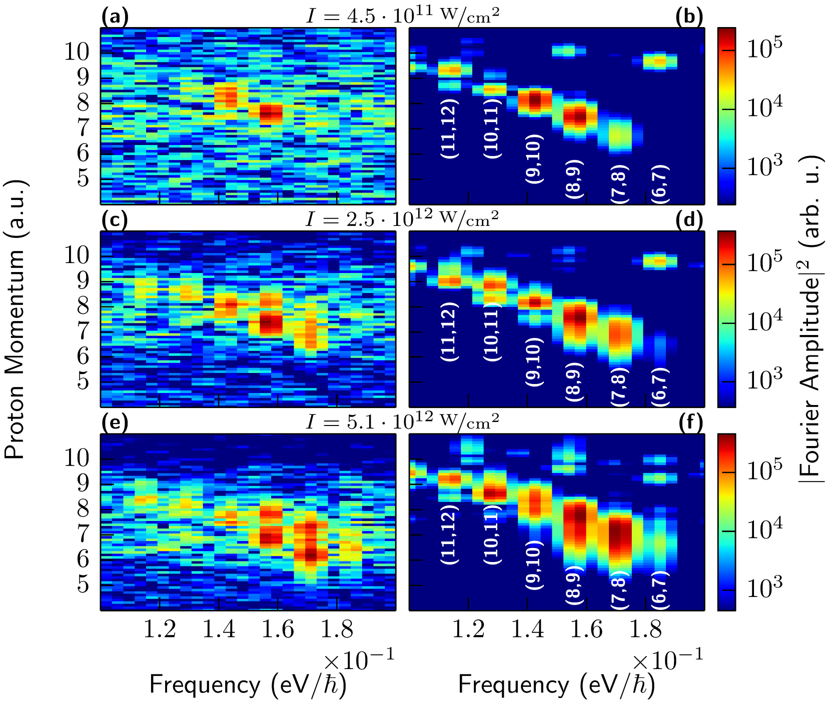

Figure 5.12: Comparison between experimental data and quantum computation. Three different intensities are shown, which are experimentally selected by choosing the angle θ between the molecular axis and the polarization axis of the laser field. Clearly visible are the lines corresponding to the beating of neighboring vibrational states ($\Delta v = 1$). We obtain very good agreement of the experiment with the simulation for all three laser intensities.

Excellent agreement between measurement and calculation is obtained for all intensities. We observe, as expected from the discussion in Sec. 5.1.4, that for increasing intensities the deeper bound vibrational states are freed. The decrease of momentum with increasing oscillation frequency of the fragments can best be understood if we consider Fig. 5.6 and Fig. 5.8, which show that for higher intensities the lower lying vibrational states can overcome the potential barrier. However, as the dissociation limit does not change for higher intensities, the momentum of the dissociating particles is smaller for more deeply bound states.

It should be highlighted (an explanation is delivered later on) that a broadening of the momentum spread of the individual Fourier lines with increasing intensities is observed. Besides this, it appears that the Fourier lines corresponding to more deeply bound vibrational states also experience a more pronounced broadening of the momentum distribution. This aspect is a key point of the analysis presented in the following sections.

5.2.3 The Fourier Phase: Footprints of Non-Energy Conserving Molecular Dynamics on Field-Dressed Potentials

The above presented Fourier analysis of the wave-packet motion and the discussion of revivals due to the de- and rephasing of a wave-packet in an anharmonic potential, has been subject to many studies, e.g. [24–27,30,31,184]. In these studies, however, only the absolute square of the Fourier amplitudes was investigated. Since the Fourier transform yields a complex signal, the modulus represents only half the information available. The other half is contained in the phase of the complex number, which holds the dynamical information of the dissociation process. Figure 5.13 (a) shows the absolute squared value of the Fourier amplitudes. When a single line's modulus and phase (here corresponding to the vibrational states $v = (7,8)$, indicated by the black box) is drawn into a one-dimensional plot [see Fig. 5.13 (b)], a proton momentum dependent phase is observed.

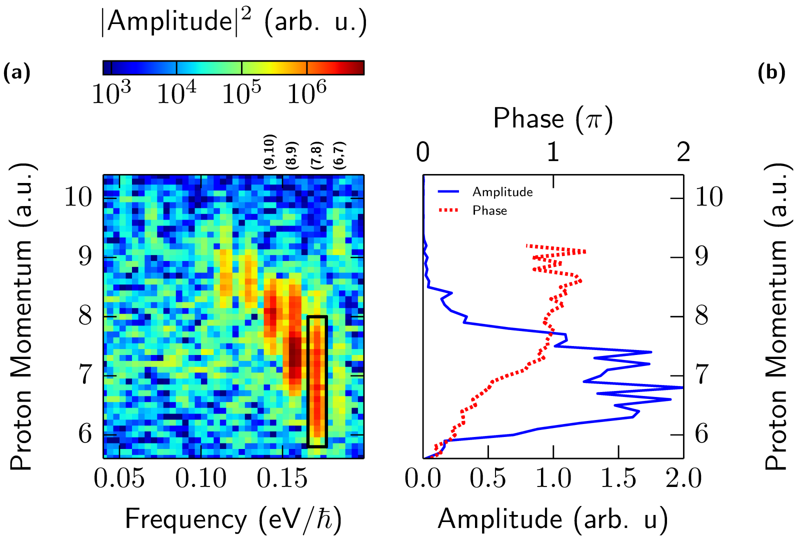

Figure 5.13: (a) Fourier transform of $C(p,\tau)$ depicted in Fig. 5.11 (a). (b) Modulus of Fourier amplitude (modulus of a complex number) and phase along the column indicated by the black box in (a). The phase changes by approximately π as a function of the proton momentum.

In order to give an intuitive meaning to this phase it is instructive to apply a windowed inverse Fourier transform, which transforms a single line of the spectrum depicted in Fig. 5.13 (a) [such a pair is shown in Fig. 5.13 (b)] back to a time-domain signal, shown in Fig. 5.14. The process of applying an inverse Fourier transform to selected frequency parts of a spectrum is called wavelet analysis. The phase change as a function of the proton momentum [see Fig. 5.13 (b)] is essentially equivalent to a time-delay dependent proton momentum of the distribution (see Fig. 5.14). Knowing that in the unperturbed molecular potential the vibrational states have a sharply defined energy, this time-delay dependent change in the observed momentum is a first indication of a non-energy conserving process which has to take place in the dissociation step. As a non-energy conserving process always requires for the time-translation-symmetry of the Hamiltonian to be broken, we conclude that the cause has to be the coupling laser initiating the dissociation by time-dependently field-dressing the PES. Therefore, the phase has to be regarded as the first signature of non-energy conserving molecular dynamics on field-dressed potential energy surfaces. It should be noted that the time-domain signal (Fig. 5.14) extracted by the inverse Fourier transformation now oscillates around zero instead of the average count number, due to the omission of the DC component. This arises from the inverse Fourier transform only considering a single beating line while neglecting the non-oscillating part of the signal (zero frequency part of the signal). This means that the obtained spectrum represents only the oscillatory part of the true time-domain signal. Physically, an amplitude of −1 corresponds to the case of minimal dissociation and 1 to the case of maximal dissociation.

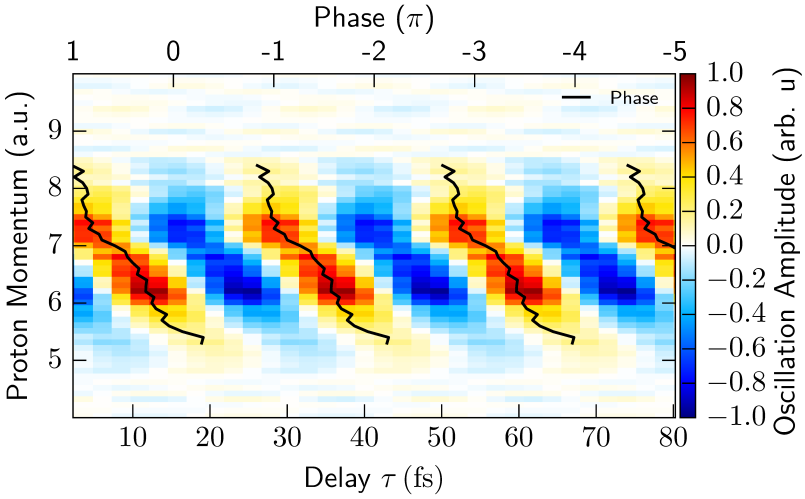

Figure 5.14: Wavelet analysis of a single Fourier line. The phase has been drawn into the time-dependent spectrum to make the phase-time correspondence more obvious. The phase is depicted as a maximum trace of the time-domain signal.

Having established the wavelet analysis as a mathematical tool to filter out a time-domain signal with a specific oscillation period, we now have to give a physical meaning to this time-domain oscillation (see Fig. 5.14). Because it is difficult to establish the validity of the following statement we simply assert at this point (and show later):

Assertion 5.2.1 *The time-domain signal extracted using the wavelet analysis (a windowed inverse Fourier transform of a single proton momentum dependent Fourier line) yields a very good approximation to the oscillatory part of the signal that would have been obtained in a measurement only involving exactly two isolated vibrational states.*

In order to motivate the truth of this assertion we consider the Fourier transform shown in Fig. 5.11 (b). We find that all significantly contributing Fourier lines can be uniquely assigned to a pair of vibrational states with $\Delta v = \{1, 2\}$. Further we know that the wave function of two vibrational states v_i and v_j with $\Delta E = [E(v_i) - E(v_j)]$ is strictly periodic with a period of $T = {}^{2\pi}/_{\Delta E}$. This implies that the probing process must also be periodic with T for this system. We know that any periodic function with periodicity T can be expanded into a Fourier series

$$f(t) = f(t+T) = \sum_{n=0}^{\infty} a_n \cos\left(n\frac{2\pi}{T}t + \phi_n\right) = \sum_{n=0}^{\infty} a_n \cos\left(n\Delta E \cdot t + \phi_n\right). \tag{5.72}$$

From this it is directly evident that if the asserted statement were not true, we would expect Fourier components at higher frequencies of multiples n of $\Delta E = n\,[E(v_i) - E(v_j)]$, as the wavelet analysis presented above only considers the fundamental frequency of the state beating [$n = 1$ in Eq. (5.72)]. These higher frequency components are not significantly present in Fig. 5.11 (b).

To justify this argument further, the next section describes a simulation verifying the discussion presented above. There, we also quantify what is meant by "*[...] [the wavelet analysis] yields a very good approximation [...]*". Only then, with the quantification of the quality of the approximation, can the assertion made above be considered a fact.

Using Wavelet Analysis to Extract the Signal of Isolated Vibrational States

This section quantifies the validity of the assertion 5.2.1. For this, two quantum simulations are performed: (I) the initial wave packet that is propagated consists of exactly two vibrational states (exemplary the states $v = 8$ and $v = 9$) shown in Fig. 5.15 (a) and (II) the initial wave function is the complete wave packet (including all vibrational states according to their Franck-Condon weight) as shown in Fig. 5.15 (b). Figure 5.15 shows the resulting time-delay spectra for both cases. We find that case (I) is, as expected, strictly periodic with the beating frequency of the two vibrational states, whereas case (II) features a much more complicated structure. In

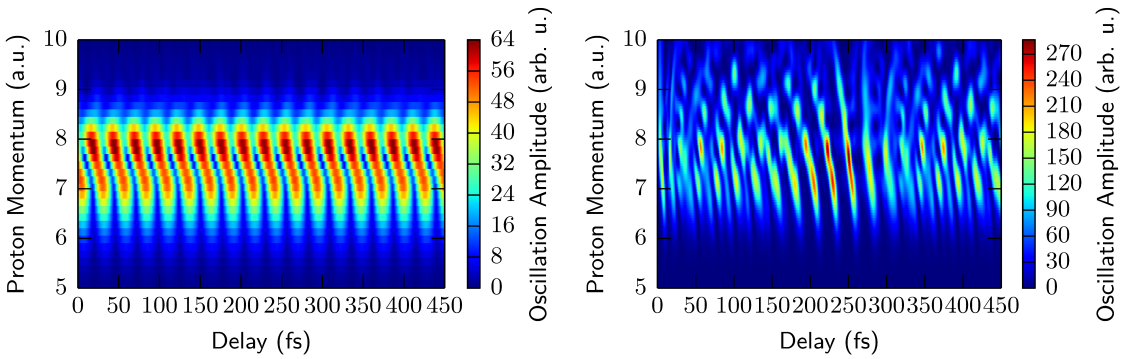

(a) Simulated time-delay spectrum for the two isolated vibrational states $v = (8, 9)$.

(b) Simulated time-delay spectrum for the complete Franck-Condon wave packet.

Figure 5.15: Left: Time-delay spectrum for case (I), where only two isolated vibrational states are initially populated. A perfectly periodic signal is obtained. Right: Time-delay spectrum for case (II), where the complete Franck-Condon wave packet was propagated. Due to the many frequency components involved in the problem, de- and rephasing of the wave packet is observed.

order to provide evidence for the assertion 5.2.1, we first extract the time-domain signal of the vibrational state pair $v = (8, 9)$ from the one shown in Fig. 5.15 (b). We then Fourier transform, the spectrum in Fig. 5.15 (a) to demonstrate that the beating of the two isolated vibrational states is described very well by the $n = 1$ term of the Fourier series [Eq. (5.72)].

In order to perform the first step, we apply the above presented wavelet analysis to the time-delay spectrum depicted in Fig. 5.15 (b). By selecting the line corresponding to the $n = 1$ contribution of the states $v = (8, 9)$ we retrieve the time-domain signal of the two states. As mentioned above the wavelet analysis is not capable of extracting the constant offset (a strictly positive oscillation always has a zero frequency component), therefore, to be able to compare the extracted signal with the two-state simulation, we subtract from the spectrum shown in Fig. 5.15 (a) line-wise (lines of equal proton momentum) the average value (DC offset). Figure 5.16 shows the two results in comparison: left the average subtracted two-state simulation and right the extracted signal from the time-domain signal. We find that the right one [simulation case (II)] very accurately matches the left one [simulation case (I)], which means that the wavelet analysis really extracts a valid approximation to the time-delay dependent oscillatory spectrum of two isolated vibrational states.

To quantify the deviation from the true signal [Fig. 5.16 (a)] we now perform a Fourier analysis of the two-state time-domain signal, shown in Fig. 5.17. As expected [compare Eq. (5.72)] the spectrum consist of Fourier lines with frequencies being integer multiples of the fundamental beating frequency ΔE of the two vibrational states. Further we observe that the amplitude of the fundamental beating frequency is by far the highest. Higher order contributions $n = \{2, \dots, \infty\}$ only contribute a

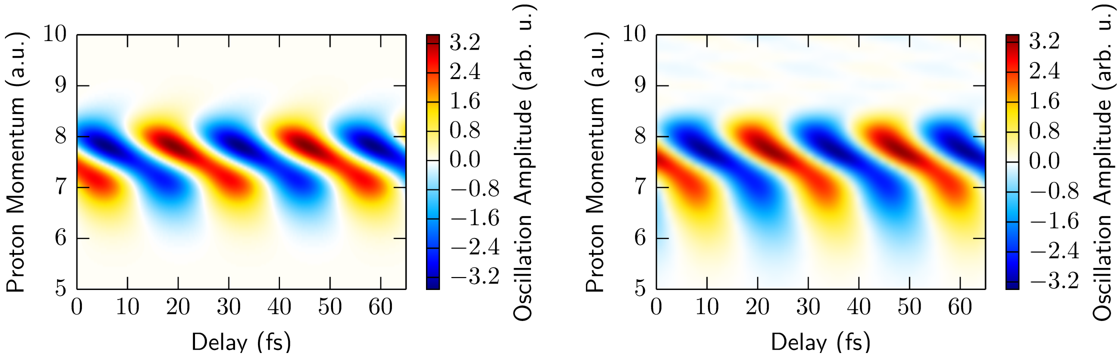

(a) TDSE with only two vibrational states. As the wavelet analysis cannot reproduce the constant signal offset, the signal was average subtracted to make a comparison easier.

(b) TDSE of full Franck-Condon wave packet with subsequently applied wavelet analysis of a single Fourier mode.

Figure 5.16: Comparison of the simulated time-domain signals corresponding to (a) a nuclear wave packet consisting of only two vibrational states and (b) filtered (wavelet analysis) time-domain signal, to extract the contribution of two vibrational states to the complete time-domain signal. Very good agreement is achieved which means that the wavelet analysis indeed reconstructs a time-domain signal equivalent to one obtained if only two vibrational states were excited by the pump-pulse.

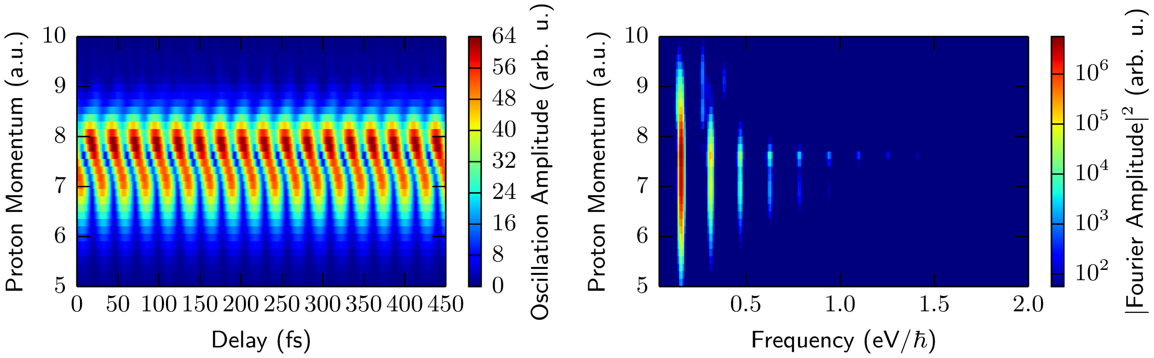

Figure 5.17: Left: Time-domain signal of a TDSE simulation considering only the two vibrational states $v = (8, 9)$. A periodic function of the delay time is observed. The expected period of $T = 26.4\,\mathrm{fs}$ is well reproduced. Right: Fourier transform of the time-domain signal (zero frequency contribution is not shown). As expected, integer multiples of the fundamental frequency corresponding to $\Delta E = 0.156\,\mathrm{eV}/\hbar$ are observed. However, we also find that the fundamental frequency has by far the strongest contribution and higher orders only contribute a few percent to the total time-domain signal. From this we conclude that the time-domain signal caused by probing two isolated vibrational states is very close to a sinusoidal signal (except for the constant offset).

few percent to the total time-domain signal. This observation ultimately justifies the assertion 5.2.1, as it means that the wavelet analysis extracts the time-domain signal of only two vibrational states with an error of only a few percent.

To conclude, this means that using the above presented wavelet analysis we are able to filter out the effect two isolated vibrational states have to the total measured signal. It further allows, in contrast to previously presented works, to directly compare experimental data to theory on a very fundamental level; the beating signature of individual vibrational state pairs becomes experimentally accessible. In the next sections, the advantages of the wavelet analysis to explore fundamental mechanisms in laser-induced photodissociation is exploited.

5.2.4 Using the Wavelet Analysis to Investigate Laser-Control in Photodissociation

In this section, we use the above discussed wavelet analysis to extract the signal of isolated vibrational states in order to obtain detailed insight in the dissociation process induced by the coupling laser (see the reaction described in Eq. 5.70). For this, we first review the results obtained by the wavelet analysis shown in Fig. 5.14 and Fig. 5.16 (b). Physically, the featured time-periodic structure corresponds to the dissociation signal that would be obtained if only two vibrational states were initially populated by the pump-process. Because the wavelet analysis cannot account for the constant offset of the dissociation signal as only one Fourier component is used [which can be written as $A\cos(\omega\tau)$]. This has the consequence that the oscillation is symmetric around the zero and the minimal (negative) signal corresponds to the least and the maximal (positive) signal to the largest dissociation. For each period of the signal, a decrease of the measured momentum as a function of the time-delay is observed which we will in the following refer to as a periodic momentum change or periodic momentum decrease.

Since this periodic momentum change (decrease with increasing time-delay) is a function of the coupling-laser's time delay (see Fig. 5.14 and Figs. 5.16), changing the delay exerts a control over the final proton velocity. The control aspect of the fragments momentum is of high interest and hence so is a detailed understanding of its underlying mechanisms.

However, the dissociation reaction involved in many of these control schemes is very complex in nature, even for the case of H_2^+, as not only many vibrational states contribute to the final momentum distribution, but in addition two electronic states are involved in the photodissociation. Further, in the high intensity regime the non-linearity of the processes renders the outcome very sensitive to the exact intensity and pulse duration. In order to simplify the description of the system, we employ a wavelet analysis to reduce the observed time-signal of quantum beating to that caused by only two individual states. With this, we gain experimental and theoretical access to one of the most elementary cases of molecular wave packet dynamics where the molecular motion is described by the superposition of exactly two vibrational states.

Figure 5.18 shows the measured data in comparison to the theoretical calculation without the application of a wavelet analysis. Very good qualitative agreement is achieved, but a quantitative comparison remains difficult. This is partly due to the time-independent background of the measured spectrum which is, among other effects, caused by experimental inaccuracies as well as incoherence effects, e.g. the finite excitation time in the pump step.

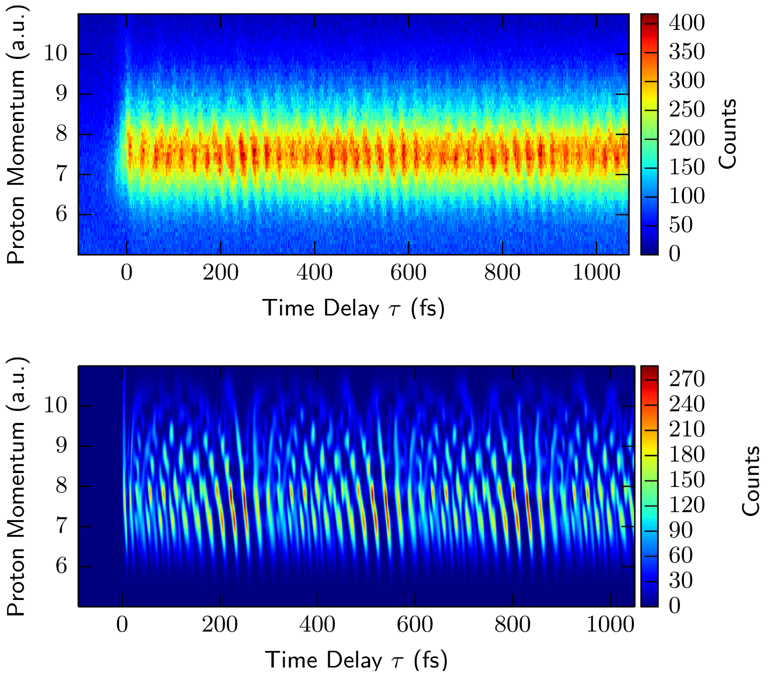

Figure 5.18: Comparison of full time-delay spectra of the experiment (top) to the quantum simulation (bottom). Very good qualitative agreement is achieved, but quantitatively comparison remains difficult.

The application of the wavelet analysis allows for a more detailed comparison of the experimental data with the simulations. The results for three different pairs of vibrational states, namely $v = (6, 7)$, $v = (7, 8)$ and $v = (8, 9)$, are shown in Fig. 5.19 (left column features the measurement and the right one the simulation). This comparison shows that the coherent part of the wave packet dynamics is very well reproduced. However, small deviations between the theory and the experiment persist and have to be assigned to the fact that the experimental conditions are not perfectly known. One of the main problems is that the coupling-laser pulse cannot be characterized precisely and in the simulation a Gaussian pulse is assumed. These factors may explain the difference between the experimental results and the calculated data.

Let us now come back to the time-dependence of the observed spectra. For all three state pairs a periodic change of the momentum of the observed proton is found with increasing time-delay. This means that by varying the time-delay of the control-pulse, we can influence the final momentum of the dissociating proton for each pair

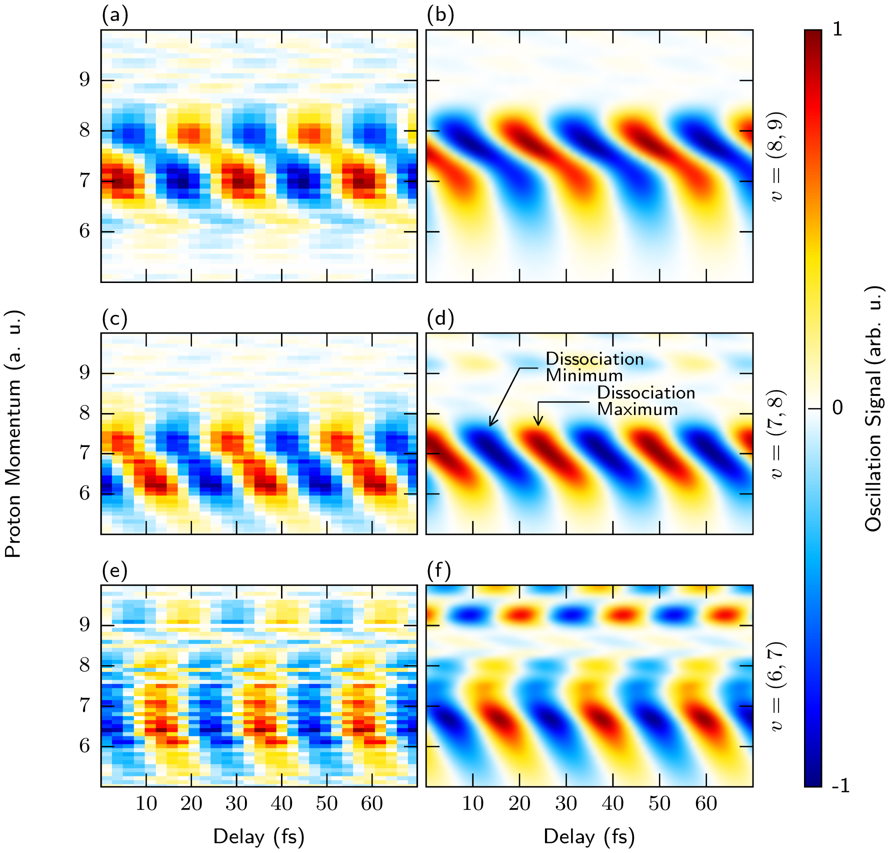

Figure 5.19: Left column: Wavelet analysis for the vibrational state pairs $v = (6, 7)$, $v = (7, 8)$ and $v = (8, 9)$ of the experimental data. Right column: Same as left for the theoretical calculation. Very good agreement of the quantum calculation to the measurement is obtained. With the wavelet analysis a quantitative comparison of theory and experiment becomes possible. Because of the inverse Fourier transform involved in the process omitting the DC component of the spectrum, the time-domain signal oscillates between -1 and 1. The negative value -1 correspond to the case of minimal dissociation and 1 to the maximal dissociation.

of vibrational states[18].

Having established the time-delay dependence for multiple vibrational state pairs, we now investigate the intensity dependence of the final proton momentum. For this consideration we choose the vibrational state pair $v = (8, 9)$ because it exhibits

---

[18] It should be noted, that the conducted experiment does not populate the vibrational state pairs selectively, which is why a control of the kinematics of individual states cannot be achieved. Only for time-delays where the complete wave packet rephases (revival) [see Fig. 5.18 (top)] does the time-domain signal become clearly delay dependent. For this time-delay region a control over the dissociation kinematics (final proton momentum) is possible. However, the aim here is not to control the dissociation kinematics, but to understand the mechanisms allowing to influence the reaction dynamics.

a pronounced time-delay dependence for high intensities and in addition it is, in contrast to more deeply bound vibrational states, dissociated even by weak coupling-laser fields. Changing the laser-intensity is achieved by selecting different angles θ between the molecular axis and the polarization axis of the electrical field. Again, the transition's selection rules allow only the electric field component parallel to the molecular axis to induce the electronic transition. Therefore, by changing the selected angle θ (between the molecular axis and the polarization axis) the effective field strength is changed. Here we have again chosen the same angles and, hence, the same intensities, as previously in Sec. 5.2.2 *Intensity Calibration*, namely $I = 5.1 \cdot 10^{12}\,\mathrm{W/cm^2}$, $I = 2.5 \cdot 10^{12}\,\mathrm{W/cm^2}$ and $I = 4.5 \cdot 10^{11}\,\mathrm{W/cm^2}$. Figure 5.20 shows the results of the intensity scan for the experimental data (left column) and for the calculation (right column). We find that with decreasing intensity the time-delay dependent control

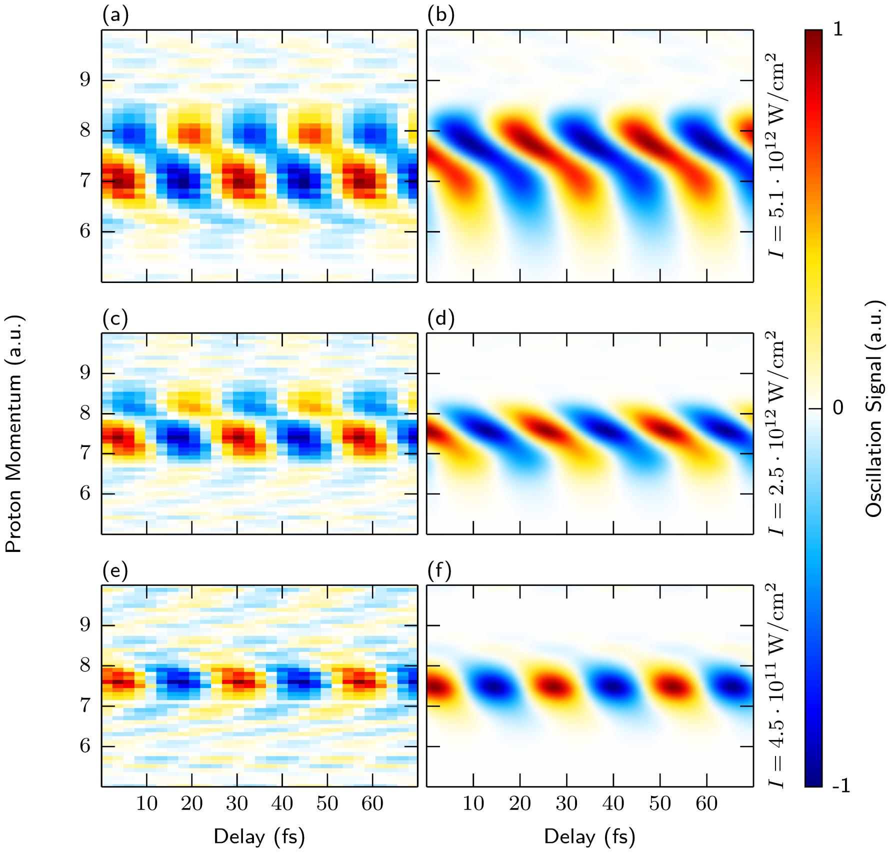

Figure 5.20: Left column: Measured proton signal corresponding to the vibrational state pair $v = (8, 9)$ as a function of the delay and momentum. For increasing intensity the proton momentum spread broadens. Right column: Same as left, but for the quantum simulation. A broadening of the observed momentum for increasing intensity is clearly visible. Therefore, with increasing laser intensity the influence on the final proton momentum becomes larger.

over the final proton momentum becomes weaker and almost vanishes for the lowest intensity. This is expected, as with a reduction of the laser intensity the time-dependent part of the Hamiltonian decreases in amplitude. In terms of the dressed PES this means that the avoided crossing opens less and thus the dissociation process becomes less non-linear. Therefore, this decrease of intensity performs the transition from a control-scheme to a traditional pump–probe scheme, in which a perturbation of the wave function by the coupling laser is an unavoidable need.

Despite being able to compute and excellently predict the behavior of the experiment through coupled-channel quantum calculations, we have so far not learned much about the mechanism changing the proton's final momenta. In order to address this issue, we present a semi-classical model in the next section which allows for an intuitive interpretation of the experimentally and theoretically obtained results.

5.2.5 Description of Control-Process by a Semi-Classical Model

In this section we introduce a semi-classical model which has the purpose of explaining the observed time-delay dependence of the measured proton fragments [see Fig. 5.19] in terms of a classical mechanism. It is clear that a classical particle in a potential is in general no substitute for a quantum mechanical simulation, as it cannot account for many observed effects. However, defining a suitable range of application such that the features of an observation can be reproduced is often very instructive, as it yields a physical interpretation of the process under investigation, which is the purpose of the model presented.

The semi-classical description which is going to be used throughout this section, regards the nuclei as classical particles on the field-dressed molecular PES. By solving Newton's equations the motion on the PES can be calculated.

In contrast to the classical description of the nuclear motion, the interaction of the laser field with the molecular potential curves has to be described quantum mechanically, as we have seen in Sec. 5.1.4. As a result, combining the classical particle propagation with the quantum mechanical effects of field-dressing of PES yields a semi-classical description.

One of the key features of a classical particle in the one-dimensional binding potential of the H_2^+ molecule is that the periodic trajectory is completely determined by the initial position and velocity of the particle. Since in the absence of a laser field the anharmonic potential is energy conservative (time independent), it is clear that the classical oscillation period has to be a function of the total energy

$$E = p^2/2m + V(R) \tag{5.73}$$

of the particle. As the semi-classical model shall describe the molecular motion induced by two neighboring vibrational states, we choose a total energy for the particle corresponding to the average energy of the two neighboring ($\Delta v = 1$) vibrational states

$$E = \frac{E(v_i) + E(v_{i+1})}{2}. \tag{5.74}$$

This causes the classic particle to oscillate with a period very close to the quantum mechanical oscillation period of a wave function consisting of these two vibrational states

$$T = \frac{2\pi}{\Delta E} = \frac{2\pi}{E(v_{i+1}) - E(v_i)}. \tag{5.75}$$

In reality, the energy of a classical particle causing an oscillation period of $T = 2\pi/\Delta E$ does not exactly correspond to the average energy of the two vibrational states, but rather the energy E solving the following equation

$$T = 2\int\limits_{x_1}^{x_2} \frac{m}{\sqrt{2m[E - V(x)]}}dx = \frac{2\pi}{E(v_2) - E(v_1)} \tag{5.76}$$

with x_1 and x_2 being the turning points of the classical particle's motion and, hence, the two roots $x_{1,2}$ of

$$V(x) - E = 0. \tag{5.77}$$

Because

$$p = \sqrt{2m[E - V(x)]} \tag{5.78}$$

is identified to be the classical momentum p of the particle, the left-hand-side of the equation is nothing but the classical oscillation period, whereas the right-hand-side corresponds to the quantum mechanical oscillation period. The numerical solution (a derivation of an analytical expression is rather involved) for the case of the $\mathrm{H}_2^+(X\,^2\Sigma_g^+)$ potential yields an energy E very close to the average energy specified in Eq. (5.74) which validates our choice.

Being able to extract the contribution of isolated pairs of vibrational states from the data presented above via wavelet analysis and to reproduce the oscillation period of these two states by means of a semi-classical model, allows to further extend this simulation to the case where a coupling laser is present. For the laser intensities considered in this work only the 1ω avoided crossing opens (see Fig. 5.6). Therefore we propagate the classical particle on this time-dependent laser induced PES as shown in Fig. 5.22 (blue (time-dependent) surface). If the crossing opens at a time where the classical particle reaches the coupling region, the particle may overcome the potential barrier and the molecule dissociates. Otherwise it remains bound and continues to oscillate in the unperturbed $\mathrm{H}_2^+(X\,^2\Sigma_g^+)$ potential.

When the conditions are such that the molecule has dissociated, we can determine the final momentum and plot this as dotted lines (as a function of the time-delay) into Fig. 5.21. As in the experimental data and the quantum simulation, we again find a time-delay dependence (a periodic decrease) of the resulting proton momenta. It appears that the semi-classical model not only qualitatively reproduces these results, but also yields acceptable quantitative predictions. From this we conclude that the mechanism responsible for influencing the proton momentum as a function of the time-delay τ is also included in this simple description.

We are now in the position to use Fig. 5.22 to obtain an intuitive picture of the mechanism leading to the periodic decrease of the proton momentum as a function of the time-delay. Figure 5.22 illustrates the deformation of the potential induced by the coupling laser as a function of time and presents three different possible dissociation trajectories. By comparing the trajectories we see that for large time-delays (take a look at the arrow labeled $\tau = 15\,\mathrm{fs}$) the particle climbs the potential barrier while the laser intensity increases. With increasing laser intensity, the height of the potential

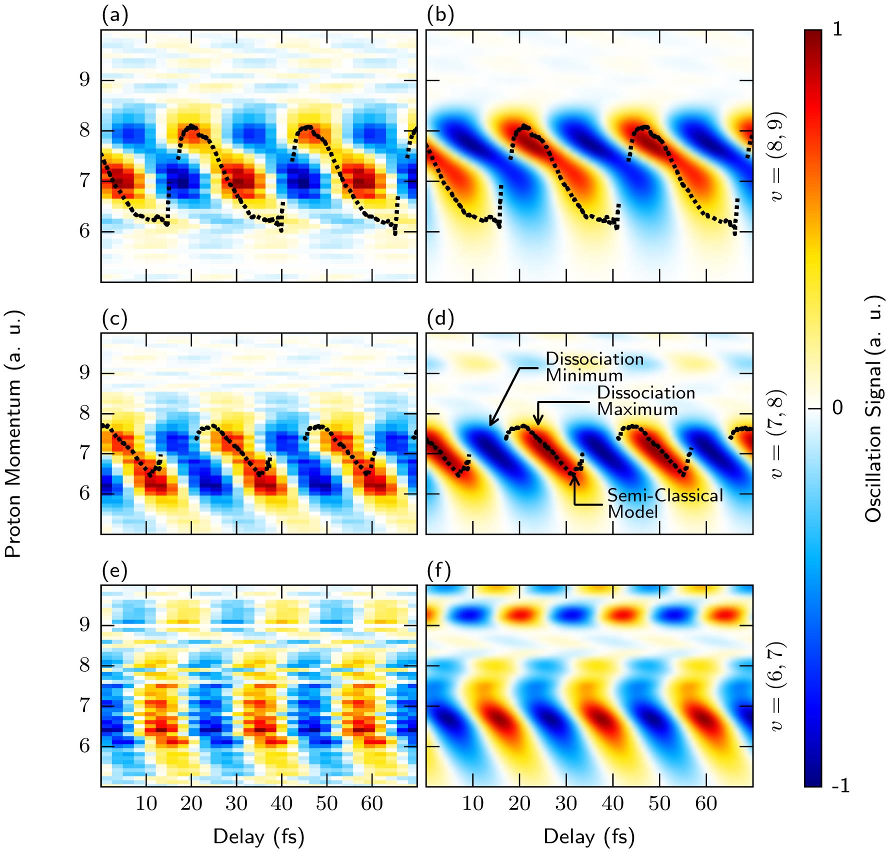

Figure 5.21: Left column: Wavelet analysis for the vibrational state pairs $v = (6,7)$, $v = (7,8)$ and $v = (8,9)$ of the experimental data. Right column: Same as left for the theoretical calculation. In addition to Fig. 5.19 the results of the semi-classical model are shown as black dotted lines. A very good quantitative agreement between the measurement, the quantum calculation and the semi-classical model is achieved. The semi-classical model does not make a prediction for the vibrational state pair $v = (6,7)$, because for the shown laser intensity of $I = 5.1 \cdot 10^{12}\,\mathrm{W/cm^2}$ the molecule is classically not dissociating.

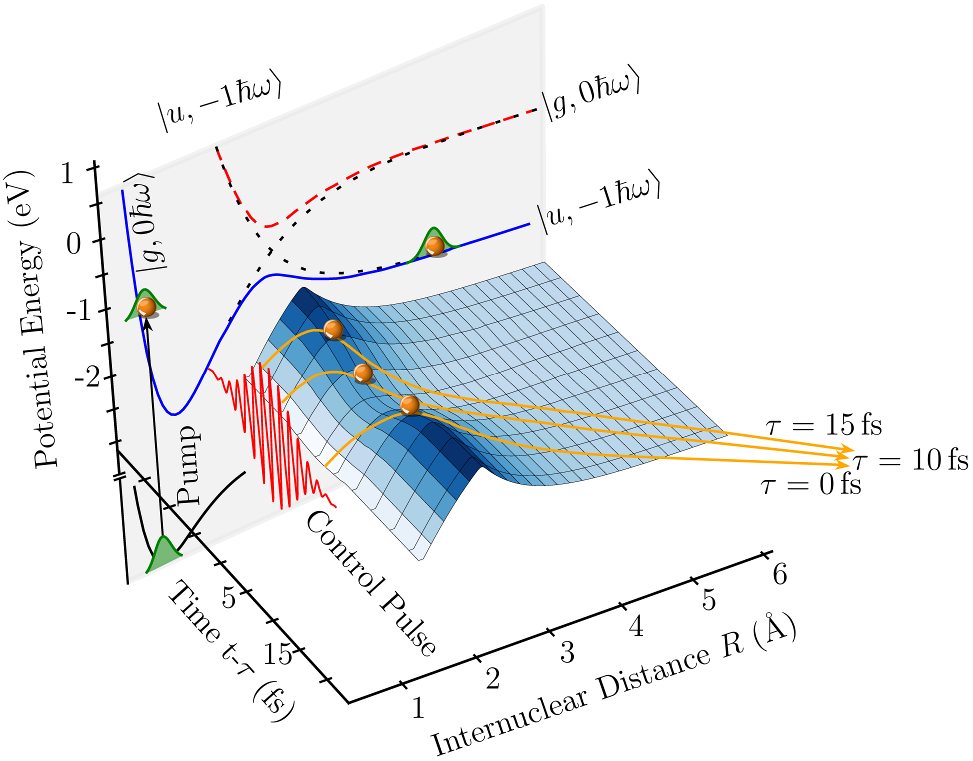

Figure 5.22: Illustration of the semi-classical model. The laser-induced potential energy curve on which the classical particles propagate is shown as blue surface (spanned by the reaction coordinate R and the time). For large laser intensities, the potential energy surface is lowered (as a function of time). This time dependency is responsible for the change of the final proton momentum. This is illustrated by three semi-classical trajectories (orange arrows), which are labeled to indicate the corresponding time-delay of the coupling laser. In the background, the lower (blue) and upper (red) laser induced potential energy curves are shown for the maximum electric field strength. In the coupling region (curve crossing) the states become maximal distorted.

barrier starts to decrease and hence the particle loses energy. On the other side of the potential, the particle again starts to accelerate, but the PES continues to decrease further lowering the total energy of the particle. After the particle has left the interaction region, the laser pulse intensity decreases, though, it no longer influences the dynamics of the particle. Since the particle lost energy during the dissociation, the final momentum is the lowest observed. The opposite case occurs for smaller time delays (compare arrow labeled $\tau = 0\,\mathrm{fs}$) when the particle traverses the interaction region while the intensity of the pulse is already decreasing. In this case, the barrier rises and the particle is elevated, gaining energy. Here, the final momentum is the largest, which is in agreement with the conduced experiment.

This up and down motion of the PES in the vicinity of the coupling region, depending on the laser intensity, can be viewed as an elevator. When the particle enters the elevator in its up-going phase, it gains energy. In contrast, when it enters the elevator going down (increasing intensity) it loses energy.

Another way of viewing the gain/loss of energy is depicted in Fig. 5.23 where

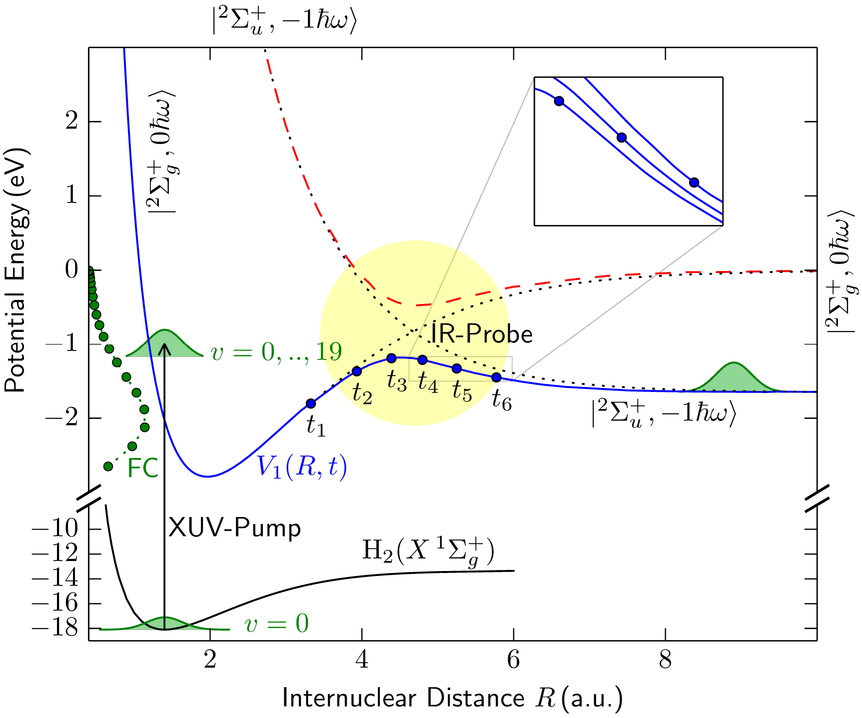

Figure 5.23: Alternative illustration of the elevator mechanism. The classical particle is shown for six time-positions (t_1-t_6). To show the elevator mechanism, the inset of the figure features the change of the field-dressed potential energy curve as a function of time (and therefore position of the particle). While the particle dissociates it is elevated by the potential energy curve and gains potential energy which manifests in a raised final proton momentum. The case where the particle losses energy is not illustrated (refer to Fig. 5.22).

the position of the classical particle is shown for six different times. The inset in the figure illustrates the energy gain when the particle traverses the PES, while the barrier height increases. The elevator mechanism occurs predominantly within the region highlighted by the yellow circle in Fig. 5.23.

The semi-classical model presented above therefore allows the interpretation of the observed dynamics in a very intuitive way, which we dub the “elevator” mechanism. Here, the particle’s potential energy is dynamically changed while traversing the coupling region. This change of potential energy ultimately manifests in a time-delay dependent final state proton momentum.

5.3 Brief Chapter Summary and Conclusion

In conclusion, by selecting the angles of the molecular axis with respect to the polarization of the coupling laser field, it is possible to select the effective intensity of the coupling laser. With this, the transition between the energy conserving dissociation dynamics to the non-conservative regime can be followed. Further, by selecting individual Fourier components, the vibrational dynamics of H_2^+ induced by the excitation of only two vibrational states has been observed. This allows the investigation of the most simple laser-induced molecular dissociation dynamics of a nuclear wave packet consisting of only two vibrational states. The TDSE calculation is, for all coupling laser intensities, in excellent agreement with the experimental results. Using this result and by employing a semi-classical model, it was possible to explain the dynamics involved in the dissociation process. It was shown that for strong fields the nuclei's kinetic energy is significantly changed during the dissociation process due to a semi-classical "elevator" effect. As molecular hydrogen, given its small mass, is the most quantum-dynamically behaving system, the accuracy of such an approach for predicting the momentum distributions of the fragments also supports the validity of the semi-classical treatment of larger molecules, where a complete quantum mechanical description fails due to the system's complexity.

6 Summary and Outlook

As a part of this thesis experiments were carried out and confirmed by calculations in which the interaction of laser light and hydrogen molecule's was investigated. In order to provide photon energies which are sufficiently high to ionize or even doubly excite the H_2, we employ the high-order harmonic generation process creating attosecond pulse trains. The photon energies lie within the range from approximately 16 eV to 40 eV (XUV radiation). Optionally, in order to be able to manipulate the ionic system following the ionization, a second infrared laser can be temporally delayed and overlaid with the XUV pulse. The time-delay is introduced by a piezo-driven delay stage which is part of a Mach-Zehnder type interferometer. The charged products of the dissociative ionization reactions were observed using a reaction microscope. With its unique capabilities the reaction microscope is able to coincidentally detect all charged particles created in a reaction with a solid angle close to 4π. Further, for processes where only a single neutral fragment is created the conservation of momentum additionally allows to reconstruct the corresponding momentum vector. With this it is possible to investigate the dissociative single-ionization of molecular hydrogen as it was done in this thesis.

The experiments conducted in this work can be split in two parts: (I) single-photon induced dissociative ionization of H_2 and (II) pump–probe investigations of the laser induced dissociation of H_2^+ molecules. The focus of the results presented in first part lies on the doubly-differential observation of a localization effect of the bound electron of the H_2^+ ion with respect to the emitted photoelectron. The effect is well explained using an intuitive semi-classical model and further confirmed by full quantum calculations which have been carried out by the group of Fernando Martín. The asymmetry is then employed in a novel technique to disentangle reaction pathways with which the lifetime of the energetically lowest doubly-excited $Q_1\,{}^1\Sigma_u^+$ state can be determined. These results are described in Chap. 4. In the second part XUV-pump pulses are used to ionize molecular hydrogen in order to prepare nuclear wave packets in the binding ground state of the H_2^+ ion. By using a second time-delayed IR-probe pulse the molecule is subsequently dissociated. A time-delay dependent momentum for the created protons is observed. Applying a Fourier analysis technique we are able to observe the dissociation dynamics for isolated pairs of vibrational states. By employing quantum calculations as well as a semi-classical model, we can explain the mechanism that leads to the time-delay dependence of the fragments momenta in an intuitive way. The results are described in Chap. 5.

Summary Part (I): Electron Localization Involving Doubly Excited States in Broadband Extreme Ultraviolet Ionization

The absorption of a high energetic XUV photon by H_2 leads to a manifold of different reaction scenarios (see Sec. 4.2). The dominant process is with 98% the creation of a stable molecular hydrogen ion. For photon energies above the threshold of 18.1 eV, in the ionizing transition to the $H_2^+(X\,^2\Sigma_g^+)$ electronic state about 2% of the vibrational states occupied are continuum states, which lead to a dissociation of the molecule. This process is referred to as ground-state dissociation yielding slow, and thus, low energetic protons.

Energetically above the $H_2^+(X\,^2\Sigma_g^+)$ electronic state many dissociative (repulsive) ionic as well as doubly-excited states exist. Since the doubly-excited states are embedded within the single-autoionization continuum they quickly autoionize due to electron-electron interactions. Further, as the dissociation occurs on the same timescale as the autoionization, excitation to the doubly-excited states contributes significantly to the ionization cross-section as well as to the dissociative ionization cross-section. The availability of a resonant and a non-resonant channel causes strong interference effects, which lead in the case of atoms to the famous Fano line shapes [103]. These line shapes contain important information such as lifetime of the excited states. In contrast, for H_2 due to the dissociative motion the Fano line shapes are not observable. However, the interference manifests as an observable electron localization in the molecular frame for which a fully coincident and kinematically complete experiment is required. In order to be able to construct the molecular frame an event-wise transformation has to be applied to the measured momentum vectors which requires a fully coincident and kinematically complete experiment.

The localization was measured doubly-differential in the electron kinetic energy as well in the proton kinetic energy (see Sec. 4.3). Only with such an approach is it possible to obtain a thorough understanding of the mechanisms responsible for the localization. As an explanation to the observed asymmetry we find that the quantum mechanical result of the two dissociation pathways can be described by means of an entangled wave function describing the bound electron as well as the photoelectron [see Eq. (4.34)]. By projecting the entangled wave function using an appropriately chosen projector a simple expression describing the asymmetry is readily derived. In order to give theoretical proof, in this thesis a differential[1] semi-classical model is used which exploits the WKB approximation. With this it is possible to explain the origin of the observed asymmetry in terms of the nuclear motion on the molecular potential energy curves. A very good agreement with the semi-classical calculations as well with a fully quantum mechanical computation (group of Fernando Martín) is achieved.

In a second step, with a working semi-classical model at hand the determination

---

[1] The model is differential in terms of kinetic energy release of the nuclei as well as in the photoelectron energy.

of the lifetime of the contributing doubly-excited state is possible (see Sec. 4.4). For this we use the interference signal which is described by the asymmetry amplitude to disentangle the contributions of the two channels. This allows the determination of the autoionization lifetime of the energetically lowest doubly-excited $Q_1\,{}^1\Sigma_u^+$ state for an experimentally unprecedented large range of internuclear distances. A lifetime as a function of the internuclear separation between 400 as and 1 fs is obtained.

Summary Part (II): XUV-Pump IR-Probe Investigation of Molecular Wave-Packet Dynamics on Laser-Induced Transition States

As mentioned above, the dominating ionization channel induced by a single photon is a transition to the $\mathrm{H}_2^+(X\,{}^2\Sigma_g^+)$ state which which is the electronic ground state of the molecular hydrogen ion. The ion is prepared in a superposition of various vibrationally excited states according to the Franck-Condon principle. As the excitation of the vibrational states happens coherently, an initially localized wave packet is formed which starts to evolve in time. The conceptual ideas behind the formation of wave-packets are conveyed in Sec. 5.1.1. Using a second, time-delayed infrared laser pulse the molecule is subsequently dissociated by coupling the $\mathrm{H}_2^+(X\,{}^2\Sigma_g^+)$ to the $\mathrm{H}_2^+(A\,{}^2\Sigma_u^+)$ state. With this it is possible to resolve the ultrafast vibrational dynamics of the molecular hydrogen ion. In the measurement a delay range of 1200 fs was scanned, which allows to analyze the wave-packet dynamics in terms of a frequency analysis using the Fourier transformation with a very high resolution of $3.4\,\mathrm{meV}/\hbar$.

Employing a windowed inverse Fourier transform it is demonstrated that the effect of isolated pairs of vibrational states can be analyzed. This approach drastically reduces the complexity of the investigated system. This allows to investigate the dissociation dynamics of the molecule on an extremely fundamental level, namely the nuclei's propagation on the laser induced transition state. The experiential results show a time-dependent momentum distribution of the measured protons. This is caused by the strong action of the coupling laser field. In order to further analyze the mechanism leading to the time-dependence, quantum calculations have been performed as part of this work which are in excellent agreement with the experimental data. In order to identify the acting mechanisms a semi-classical model which treats the effects of the laser onto the potential curves in the Floquet picture was developed. In this, the particles are propagated by solving Newton's equations of motion where the acting forces are given by the field-dressed (Floquet picture) potential energy curves. It is surprising that this classical approach is capable of not only predicting the momentum distributions of the protons qualitatively but also quantitatively. With this model it is possible to identify the mechanism responsible for the delay dependence of the proton's momenta as a classical "elevator". Essentially the "elevator" is the time-dependent potential energy curve of the laser induced transition state which changes as a function of the laser's electric field envelope. This time dependence of the potential energy curve increases or lowers the nuclei's energy as they move on the potential curve. Thus the “elevator” is capable of increasing or decreasing the fragments’ kinetic energy in their final state.

The validity of the above described semi-classical model for the lightest, and hence the most quantum mechanical system, indicates a broad applicability in quantum chemistry. It could for instance be used to predict and describe quantum control processes in larger molecules, where a quantum mechanical treatment is not possible. However, even shedding much light on the dissociation dynamics on a very fundamental level, so far we only have limited control over the reaction kinematics. This is due to the fact, that the XUV excitation populates many vibrational states and not just an isolated pair. It is therefore plausible that in future experiments employing theoretically described laser-induced vibrational state redistribution methods [185] will permit the preparation of wave packets of only two vibrational states. For such a system, the mechanism described here would allow a well controllable scheme for a targeted influencing of photochemical reactions.

A Atomic Units

Throughout this work atomic units are used (abbreviated as *a.u.*), as these simplify numerical calculations performed for atomic systems and are therefore often used in atomic physics. These atomic units are obtained by setting Planck's reduced constant $\hbar = {}^{h}/_{2\pi}$, the electron mass m_e, the elementary charge e and Coulomb's constant $k_e = {}^{1}/_{4\pi\epsilon_0}$ to unity (i.e. $\hbar = m_e = e = k_e$). Obviously, introducing this definition has an impact on other constants as well, e.g. the speed of light becomes $c = {}^{1}/_{\alpha} \approx 137\,\mathrm{a.u.}$ and the proton mass can be expressed as $m_p \approx 1836\,\mathrm{a.u.}$. Further, with this definition it is often important to convert from SI- to atomic-units, therefore a table showing conversion factors is given at this point (see Tab. A.1). Throughout this work, for the intensity I of an electric field with peak field strength of $E = 1\,\mathrm{a.u.}$ the value $I = {}^{1}/_{2}\epsilon_0 c E^2 = 3.51 \cdot 10^{16}\,{}^{\mathrm{W}}/_{\mathrm{cm}^2}$ is used.

Table A.1: Conversion factors from atomic- to SI units, based on the data given in Ref. [186].

Dimension	Value SI units	Value in other common unit
Time	$1\,\mathrm{a.u.} = 2.4188843265502(12) \cdot 10^{-17}\,\mathrm{s}$	
Length	$1\,\mathrm{a.u.} = 0.52917721092(17) \cdot 10^{-10}\,\mathrm{m}$	$1\,\mathrm{a.u.} = 0.52917721092(17)\,\mathrm{Å}$
Force	$1\,\mathrm{a.u.} = 8.23872278(36) \cdot 10^{-8}\,\mathrm{N}$	$51.4220652(11)\,\mathrm{eV/Å}$
Energy	$1\,\mathrm{a.u.} = 4.35974434(19) \cdot 10^{-18}\,\mathrm{J}$	$1\,\mathrm{a.u.} = 27.21138505(60)\,\mathrm{eV}$
Momentum	$1\,\mathrm{a.u.} = 1.992851740(88) \cdot 10^{-24}\,{}^{\mathrm{kg\,m}}/_{\mathrm{s}}$	
Velocity	$1\,\mathrm{a.u.} = 2.18769126379(71) \cdot 10^{6}\,{}^{\mathrm{m}}/_{\mathrm{s}}$	
Angular Momentum	$1\,\mathrm{a.u.} = 1.054571726(47) \cdot 10^{-34}\,\mathrm{Js}$	
Mass	$1\,\mathrm{a.u.} = 9.10938291(40) \cdot 10^{-31}\,\mathrm{kg}$	
Electric Field	$1\,\mathrm{a.u.} = 5.14220652(11) \cdot 10^{11}\,\mathrm{V}m$	$51.4220652(11)\,\mathrm{V/Å}$

When taking a look at the Bohr model, it becomes evident that atomic units are "custom made" to describe the atomic world. Considering an electron in the electronic ground state of the hydrogen atom then it has an ionization energy of ${}^{1}/_{2}\,\mathrm{a.u.}$, the velocity of $1\,\mathrm{a.u.}$, the angular momentum of $1\,\mathrm{a.u.}$ and an orbit period of $2\pi\,\mathrm{a.u.}$, where the orbit radius is $1\,\mathrm{a.u.}$.

Bibliography

[1] T. S. Rose, M. J. Rosker, and A. H. Zewail,
Femtosecond real-time observation of wave packet oscillations (resonance) in dissociation reactions,
The Journal of Chemical Physics **88**, 6672 (1988).

[2] A. H. Zewail,
Femtosecond transition-state dynamics,
Faraday Discuss. Chem. Soc. **91**, 207 (1991).

[3] A. H. Zewail,
Coherence - a powerful concept in the studies of structures and dynamics,
Laser Physics **5**, 417 (1995).

[4] A. H. Zewail,
Femtochemistry: Recent progress in studies of dynamics and control of reactions and their transition states,
J. Phys. Chem. **100**, 12701 (1996).

[5] A. H. Zewail,
Femtochemistry: Atomic-Scale Dynamics of the Chemical Bond,
J. Phys. Chem. A **104**, 5660 (2000).

[6] A. H. Zewail,
Femtochemistry. Past, present, and future,
Pure Appl. Chem. **72**, 2219 (2000).

[7] R. L. Platzman,
Superexcited States of Molecules,
Radiat. Res. **17**, 419 (1962).

[8] R. L. Platzman,
Superexcited states of molecules, and the primary action of ionizing radiation,
Vortex **23**, 372 (1962).

[9] N. Kouchi, M. Ukai, and Y. Hatano,
Dissociation dynamics of superexcited molecular hydrogen,
Journal of Physics B: Atomic, Molecular and Optical Physics **30**, 2319 (1997).

[10] R. Browning and J. Fryar,

Dissociative photoionization of H_2 and D_2 through the $1s\sigma$ ionic state,
J. Phys. B: At. Mol. Phys. **6**, 364 (1973).

[11] I. Sánchez and F. Martín,
The doubly excited states of the H_2 molecule,
The Journal of Chemical Physics **106**, 7720 (1997).

[12] S. Strathdee and R. Browning,
Dissociative photoionization of H_2 at 26.9 eV,
J. Phys. B: At. Mol. Phys. **9**, L505 (1976).

[13] S. Arai, T. Yoshimi, M. Morita, K. Hironaka, T. Yoshida, H. Koizumi, K. Shinsaka, Y. Hatano, A. Yagishita, and K. Ito,
Lyman-α excitation spectra in the photodissociation of the doubly excited states of H_2,
Z Phys D - Atoms, Molecules and Clusters **4**, 65 (1986).

[14] C. J. Latimer, K. F. Dunn, N. Kouchi, M. A. McDonald, V. Srigengan, and J. Geddes,
A dissociative photoionization study of the autoionization lifetime of the lowest $^1\Sigma_u$ superexcited state in hydrogen and deuterium,
J. Phys. B: At. Mol. Opt. Phys. **26**, L595 (1993).

[15] Y. M. Chung, E.-M. Lee, T. Masuoka, and J. A. R. Samson,
Dissociative photoionization of H_2 from 18 to 124 eV,
The Journal of Chemical Physics **99**, 885 (1993).

[16] C. J. Latimer, K. F. Dunn, F. P. O'Neill, M. A. MacDonald, and N. Kouchi,
Photoionization of hydrogen and deuterium,
The Journal of Chemical Physics **102**, 722 (1995).

[17] K. Ito, R. I. Hall, and M. Ukai,
Dissociative photoionization of H_2 and D_2 in the energy region of 25–45 eV,
The Journal of Chemical Physics **104**, 8449 (1996).

[18] T. Odagiri, M. Murata, M. Kato, and N. Kouchi,
(γ, 2γ) studies on doubly excited states of molecular hydrogen,
J. Phys. B: At. Mol. Opt. Phys. **37**, 3909 (2004).

[19] I. Borges Jr and C. E. Bielschowsky,
Doubly excited states of molecular hydrogen: theoretical absorption and photodissociation cross sections,
J. Phys. B: At. Mol. Opt. Phys. **33**, 1713 (2000).

[20] A. Lafosse, M. Lebech, J. C. Brenot, P. M. Guyon, L. Spielberger, O. Jagutzki, J. C. Houver, and D. Dowek,
Molecular frame photoelectron angular distributions in dissociative photoionization

of H_2 in the region of the Q_1 and Q_2 doubly excited states,
Journal of Physics B: Atomic, Molecular and Optical Physics **36**, 4683 (2003).

[21] F. Martín, J. Fernández, T. Havermeier, L. Foucar, T. Weber, K. Kreidi, M. Schöffler, L. Schmidt, T. Jahnke, O. Jagutzki, A. Czasch, E. P. Benis, T. Osipov, A. L. Landers, A. Belkacem, M. H. Prior, H. Schmidt-Böcking, C. L. Cocke, and R. Dörner,
Single Photon-Induced Symmetry Breaking of H_2 Dissociation,
Science **315**, 629 (2007).

[22] P. Agostini and L. F. DiMauro,
The physics of attosecond light pulses,
Rep. Prog. Phys. **67**, 813 (2004).

[23] A. Palacios, H. Bachau, and F. Martín,
Excitation and ionization of molecular hydrogen by ultrashort VUV laser pulses,
Phys. Rev. A **75**, 013408 (2007).

[24] R. W. Robinett,
Quantum wave packet revivals,
Physics Reports **392**, 1 (2004).

[25] A. S. Alnaser, B. Ulrich, X. M. Tong, I. V. Litvinyuk, C. M. Maharjan, P. Ranitovic, T. Osipov, R. Ali, S. Ghimire, Z. Chang, C. D. Lin, and C. L. Cocke,
Simultaneous real-time tracking of wave packets evolving on two different potential curves in H_2^+ and D_2^+,
Phys. Rev. A **72**, 030702 (2005).

[26] F. Légaré, K. F. Lee, I. V. Litvinyuk, P. W. Dooley, A. D. Bandrauk, D. M. Villeneuve, and P. B. Corkum,
Imaging the time-dependent structure of a molecule as it undergoes dynamics,
Phys. Rev. A **72**, 052717 (2005).

[27] H. Niikura, D. M. Villeneuve, and P. B. Corkum,
Controlling vibrational wave packets with intense, few-cycle laser pulses,
Phys. Rev. A **73**, 021402 (2006).

[28] T. Ergler, A. Rudenko, B. Feuerstein, K. Zrost, C. D. Schröter, R. Moshammer, and J. Ullrich,
Spatiotemporal Imaging of Ultrafast Molecular Motion: Collapse and Revival of the D2+ Nuclear Wave Packet,
Phys. Rev. Lett. **97**, 193001 (2006).

[29] B. Feuerstein, T. Ergler, A. Rudenko, K. Zrost, C. D. Schröter, R. Moshammer, J. Ullrich, T. Niederhausen, and U. Thumm,

Complete Characterization of Molecular Dynamics in Ultrashort Laser Fields,
Phys. Rev. Lett. **99**, 153002 (2007).

[30] M. Magrakvelidze, F. He, T. Niederhausen, I. V. Litvinyuk, and U. Thumm,
Quantum-beat imaging of the nuclear dynamics in D_2^+*: Dependence of bond softening and bond hardening on laser intensity, wavelength, and pulse duration*,
Phys. Rev. A **79**, 033410 (2009).

[31] F. Kelkensberg, C. Lefebvre, W. Siu, O. Ghafur, T. T. Nguyen-Dang, O. Atabek, A. Keller, V. Serov, P. Johnsson, M. Swoboda, T. Remetter, A. L'Huillier, S. Zherebtsov, G. Sansone, E. Benedetti, F. Ferrari, M. Nisoli, F. Lépine, M. F. Kling, and M. J. J. Vrakking,
Molecular Dissociative Ionization and Wave-Packet Dynamics Studied Using Two-Color XUV and IR Pump-Probe Spectroscopy,
Phys. Rev. Lett. **103**, 123005 (2009).

[32] F. He and U. Thumm,
Dissociative ionization of H_2 *in an attosecond pulse train and delayed laser pulse*,
Phys. Rev. A **81**, 053413 (2010).

[33] A. M. Weiner, D. E. Leaird, G. P. Wiederrecht, and K. A. Nelson,
Femtosecond Pulse Sequences Used for Optical Manipulation of Molecular Motion,
Science **247**, 1317 (1990).

[34] W. Jakubetz, J. Manz, and H. J. Schreier,
Theory of optimal laser pulses for selective transitions between molecular eigenstates,
Chemical Physics Letters **165**, 100 (1990).

[35] R. S. Judson and H. Rabitz,
Teaching lasers to control molecules,
Phys. Rev. Lett. **68**, 1500 (1992).

[36] A. M. Weiner,
Femtosecond pulse shaping using spatial light modulators,
Review of Scientific Instruments **71**, 1929 (2000).

[37] A. Assion, T. Baumert, M. Bergt, T. Brixner, B. Kiefer, V. Seyfried, M. Strehle, and G. Gerber,
Control of Chemical Reactions by Feedback-Optimized Phase-Shaped Femtosecond Laser Pulses,
Science **282**, 919 (1998).

[38] B. J. Sussman, D. Townsend, M. Y. Ivanov, and A. Stolow,
Dynamic Stark Control of Photochemical Processes,
Science **314**, 278 (2006).

[39] M. E. Corrales, J. González-Vázquez, G. Balerdi, I. R. Solá, R. de Nalda, and

L. Bañares,
Control of ultrafast molecular photodissociation by laser-field-induced potentials,
Nat Chem (2014).

[40] M. V. Ammosov, N. B. Delone, and V. P. Krainov,
Tunnel ionization of complex atoms and of atomic ions in an alternating electromagnetic field,
Zh. Eksp. Teor. Fiz **91**, 2008 (1986).

[41] V. S. Popov,
Tunnel and multiphoton ionization of atoms and ions in a strong laser field (Keldysh theory),
Phys.-Usp. **47**, 855 (2004).

[42] X. M. Tong, Z. X. Zhao, and C. D. Lin,
Theory of molecular tunneling ionization,
Phys. Rev. A **66**, 033402 (2002).

[43] L. V. Keldysh,
Ionization in the Field of a Strong Electromagnetic Wave,
JETP **20**, 1307 (1965).

[44] F. A. Ilkov, J. E. Decker, and S. L. Chin,
Ionization of atoms in the tunnelling regime with experimental evidence using Hg atoms,
J. Phys. B: At. Mol. Opt. Phys. **25**, 4005 (1992).

[45] L. Fechner,
High resolution experiments on strong-field ionization of atoms and molecules: test of tunneling theory, the role of doubly excited states, and channel-selective electron spectra,
PhD Thesis, Max-Planck-Institut für Kernphysik, 2014.

[46] X. M. Tong, Z. X. Zhao, and C. D. Lin,
Correlation dynamics between electrons and ions in the fragmentation of D_2 molecules by short laser pulses, Phys. Rev. A **68**, 043412 (2003).

[47] T. Brabec and F. Krausz,
Intense few-cycle laser fields: Frontiers of nonlinear optics,
Reviews of Modern Physics **72**, 545 (2000).

[48] A. McPherson, G. Gibson, H. Jara, U. Johann, T. S. Luk, I. A. McIntyre, K. Boyer, and C. K. Rhodes,
Studies of multiphoton production of vacuum-ultraviolet radiation in the rare gases,
J. Opt. Soc. Am. B **4**, 595 (1987).

[49] M. Ferray, A. L'Huillier, X. F. Li, L. A. Lompre, G. Mainfray, and C. Manus,

Multiple-harmonic conversion of 1064 nm radiation in rare gases,
Journal of Physics B: Atomic, Molecular and Optical Physics **21**, L31 (1988).

[50] K. C. Kulander and B. W. Shore,
Calculations of Multiple-Harmonic Conversion of 1064-nm Radiation in Xe,
Phys. Rev. Lett. **62**, 524 (1989).

[51] A. L'Huillier, K. J. Schafer, and K. C. Kulander,
Higher-order harmonic generation in xenon at 1064 nm: The role of phase matching,
Phys. Rev. Lett. **66**, 2200 (1991).

[52] P. B. Corkum,
Plasma perspective on strong field multiphoton ionization,
Phys. Rev. Lett. **71**, 1994 (1993).

[53] P. M. Paul, E. S. Toma, P. Breger, G. Mullot, F. Augé, P. Balcou, H. G. Muller, and P. Agostini,
Observation of a Train of Attosecond Pulses from High Harmonic Generation,
Science **292**, 1689 (2001).

[54] J. G. Eden,
High-order harmonic generation and other intense optical field–matter interactions: review of recent experimental and theoretical advances,
Progress in Quantum Electronics **28**, 197 (2004).

[55] H. C. Kapteyn, M. M. Murnane, and I. P. Christov,
Extreme nonlinear optics: Coherent x-rays from lasers,
Physics Today **58**, 39 (2005).

[56] J.-C. Diels and W. Rudolph,
Ultrashort Laser Pulse Phenomena: Fundamentals, Techniques, and Applications on a Femtosecond Time Scale,
Academic Press, 2006.

[57] H. Rietz,
Attosekundenphysik mit dem Reaktionsmikroskop: Eine Konzeptstudie, erste Experimente und mögliche Anwendungen,
PhD Thesis, Max-Planck-Institut für Kernphysik, 2012.

[58] R. Gopal,
Electron Wave Packet Interferences in Ionization with Few-Cycle Laser Pulses and the Dissociative Photoionization of D_2 with Ultrashort Extreme Ultraviolet Pulses,
PhD Thesis, Max-Planck-Institut für Kernphysik, 2007.

[59] A. Sperl,
XUV-IR pump-probe experiments: Exploring nuclear and electronic correlated quan-

tum dynamics in the hydrogen molecule,
PhD Thesis, Max-Planck-Institut für Kernphysik, 2013.

[60] J. L. Krause, K. J. Schafer, and K. C. Kulander,
High-order harmonic generation from atoms and ions in the high intensity regime,
Phys. Rev. Lett. **68**, 3535 (1992).

[61] K. J. Schafer, B. Yang, L. F. DiMauro, and K. C. Kulander,
Above threshold ionization beyond the high harmonic cutoff,
Phys. Rev. Lett. **70**, 1599 (1993).

[62] Z. Chang,
Fundamentals of Attosecond Optics,
CRC Press, 2011.

[63] M. Lewenstein, P. Balcou, M. Y. Ivanov, A. L'Huillier, and P. B. Corkum,
Theory of high-harmonic generation by low-frequency laser fields,
Phys. Rev. A **49**, 2117 (1994).

[64] M. Y. Ivanov, M. Spanner, and O. Smirnova,
Anatomy of strong field ionization,
Journal of Modern Optics **52**, 165 (2005).

[65] H. Friedrich,
Theoretical Atomic Physics,
Springer, 2005.

[66] F. Engelke,
Aufbau der Moleküle: Eine Einführung,
Teubner Verlag, Stuttgart, 3. edition, 1996.

[67] D. Willock,
Molecular Symmetry,
John Wiley & Sons, Chichester, UK, 1. edition, 2009.

[68] P. Bunker,
Molecular Symmetry and Spectroscopy,
Bertrams, Ottawa, 2nd revised edition, 2009.

[69] P. W. Atkins and R. S. Friedman,
Molecular Quantum Mechanics,
Oxford University Press, Oxford; New York, 5th. edition, 2010.

[70] P. YU and M. Cardona,
Fundamentals of Semiconductors: Physics and Materials Properties,
Springer Science & Business Media, 2010.

[71] J. Ullrich, R. Moshammer, A. Dorn, R. Dörner, L. P. H. Schmidt, and H. Schmidt-Böcking,
Recoil-ion and electron momentum spectroscopy: reaction-microscopes,
Reports on Progress in Physics **66**, 1463 (2003).

[72] R. Moshammer, D. Fischer, and H. Kollmus,
Recoil-Ion Momentum Spectroscopy and "Reaction Microscope", in *Many-Particle Quantum Dynamics in Atomic and Molecular Fragmentation*, edited by J. Ullrich and V. Shevelko, number 35 in Springer Series on Atomic, Optical, and Plasma Physics, pages 33–58,
Springer Berlin Heidelberg, 2003.

[73] D. E. Spence, P. N. Kean, and W. Sibbett,
60-fsec pulse generation from a self-mode-locked Ti:sapphire laser,
Opt. Lett. **16**, 42 (1991).

[74] T. Brabec, C. Spielmann, P. F. Curley, and F. Krausz,
Kerr lens mode locking,
Opt. Lett. **17**, 1292 (1992).

[75] G. Cerullo, S. De Silvestri, V. Magni, and L. Pallaro,
Resonators for Kerr-lens mode-locked femtosecond Ti:sapphire lasers,
Opt. Lett. **19**, 807 (1994).

[76] C. E. Cook,
Pulse compression-key to more efficient radar transmission,
Proceedings of the IRE **48**, 310 (1960).

[77] D. Strickland and G. Mourou,
Compression of amplified chirped optical pulses,
Optics communications **55**, 447 (1985).

[78] A. Ghatak,
Optics,
Science Engineering & Math, 1st edition, 2011.

[79] R. Szipöcs, C. Spielmann, F. Krausz, and K. Ferencz,
Chirped multilayer coatings for broadband dispersion control in femtosecond lasers,
Opt. Lett. **19**, 201 (1994).

[80] R. L. Fork, C. H. B. Cruz, P. C. Becker, and C. V. Shank,
Compression of optical pulses to six femtoseconds by using cubic phase compensation,
Opt. Lett. **12**, 483 (1987).

[81] A. Baltuska, Z. Wei, M. S. Pshenichnikov, and D. A. Wiersma,
Optical pulse compression to 5 fs at a 1-MHz repetition rate,
Opt. Lett. **22**, 102 (1997).

[82] P. Kirkpatrick and A. V. Baez,
Formation of Optical Images by X-Rays,
Journal of the Optical Society of America **38**, 766 (1948).

[83] H. Rietz,
Aufbau und Inbetriebnahme einer Apparatur zur Erzeugung hoher harmonischer Strahlung und deren Charakterisierung,
Diploma Thesis, Max-Planck-Institut für Kernphysik, 2007.

[84] P. Cörlin,
Laser induced Coulomb-explosions of allene molecules: Experiment and simulation,
Diploma Thesis, Max-Planck-Institut für Kernphysik, 2012.

[85] D. Fischer,
Mehr-Teilchen-Dynamik in der Einfach- und Doppelionisation von Helium durch geladene Projektile,
PhD Thesis, Max-Planck-Institut für Kernphysik, 2003.

[86] G. Scoles,
Atomic and Molecular Beam Methods (Vol. I),
Oxford University Press, 1988.

[87] H. T. Schmidt, H. Cederquist, R. Schuch, L. Bagge, A. Källberg, J. Hilke, K.-G. Rensfelt, V. Mergel, M. Achler, R. Dörner, L. Spielberger, O. Jagutzki, H. Schmidt-Böcking, J. Ullrich, H. Reich, M. Unverzagt, W. Schmitt, and R. Moshammer,
A design study for an internal gas-jet target for the heavy-ion storage ring CRYRING,
Hyperfine Interactions **108**, 339 (1997).

[88] S. Zhang, X. Ma, H. Liu, B. Li, and X. Zhu,
Properties and applications of cold supersonic gas jet,
SCI CHINA SER G **49**, 709 (2006).

[89] J. L. Wiza,
Microchannel plate detectors,
Nuclear Instruments and Methods **162**, 587 (1979).

[90] O. Jagutzki, V. Mergel, K. Ullmann-Pfleger, L. Spielberger, U. Spillmann, R. Dörner, and H. Schmidt-Böcking,
A broad-application microchannel-plate detector system for advanced particle or photon detection tasks: large area imaging, precise multi-hit timing information and high detection rate,
Nuclear Instruments and Methods in Physics Research Section A: Accelerators, Spectrometers, Detectors and Associated Equipment **477**, 244 (2002).

[91] T. Pflüger,
Electron Impact Single Ionization of Small Argon Clusters,
PhD Thesis, Max-Planck-Institut für Kernphysik, 2008.

[92] A. Senftleben,
Kinematically complete study on electron impact ionisation of aligned hydrogen molecules,
PhD Thesis, Max-Planck-Institut für Kernphysik, 2009.

[93] T. J. Reddish, A. Padmanabhan, M. A. MacDonald, L. Zuin, J. Fernández, A. Palacios, and F. Martín,
Observation of Interference between Two Distinct Autoionizing States in Dissociative Photoionization of H_2,
Physical Review Letters **108**, 023004 (2012).

[94] R. E. F. Silva, P. Rivière, and F. Martín,
Autoionizing decay of H_2 *doubly excited states by using xuv-pump infrared-probe schemes with trains of attosecond pulses*,
Physical Review A **85**, 063414 (2012).

[95] M. F. Kling, C. Siedschlag, A. J. Verhoef, J. I. Khan, M. Schultze, T. Uphues, Y. Ni, M. Uiberacker, M. Drescher, F. Krausz, and M. J. J. Vrakking,
Control of Electron Localization in Molecular Dissociation,
Science **312**, 246 (2006).

[96] M. Kremer, B. Fischer, B. Feuerstein, V. L. B. de Jesus, V. Sharma, C. Hofrichter, A. Rudenko, U. Thumm, C. D. Schröter, R. Moshammer, and J. Ullrich,
Electron Localization in Molecular Fragmentation of H_2 *by Carrier-Envelope Phase Stabilized Laser Pulses*,
Physical Review Letters **103**, 213003 (2009).

[97] B. Fischer, M. Kremer, T. Pfeifer, B. Feuerstein, V. Sharma, U. Thumm, C. D. Schröter, R. Moshammer, and J. Ullrich,
Steering the Electron in H_2^+ *by Nuclear Wave Packet Dynamics*,
Phys. Rev. Lett. **105**, 223001 (2010).

[98] G. Sansone, F. Kelkensberg, J. F. Pérez-Torres, F. Morales, M. F. Kling, W. Siu, O. Ghafur, P. Johnsson, M. Swoboda, E. Benedetti, F. Ferrari, F. Lépine, J. L. Sanz-Vicario, S. Zherebtsov, I. Znakovskaya, A. L'Huillier, M. Y. Ivanov, M. Nisoli, F. Martín, and M. J. J. Vrakking,
Electron localization following attosecond molecular photoionization,
Nature **465**, 763 (2010).

[99] K. P. Singh, F. He, P. Ranitovic, W. Cao, S. De, D. Ray, S. Chen, U. Thumm, A. Becker, M. M. Murnane, H. C. Kapteyn, I. V. Litvinyuk, and C. L. Cocke,

Control of Electron Localization in Deuterium Molecular Ions using an Attosecond Pulse Train and a Many-Cycle Infrared Pulse,
Physical Review Letters **104**, 023001 (2010).

[100] F. Kelkensberg, W. Siu, J. F. Pérez-Torres, F. Morales, G. Gademann, A. Rouzée, P. Johnsson, M. Lucchini, F. Calegari, J. L. Sanz-Vicario, F. Martín, and M. J. J. Vrakking,
Attosecond Control in Photoionization of Hydrogen Molecules,
Physical Review Letters **107**, 043002 (2011).

[101] J. F. Pérez-Torres, F. Morales, J. L. Sanz-Vicario, and F. Martín,
Asymmetric electron angular distributions in resonant dissociative photoionization of H_2 *with ultrashort XUV pulses*,
Physical Review A **80**, 011402 (2009).

[102] P. Billaud, M. Géléoc, Y. J. Picard, K. Veyrinas, J. F. Hergott, S. Marggi Poullain, P. Breger, T. Ruchon, M. Roulliay, F. Delmotte, F. Lepetit, A. Huetz, B. Carré, and D. Dowek,
Molecular frame photoemission in dissociative ionization of H_2 *and* D_2 *induced by high harmonic generation femtosecond XUV pulses*,
J. Phys. B: At. Mol. Opt. Phys. **45**, 194013 (2012).

[103] U. Fano,
Effects of Configuration Interaction on Intensities and Phase Shifts,
Phys. Rev. **124**, 1866 (1961).

[104] A. Palacios, J. Feist, A. González-Castrillo, J. L. Sanz-Vicario, and F. Martín,
Autoionization of Molecular Hydrogen: Where do the Fano Lineshapes Go?,
ChemPhysChem **14**, 1456–1463 (2013).

[105] L. A. Collins, B. I. Schneider, C. J. Noble, C. W. McCurdy, and S. Yabushita,
Interfering Resonances: Avoided Crossings of Autoionizing States in Molecules,
Phys. Rev. Lett. **57**, 980 (1986).

[106] L. A. Collins, B. I. Schneider, and C. J. Noble,
Electron scattering from H_2^+*: Resonances in the* Π *symmetries*,
Phys. Rev. A **45**, 4610 (1992).

[107] M. Iwai, S. Lee, and H. Nakamura,
Electron correlation in doubly excited states of the hydrogen molecule,
Phys. Rev. A **47**, 2686 (1993).

[108] J. Geddes, K. F. Dunn, N. Kouchi, M. A. McDonald, V. Srigengan, and C. J. Latimer,
Isotope effects in the autoionization of superexcited $^1\Sigma_u^+(Q_1)$ *states in hydrogen*,
J. Phys. B: At. Mol. Opt. Phys. **27**, 2961 (1994).

[109] L. A. Collins, B. I. Schneider, D. L. Lynch, and C. J. Noble,
Electron scattering from H_2^+*: Resonances in the* Σ *and* Π *symmetries*,
Phys. Rev. A **52**, 1310 (1995).

[110] J. Fernández and F. Martin,
Autoionizing $^1\Sigma_u^+$ *and* $^1\Pi_u$ *states of H2 above the third and fourth ionization thresholds*,
J. Phys. B: At. Mol. Opt. Phys. **34**, 4141 (2001).

[111] J. L. Sanz-Vicario, H. Bachau, and F. Martín,
Time-dependent theoretical description of molecular autoionization produced by femtosecond xuv laser pulses,
Phys. Rev. A **73**, 033410 (2006).

[112] S. Gasiorowicz,
Quantenphysik,
Oldenbourg Wissenschaftsverlag, vollständig überarbeitete und erweiterte 9. edition, 2005.

[113] B. H. Bransden and C. J. Joachain,
Physics of Atoms and Molecules,
Addison-Wesley, 2nd edition, 2003.

[114] M. A. M. de Aguiar,
The WKB Approximation,
`http://www.ifi.unicamp.br/~aguiar/Cursos/FI001/wkb.pdf`, 2013.

[115] B. H. Bransden and C. J. Joachain,
Quantum Mechanics,
Prentice Hall, revised 2nd edition, 2000.

[116] D. Bohm,
A Suggested Interpretation of the Quantum Theory in Terms of "Hidden" Variables. I,
Phys. Rev. **85**, 166 (1952).

[117] D. Bohm,
A Suggested Interpretation of the Quantum Theory in Terms of "Hidden" Variables. II,
Phys. Rev. **85**, 180 (1952).

[118] S. Garashchuk and V. A. Rassolov,
Semiclassical dynamics based on quantum trajectories,
Chemical Physics Letters **364**, 562 (2002).

[119] A. C. Randono,

In Search of Quantum de Sitter Space: Generalizing the Kodama State,
ProQuest, 2007.

[120] K. B. Lipkowitz,
Reviews in Computational Chemistry,
John Wiley & Sons, 2010.

[121] E. Rebhan,
Theoretische Physik, Bd. 1, Mechanik, Elektrodynamik, Spezielle und Allgemeine Relativitätstheorie, Kosmologie,
Spektrum Akademischer Verlag, Heidelberg; Berlin, auflage: 1. aufl. 1999. korr. nachdruck edition, 1999.

[122] E. U. Condon,
Nuclear Motions Associated with Electron Transitions in Diatomic Molecules,
Phys. Rev. **32**, 858 (1928).

[123] W. Demtröder,
Experimentalphysik 3: Atome, Moleküle und Festkörper,
Springer, 2005.

[124] H. Haken and H. C. Wolf,
Molekülphysik und Quantenchemie: Einführung in die experimentellen und theoretischen Grundlagen,
Springer, Berlin u.a., 5th edition, 2006.

[125] I. V. Hertel and C.-P. Schulz,
Atome, Moleküle und optische Physik 2: Moleküle und Photonen - Spektroskopie und Streuphysik,
Springer, Berlin, 2010.

[126] J. Förster, A. Saenz, and U. Wolff,
Matrix algorithm for solving Schrödinger equations with position-dependent mass or complex optical potentials,
Phys. Rev. E **86**, 016701 (2012).

[127] M. Glass-Maujean,
Photodissociation of doubly excited states of H_2: Emission of Balmer lines,
The Journal of Chemical Physics **89**, 2839 (1988).

[128] I. Borges Jr. and C. E. Bielschowsky,
On the semiclassical dissociation yields of the doubly excited states of H_2,
Chemical Physics Letters **342**, 411 (2001).

[129] M. Glass-Maujean and H. Schmoranzer,
Dissociation dynamics of doubly excited states of molecular hydrogen,
Journal of Physics B: Atomic, Molecular and Optical Physics **38**, 1093 (2005).

[130] I. Sánchez and F. Martín,
Multichannel Dissociation in Resonant Photoionization of H_2,
Phys. Rev. Lett. **82**, 3775 (1999).

[131] A. Fischer, A. Sperl, P. Cörlin, M. Schönwald, H. Rietz, A. Palacios, A. González-Castrillo, F. Martín, T. Pfeifer, J. Ullrich, A. Senftleben, and R. Moshammer,
Electron Localization Involving Doubly Excited States in Broadband Extreme Ultraviolet Ionization of H_2,
Phys. Rev. Lett. **110**, 213002 (2013).

[132] A. Fischer, A. Sperl, P. Cörlin, M. Schönwald, S. Meuren, J. Ullrich, T. Pfeifer, R. Moshammer, and A. Senftleben,
Measurement of the autoionization lifetime of the energetically lowest doubly excited $Q_1\,{}^1\Sigma_u^+$ *state in* H_2 *using electron ejection asymmetry*,
J. Phys. B: At. Mol. Opt. Phys. **47**, 021001 (2014).

[133] I. Sánchez and F. Martín,
Origin of Unidentified Structures in Resonant Dissociative Photoionization of H_2,
Phys. Rev. Lett. **79**, 1654 (1997).

[134] J. C. Browne and A. Dalgarno,
Detachment in collisions of H and H^-,
Journal of Physics B: Atomic and Molecular Physics **2**, 885 (1969).

[135] W. H. Miller,
Theory of Penning Ionization. I. Atoms,
The Journal of Chemical Physics **52**, 3563 (1970).

[136] A. Scrinzi, M. Y. Ivanov, R. Kienberger, and D. M. Villeneuve,
Attosecond physics,
J. Phys. B: At. Mol. Opt. Phys. **39**, R1 (2006).

[137] M. Magrakvelidze, A. Kramer, K. Bartschat, and U. Thumm,
Complementary imaging of the nuclear dynamics in laser-excited diatomic molecular ions in the time and frequency domains,
J. Phys. B: At. Mol. Opt. Phys. **47**, 124003 (2014).

[138] S. De, M. Magrakvelidze, I. A. Bocharova, D. Ray, W. Cao, I. Znakovskaya, H. Li, Z. Wang, G. Laurent, U. Thumm, M. F. Kling, I. V. Litvinyuk, I. Ben-Itzhak, and C. L. Cocke,
Following dynamic nuclear wave packets in N_2,O_2, *and CO with few-cycle infrared pulses*,
Phys. Rev. A **84**, 043410 (2011).

[139] C. Ott, A. Kaldun, P. Raith, K. Meyer, M. Laux, J. Evers, C. H. Keitel, C. H.

Greene, and T. Pfeifer,
Lorentz Meets Fano in Spectral Line Shapes: A Universal Phase and Its Laser Control,
Science **340**, 716 (2013).

[140] C. D. Lin and W.-C. Chu,
Controlling Atomic Line Shapes,
Science **340**, 694 (2013).

[141] A. Kaldun, C. Ott, A. Blättermann, M. Laux, K. Meyer, T. Ding, A. Fischer, and T. Pfeifer,
Extracting Phase and Amplitude Modifications of Laser-Coupled Fano Resonances,
Phys. Rev. Lett. **112**, 103001 (2014).

[142] M. Magrakvelidze, C. M. Aikens, and U. Thumm,
Dissociation dynamics of diatomic molecules in intense laser fields: A scheme for the selection of relevant adiabatic potential curves,
Phys. Rev. A **86**, 023402 (2012).

[143] M. Magrakvelidze, O. Herrwerth, Y. H. Jiang, A. Rudenko, M. Kurka, L. Foucar, K. U. Kühnel, M. Kübel, N. G. Johnson, C. D. Schröter, S. Düsterer, R. Treusch, M. Lezius, I. Ben-Itzhak, R. Moshammer, J. Ullrich, M. F. Kling, and U. Thumm,
Tracing nuclear-wave-packet dynamics in singly and doubly charged states of N_2 *and* O_2 *with XUV-pump–XUV-probe experiments*,
Phys. Rev. A **86**, 013415 (2012).

[144] S. H. Ashworth, T. Hasche, M. Woerner, E. Riedle, and T. Elsaesser,
Vibronic excitations of large molecules in solution studied by two-color pump-probe experiments on the 20 fs time scale,
The Journal of Chemical Physics **104**, 5761 (1996).

[145] A. Assion, M. Geisler, J. Helbing, V. Seyfried, and T. Baumert,
Femtosecond pump-probe photoelectron spectroscopy: Mapping of vibrational wave-packet motion,
Phys. Rev. A **54**, R4605 (1996).

[146] A. Stolow, A. E. Bragg, and D. M. Neumark,
Femtosecond Time-Resolved Photoelectron Spectroscopy,
Chem. Rev. **104**, 1719 (2004).

[147] F. Lépine, M. Y. Ivanov, and M. J. J. Vrakking,
Attosecond molecular dynamics: fact or fiction?,
Nat. Photon **8**, 195 (2014).

[148] R. J. Levis, G. M. Menkir, and H. Rabitz,

Selective Bond Dissociation and Rearrangement with Optimally Tailored, Strong-Field Laser Pulses,
Science **292**, 709 (2001).

[149] A. Szabo,
Modern Quantum Chemistry: Introduction to Advanced Electronic Structure Theory,
Courier Dover Publications, 1996.

[150] R. Bluhm, V. Alan Kostelecký, and B. Tudose,
Wave-packet revivals for quantum systems with nondegenerate energies,
Physics Letters A **222**, 220 (1996).

[151] I. S. Averbukh and N. F. Perelman,
Fractional revivals: Universality in the long-term evolution of quantum wave packets beyond the correspondence principle dynamics,
Physics Letters A **139**, 449 (1989).

[152] S. I. Vetchinkin, A. S. Vetchinkin, V. V. Eryomin, and I. M. Umanskii,
Gaussian wavepacket dynamics in an anharmonic system,
Chemical Physics Letters **215**, 11 (1993).

[153] M. J. J. Vrakking, D. M. Villeneuve, and A. Stolow,
Observation of fractional revivals of a molecular wave packet,
Phys. Rev. A **54**, R37 (1996).

[154] P. M. Morse,
Diatomic Molecules According to the Wave Mechanics. II. Vibrational Levels,
Phys. Rev. **34**, 57 (1929).

[155] E. Schrödinger,
Quantisierung als Eigenwertproblem I,
Ann. Phys. **79**, 361 (1926).

[156] E. Schrödinger,
Qunatisierung als Eigenwertproblem II,
Ann. Phys. **79**, 489 (1926).

[157] E. Schrödinger,
Qunatisierung als Eigenwertproblem III,
Ann. Phys. **80**, 734 (1926).

[158] E. Schrödinger,
Qunatisierung als Eigenwertproblem IV,
Ann. Phys. **81**, 109 (1926).

[159] J. J. Sakurai,
Modern Quantum Mechanics,
Prentice Hall, Reading, Mass, revised edition, 1993.

[160] E. Rebhan,
Theoretische Physik Bd.2 Quantenmechanik, Relativistische Quantenmechanik, Quantenfeldtheorie, Elementarteilchentheorie, Thermodynamik und Statistik,
Spektrum Akademischer Verlag, Heidelberg u.a., 1st edition, 2005.

[161] J. A. Fleck Jr., J. R. Morris, and M. D. Feit,
Time-dependent propagation of high energy laser beams through the atmosphere,
Appl. Phys. **10**, 129 (1976).

[162] M. D. Feit, J. A. Fleck Jr., and A. Steiger,
Solution of the Schrödinger equation by a spectral method,
Journal of Computational Physics **47**, 412 (1982).

[163] A. Askar and A. S. Cakmak,
Explicit integration method for the time-dependent Schrödinger equation for collision problems,
The Journal of Chemical Physics **68**, 2794 (1978).

[164] M. R. Hermann and J. A. Fleck,
Split-operator spectral method for solving the time-dependent Schrödinger equation in spherical coordinates,
Phys. Rev. A **38**, 6000 (1988).

[165] A. D. Bandrauk and H. Shen,
Exponential split operator methods for solving coupled time-dependent Schrödinger equations,
The Journal of Chemical Physics **99**, 1185 (1993).

[166] T. Y. Mikhailova and V. I. Pupyshev,
Symmetric approximations for the evolution operator,
Physics Letters A **257**, 1 (1999).

[167] R. I. McLachlan and G. R. W. Quispel,
Splitting methods,
Acta Numerica **11**, 341 (2002).

[168] J. P. Hansen, T. Matthey, and T. Sørevik,
A Parallel Split Operator Method for the Time Dependent Schrödinger Equation, in *Recent Advances in Parallel Virtual Machine and Message Passing Interface*, edited by J. Dongarra, D. Laforenza, and S. Orlando, number 2840 in Lecture Notes in Computer Science, pages 503–510,
Springer Berlin Heidelberg, 2003.

[169] H. Bauke and C. H. Keitel,
Accelerating the Fourier split operator method via graphics processing units,
Computer Physics Communications **182**, 2454 (2011).

[170] J. H. Shirley,
Solution of the Schrödinger Equation with a Hamiltonian Periodic in Time,
Phys. Rev. **138**, B979 (1965).

[171] S.-I. Chu,
Floquet theory and complex quasivibrational energy formalism for intense field molecular photodissociation,
The Journal of Chemical Physics **75**, 2215 (1981).

[172] S. H. Autler and C. H. Townes,
Stark Effect in Rapidly Varying Fields,
Phys. Rev. **100**, 703 (1955).

[173] A. M. F. Lau,
Radiative-dressed molecules: Ab initio theory and single/multiphoton dissociation with electronic transitions,
Phys. Rev. A **16**, 1535 (1977).

[174] P. R. Berman and J. Ziegler,
Generalized dressed-atom approach to atom-strong-field interactions—application to the theory of lasers and Bloch-Siegert shifts,
Phys. Rev. A **15**, 2042 (1977).

[175] C. Kittel,
Introduction to Solid State Physics,
John Wiley & Sons, Hoboken, NJ, 2004.

[176] S. Hunklinger,
Festkörperphysik,
Oldenbourg Wissenschaftsverlag, 2014.

[177] F. Grossmann,
Theoretical Femtosecond Physics: Atoms and Molecules in Strong Laser Fields,
Springer, Berlin, 2008.

[178] P. C. J. Joachain, N. J. Kylstra, and R. M. Potvliege,
Atoms in Intense Laser Fields,
Cambridge University Press, 2014.

[179] H. Sambe,
Steady States and Quasienergies of a Quantum-Mechanical System in an Oscillating Field,
Phys. Rev. A **7**, 2203 (1973).

[180] M. V. Kuz'min and V. N. Sazonov,
Complete population inversion in a multilevel quantum system on adiabatic applica-

tion of an external resonance field,
JETP **79**, 1759 (1980).

[181] D. Pavičić,
Coulomb Explosion and Intense-Field Photodissociation of Ion-Beam H_2^+ *and* D_2^+,
PhD Thesis, Ludwig–Maximilians–Universität Müunchen, 2004.

[182] T. Ergler,
Zeitaufgelöste Untersuchungen zur Fragmentationsdynamik von H_2 *(*D_2*) in ultrakurzen Laserpulsen*,
PhD Thesis, Max-Planck-Institut für Kernphysik, 2006.

[183] J. Fernández and F. Martín,
Electron and ion angular distributions in resonant dissociative photoionization of H_2 *and* D_2 *using linearly polarized light*,
New J. Phys. **11**, 043020 (2009).

[184] C. Lefebvre, T. T. Nguyen-Dang, F. Dion, M. J. J. Vrakking, V. N. Serov, and O. Atabek,
Attosecond pump-probe transition-state spectroscopy of laser-induced molecular dissociative ionization: Adiabatic versus nonadiabatic dressed-state dynamics,
Phys. Rev. A **88**, 053416 (2013).

[185] T. Niederhausen, U. Thumm, and F. Martín,
Laser-controlled vibrational heating and cooling of oriented H_2^+ *molecules*,
Journal of Physics B: Atomic, Molecular and Optical Physics **45**, 105602 (2012).

[186] P. J. Mohr, B. N. Taylor, and D. B. Newell,
CODATA Recommended Values of the Fundamental Physical Constants: 2010,
arXiv:1203.5425 [physics] (2012), arXiv: 1203.5425.

Danksagung

Abschließend möchte ich allen danken, die zum Gelingen dieser Arbeit beigetragen haben:

In erster Linie gilt mein ganz besonderer Dank meinem Betreuer **Robert Moshammer**, der mir die Gelegenheit bot meine Doktorarbeit an einem spannenden Thema zur Molekülphysik durchzuführen. Du hast mir mit deinem intuitiven Verständnis von Physik in unzähligen Diskussionen viel vermittelt und meine Begeisterung für die Physik angefacht. *"Ich hab da mal eine ganz einfache Frage ..."* und *"Jetzt mal Butter bei die Fisch ..."* waren der Anfang von vielen Erkenntnissen für mich.

Thomas Pfeifer möchte ich für seine vielen guten Ratschläge danken. Besonders die ständige Motivation die du mir gegeben hast, hat mir geholfen meine Ziele zu erreichen.

Ich danke **Joachim Ullrich** für die freundliche Aufnahme in seiner Gruppe. Selbst nach deinem Umzug an die PTB hast du mir in vielen Gesprächen wertvolle Tipps gegeben.

Selim Jochim, der sofort als Zweitkorrektor eingesprungen ist und mir so sehr geholfen hat.

Nicht zu vergessen sind **Alexander Sperl** und **Philipp Cörlin**. Ohne euch wäre diese Arbeit nicht Denkbar gewesen. Außerdem habt ihr durch eure gute Laune eine hervorragende Arbeitsatmosphäre geschaffen.

Martin Gärttner, der seit dem Mathe-Vorkurs an meiner Seite durch das Physikstudium ging. Die Teepausen auf unserem "Denkstein" bleiben unvergessen. Deine Freude an Physik spornte zu vielen spannenden Diskussionen an und gab mir ständig neue Motivation. Auch für das unermüdliche Korrekturlesen von Arbeiten und Manuskripten danke ich dir sehr.

Andreas Kaldun, der mir die Gelegenheit gegeben hat an anderen Physikprojekten mitzuarbeiten. Du hast mich in den letzten Jahren stets motiviert und immer wieder aufgebaut wenn ich am Boden war.

Sebastian Meuren möchte ich für seinen anhaltenden Theorie-Support danken. Die enge Zusammenarbeit mit dir, bei der wir immer viel Spaß hatten, wird mir stets in bester Erinnerung bleiben.

Aber auch meinen Laborkollegen **Michael Schönwald**, **Tomoya Mizuno**, **Helga Rietz** und **Ram Gopal** gebührt mein Dank.

Arne Senftleben, der mir viel über Moleküle beigebracht hat möchte ich hier auch danken.

Giuseppe Sansone, mit dem man auch auf Hochzeiten Probleme und Möglichkeiten des experimentellen Aufbaus diskutieren kann. Ich danke dir auch für deine vielen Hinweise die du mir im Laufe der Jahre gegeben hast.

Bernold Feuerstein der immer ein offenes Ohr für allerlei physikalischer Probleme hatte und mit seinem *Know-How* oft helfen konnte diese zu lösen.

Meinen Kollegen und ehemaligen Kollegen **Nicolas Camus**, **Lutz Fechner**, **Johannes Goullon**, **Kilian Heeg**, **Renate Hubele**, **Siva Rama Krishnan**, **Christian Ott**, **Thomas Pflüger**, **Kirsten Schnorr**, **Michael Schuricke**, **Vandana Sharma**, **Marvin Weyland** und **Lida Zhang** möchte ich für die gute Zeit am MPI danken.

Ich möchte mich auch bei **Konstantinos Simeonidis**, **Bernd Knape** und **Claus Dieter Schröter** bedanken, die mir oft mit Rat-und-Tat geholfen haben Probleme im Labor zu lösen.

Ich danke allen **Korrekturlesern**, denn ihr habt mir einige Peinlichkeiten erspart.

Ganz besonderer Dank gebührt an dieser Stelle meiner Familie. **Alfred**, **Marion**, **Kevin** und **Julie**, ihr habt mich immer unterstützt, zu mir gestanden und mir somit, nach meinem Studium, auch die Promotion möglich gemacht.